ELECTRONIC AND OPTICAL PROPERTIES OF HYBRID GOLD – ORGANIC DYE SYSTEMS

A Dissertation
Presented to
The Academic Faculty

By

Michal Malicki

In Partial Fulfillment
Of the Requirements for the Degree
Doctor of Philosophy in Chemistry

Georgia Institute of Technology

December 2009

ELECTRONIC AND OPTICAL PROPERTIES OF HYBRID GOLD – ORGANIC DYE SYSTEMS

Dr. Seth R. Marder
School of Chemistry and Biochemistry
Georgia Institute of Technology

Dr. Robert M. Dickson
School of Chemistry and Biochemistry
Georgia Institute of Technology

Dr. Joseph W. Perry
School of Chemistry and Biochemistry
Georgia Institute of Technology

Dr. Elisa Riedo
School of Physics
Georgia Institute of Technology

Dr. Mostafa A. El-Sayed
School of Chemistry and Biochemistry
Georgia Institute of Technology

Date Approved: *September 28, 2009*

Pracę tę Dedykuję Moim Wspaniałym Rodzicom,

bez których Pomocy i Wsparcia

ta Rozprawa Doktorska Nigdy nie Zostałaby Sfinalizowana.

ACKNOWLEDGEMENTS

The first person I feel I must thank to is my uncle, Prof. Jerzy Pączkowski. I can still remember my childhood conversations with him about astronomy, physics and chemistry. His passion for science and the will to share that passion with me sparked my interest in physics and chemistry, and today I can say with certainty that he was the one person without whom I would not choose to be a scientist. I want to thank him especially for bringing my attention to physical chemistry and to spectroscopy in particular.

I want to thank Prof. Seth Marder, my advisor, for patience and for leaving it for me to decide when to start doing science. I feel like I have started and it would not have happened if it were not for Seth's patience. I am also grateful to him for teaching me to question everything.

I am eternally grateful to Prof. Joseph Perry for the opportunity to carry out research in his laboratory. I also want to thank Joe for being patient with me and for giving me the scientific freedom to pursue my interests.

I must thank to Dr. Stephen Barlow for much help throughout the years, both in his professional capacity and on the personal level. I appreciate very much Steve's passion for chemistry and his vast knowledge and I feel privileged I could work with him. My highest gratitude goes to Dr. Mariacristina Rumi who had the greatest influence on me in terms of the clarity and precision of her scientific arguments. I want to thank Cristina for all the help throughout the years but especially I am grateful to her for taking the time and showing me how to formulate precise scientific arguments. This will stay

with me forever. I also want to thank to both Steve and Cristina for all the help with the preparation of this thesis.

I want to acknowledge Dr. Joel Hales for all the help in the laser lab. It is clear to me that without Joel this thesis would not be finished. For this I am grateful.

My thanks for all the help go to Sarah Chi, Matteo Cozzuol and Vincent Chen. I am forever grateful to my dear friend Wojtek Haske for all the help he gave me in the lab and on the personal level.

I feel thankful to Dr. Simon Jones who was very helpful to me in my early days in the laboratory. I want to acknowledge Chun Huang, Dr. Yulia Getmanenko, Dr. Susan Odom, Dr. Peter Hotchkiss, Dr. Luca Beverina, and many other members of the Marder group who helped me throughout the years.

Special thanks go to collaborators at Princeton University: Prof. Antoine Kahn, Dr. Zelei Guan and Dr. Sieu Ha.

I also want to acknowledge all friends and coworkers with whom I share great memories.

Finally, I want to thank my dearest friend Sabriya Rice who always supported me unconditionally, for which I am eternally grateful.

TABLE OF CONTENTS

ACKNOWLEDGEMENTS iv
LIST OF TABLES xi
LIST OF FIGURES xii
LIST OF SYMBOLS AND ABBREVIATIONS xxi
SUMMARY xxii

CHAPTER 1 INTRODUCTION 1
1.1. Influence of Organic Thiols on the Work Function of Coinage Metals 3
1.1.1. Work Function of Metals – Physical Description 3
1.1.2. Work Function of Metallic Surfaces – Methods of Measurement 5
1.1.3. Work Function of Metals – Implications for Organic Electronics Applications 9
1.1.4. Work Function of Metals – Influence of Adsorbates 12
1.1.5. Self-Assembled Monolayers of Organic Thiols on Metals 14
1.1.6. Self-Assembled Monolayers of Alkanethiols and their Influence on the Work Function of Metals 15
1.1.7. Self-Assembled Monolayers of Conjugated Thiols and their Influence on the Work Function of Metals 23
1.1.8. Self-Assembled Monolayers on Gold - Thesis Motivation 29
1.2. The Fates of Excited States of Organic Dyes on Gold Nanoparticles 31
1.2.1. Gold Nanoparticles – Historical Perspective 31
1.2.2. Gold Nanoparticles – Surface Plasmon Resonance 34
1.2.3. Gold Nanoparticles – Surface Plasmon Resonance Dynamics 39
1.2.4. Noble Metal Nanoparticles – Local Field Effects 42
1.2.5. Gold Nanoparticle / Organic Dye Systems and their Photophysics 44
1.2.5.1. Energy Transfer to the Nanoparticle and Radiative Rate Modification 46
1.2.5.2. Electron Transfer to the Nanoparticle 53
1.2.5.3. Intermolecular Interactions 55
1.2.6. Gold Nanoparticles – Thesis Motivation 58

1.3. References 61
CHAPTER 2 MATERIALS AND METHODS 66
2.1 Materials 66
2.1.1 General 66
2.1.2 Synthesis 67
2.2. Experimental Methodology 89
2.2.1. Sample Preparation and Manipulation 89
2.2.1.1. SAMs on Flat Gold 89
2.2.1.2. Gold Nanoparticle Samples 90
2.2.2. Measurement Details 91
2.2.2.1. FT-IR 91
2.2.2.2. XPS 92
2.2.2.3. UPS 92
2.2.2.4. Ellipsometry 93
2.2.2.5. STM 94
2.2.2.6. Calculations 95
2.2.2.7. Steady-state UV-Vis-NIR absorption and fluorescence spectroscopy 95
2.2.2.8. NMR experiments for establishing T_1 and T_2 relaxation times 95
2.2.2.9. Transmission Electron Microscopy (TEM) 96
2.2.2.10. Electrochemical Measurements 96
2.2.2.11. Time-Correlated Single Photon Counting (TC-SPC) 96
2.2.2.12. Nanosecond Transient Absorption (TA) 99
2.2.2.13. Femtosecond Broad-Band-NIR Transient Absorption 101
2.3. References 109
CHAPTER 3 PREPARATION AND CHARACTERIZATION OF SELF ASSEMBLED MONOLAYERS OF STILBENE THIOLATES ON FLAT GOLD SURFACES 110
3.1. Introduction 110
3.2. Synthesis and Monolayer Preparation 111
3.2.1. Synthesis of S-thioacetyl Protected Stilbenes 111
3.2.2. Preparation of Monolayers 112
3.3. Characterization of SAMs 114
3.3.1. XPS 114

3.3.1.1. Elemental Composition 114
3.3.1.2. Monolayer Thickness and Coverage 116
3.3.2. Ellipsometry 117
3.3.3. Infrared Reflection-Absorption Spectroscopy Analysis 120
3.3.3.1. IRRAS of SAM1 121
3.3.3.2. IRRAS of SAM2 123
3.3.3.3. IRRAS of SAM3 124
3.3.4. Scanning Tunneling Microscopy 127
3.4. Conclusions 128
3.5. References 129
CHAPTER 4 ELECTRONIC PROPERTIES OF STILBENE THIOLATE MONOLAYERS ON GOLD 131
4.1. Introduction 131
4.2. Work Function of Gold Coated with Stilbene Thiolate SAMs 132
4.2.1. UPS Measurements 132
4.2.2. Analysis of the Work-Function Changes 134
4.2.2.1. Comparison of the Experimental Work-Function Changes with Theoretical Predictions 134
4.2.2.2. Factors Influencing the Measured Work-Function Changes 137
4.3. Molecular Energy Levels of Stilbene Thiolate Monolayers on Gold 139
4.3.1. UPS Measurements 139
4.3.2. Analysis of the Molecular Energy Levels in SAM1-3 146
4.3.2.1. Electrochemical Measurements 146
4.3.2.2. Energy Diagram for SAM1-3 149
4.4. Conclusions 152
4.5. References 154
CHAPTER 5 PREPARATION AND CHARACTERIZATION OF BIS(DIARYLAMINO)BIPHENYL-FUNCTIONALIZED GOLD NANOPARTICLES 156
5.1. Introduction 156
5.2. Synthesis of Organic Ligands and Preparation of Gold Nanoparticles 158
5.2.1. Synthesis of TPD-thiol molecules 158
5.2.2. Preparation of Gold Nanoparticles 160
5.3. Characterization of Gold Nanoparticles Coated with TPD-Thiol Ligands 163

5.3.1. Transmission Electron Microscopy....163
5.3.2. FT-IR Spectroscopy....166
5.3.3. UV-Vis absorption spectroscopy....170
5.3.4. NMR analysis....176
5.3.5. Thermogravimetric analysis (TGA)....188
5.3.6. Calculations of TPD-thiol ligand coverages....189
5.3.6.1. Calculations based on UV-Vis absorption and TEM analysis....189
5.3.6.2. Calculations based on TGA and TEM analysis....192
5.3.6.3. Summary and discussion of the TPD-thiol coverage and TPD-thiol footprint data....193
5.4. Conclusions....198
5.5. References....201
CHAPTER 6 PHOTOPHYSICAL PROPERTIES OF BIS(DIARYLAMINO)BIPHENYL-FUNCTIONALIZED GOLD NANOPARTICLES....203
6.1. Introduction....203
6.2. Photophysical Properties of Gold Nanoparticles Coated with TPD-thiol Ligands....204
6.2.1. The Photophysics of the Model Compound – TPD-C12....204
6.2.1.1. Solution Properties....205
6.2.1.2. Solid-state properties....214
6.2.2. The Photophysics of TPD-coated Gold Nanoparticles....223
6.2.2.1. Fs NIR-TA of AuS-Cx-TPD Systems (x = 3, 4, 8, 12)....223
6.2.2.2. Fs NIR-TA of AuS-Cx-TPD(DDT_{60}) systems (x = 3, 4, 8, 12)....232
6.2.2.3. Discussion of the fs NIR-TA data....235
6.2.2.4. Ultrafast depolarization of TPD-thiol-coated Au NPs....241
6.3. Conclusions....246
6.4. References....248
CHAPTER 7 CONCLUSIONS....250
7.1. Introduction....250
7.2. Influence of π-Conjugated Stilbene Thiols on the Work Function of Gold and the Energy Level Alignment at the Organic / Metal Interface....250
7.3. Ultrafast Excited-state Deactivation of Bis(diarylamino)biphenyl-based Fluorophores Attached to Gold Nanoparticles....253

7.4. References 256

LIST OF TABLES

Table 1.1. Experimentally measured values of work function for different metals. 9

Table 1.2. Experimentally measured changes in the work function, $\Delta\Phi_m$, of coinage metals upon adsorption of inert gases. Values adapted from ref. 24. The dipole-moment surface densities calculated according to Equation 1.3 are given in the third column....14

Table 1.3. Experimentally measured molar extinction coefficient values, ε_M, of selected organic dyes at their absorption maxima, and of solutions of gold nanoparticles with different diameter, D, at the maximum of the surface plasmon resonance band. Values for the organic dyes were taken from ref. 76 and data for Au NPs were taken from ref. 77. 38

Table 3.1. Thickness and coverage data of stilbene thiolate monolayers on gold. The coverage was obtained from XPS measurements.....119

Table 3.2. Vibrational Frequencies (in cm^{-1}) of the Most Prominent IR Modes Measured for Solutions of 4'-Substituted-4-(Methylthio)stilbenes and the Corresponding SAMs. 126

Table 4.1. Summary of the results obtained from the fitting of the experimentally measured asymmetric band in **SAM1-3** with a sum of three Gaussian functions with fixed FWHM of 0.45 eV. The energy at the peak of each of the three Gaussian functions with respect to Fermi level and their corresponding amplitudes are shown for all samples.....146

Table 5.1. Comparison of the percentages of **TPD-Cx-thiols** (x = 3, 4, 8, 12) in the mixtures of two thiols used in the preparation of the Au NPs with the percentages of TPD moieties calculated from the UV-Vis analysis. 175

Table 5.2. Summary of the UV-Vis-based TPD-thiol coverages, $\chi_{TPD(Abs)}$, and TPD-thiol footprints, $\theta_{TPD(Abs)}$, calculated according to the discussion in sections 5.3.6.1 and 5.3.6.2 for NP samples studied herein. Also, TGA-based TPD-thiol coverages, $\chi_{TPD(TGA)}$, and TPD-thiol footprints, $\theta_{TPD(TGA)}$, calculated for **AuS-Cx-TPD** systems (x = 3, 4, 8, 12) are given.....194

Table 5.3. Summary of the average TPD-thiol coverages, $\chi_{TPD(Av)}$, and TPD-thiol footprints, $\theta_{TPD(Av)}$, calculated according to the discussion in section 5.3.6.3 for **AuS-Cx-TPD** systems (x = 3, 4, 8, 12). 197

LIST OF FIGURES

Figure 1.1. a) Potential energy of an electron in vacuum at an infinite distance from a metal surface, $E_{vac}(\infty)$, and the Fermi level of the metal, E_F. b) Potential landscape the electron experiences along a travel path towards the metal surface (thick line). 4

Figure 1.2. Energetics of electrons in a photoelectric-effect-based measurement of the work function. The photon energy, hν, is shown as a red arrow. After ejection from the metal the electrons experience the potential shown with the thick black line. The kinetic energies of two photoelectrons originating from different energy levels in the metal are shown with thick green lines. 7

Figure 1.3. Energy diagram of an organic electroluminescent device. The charge carriers – electrons (e-) and holes (h+) – are injected respectively from the metal cathode (right-hand side of the diagram) and the anode (left-hand side of the diagram) into the organic active layers – the electron-transport layer (ETL) and the hole-transport layer (HTL). At the ETL / HTL interface the charge carriers recombine generating photons. The Fermi levels of both the metal cathode and the anode and the energy levels of the organic layers (HOMO and LUMO energy levels) have to be matched in order to achieve an efficient charge injection into the organic layers. Based on Ref. 13. 11

Figure 1.4. Schematic diagram of a SAM of organic thiolates supported on a metal surface. The anatomy and characteristics of the SAM are highlighted. Based on ref. 1. 15

Figure 1.5. Schematic diagram of an alkanethiol SAM on gold. The organic adlayer can be envisaged as two layers of dipoles with dipole moments μ_1 and μ_2 and the corresponding dielectric constants ε_1 and ε_2. The net dipole moment, μ_{net} is also shown. Based on ref. 39. 17

Figure 1.6. Schematic diagram of gold coated with alkanethiol SAMs containing polar aromatic groups studied by Evans et al. in ref. 40. The differences in the structures of SAMs are highlighted as well as the direction of the effective dipole moments of the organic adlayers. 18

Figure 1.7. Schematic diagram of SAMs on gold studied by Alloway et al. The projections of the dipole moment of polar trifluoromethyl group onto the surface normal (dashed line) are shown by the vertical arrows. Based on ref. 42. 20

Figure 1.8. Schematic diagram of a) Ag anode / MEH-PPV interface and b) Ag anode / perfluoroalkylthiol SAM / MEH-PPV interface. Vacuum levels close to the surface, $E_{vac}(s)$, SAM induced change of the work function, $\Delta\Phi_m$, and hole-injection barriers, Δ_h, for both devices are shown. Based on ref. 21. 22

Figure 1.9. Schematic representation of SAMs on gold studied by Chen et al. The measured work functions for the SAM-coated substrates, Φ_m, as well as the hole-injection barriers measured for Au / SAM / CuPc systems, $\triangle_h$, are shown. Based on ref. 52.....26

Figure 1.10. Schematic representation of biphenylthiolate SAMs on gold studied theoretically by Heimel et al. The calculated changes of the work function caused by the SAMs, $\triangle\Phi_m$, and the offsets between the HOMO and the Fermi level, $\triangle_{HOMO}$, are shown. Results from ref. 55.....27

Figure 1.11. Schematic representation of stilbene thiolate SAMs on gold studied herein. The labels of the SAMs as they are used throughout this thesis are shown above the structures.....30

Figure 1.12. Lycurgus Cup under illumination from the inside (left), and under ambient light (right). Source: www.britishmuseum.org/.....31

Figure 1.13. Schematic of surface plasmon oscillations induced by an oscillating electric field in a metal sphere. The displacement of the conduction electrons (green color) relative to the nuclei (gray color) is shown. The frequency of the surface plasmon resonance is denoted ω_p. Based on ref. 75. 35

Figure 1.14. UV-Vis absorption spectra acquired for toluene solutions of oleylamine-coated gold nanoparticles with different diameters. The spectra were normalized at 450 nm. 39

Figure 1.15. Schematic representation of the possible processes leading to excited-state deactivation of an organic dye anchored to the surface of a gold nanoparticle. Based on ref. 97.....46

Figure 1.16. Schematic representation of the systems studied by Ipe and Thomas. Based on ref. 115. 55

Figure 1.17. Representation of the reaction studied by Werts et al. Based on ref. 116. 57

Figure 1.18. Schematic representation of the systems described in this thesis. 59

Figure 2.1. X-ray diffraction of the gold substrates acquired from EMF Corporation. The measurements were performed on a Scintag X1 powder diffractometer.....89

Figure 2.2. Scheme of the optical layout of TC-SPC experiment; L = lens, A = aperture, $\lambda/2$ = Half-wave plate. 99

Figure 2.3. Scheme of the optical layout of the nanosecond TA experiment; BS = beam splitter, L = lens, F = filter, M = mirror, A = aperture, C = collimator, O = microscope objective, Mono = monochromator. 101

Figure 2.4. Normalized OKE signal as a function of pump-probe delay measured at different wavelengths.....103

Figure 2.5. Transient spectra measured for a toluene solution of Au NPs coated with dodecanethiol. The delay values are shown in the legend.....105

Figure 2.6. Kinetic traces before (black circles) and after (blue circles) subtraction of scaled trace of **AuS-C12** (red circles) from traces measured for **AuS-C12-TPD** at a) 900 nm, b) 1200 nm, and c) 1600 nm.....107

Figure 3.1. Schematic representation of SAMs studied herein. The color coding will be used throughout Chapters 2 and 3.....111

Figure 3.2. Synthesis of 4'-substituted-4-(acetylthio)stilbenes. 112

Figure 3.3. Comparison of IR spectra of $CDCl_3$ solutions of compounds **Ac1**, **Ac2**, and **Ac3** and IRRAS spectra of the corresponding monolayers.....113

Figure 3.4. XPS spectra of stilbene thiolate SAMs in different spectral regions. The spectra are displaced vertically for clarity. 115

Figure 3.5. Influence of the assumed refractive index of the monolayer on the extracted thickness values of the stilbene SAMs on gold from the ellipsometry measurements. 119

Figure 3.6. Summary of the thickness values extracted from ellipsometry (○) and XPS measurements (□). The triangles correspond to the DFT calculated distance from sulfur atom to terminal hydrogen along the long molecular axis for the relaxed geometry. 120

Figure 3.7. Comparison of IRRAS spectrum of **SAM1** and FT-IR spectra of solutions of M1. The absorbance of solutions of M1 was scaled to match the absorbance measured for **SAM1** at 1496 cm^{-1}. 122

Figure 3.8. Comparison of IRRAS spectrum of **SAM2** and FT-IR spectra of solutions of M2. The absorbance of solutions of M2 was scaled to match the absorbance measured for **SAM2** at 1511 cm^{-1}. 123

Figure 3.9. Comparison of IRRAS spectrum of **SAM3** and FT-IR spectra of solutions of M3. The absorbance of solutions of M3 was scaled to match the absorbance measured for **SAM3** at 1523 cm^{-1}. 125

Figure 3.10. STM image of **SAM1** on gold. The rhombus in the upper left represents the unit cell of the hexagonal lattice. 128

Figure 4.1. Secondary-photoelectron cutoff regions of the UPS spectra of stilbene thiolate monolayers on gold. 133

Figure 4.2. Work function values measured for **SAM1-3** on gold in this study and literature values found for OPET and TPT on gold. 134

Figure 4.3. Work function changes caused by substituted stilbene thiolate monolayers on gold as a function of DFT-calculated dipole moments along the long molecular axis of the corresponding thiols projected on the surface normal: the circles are experimentally determined from UPS measurements and the squares are calculated from Equation 4.3 assuming $\mu_{BD} = 0$; the solid and dashed lines are the corresponding linear fits for each data set. 137

Figure 4.4. Schematic representation of a possible arrangement of water molecules hydrogen-bound on top of **SAM3**. Projections of the depolarized dipole moments of the monolayer, μ_{mono}/κ_{mono}, bond dipole, μ_{BD}/κ_{BD}, and the water-molecule dipole moment, μ_{water}, onto the surface normal are shown with the arrows. 139

Figure 4.5. UPS spectra of clean gold (Au) and gold coated with stilbene thiolate monolayers (as measured). 140

Figure 4.6. Fermi-level region of the UPS spectra measured for clean gold (Au) and for gold coated with stilbene thiolate monolayers. The vertical dashed line dissecting the abrupt signal-increase step represents the position of the Fermi level and can be related to E_{max} in Figure 1.2 (Chapter 1, section 1.1.2). 141

Figure 4.7. a) Molecular contribution to the UPS spectra measured for **SAM1-3**. b) High-kinetic-energy region of the UPS-measured molecular contributions for **SAM1-3**. The spectra were normalized at the maximum of the first feature below the Fermi level. 142

Figure 4.8. Experimentally measured UPS spectra (open circles) for **SAM1-3** and best fits obtained from fitting the band with a sum of two Gaussian functions (solid lines). 144

Figure 4.9. Comparison of the experimentally measured UPS spectra (open circles) for **SAM1-3** with the best fits obtained from fitting the band with a sum of three Gaussian functions (solid lines). Only the data range in which the fitted curve is drawn was used for fitting. 145

Figure 4.10. Cyclic voltammograms measured for dry dichloromethane solutions of **M1-3**. The wave corresponding to $FeCp_2^+$ / $FeCp_2$ redox process defines 0 V. 148

Figure 4.11. Plot of the position of HOMOs of stilbene thiolates in SAMs on gold with respect to the Fermi level calculated from Equation 4.2 for: a) a system in which the vacuum level close to the surface, $E_{vac}(s) = E_F + \Phi_m$, is governed by the work function of clean gold, ΔE_{HOMO}(Au), and b) a system in which the work function is altered by the adsorbed **SAM1-3**, ΔE_{HOMO}(SAM). The calculated gas-phase IPs for M1-3 (vertical arrows) were used to position the HOMO of each system with respect to E_F (ΔE_{HOMO}, double-sided arrows) according to Equation 4.2. 150

Figure 4.12. Plot of the position of (○) HOMO of **SAM1-3** with respect to the Fermi level extracted from UPS measurements, ΔE_{HOMO}(UPS), and (✕) ΔE_{HOMO}(SAM) corrected for the solid-state polarization effects as a function of ΔE_{HOMO}(Au) (see Figure 4.11a). The slope of the linear fit of ΔE_{HOMO}(UPS) (dashed line) is 0.18. 152

Figure 5.1. Schematic representation of the systems whose studies are described in this chapter.....157

Figure 5.2. Synthesis of **TPD-C3-thiol**.....159

Figure 5.3. Synthesis of **TPD-C4-thiol** (x = 4), **TPD-C8-thiol** (x = 8), **TPD-C12-thiol** (x = 12), and **C12-TPD**. 160

Figure 5.4. Synthesis of gold nanoparticles coated with **TPD-Cx-thiols** (x= 3, 4, 8, 12).....161

Figure 5.5. Synthesis of gold nanoparticles coated with a mixture of dodecanethiol and **TPD-Cx-thiols** (x = 3, 4, 8, 12). The relative amounts of **TPD-Cx-thiol** (x = 3, 4, 8, 12) and DDT relative to each other were varied. 162

Figure 5.6. TEM micrograph of **Au-S-C3-TPD**. 163

Figure 5.7. Histograms of diameters of Au NPs studied herein. Average diameters (**d**) and their standard deviations are shown 165

Figure 5.8. FT-IR spectra of neat films of **AuS-Cx-TPD** systems (x= 3, 4, 8, 12) and of **TPD-C12**. The spectra were normalized at 1600 cm^{-1} and displaced vertically for clarity.....166

Figure 5.9. FT-IR spectra of neat films of **AuS-Cx-TPD** (x= 3, 4, 8, 12) systems and of **AuS-C12** in the spectral region of C-H stretching mode. The spectra were normalized at 2920 cm^{-1} and displaced vertically for clarity. 168

Figure 5.10. FT-IR spectra of neat films of Au NP samples coated with different mixtures of a) **TPD-C3-thiol** and dodecanethiol, b) **TPD-C4-thiol** and dodecanethiol, c) **TPD-C8-thiol** and dodecanethiol, and d) **TPD-C12-thiol** and dodecanethiol. All

spectra were normalized at 1600 cm^{-1} and displaced vertically for clarity. 169

Figure 5.11. UV-Vis absorption spectra of toluene solutions of **AuS-Cx-TPD** (x = 3, 4, 8, 12), **AuS-C12**, and **TPD-C12**. Each spectrum of NPs was normalized at the maximum of the surface plasmon resonance band and the spectrum of **TPD-C12** was normalized at 353 nm. 170

Figure 5.12. Position of the SPR band maximum as a function of the alkyl linker length in **AuS-Cx-TPD** (x = 2, 4, 8, 12) 171

Figure 5.13. Comparison of UV-Vis absorption spectra of toluene solutions of **AuS-C12** with NP systems incorporating a) **TPD-C3-thiol**, b) **TPD-C4-thiol**, c) **TPD-C8-thiol**, and d) **TPD-C12-thiol** studied herein. Each spectrum was normalized at the maximum of the surface plasmon resonance band. 173

Figure 5.14. Spectra of residual optical density (ΔA) after subtracting a normalized UV-Vis absorption spectrum of toluene solution of **AuS-C12** from normalized spectra of NP systems incorporating a) **TPD-C3-thiol**, b) **TPD-C4-thiol**, c) **TPD-C8-thiol**, and d) **TPD-C12-thiol**. 174

Figure 5.15. ^1H NMR spectra of $CDCl_3$ solutions of **AuS-Cx-TPD** systems (x = 3, 4, 8, 12) studied herein and of a $CDCl_3$ solution of **TPD-C4-thiol**. All spectra were normalized at the highest peak in the aromatic-proton region (6 – 8 ppm). The residual $CHCl_3$ and toluene solvent peaks were masked out. 176

Figure 5.16. ^1H NMR spectra of $CDCl_3$ solutions of Au NP systems incorporating: a) **TPD-C3-thiol**, b) **TPD-C4-thiol**, c) **TPD-C8-thiol**, and d) **TPD-C12-thiol**. All spectra were normalized at the highest peak in the aromatic-proton region (6 – 8 ppm). The residual $CHCl_3$ and toluene solvent peaks were masked out. 179

Figure 5.17. ^1H NMR spectra of $CDCl_3$ solutions of **AuS-Cx-TPD(DDT$_{90}$)** systems (x = 3, 4, 8, 12) studied herein and of a $CDCl_3$ solution of **TPD-C4-thiol**. All spectra were normalized at the highest peak in the aromatic-proton region (6 – 8 ppm). The residual $CHCl_3$ and toluene solvent peaks were masked out....181

Figure 5.18. ^1H NMR spectra of $CDCl_3$ solutions of **AuS-Cx-TPD** systems (x = 3, 4, 8, 12) studied herein. All spectra were normalized at the highest peak in the aromatic-proton region (6 – 8 ppm). The residual $CHCl_3$ and toluene solvent peaks were masked out and the data points in these areas were then interpolated. 184

Figure 5.19. Decays of ^1H NMR signals as a function of delay between pulses in the CPMG pulse sequence measured at a) 2.05 ppm

and b) 6.90 ppm, for $CDCl_3$ solutions of **AuS-Cx-TPD** systems (x = 3, 4, 8, 12).....185

Figure 5.20. Average T_2 relaxation times as a function of the number of methylene groups in the alkyl linker between thiol group and the TPD moiety for $CDCl_3$ solutions of **AuS-Cx-TPD** systems (x = 3, 4, 8, 12).....186

Figure 5.21. Schematic representations of the high-TPD-coverage systems: one with the shortest and one with the longest alkyl linker between the thiol group and the TPD moiety (the particle size and the organic ligand size are not to scale). Note the difference in the average distance between TPD moieties between both systems. 188

Figure 5.22. Thermogravimetric plots recorded for **AuS-Cx-TPD** systems (x = 3, 4, 8, 12) studied herein. 189

Figure 5.23. Changes in the optical density observed after 2 days of the reaction of **AuS-C12-TPD** with dodecanethiol in toluene. 196

Figure 6.1. Spectral distribution of the molar extinction coefficient, ε, for **TPD-C12** in a toluene solution (blue line) and normalized fluorescence spectrum measured for a toluene solution of **TPD-C12** (red line). The excitation wavelength was 355 nm. 205

Figure 6.2. Fluorescence decays measured for deoxygenated (Deox decay, red circles) and air-equilibrated (Aerated decay, blue circles) toluene solutions of **TPD-C12**, and corresponding best-fit functions (solid lines). 365 nm was used as the excitation wavelength and the emission was collected at 420 nm.....206

Figure 6.3. Optical density transients at 1250 nm acquired for deoxygenated (black line) and aerated (red line) toluene solutions of **TPD-C12**. 355 nm was used as the excitation wavelength. 207

Figure 6.4. Transient NIR absorption spectrum of the excited triplet state of **TPD-C12** in degassed toluene solution calculated from fitting the transients measured at each individual wavelength (excitation wavelength: 355 nm). 208

Figure 6.5. a) Transient spectra recorded at different pump-probe delays (given here as labels on the right-hand side of the spectra) measured for a 0.1 M toluene solution of **TPD-C12**; b) kinetic traces at different wavelengths, measured for the same sample as in a). The excitation wavelength was 350 nm and the average power of pump beam was 1.1 mW. 209

Figure 6.6. a) Spectral distribution of preexponential amplitudes obtained by fitting the data for a **C12-TPD** 0.1M toluene solution with a sum of three exponential functions. The corresponding lifetimes were: $\tau_1 = 2.4 \pm 0.04$ ps, $\tau_2 = 49 \pm 2$ ps, and $\tau_3 = 700 \pm$

12 ps ; b) kinetic traces (circles) and the corresponding curves from fitting the data (solid lines) with a sum of three exponential functions for the same sample as in a). 210

Figure 6.7. The molecular origin of photoinduced anisotropy.....211

Figure 6.8. Anisotropy decay, $R(t)$, of photoexcited **TPD-C12** in toluene (circles) and the best-fit curve based on a sum of two exponential functions. 213

Figure 6.9. Transient spectra recorded at different pump-probe delays measured for a neat film of **TPD-C12**. The arrows show the direction of the evolution of ΔOD for the first two spectra. 214

Figure 6.10. a) Spectral distribution of preexponential amplitudes obtained by fitting the data for a neat film of **TPD-C12** on glass with a sum of three exponential functions. The corresponding lifetimes were: $\tau_1 = 1.1 \pm 0.02$ ps, $\tau_2 = 22 \pm 1$ ps, and $\tau_3 = 370 \pm 20$ ps ; b) kinetic traces (circles) and the corresponding curves from fitting the data (solid lines) with a sum of three exponential functions for the same sample as in a). 215

Figure 6.11. Spectral profiles of the early-time (0.2 ps) spectrum of photoexcited **TPD-C12** neat film (normalized at 900 nm), preexponential amplitudes $A_1(\lambda)$ (normalized at 900 nm) from the fitting routine on the data acquired for **TPD-C12** neat film, the result of the subtraction of the normalized $A_1(\lambda)$ from the normalized early-time spectrum of photoexcited **TPD-C12**, $\varepsilon_X(\lambda)$, and $A_3(\lambda)$ which was multiplied by a constant to match the value of $\varepsilon_X(\lambda)$ at 1500 nm. See text for details.....220

Figure 6.12. Preexponential amplitudes $A_3(\lambda)$ found from the fitting of the fs NIR-TA data acquired for neat film of **TPD-C12** and NIR absorption spectrum of a chemically-generated **TPD-C12** radical cation in toluene solution. Both spectra were multiplied by a constant to match their intensity at 1400 nm. 222

Figure 6.13. Transient spectra, as measured, at different pump-probe delays for toluene solutions of a) **AuS-C3-TPD** and c) **AuS-C4-TPD**. Transients at different wavelengths after subtraction of the contributions to ΔOD from the metallic core of Au NPs for: b) **AuS-C3-TPD** and d) **AuS-C4-TPD**. The solid lines in b) and d) represent the best-fit functions based on the fitting of the data with a sum of two exponential functions. 225

Figure 6.14. Transient spectra, as measured, at different pump-probe delays for toluene solutions of a) **AuS-C8-TPD** and c) **AuS-C12-TPD**. Transients at different wavelengths after subtraction of the contributions to ΔOD from the metallic core of Au NPs for: b) **AuS-C8-TPD** and d) **AuS-C12-TPD**. The solid lines in b) and d) represent the best-fit functions based on the fitting of the data with a sum of two exponential functions. 227

Figure 6.15. Spectral distributions of preexponential amplitudes and the corresponding lifetimes obtained by fitting the fs NIR-TA data obtained for toluene solutions of a) **AuS-C3-TPD**, b) **AuS-C4-TPD**, c) **AuS-C8-TPD**, and d) **AuS-C12-TPD**. A sum of two exponential functions was used in the fitting routine. The black solid lines in c) and d) correspond to a transient spectrum of photoexcited **TPD-C12** in 0.1 M toluene solution after pump-probe delay of ca. 1 ps. 229

Figure 6.16. Normalized spectral distributions of preexponential amplitudes found for **AuS-Cx-TPD** (x = 3, 4), $A_2(\lambda)$, and for the long-lived component found for the neat film of **TPD-C12** ($A_3(\lambda)$ in Figure 6.10a). A normalized NIR absorption spectrum of the **TPD-C12** radical cation is shown for comparison. 231

Figure 6.17. Spectral distributions of preexponential amplitudes and the corresponding lifetimes obtained by fitting the fs NIR-TA data for toluene solutions of a) **AuS-C3-TPD(DDT$_{60}$)**, b) **AuS-C4-TPD(DDT$_{60}$)**, c) **AuS-C8-TPD(DDT$_{60}$)**, and d) **AuS-C12-TPD(DDT$_{60}$)**.....233

Figure 6.18. Normalized kinetic traces at 1600 nm for a) Au NPs incorporating **TPD-C3-thiol** and b) Au NPs incorporating **TPD-C4-thiol**. The contributions of metallic cores of Au NPs were subtracted as described in section 2.2.2.13 of Chapter 2. 235

Figure 6.19. Dependence of the rate of deactivation of the excited state of TPD in the NP systems studied herein on the number of methylene units in the alkyl spacer between the TPD moiety and the surface-anchoring thiol group. 239

Figure 6.20. Anisotropy decays at 1500 nm measured for toluene solutions of **AuS-Cx-TPD** (x = 3, 4, 8, 12). 241

Figure 6.21. Anisotropy decays at 1500 nm measured for toluene solutions of **AuS-Cx-TPD** and **AuS-Cx-TPD(DDT$_{60}$)** systems (x = 3, 4 , 8, 12).. 244

Figure 7.1. SAMs with different Schiff base backbones which could potentially result in opposite dipole moments on the surface.....253

LIST OF ABBREVIATIONS

SAM	Self-Assembled Monolayer
Au NP	Gold Nanoparticle
XPS	X-ray Photoelectron Spectroscopy
UPS	Ultraviolet Photoelectron Spectroscopy
IRRAS	Infrared Reflection-Absorption Spectroscopy
NMR	Nuclear Magnetic Resonance
NIR	Near Infrared
UV-Vis	Ultra Violet – Visible
TA	Transient Absorption
TC-SPC	Time-correlated Single Photon Counting
IP	Ionization Potential

Other abbreviations and symbols are explained in the text.

SUMMARY

In order to gain insights into the electronic interactions between metallic gold and self-assembled monolayers composed of π-conjugated thiols, a series of thiol-containing molecules based on a stilbene backbone were synthesized and assembled on gold surface. The resulted monolayers were characterized with a variety of surface-sensitive techniques and the electronic properties of the obtained surfaces were studied with the use of ultraviolet photoelectron spectroscopy. Work-function changes and alignment of the molecular energy levels with respect to the Fermi level of the metal were investigated and important insights regarding the electronic properties of the metal / organic interfaces were obtained.

Another aspect of interactions between organic dyes and metallic gold was studied in the context of spectroscopic properties of systems incorporating gold nanoparticles with organic fluorophores covalently attached to the nanoparticle surface. Ultrafast dynamics of the excited-state deactivation of the organic fluorophores attached to the surface of gold nanoparticles were studied with the use of a fs transient absorption technique. It was found that the close proximity of a gold nanoparticle had a profound impact on the excited-state lifetime of the studied organic fluorophore. The influence of the structure of the studied systems on the excited-state deactivation dynamics of the organic fluorophores was described.

CHAPTER 1

INTRODUCTION

Systems comprised of organic molecules covalently attached to metal surfaces received considerable attention in recent years.[1,2] In particular, the discovery of the formation of self-assembled monolayers (SAMs) of organic thiols on flat gold surfaces defined a vibrant field of research that led to many important scientific insights.[1,3,4] Proposed applications of SAMs include their use as agents for improving the wettability of surfaces,[5] anticorrosive layers,[6] biosensors,[7] and resists for lithography.[1] At the same time there has been a tremendous effort in the research of chemistry and physics of organic thiols assembled on the surface of metal nanoparticles.[2] Reports on the use of these three-dimensional counterparts of SAMs in sensing,[8,9] cancer treatment,[10] and nonlinear optical applications[11] make them rather promising in the context of their potential use. In addition, metal nanoparticles are often considered as an important component of the future nanotechnology toolbox.[1,2]

This thesis is concerned with the studies of physical properties of systems incorporating organic thiols on gold surfaces. Two major threads of research activities are described. The first theme involves the preparation and characterization of monolayers of π-conjugated organic thiols on flat gold surfaces and the investigation of the electronic properties of these hybrid systems. The particular focus of this part of the thesis is directed at the work-function changes of the metal that are induced by the organic monolayers, as well as at the alignment of electronic levels of the organic molecules in close contact with gold with respect to Fermi level of the metal. The second theme is

related to the photophysics of organic dyes linked to the surface of gold nanoparticles. The main interest is associated with the effects of the proximal nanoparticle on the photophysics of the organic dye.

The remaining sections of this chapter offer a short theoretical background and a review of the existing literature relevant to the research described in this thesis. This introductory chapter is divided into two parts. According to the two themes mentioned above the first part introduces the concept and importance of the work function, and discusses the existing knowledge regarding the influence of adsorbates on the work function of metals, with particular focus on organic-thiol monolayers on coinage metals. The second part of this chapter deals with the spectroscopic properties of gold nanoparticles. A historical background is presented followed by the description of the photophysics of gold nanoparticles. Next, a short review of the existing literature on the interactions between gold nanoparticles and organic dyes can be found with the particular stress placed on the influence of gold nanoparticles on the photophysics of organic dyes anchored to the nanoparticle surface. The motivation for the work described in this thesis is provided after each background part.

Chapter 2 describes the preparation and characterization of the materials and the experimental methodologies used in this work. Chapter 3 reports the preparation and characterization of self-assembled monolayers of stilbene thiolates on gold surfaces. The exploration of the electronic properties of the monolayers is described in Chapter 4. Finally, Chapters 5 and 6 discuss the preparation and characterization of systems incorporating gold nanoparticles coated with organic dyes and the ultrafast photophysics of the hybrid systems. Conclusions are given in Chapter 7.

1.1. Influence of Organic Thiols on the Work Function of Coinage Metals

1.1.1. Work Function of Metals – Physical Description

Let us consider an electron at rest in a vacuum at an infinite distance from a metal surface, as depicted in Figure 1.1a. The total energy, E_{tot}, of such an electron is equal to its potential energy, which can be defined after Cahen and Kahn as the *vacuum level at infinity*, $E_{vac}(\infty)$.[12] Let us supply the electron with some kinetic energy, E_k, and allow it to travel towards the surface. The total energy of the electron outside the metal can be expressed as the sum of its potential energy, E_V, and kinetic energy, E_k:

$$E_{tot} = E_V + E_k \qquad \textbf{Equation 1.1}$$

As the distance between the electron and the metal surface decreases the potential energy of the electron will increase, thus slowing it down, according to Equation 1.1 (see Figure 1.1b). If the kinetic energy is sufficient to overcome the potential barrier at the metal / vacuum interface the electron will go over the barrier and then will rapidly lose its potential energy due to the interaction with the positively charged ion lattice within the metal, resulting in the increase of kinetic energy. Once the electron is within the metal Equation 1.1 no longer holds as the interactions with other electrons and the ion lattice result in energy dissipation and thermal equilibration. The electron is now trapped within the metal.

A similar thought experiment can be performed in an opposite direction. Let us choose an electron from one of the highest occupied energy levels at the particular temperature of the system. The potential energy of this electron is approximately at the

Fermi level, E_F.[a,13,14] The electron is then supplied with some kinetic energy, E'_k, sufficiently large to overcome the potential barrier existing at the metal surface. Right after escaping the metal, the greatly slowed-down electron has a potential energy which can be defined as the *vacuum level close to the surface*, $E_{vac}(s)$.[12] The drop in the kinetic energy of the electron caused by the potential energy barrier is defined as the work function of the metal surface, Φ_m: [12,13]

$$\Phi_m = E_{vac}(s) - E_F \qquad \textbf{Equation 1.2}$$

After escaping from the metal the electron is moving away further from the surface experiencing acceleration as the potential drops to the value of $E_{vac}(\infty)$.

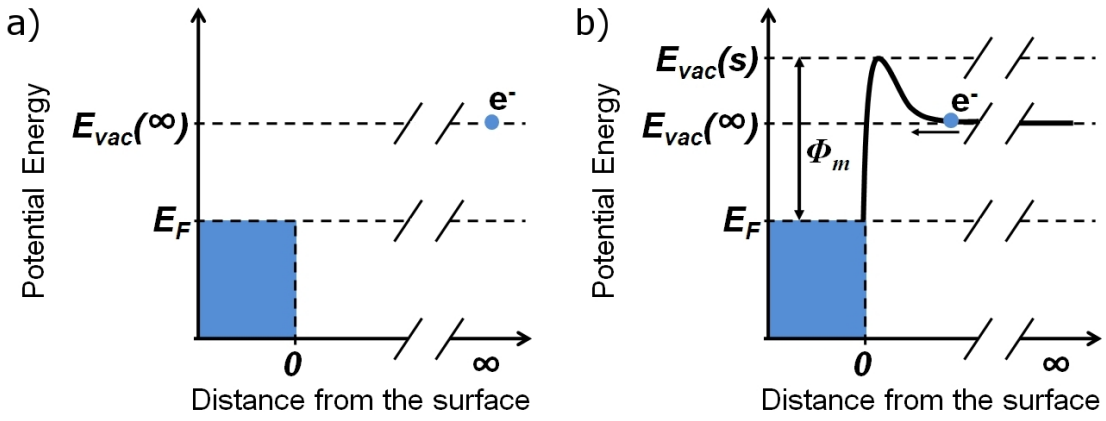

Figure 1.1. a) Potential energy of an electron in vacuum at an infinite distance from a metal surface, $E_{vac}(\infty)$, and the Fermi level of the metal, E_F. b) Potential landscape the electron experiences along a travel path towards the metal surface (thick line). The difference between the electron energy just outside the metal surface, $E_{vac}(s)$, and E_F defines the work function of the metal surface, $\Phi_m = E_{vac}(s) - E_F$.

[a] In terms of Fermi – Dirac statistics the Fermi level is defined as the energy at which the probability of finding an electron is 0.5 for a system at thermal equilibrium. For metals at room temperature the probability of finding an electron below the Fermi level is close to unity.

It is important to describe the physical origin of the potential landscape illustrated in the above thought experiment. As already mentioned, the sharp potential drop the electron experiences when it enters the metal is related to the electrostatic attraction force between the negative charge of the electron and the positively charged ion lattice of the metal. However, at the vacuum / metal interface the electron experiences a potential energy barrier. This implies that in that region of space there must be a repulsive force that acts upon the electron. Indeed, the lack of positively charged metal ions on the vacuum side of the aforementioned interface causes a negative charge to exist just outside of the metal and, conversely, an uncompensated positive charge within the metal. The spilling of the electronic density outside of the solid causes a formation of a sheet of dipoles, which are often referred to as *the surface dipoles*.[12-14]

1.1.2. Work Function of Metallic Surfaces – Methods of Measurement

The work function of solid surfaces can be determined experimentally using absolute or relative approaches. Absolute methods allow one to measure the work function value directly. Here, the electrons in the metal are supplied with sufficient kinetic energy to overcome the barrier at the metal / vacuum interface, and can thus escape the metal, and the work function can be obtained from the resulting electric current. Absolute methods include measurements based on *thermionic emission*, *field emission*, and the *photoelectric effect*. Briefly, in the thermionic emission method electrons are ejected from the material after receiving sufficient thermal energy to overcome the energy barrier at the metal / vacuum interface. The appropriate thermal energy is supplied by incremental heating of the sample to temperatures at which the

Fermi-Dirac distribution of the electrons in the metal allows for substantial population of electrons at energies higher than the interface energy barrier. The resulting electric current is measured as a function of temperature; this allows one to extract the work function of the surface. The temperature range used in the thermionic emission method is often very high (thousands of Kelvins), making this method of limited value for studying materials and surfaces which are unstable at high temperatures.[15] The field-emission method utilizes an electric field to accelerate the electrons inside of the metal to kinetic energies sufficiently high to overcome the interface barrier. The resulting electric current is analyzed as a function of the applied field and the work function is calculated.[15,16]

Photoelectric-effect-based methods use light, typically in the UV range, as the source of energy for the electrons. As in other absolute methods, the resulting electric current (here called *photocurrent*) is analyzed. Figure 1.2 shows the energetics of a photoelectric-effect-based measurement of the work function.

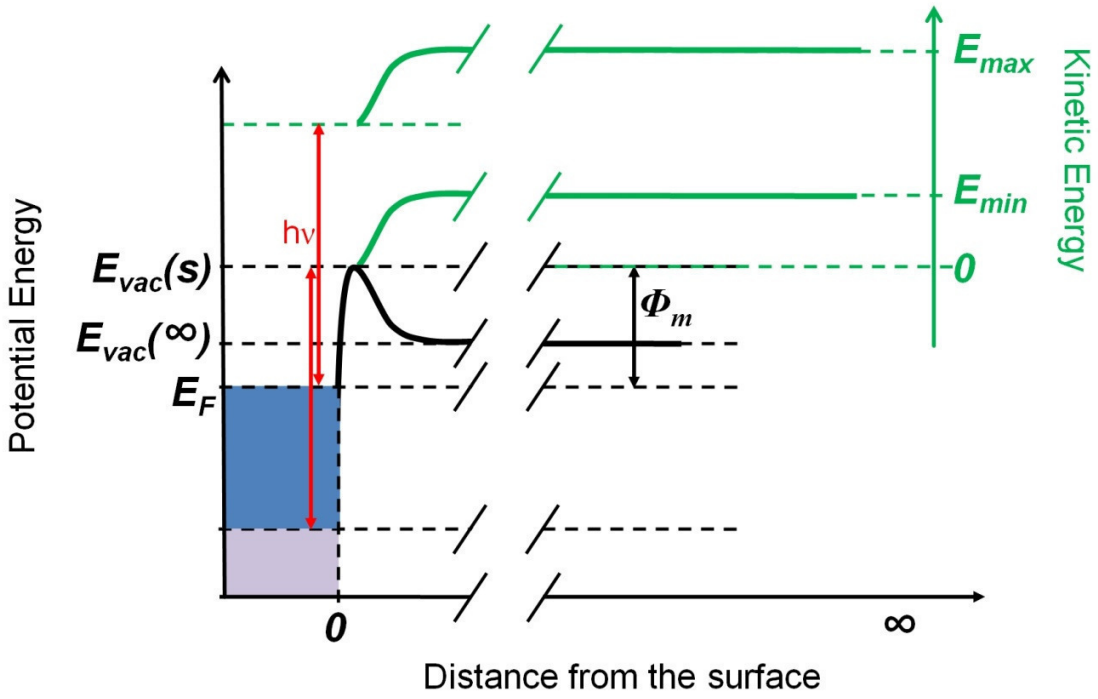

Figure 1.2. Energetics of electrons in a photoelectric-effect-based measurement of the work function. The photon energy, *hv*, is shown as a red arrow. After ejection from the metal the electrons experience the potential shown with the thick black line. The kinetic energies of two *photoelectrons* originating from different energy levels in the metal are shown with thick green lines.[b]

In this experiment the electrons are provided with a known energy, *hv* (red arrows in Figure 1.2). Electrons with sufficient kinetic energy to overcome the barrier at the interface are able to escape the metal – these are represented with the blue box in Figure 1.2. These *photoelectrons* then travel away from the metal surface experiencing the potential depicted with the thick black line in Figure 1.2. As the electrons move further away from the surface their kinetic energy increases, according to Equation 1.1. The generated photocurrent is then measured as a function of the photoelectron kinetic

[b] In a real experiment the photoelectron-kinetic-energy analyzer causes an additional drop in the potential, which adds a rigid offset to the kinetic energy of the photoelectrons. More on this can be found in Ref. 12.

energy. Two important features are present in a typical plot of photocurrent – kinetic energy. First, a sharp onset at low photoelectron kinetic energy, E_{min} is present. As already mentioned, this onset defines the lowest energy electrons able to overcome the work function of the surface. The second feature is the high kinetic energy onset of the photocurrent, E_{max}, and it is a manifestation of the electron population around the Fermi level of the metal; i.e., since there is an abrupt decrease in the electron population above the Fermi level, there are essentially no photoelectrons with $E_{tot} > E_F + h\nu$ right after ejection from the surface. Using the definition of the work function in Equation 1.2 (see also Figure 1.1b), it follows that $\Phi_m = E_{min} + h\nu - E_{max}$.[c] Thus, the work function can be obtained from the onsets of the photocurrent as a function of the kinetic energy of the photoelectrons.[12,13]

Relative methods employ a reference made of a material with a known work function and focus on measuring differences in electrical quantities between the studied material and the reference. These methods include *diode methods* and *condenser methods* (Kelvin probe) and will not be discussed further.[16]

Table 1.1 shows experimentally measured work-function values for a variety of metallic surfaces. The presented data show a variation of the work function in the range of 2.7 – 5.65 eV, revealing that the chemical composition of the surface has a large effect on the work function value.

[c] In practice the photoelectrons are additionally accelerated by an external electric field, which has to be taken account in the calculations.

Table 1.1. Experimentally measured values of work function for different metals.*

Element	Φ_m [eV]	Element	Φ_m [eV]	Element	Φ_m [eV]
Sc	3.5 ± 0.15	Ni	5.15 ± 0.1	Ag	4.0 ± 0.15
Ti	4.3 ± 0.1	Cu	4.65 ± 0.05	La	3.5 ± 0.2
V	4.3 ± 0.1	Y	3.1 ± 0.15	Ce	2.9 ± 0.2
Cr	4.5 ± 0.15	Zr	4.05 ± 0.1	Sm	2.7 ± 0.3
Mn	4.1 ± 0.2	Nb	4.3 ± 0.15	Gd	3.1 ± 0.15
Fe	4.5 ± 0.15	Mo	4.6 ± 0.15	Pt	5.65 ± 0.1
Co	5.0 ± 0.1	Pd	5.55 ± 0.1	Au	5.1 ± 0.1

* From photoelectric-effect-based measurements. Values taken from ref. 17

1.1.3. Work Function of Metals – Implications for Organic Electronics Applications

The presence of the surface dipole on the metal surface has important implications for electronics applications. Charge-carrier injection from a metal electrode to an active layer in a variety of optoelectronic devices is considered to be one of the crucial processes essential to the overall device performance.[13,14] The energetics of the charge-injection process are defined by the relative positions of the Fermi level of the metal and the accessible energy levels of the organic active layer. This is depicted in Figure 1.3 for the case of a hypothetical simplified organic electroluminescent (EL) device.[13] Consider the right-hand side of the energy diagram. In order for an electron to undergo a transfer from the metal cathode to the organic layer it must be supplied with sufficient energy to overcome the barrier existing at the interface. The electron-injection barrier, Δ_e, is defined as the energy difference between the work function of the metal and the solid-

state electron affinity, EA, of the organic layer: $\Delta_e = \Phi_m - EA$.[d] In the case of an EL device the energy needed to overcome the electron-injection barrier is supplied by applying a voltage between the electrodes. From the technological perspective the applied voltage must satisfy certain requirements, for example fall in a range that minimizes the power loss of the device, and allows for integration of the device into a standardized circuit. Thus, matching the solid-state electron affinity and solid-state ionization potential of the organic layers with the work functions of the metal electrodes is the key to obtaining a suitable charge injection during device operation.

[d] The solid-state electron affinity and solid-state ionization potential discussed here are not the same as the corresponding values measured for bulk organic layer. The contact with the metal electrode causes so-called "band bending", which influences the values of both electron affinity and ionization potential. This is discussed in more detail in Ref. 13.

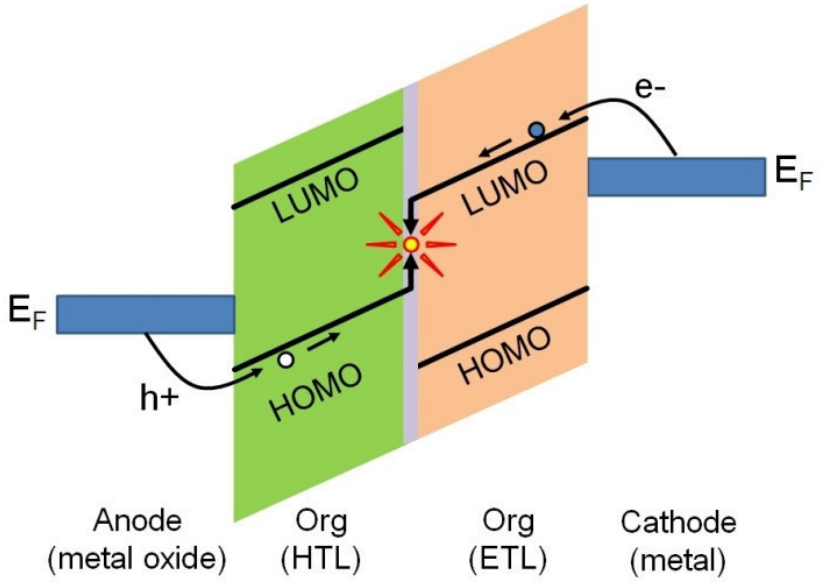

Figure 1.3. Energy diagram of an organic electroluminescent device. The charge carriers – electrons (e-) and holes (h+) – are injected respectively from the metal cathode (right-hand side of the diagram) and the anode (left-hand side of the diagram) into the organic active layers – the electron-transport layer (ETL) and the hole-transport layer (HTL). At the ETL / HTL interface the charge carriers recombine generating photons. The Fermi levels of both the metal cathode and the anode and the energy levels of the organic layers (HOMO and LUMO energy levels) have to be matched in order to achieve an efficient charge injection into the organic layers. Based on Ref. 13.

The EL device described above is only one of the examples in which the metal electrode work function plays a crucial role in the overall device performance. Matching the work function of the electrodes with the organic-layer energy levels in order to balance the charge-carrier-injection barriers is very important in organic field-effect transistors (OFETs), photovoltaic devices, or organic light-emitting transistors (OLETs).[14,18,19] Traditionally this has been addressed by choosing metals with low work function for the cathode, high-work-function materials for the anode, and matching the

organic layer energy levels appropriately.[14] Lately however, there has been a substantial effort to employ metal electrodes whose work function has been tuned by adsorbates.[20,21] This approach is, in principle, more versatile than the use of different, often reactive metals, as it opens the possibility of using relatively chemically stable metals (such as coinage metals) with a layer of work-function-tuning adsorbate as electrodes in organic electronic applications.

1.1.4. Work Function of Metals – Influence of Adsorbates

The work function of a metal is very sensitive to the presence of any adsorbates present on the surface. Experiments have revealed that even physisorbed atoms of inert gases such as argon or xenon influence the work function on a variety of metallic substrates.[22-24] Even though there is no significant charge redistribution in the inert-gas atoms near the metal surface, due to a chemical reaction, there is a substantial charge redistribution on the surface after the physisorption has taken place, which changes the surface dipole on the surface. Two major physical phenomena are responsible for this. First, the electronic density extending outside of the metal surface is pushed back by the repulsive force of the electronic cloud of the inert gas atoms; this is referred to as Pauli push-back, or sometimes as the "pillow effect".[14,25] Second, van der Waals interactions between the inert-gas atom and the metal surface cause polarization of the otherwise highly symmetric electronic cloud of the inert-gas atom.[e] This results in the formation of a sheet of dipoles in the space occupied by the adsorbed atoms which alters the potential landscape at the vacuum / metal interface.[23,24]

[e] The two described mechanisms provide an oversimplified picture of the charge-redistribution process. Contribution from orbital interactions is also invoked as another mechanism of charge redistribution. See Ref. 24 for further details.

On the basis of simple electrostatic considerations one can calculate the dipole-moment surface density corresponding to the measured change of the work function.[14] The work function change, $\Delta\Phi_m$, caused by a sheet of dipoles residing on the surface is expressed by the Helmholtz equation:[14,26]

$$\Delta\Phi_m = -\frac{e\mu}{A\varepsilon\varepsilon_0} \qquad \textbf{Equation 1.3}$$

where e is the elementary charge, μ is the dipole moment in the direction of the surface normal, A is the area of the metal surface, ε is the dielectric constant of the dipole layer, and ε_0 is the vacuum permittivity. Table 1.2 shows experimentally measured values of the work-function changes for a series of inert-gas / metal-surface systems together with the dipole-moment surface density induced by the inert-gas atoms calculated according to Equation 1.3.[24] It can be seen that the adsorption of inert-gas atoms can lower the work function of coinage-metal surfaces by as much as 0.62 eV, which in the case of Cu(111) surface corresponds to ca. 13% drop in the work function upon adsorption of xenon. The dipole-moment surface densities calculated according to Equation 1.3 from the measured work-function changes in Table 1.2 are on the order of 1.5 D / nm^2. This corresponds roughly to a separation of a whole elementary charge by 1 Å in each 3 nm^2 of the surface.

The changes in the work function due physisorption of inert-gas atoms are interesting from the perspective of fundamental understanding of the electronic processes at the surfaces. However, inert gases do not form robust layers upon adsorption and they do not allow for much control of the dipole moment present on the surface after adsorption. The possibility of such control via synthetic design was opened with the development of the field of self-assembled monolayers (SAMs) of organic thiols on metals.

Table 1.2. Experimentally measured changes in the work function, $\Delta\Phi_m$, of coinage metals upon adsorption of inert gases.* Values adapted from ref. 24. The dipole-moment surface densities calculated according to Equation 1.3 are given in the third column.

System	$\Delta\Phi_m$ [eV]	μ / A [D/nm^2]
Kr on Au(111)	-0.42	1.1
Xe on Au(111)	-0.53	1.4
Kr on Ag(111)	-0.46	1.2
Xe on Ag(111)	-0.59	1.6
Kr on Cu(111)	-0.49	1.3
Xe on Cu(111)	-0.62	1.6

* The change in the work function, $\Delta\Phi_m$, is defined as the difference in the work function of the clean substrate and the work function of the surface after the adsorption of inert gas atoms.

1.1.5. Self-Assembled Monolayers of Organic Thiols on Metals

Self-Assembled Monolayers of organic thiols on metals have received considerable attention over the last two decades.[1,3,27,28] From a purely scientific standpoint these structurally ordered systems offer a great opportunity for studying structure–property relationships of organic-inorganic interfaces. Studies of the influence of the molecular structure on the packing of thiols on noble-metal surfaces have led to important insights into the molecular scale morphology of the monolayers. It is now understood that the thiol group binds to gold and often long-range order is observed in the resulting organic adlayer.[1,27-32] This understanding has further led to studies of the influence of synthetically accessible adsorbate structures on a variety of surface characteristics including wetting properties,[5,29] electronic characteristics,[33-35] and

chemical reactivity.[36-38] Figure 1.4 shows a schematic of a structure of an organic thiolate SAM on a metal surface, together with design motifs that can be used to tune the properties of the surface.

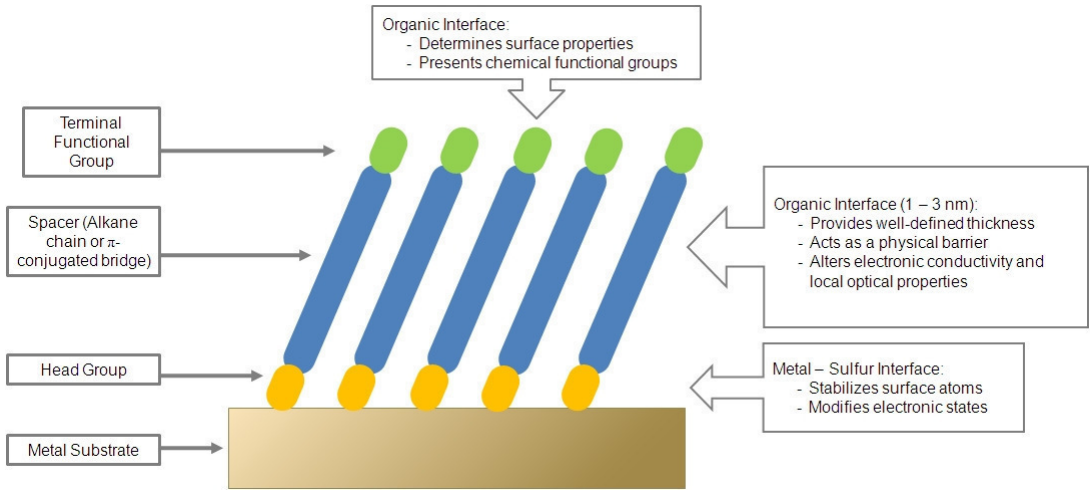

Figure 1.4. Schematic diagram of a SAM of organic thiolates supported on a metal surface. The anatomy and characteristics of the SAM are highlighted. Based on ref. 1.

As discussed earlier, the work function of metals is affected by adsorbates present on the surface. The knowledge of adsorption characteristics of organic thiols on metals and the synthetic accessibility of a variety of structures makes these SAMs excellent systems to be employed in the systematic study of the influence of adsorbates on the work function of the metallic substrates.

1.1.6. Self-Assembled Monolayers of Alkanethiols and their Influence on the Work Function of Metals

The first study addressing the effects of organic thiol SAMs on the work function of gold was published by Evans and Ulman.[39] The authors performed ellipsometry and

Kelvin-probe measurements on a series of alkanethiol SAMs with varying alkyl spacer lengths on a gold surface. Ellipsometry revealed that the thickness of the monolayers systematically increased with the alkyl chain length, which supported the formation of dense thiolate-bound monolayers on gold. The studied alkanethiol SAMs showed a linear decrease of the work function of the metal with the number of methylene units in the alkyl chain length on the monolayer constituent, with a slope of -9.3 meV / methylene group. This has been interpreted using a model involving a dipole layer residing on top of the metal, as depicted in Figure 1.5. The net dipole moment of the organic SAMs was found to have the positive end at the organic / air interface, thus effectively decreasing the work function as compared to clean gold (see Equation 1.3). The addition of methylene units in the alkyl chain increased the magnitude of the dipole moment showing the abovementioned trend in the work-function change with alkyl chain length. Extrapolating the measured changes of the work function to a hypothetical monolayer without methylene groups revealed that Au – S layer decreases the work function of the substrate by as much as ca. 0.5 eV, which is qualitatively consistent with charge rearrangement due to the formation of a chemical bond. Additionally, the dielectric constant of the alkyl chain layer, ε_2 in Figure 1.5, was suggested to change with the alkyl chain length thus highlighting that both the SAM dipole moment and the dielectric constant influence the metal work function, the latter parameter because it effectively depolarizes the dipole layer. The decrease of the gold work function caused by the alkanethiols studied by Evans and Ulman was as large as 0.70 eV. However, it should be stressed that the method applied to measure the work function did not take into account any adsorbates that might have been present on the reference (in this case a “clean” gold

surface); thus, the absolute value of the work function depression with respect to truly clean gold surface was most likely underestimated.

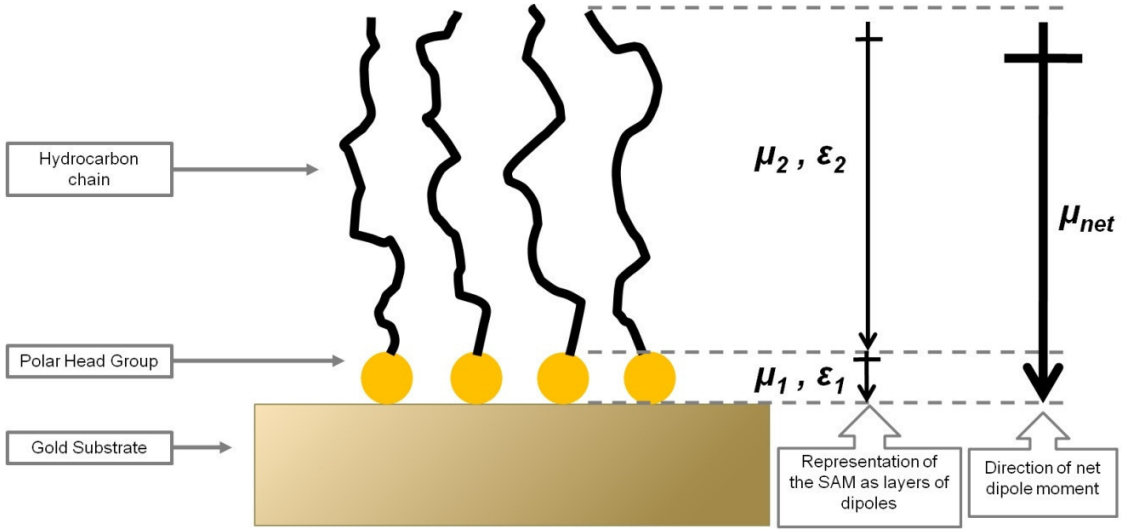

Figure 1.5. Schematic diagram of an alkanethiol SAM on gold. The organic adlayer can be envisaged as two layers of dipoles with dipole moments μ_1 and μ_2 and the corresponding dielectric constants ε_1 and ε_2. The net dipole moment, μ_{net} is also shown. Based on ref. 39.

Further investigations of alkyl thiol monolayers containing a polar aromatic group showed that both the direction and the magnitude of the dipole moment of the molecules forming the monolayer are important factors determining the work function of the underlying metal. Evans et al. used Kelvin probe measurements to show that the structure of the organic adsorbate had a critical effect on the magnitude and the sign of the work-function change.[40] In particular, the substitution of the terminal alkyl chain in one of the studied SAMs to a fluoroalkyl chain resulted in a net dipole moment of opposite direction to that of the SAM with the terminal alkyl chain (see Figure 1.6). In effect, while the terminal-alkyl-chain SAM causes a *depression* of the work function of gold by ca. 0.45

eV, the SAM with terminal fluoroalkyl chain *increases* the work function by as much as 0.75 eV. Thus, the authors clearly showed that the structure of the organic SAM, and in particular the effective net dipole moment of the organic structure, has a dramatic effect on the work-function change of the underlying metal.

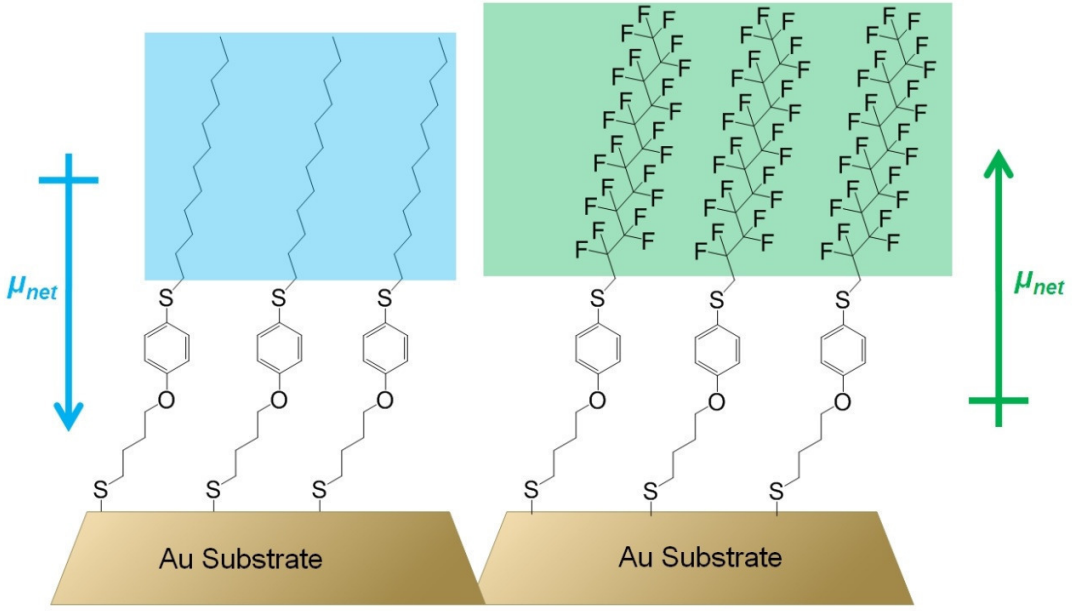

Figure 1.6. Schematic diagram of gold coated with alkanethiol SAMs containing polar aromatic groups studied by Evans et al. in ref. 40. The differences in the structures of SAMs are highlighted as well as the direction of the effective dipole moments of the organic adlayers.

Lu et al. successfully used Kelvin-probe force microscopy (KPFM) to image a gold surface patterned with a mixed alkylthiolate monolayer.[41] Alkylthiol terminated with a methyl group and another alkylthiol terminated with a carboxylic acid group were patterned via the microcontact printing technique.[1] The observed contrast in the KPFM images was an effect of the difference in the work function of the gold-surface regions coated with the two adsorbates possessing different dipole moments. In the case of the

two different alkyl thiolates studied by Lü the contrast was as large as 0.4 eV. Furthermore, a gold surface patterned with methyl-group-terminated alkylthiols containing different numbers of methylene units showed a trend in the measured surface potential, corresponding to a linear decrease of the work function with the slope of ca. -14 meV / methylene group, a behavior qualitatively similar to that reported by Evans.[39]

In an elegant and comprehensive study Alloway and coworkers investigated the influence of alkanethiol and partially-fluorinated-alkanethiol SAMs on the work function of gold.[42] In contrast to the reports Evans and Lu, the work of Alloway et al. was based on ultraviolet photoelectron spectroscopy (UPS), which is an absolute method performed under ultrahigh vacuum conditions, and thus it is anticipated to reflect the true values of the work function changes caused by thiolate SAMs on gold substrates.[f] All of the samples of alkylthiolate SAMs on gold showed a work function more than 1 eV *lower* than the work function of clean gold. Similarly to previously mentioned reports,[39,41] the authors showed that a change in the number of methylene units results in a change in the work function. Fitting the data points with a linear function yielded the slope of -19 meV / methylene unit, an absolute value larger than the values reported by both Evans et al. and Lu et al. Partially fluorinated alkyl thiolate SAMs showed an *increase* in the work function of the underlying substrate by as much as ca. 0.5 eV, consistent with the different direction of the dipole moment of the surface-attached molecules in the case of fluorinated and non-fluorinated chains. Analysis of the measured changes in the work function of gold as a function of the calculated projection of the molecular dipole moment onto the surface normal in the alkyl- and perfluoroalkylthiolate SAMs revealed

[f] As mentioned in section 1.1.4 any adsorbate will change the work function of a metallic surface. Thus, only working under ultrahigh vacuum conditions with properly cleaned metal surfaces can yield true work function values of the metal surface.

that the Au – sulfur interaction depresses the work function by ca. 0.5 eV, which is the same value as that found by Evans et al. for similar systems.[39] An interesting behavior was observed in a series of SAMs formed with alkylthiolates of different length terminated with a trifluoromethyl group. Figure 1.7 shows a schematic representation of these systems.

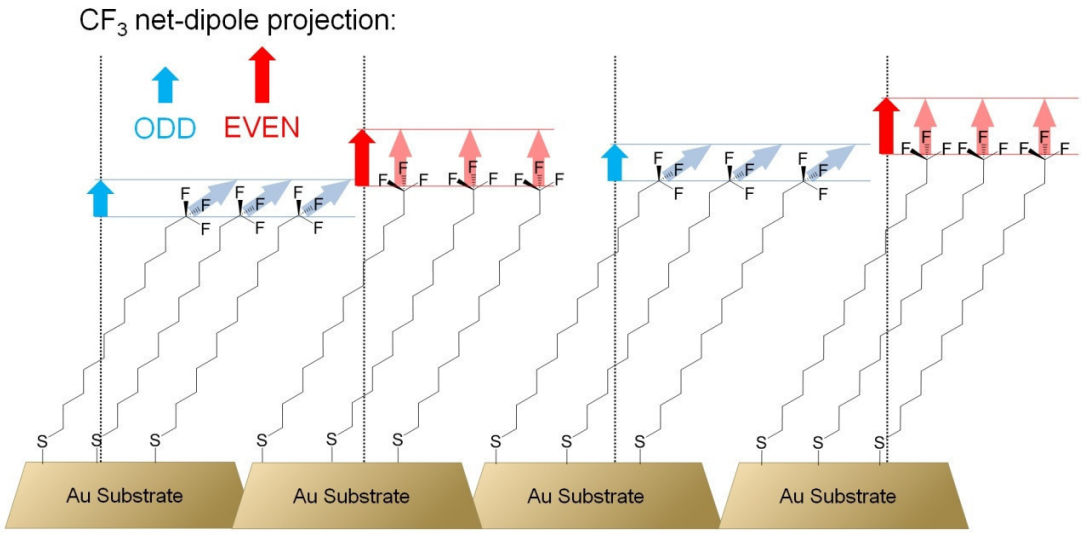

Figure 1.7. Schematic diagram of SAMs on gold studied by Alloway et al. The projections of the dipole moment of polar trifluoromethyl group onto the surface normal (dashed line) are shown by the vertical arrows. Based on ref. 42.

Due to the different orientation of the polar CF_3 groups with respect to the surface normal in odd- and even-numbered alkylthiolate SAMs, the magnitude of the effective-dipole-moment projection onto the surface normal, shown in Figure 1.7 with blue and red arrows, is different and manifests itself with an odd-even effect on the measured work function of the underlying gold substrate.

De Boer et al. studied the effects of alkylthiolate and perfluoroalkylthiolate SAMs on the work function of gold and silver.[21] Using the Kelvin probe technique the researchers found qualitatively similar changes of the work function, caused by the studied SAMs, for both metals. In particular, the perfluorinated alkylthiolate SAMs *increased* the work function by 0.6 eV and 1.1 eV for gold and silver, respectively. The alkylthiolate SAMs, on the other hand, *decreased* the work function for both metals respectively by 0.8 eV, and 0.6 eV. Again, the changes in the work function caused by the organic monolayers were rationalized in terms of the SAM dipole layer and the resulting surface potential difference for different molecular structures. De Boer et al. took one step further and demonstrated the effect of the SAMs on the performance of organic diodes employing silver electrodes. These devices were built as models for organic light emitting diodes (OLEDs) based on the use of a semitransparent silver anode. The ionization potential of the active organic layer used in these OLEDs – poly[2-methoxy-5-(2'-ethyl-hexyloxy)-1,4-phenylene vinylene] (MEH-PPV) – is not matched with the untreated anode's work function, resulting in a hole injection barrier of ca. 0.9 eV, which is a rather large value requiring operation of the device at high voltage. The devices described by the authors were prepared in a few configurations: a) Ag anode / MEH-PPV / Ag, b) Ag anode / perfluoroalkylthiolate SAM / MEH-PPV / Ag, and c) Ag anode / alkylthiolate SAM / MEH-PPV / Ag. Figure 1.8 shows the energy diagram of the Ag anode / organic layer interface for configurations a) and b). Due to the dipole layer of the perfluoroalkylthiolate SAM the work function of the silver anode surface was increased by 1.1 eV, thus effectively eliminating the hole-injection barrier, Δ_h, from the electrode to the organic layer and forming an ohmic contact. Indeed, the current – voltage

characteristics for the investigated devices showed ohmic behavior in the device incorporating perfluoroalkylthiolate SAM, in contrast to the device without the SAM on top of the silver anode, which showed an onset voltage for the conduction. Interestingly, the presence of alkylthiolate SAM on the silver anode (configuration c) of the device) increased the onset voltage of the diode even further when compared to the device without any SAM. This was rationalized in terms of the reduction of the work function of silver by the alkylthiolate SAM, which resulted in the increase of the hole-injection barrier with respect to case a).

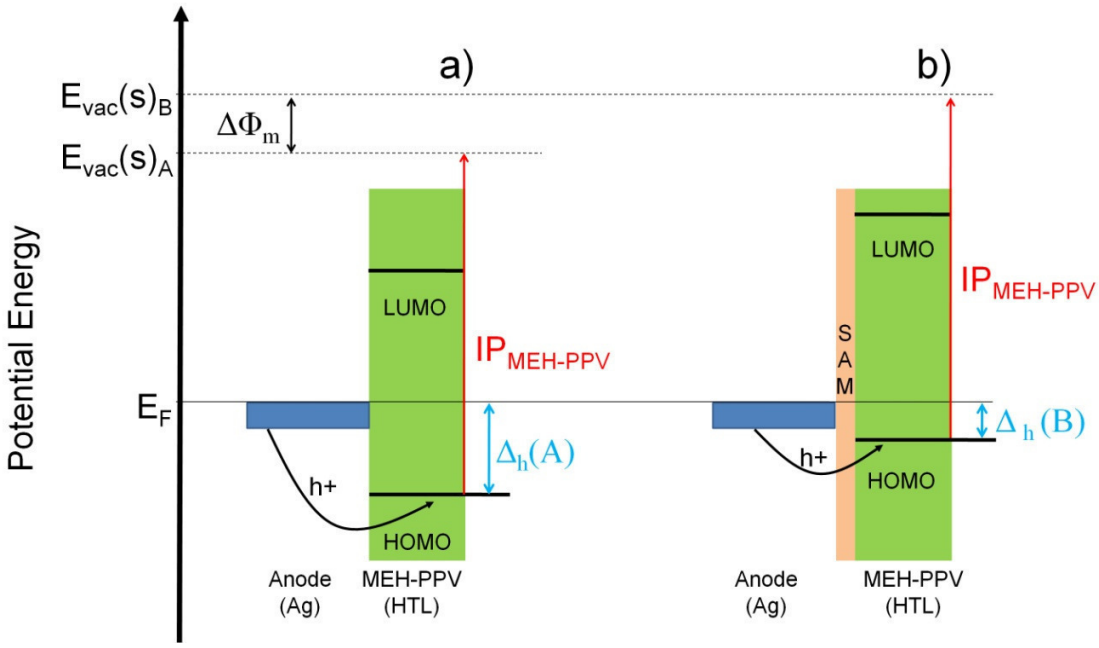

Figure 1.8. Schematic diagram of a) Ag anode / MEH-PPV interface and b) Ag anode / perfluoroalkylthiol SAM / MEH-PPV interface. Vacuum levels close to the surface, $E_{vac}(s)$, SAM induced change of the work function, $\Delta\Phi_m$, and hole-injection barriers, Δ_h, for both devices are shown. Based on ref. 21.

In summary, alkylthiolate-based monolayers on coinage metals have been shown to reproducibly modify the work function of the underlying substrates. Additionally, the molecular structure of constituents of SAMs, together with simple electrostatic considerations, has been shown to be useful in terms of designing surfaces with a desired work-function change. It is important to stress that the modification of the work function of metal electrodes with alkylthiolate SAMs has been demonstrated independently by different research groups, and that the ability to tune the work function has been successfully applied to solve specific technological problems.[20,21]

1.1.7. Self-Assembled Monolayers of Conjugated Thiols and their Influence on the Work Function of Metals

A limitation on the use of monolayers consisting of long-chain alkyl thiols for modifying injection barriers between metals and organics is the intrinsic electrically insulating characteristics of the alkyl chains. Monolayers consisting of π-conjugated thiols, which have been shown to exhibit considerably enhanced conductivity,[34,43] may be more promising for this type of application. Monolayers composed of π-conjugated systems based on oligo(phenylethynyl)benzenethiols and oligo(phenyl)benzenethiols have been shown to form self-assembled domains on gold.[30,31,44-46] A variety of data from different measurement techniques supports the formation of these SAMs on gold and silver with the thiol group binding to the underlying metal and the molecular backbone orienting itself nearly perpendicularly to the surface plane of the substrate.[30,31,44,47-49] Even in the case of molecular structures based on biphenyl thiols with very polar substituents this structural arrangement seems to hold, as demonstrated by Kang et al. in

their comprehensive report.[31] As with alkylthiolate SAMs, the understanding of the structure of π-conjugated thiolate SAMs on metal substrates opened the possibility to study the influence of the molecular structure on the electronic properties of the underlying substrates.

Campbell et al. studied the effects of oligo(phenylethynyl)benzenethiolate SAMs on copper on the performance of organic diodes.[50] Two molecular systems were compared, with the substitution of a terminal hydrogen atom for a fluorine atom as the only difference between the SAM constituents. The researchers compared the current – voltage characteristics of organic diodes with different structures – Cu anode / MEH-PPV / Ca, and Cu anode / SAM / MEH-PPV / Ca. The onset voltage for the conduction in the studied devices showed the expected trend, with the lowest onset recorded for the SAM composed of the fluorine-substituted molecules and the highest onset voltage for the corresponding SAM without fluorine substitution. The rationalization of the observed effect invoked the difference in the hole-injection barrier from the electrode to the organic layer due to the change in the work function caused by the formation of SAMs. Kelvin probe measurements indeed showed that the work function of the copper electrodes coated with the different SAMs qualitatively follows the prediction based on the well known effect of the sheet of dipole moments on top of the metal.

Zehner et al. were the first to systematically study the work function modification of gold by conjugated thiols.[51] The authors applied Kelvin-probe measurements to a series of oligo(phenylethynyl)benzenethiolate SAMs on gold. The rather impressive number of studied systems included molecular structures with different lengths of the π-conjugated backbones as well as different polar end-substituents. The trends of the work-

function change reported in this work are actually not consistent with the predictions based on the molecular dipole moment. In particular, the molecular systems with dipole moments that should theoretically lower the work function actually increase it. Nevertheless, the authors attributed the observed work-function changes to the different dipole moment values of the studied molecular systems, and further conclusions followed.

Chen et al. investigated work function of gold substrates coated with a series of differently substituted terphenyl thiolate SAMs.[52] All of the studied systems showed a depression of the work function when compared with clean gold. A gold surface with an overlayer of a SAM of terphenylthiolate, characterized by only a small dipole moment, showed a work-function value 0.90 eV lower than that measured for the clean gold. Because the dipole moment of the molecule is small, this change has to be attributed to the charge redistribution caused by the formation of Au – S bond. Substitution of hydrogen on phenyl rings in the terphenylbackbone with fluorine atoms showed an increase of the work function of the underlying substrate, in accordance with qualitative predictions based on the dipole moment considerations. The authors showed their ability to tune the work function from 4.30 eV to 4.95 eV by simply using different SAMs on top of the gold electrodes. The structures of the SAMs and the corresponding values of the measured work function are shown in Figure 1.9. Further, the authors showed changes in the hole-injection barrier, Δ_h, into a copper-phthalocyanine (CuPc) layer deposited on top of the different SAM-coated gold substrates. This was done by measuring the position of the highest molecular energy level of CuPc (HOMO) with respect to the Fermi level for the different samples. The changes in the *measured* hole-

injection barrier roughly follow the dependence: $\Delta_h \propto \Phi_m$, where Φ_m is the work function *measured* for the SAM-coated gold substrates. Thus, the use of the different π-conjugated-thiolate SAMs allowed for tuning the hole-injection barrier from the gold electrode into CuPc organic layer. The values of the hole-injection barrier, $\triangle_h$, are also shown in Figure 1.9.

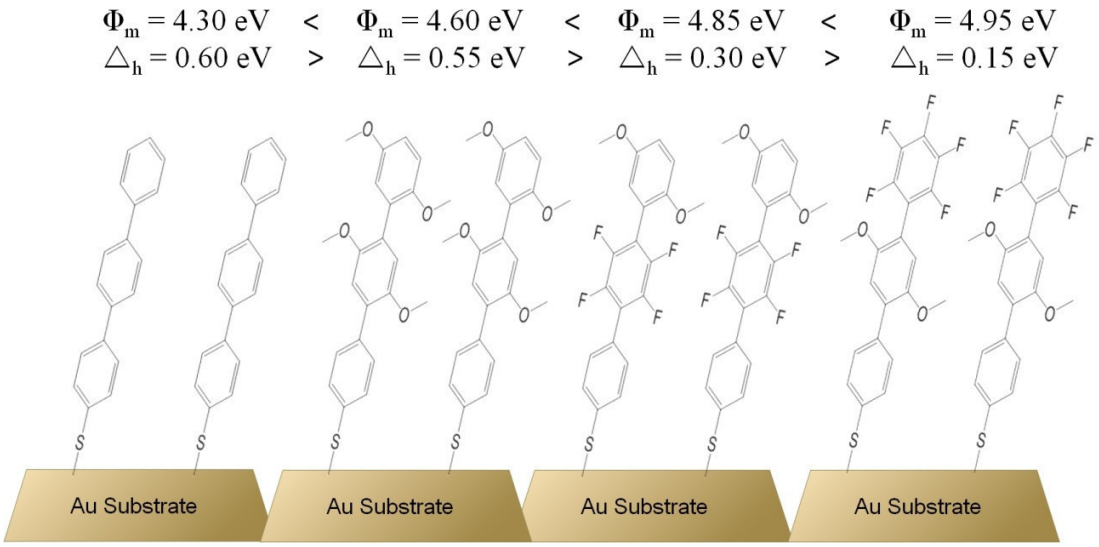

Figure 1.9. Schematic representation of SAMs on gold studied by Chen et al. The measured work functions for the SAM-coated substrates, Φ_m, as well as the hole-injection barriers measured for Au / SAM / CuPc systems, $\triangle_h$, are shown. Based on ref. 52.

Apart from other experimental reports on the metal-work-function changes induced by π-conjugated SAMs,[53,54] particular attention should be brought to theoretical work dealing with the energy level alignment of organic overlayers on gold. Among those, the reports by Heimel et al.,[14,55] and Romaner et al.[26,56] are perhaps of the highest interest in the context of this thesis. These studies focus on theoretical description of biphenylthiolate-based systems as there is a vast amount of data showing these SAMs

possess two dimensional order and their structure has been studied extensively, thus making them good model systems for theoretical investigations.[1,31] Employing density functional theory (DFT), Heimel et al. showed that biphenylthiolate SAMs terminated with three different end-groups (a weak π-donor –SH, a strong π-donor $–NH_2$, and a strong π-acceptor –CN; see Figure 1.10) can result in large changes of the work function of the underlying gold substrate.[14,55]

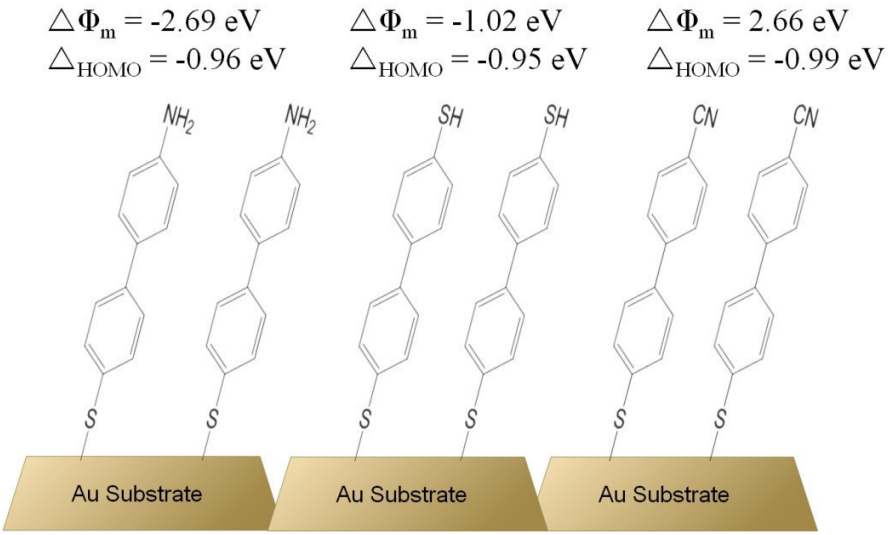

Figure 1.10. Schematic representation of biphenylthiolate SAMs on gold studied theoretically by Heimel et al. The calculated changes of the work function caused by the SAMs, $\triangle\Phi_m$, and the offsets between the HOMO and the Fermi level, $\triangle_{HOMO}$, are shown. Results from ref. 55.

Because of the electron-donating ability of the amino group to the π-conjugated biphenyl backbone, this system exhibits a dipole moment with the positive end at the organic / vacuum interface, thus *decreasing* the work function of the substrate by 2.7 eV. On the other hand, a strongly electron-withdrawing substituent, the cyano group, forms a dipole with its positive end at the metal / organic interface. This results in an *increased*

work function of the substrate by as much as 2.7 eV. Interestingly, the mercapto-substituted biphenylthiolate SAM on gold (the structure in the middle of Figure 1.10), a system with essentially no dipole moment along the long molecular axis, showed the work function to be *decreased* by 1.0 eV when compared to that of clean gold. This has been attributed to the dipole layer formed by the charge rearrangement due to the Au – S bond formation, and labeled a *bond dipole*. Analysis of the charge-density distribution led the authors to conclude that the bond dipole in all three studied systems is the same and, thus, that the charge rearrangement due to Au – S binding does not depend on the end-substituent of the biphenylthiolate backbone. Surprisingly, the offsets of the highest molecular orbital and the Fermi level for all three systems were calculated to be the same, despite the large differences in the gas-phase molecular ionization potentials. This has serious consequences for tuning of the hole-injection barrier from the gold electrode to the organic monolayer, as the authors clearly showed that the use of SAM constituents with clearly different molecular ionization potentials does not necessarily translate into a different offset between the HOMO and the Fermi level. However, it would be prudent not to draw general conclusions from these findings, as the results were obtained for biphenyl-based systems only and it is not clear if the used DFT methodology describes the studied systems in sufficient detail and accuracy.

Using the same DFT approach as in Ref. 55, Romaner et al. studied the influence of the surface coverage on the work-function changes induced by substituted biphenylthiolate SAMs on gold.[56] Though some of the theoretically studied systems are not likely to be synthetically accessible, rather important conclusions were reached. Due to the polarizable nature of the biphenyl backbone of the SAM constituents the molecule

– molecule distance on the gold surface has a large effect on the effective dipole-moment-layer depolarization. It was found that the increase of the surface coverage of the biphenylthiolate moieties not only increases the surface density of the dipole moments, but also leads to an increase in molecule – molecule depolarization effects, which effectively decreases the contribution of the additional dipoles to the change of the work function. Also, while the high-coverage systems showed the same behavior as those studied by Heimel et al.,[55] at lower coverages there seemed to be a dependence of the energy offset between the HOMO and the Fermi level on the molecular ionization potential of the SAM constituents.

1.1.8. Self-Assembled Monolayers on Gold - Thesis Motivation

It should be stressed that although a body of both experimental and theoretical data on the influence of SAMs composed of substituted π-conjugated thiols on the work function of the underlying metal substrates already exists, as discussed in the previous sections, the understanding of this influence is still rather inchoate. One of the goals of the work described in this thesis was to prepare and characterize a series of substituted π-conjugated thiolate SAMs on gold and study the electronic properties of the gold / SAM interface. Substituted stilbene thiolates were chosen as the systems of interest for two major reasons. First, even though rigid biphenylthiolates have been shown to form assembled monolayers on noble-metal surfaces, the domain size of the two-dimensional assemblies has been shown to be rather small.[32,57] Due to the rigidity of the biphenyl backbone and the mismatch between the crystal structure of biphenyl and the packing mode of the corresponding thiolates on gold there is a fair amount of stress in the

molecular overlayer, which can limit the domain size.[57] The stilbene backbone is less rigid than that of biphenyl and may result in lower stress in the monolayer and, thus, assembled domain sizes larger than those found for biphenylthiolates. Second, while biphenyl- and tolane-based π-conjugated-thiolate SAMs on noble metals have been reported, stilbene thiolate SAMs on gold have not. Certainly the study of SAMs of the systems described herein will add to the total understanding of the formation and characteristics of π-conjugated-thiolate SAMs on gold.

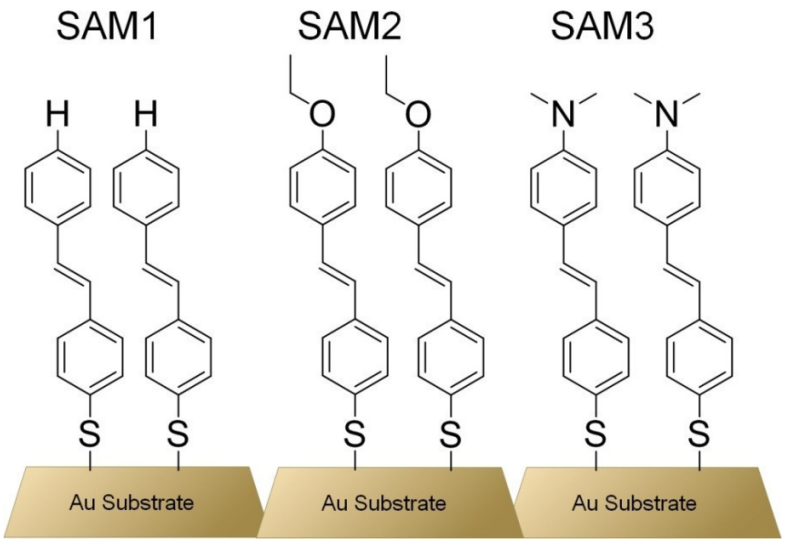

Figure 1.11. Schematic representation of stilbene thiolate SAMs on gold studied herein. The labels of the SAMs as they are used throughout this thesis are shown above the structures.

The stilbene thiolates studied in this work bear different π-electron-donating substituents on the terminal phenyl ring and are presented in Figure 1.11. The different π-electron-donating ability of the three substituents allows for studying the substituent effect on the work function of the underlying gold substrate.

1.2. The Fates of Excited States of Organic Dyes on Gold Nanoparticles

1.2.1. Gold Nanoparticles – Historical Perspective

Metal nanoparticles show very interesting optical properties. The use of these miniscule objects for glass staining dates back to the ancient times. "Ruby glass", which is essentially glass containing gold nanoparticles, has been used since antiquity until the present.[58] A classic example of an ancient piece of art gaining its appeal from the color produced by metal nanoparticles is the late Roman "Lycurgus Cup", which is exhibited in the British Museum.[2,58,59] Depicting the mythological scene of Lycurgus's entrapment by the vine-turned Ambrosia, a maenad of Dionysus, the cup shows extraordinary dichroic behavior exhibiting red color in transmission and green color in reflection (see Figure 1.12). This beautiful effect is due to absorption and scattering of gold and silver nanoparticles which are present in the glass from which the cup is made.[58,59]

Figure 1.12. Lycurgus Cup under illumination from the inside (left), and under ambient light (right). Source: www.britishmuseum.org/.

A revolution in the use of gold metal for glass and ceramic staining did not take place until late 17th century when it was discovered that combining aqua regia solution of gold and tin produces a precipitate with deep and vibrant red color.[60] Named "purple of Cassius", after its alleged inventor,[g] the colorant became one of the most successful red pigments used in the production of glass and ceramics, and it is still in use today.[60,61]

Apart from their use for staining glass and ceramics, gold particles were also employed in photography. In 1842 Sir John Herschel developed his "chrysotype" process in which a photochemically reduced iron(II) salt was exposed to a tetrachloroaurate(III) salt, resulting in the reduction of gold(III) to gold(0), with subsequent formation of gold particles.[62] Even though this method did not survive competition from the silver photography invented earlier by Talbot, gold particles were successfully and routinely used for toning silver photographs, which gave them increased stability.[62]

Much work in the early days of chemistry was stimulated by the "purple of Cassius". The question of the composition and nature of the dye constituted a serious, often raucously argued, scientific problem in the 19th century. The first time it was recognized that "purple of Cassius" is composed of *"extremely finely divided gold"* was in 1802. This was published by Jeremias Benjamin Richter, the same chemist who bequeathed us the law of definite proportions. A number of historically famous chemists took part in the discussion – Joseph Proust, Jöns Jacob Berzelius, and Joseph Louis Gay-Lussac, just to name a few. The main argument in those days revolved around the

[g] Even though Andreas Cassius had been given the credit of the discovery and the 1685 recipe of the "purple of Cassius" he was not the first to discover the recipe for the preparation of the famous colorant. By 1659 a report of the preparation of the red pigment had already been published by Johann Rudolf Glauber, and by about 1679 the colorant had been in use in a glass factory at Potsdam. The history of this is rather fascinating as there were apparently two persons named Andreas Cassius – a father and the son to whom the discovery of "purple of Cassius" was attributed – and it is not clear what the role of each one of them was in the development of the dye. More on this can be found in Ref. 61.

question whether the gold in "purple of Cassius" is in the form of an oxide or in its metallic form.[60] In the contemporary literature the moment considered as the definitive recognition of gold particles as the main constituents of "purple of Cassius" seems to be the Bakerian Lecture Michael Faraday gave to the Royal Society in 1857.[63] Faraday devoted a part of his scientific career to studying the interactions of *"finely divided"* metals, especially gold, with light by which, as his writing implies, he was fascinated. It is captivating to read about his motivation to study the metal particles in the context of these interactions. Being an exceptional experimentalist, Faraday intuitively felt that experiments with highly absorbing metal particles with sizes smaller than the wavelength of light may give useful insights supporting the theory of ether, which he accepted.[63] Though the legacy of Faraday's work obviously does not include a proof for the existence of ether, the body of his work on the interaction of metal particles with light marks the beginning of modern spectroscopy research on colloidal gold.[2,64]

It is important to add that the discussion on the composition of "purple of Cassius", which animated the scientific discourse in the 19th century, found its definitive conclusion in the work of Richard Zsigmondy reported in 1898.[65] The Hungarian-born chemist used his invention – the ultramicroscope – to show that the red color in "purple of Cassius" comes from tiny gold particles – colloidal gold.[60,65] In 1925 he was awarded the Nobel Prize in chemistry "for his demonstration of the heterogeneous nature of colloid solutions and for the methods he used, which have since become fundamental in modern colloid chemistry".[66]

A mathematically rigorous description of the color of gold particles was demonstrated at the beginning of 20th century in terms of classical electromagnetic

theory. James Maxwell Garnett and Gustav Mie independently described the interaction of metallic nanoparticles with light and rationalized the observed nanoparticle colors using classical electromagnetism.[67-69] This purely classical description of light absorption and scattering by metal nanoparticles still dominates today and is a source of fruitful scientific findings.[2,64,70,71]

Not to downgrade numerous research activities throughout the 20th century, but one late report appears to be an important milestone in the gold nanoparticle research. Published by Brust et al. in 1994, it described a successful preparation of gold nanoparticles in organic solvents with the use of organic thiols as stabilizers of the resulting colloidal gold.[72] This started a renaissance in gold-nanoparticle research as the organic-soluble particles could be treated like typical organic compounds; i.e., standard organic chemistry techniques could be used for the manipulation of these species. Additionally, the synthetic accessibility and flexibility of the organic-thiol stabilizers made it possible to systematically study a variety of effects of the stabilizer molecules on the physical properties of the gold particles and vice versa.

1.2.2. Gold Nanoparticles – Surface Plasmon Resonance

A prominent spectroscopic feature of noble metal nanoparticles (NPs) is the so-called surface plasmon resonance, which gives rise to a sharp and intense absorption band in the visible range. The physical origin of the absorption is a collective resonant oscillation of the free electrons of the conduction band of the metal.[64,70,73] Figure 1.13 shows a representation of the displacement of the conduction-band electrons induced by a resonant incident electric field.

For a spherical nanoparticle that is much smaller than the wavelength of the incident light its response to the oscillating electric field can be described by the so-called dipole approximation of Mie theory.[64,71] In this approximation the wavelength-dependent extinction cross section of a single particle, $C_{ext}(\lambda)$, which defines the energy losses in the direction of propagation of the incident light due to both scattering and absorption by the particle,[h] is described in terms of the dielectric function of the metal, $\varepsilon(\lambda) = \varepsilon'(\lambda) + i\varepsilon''(\lambda)$, and the dielectric constant of the medium, ε_m, as shown below:[71]

$$C_{ext}(\lambda) = \frac{24\pi^2 R^3 \varepsilon_m^{3/2}}{\lambda} \frac{\varepsilon''(\lambda)}{(\varepsilon'(\lambda)+2\varepsilon_m)+\varepsilon''(\lambda)^2} \qquad \textbf{Equation 1.4}$$

where λ is wavelength of the incident light and R is the particle radius.

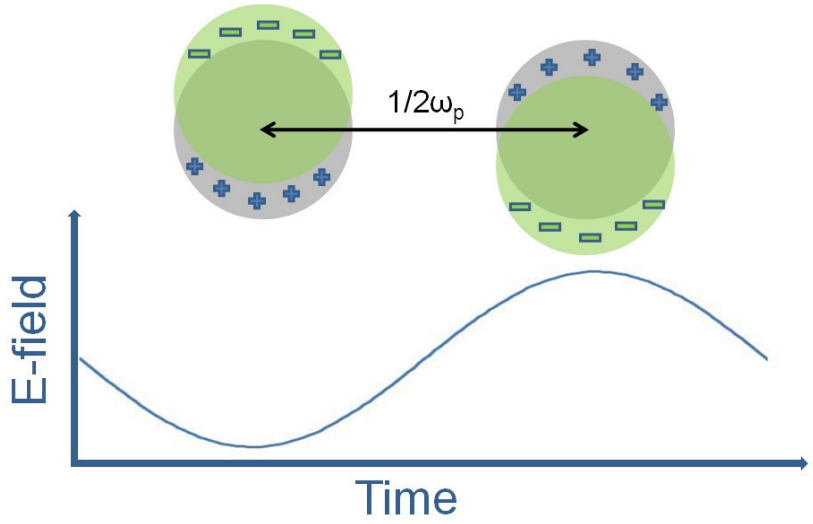

Figure 1.13. Schematic of surface plasmon oscillations induced by an oscillating electric field in a metal sphere. The displacement of the conduction electrons (green color) relative to the nuclei (gray color) is shown. The frequency of the surface plasmon resonance is denoted ω_p. Based on ref. 75.

[h] For gold nanoparticles smaller than 60 nm the scattering cross section is negligible when compared to the absorption cross section.[74]

As can be seen from Equation 1.4, the extinction cross-section of a particle depends on the dielectric function of the metal of which the particle is composed. This gives rise to very different absorption and scattering characteristics for different metal nanoparticles. The maximum of $C_{ext}(\lambda)$, or the resonance condition, will take place when the denominator of the right-hand side of the equation becomes minimal. This is fulfilled approximately at the wavelength λ_p for which $\varepsilon'(\lambda_p) = -2\varepsilon_m$, if the imaginary part of the metal dielectric function, $\varepsilon''(\lambda_p)$ is small.[64,71] The frequency of the surface plasmon resonance, ω_p, is then observed at $\omega_p = c / \lambda_p$ where c is the speed of light in the medium. The frequency of the surface plasmon resonance, ω_p, is depicted in Figure 1.13 in terms of the period of the oscillation of the electric field and the conduction electrons within a metal nanoparticle. Mie theory and its dipolar approximation in the case of small particles can be successfully used to calculate extinction spectra of metal nanoparticles. Using an experimental determination of the dielectric function of the bulk metal and the particle radius, calculations based on Equation 1.4 yield extinction cross section often in excellent agreement with measured absorption spectra of the corresponding nanoparticles.[73]

The resonance condition implies that the surface plasmon resonance frequency depends heavily on the dielectric constant of the medium, ε_m. Indeed, the color of colloidal gold changes with the dielectric constant of the solvent. Underwood and Mulvaney demonstrated that effect by measuring UV-Vis absorption spectra of polymer-stabilized gold nanoparticles of 16 nm in diameter in a series of solvents with different refractive indices. The authors showed that a change in the solvent refractive index from 1.30 to 1.60 lead to a shift in the measured maximum of the surface plasmon resonance

band from 520 nm to 545 nm. Additionally, the measured positions of the maxima agreed perfectly with the values calculated with the use of Mie theory.[70]

From the perspective of a chemist it is interesting to ask how the absorption efficiency of gold nanoparticles compares with that of typical organic dyes. After all, the *collective oscillation of the conduction band electrons* in metal nanoparticles that gives rise to the surface-plasmon absorption band is a rather exotic concept to a chemist when put side-by-side with an absorption process in typical organic dyes, which often can be well-described as a *one-electron transition* between two molecular orbitals. Comparing experimentally determined molar extinction coefficients for gold nanoparticles with extinction coefficients of well-known dyes shows just how much more efficient an absorber a nanoparticle is when compared to an organic dye. As can be seen in Table 1.3, even for rather small nanoparticles (ca. 4 nm in diameter) the molar extinction coefficient is almost two orders of magnitude larger than that of Rhodamine B, which is considered to be an efficient absorber.

Table 1.3. Experimentally measured molar extinction coefficient values, ε_M, of selected organic dyes at their absorption maxima, and of solutions of gold nanoparticles with different diameter, D, at the maximum of the surface plasmon resonance band. Values for the organic dyes were taken from ref. 76 and data for Au NPs were taken from ref. 77.

System	D [nm]	ε_M [L (mol × cm)$^{-1}$]
Terphenyl[a]	-	3.3×10^4
Rose Bengal[b]	-	8.0×10^4
1,6-diphenylhexatriene[a]	-	8.0×10^4
Rhodamine B[b]	-	11×10^4
Au NP[c]	3.8	3.6×10^6
Au NP[d]	4.6	8.6×10^6
Au NP[d]	8.6	51×10^6
Au NP[d]	21	88×10^6
Au NP[d]	34	610×10^6

Solutions in: [a] - cyclohexane, [b] - ethanol, [c] - toluene, [d] - water

The molar extinction coefficient of gold nanoparticles increases roughly cubically with the particle radius reaching impressive values on the order of 10^8 L (mol × cm)$^{-1}$ for particles larger than 20 nm.[77,78] The cubic dependence of the experimentally measured molar extinction coefficient on the particle diameter is in agreement with Mie theory (see Equation 1.4),[78] and it is a manifestation of the *collective oscillation* of the electrons in the nanoparticle, since the total number of electrons within the nanoparticle depends on its volume and, thus, on the third power of the diameter. Figure 1.14 shows absorption spectra of oleylamine-stabilized Au NPs in toluene solutions. As can be seen from the

graph the most prominent feature in the spectra of two sets of particles with different diameter is the band around 520 nm, which is a manifestation of the surface plasmon resonance. The spectra were normalized at 450 nm, at which wavelength the majority of the absorption signal comes from the interband transitions of the metal.[79] Presented in such way the spectra show that the surface plasmon resonance band is much more pronounced and sharper for large particles (12 nm diameter) than for smaller particles (2.5 nm diameter), qualitatively consistent with the discussion above.

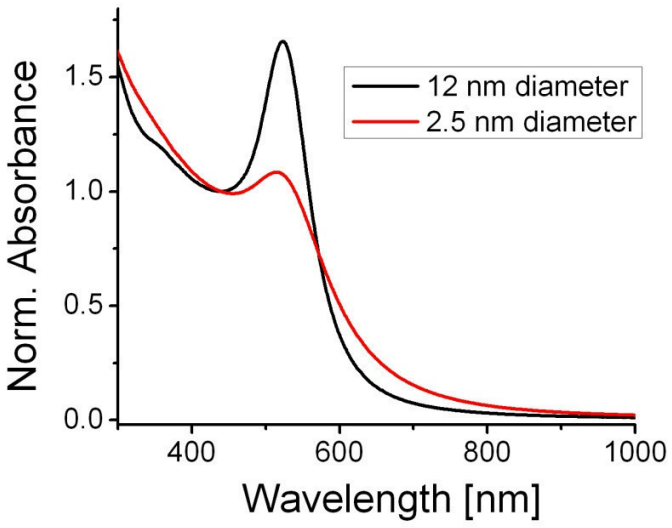

Figure 1.14. UV-Vis absorption spectra acquired for toluene solutions of oleylamine-coated gold nanoparticles with different diameters. The spectra were normalized at 450 nm.

1.2.3. Gold Nanoparticles – Surface Plasmon Resonance Dynamics

The large absorption cross-section values of the surface-plasmon resonance band imply that a NP is able to efficiently acquire a vast amount of energy when irradiated with light at the appropriate wavelength. Thus, it is interesting to ask questions about the

excited-state deactivation pathways and their corresponding dynamics in gold nanoparticles.[i] In other words, how efficient is the deactivation of a photoexcited gold nanoparticle?

Emission of a photon is one of the pathways of energy dissipation in Au NPs. The efficiency of this process is, however, rather low. Dulkeith et al. demonstrated that gold nanoparticles exhibited a luminescence quantum yield of ca. 0.0001 %, independent of the particle size within the investigated range from 2 nm to 35 nm.[80]

A second process responsible for the equilibration of the photoexcited electrons in the Au NP after photoexcitation is electron-electron relaxation. The high-energy electrons after the photoexcitation can undergo collisions with other electrons present in the volume of the nanoparticle, leading to the partition of the energy between the electrons. This process leads to a change in the energetic distribution of electrons from the highly non-thermal distribution present immediately after the photoexcitation to a statistical Fermi-Dirac distribution with a high-temperature Fermi level.[j,64] Sun et al. found experimentally that in bulk gold this thermalization process is ultrafast, reporting a time constant of ca. 0.5 ps.[82]

[i] It is useful to clarify what is meant by excited-state deactivation in the context of the surface plasmon resonance in metal nanoparticles. Because the surface plasmon resonance is a manifestation of a *coherent oscillation* of the conduction band electrons, the loss of coherence is a form of deactivation of the excited state and it may have observable effects. However, this loss of coherence does not involve any energy redistribution, but merely the change of the plane in which each electron oscillates (i.e. the change of the plasmon wave vector), thus leading to the loss in coherence. This process is very fast, on the order of a few femtoseconds. More on this can be found in Ref. 64. We are instead interested in the deactivation of the NP excited state via energy dissipation and the discussion in this section focuses on this process only.

[j] Since the particle is metallic, there is essentially a continuum of states available for the electrons and it is useful to talk about the electrons in terms of their kinetic energy / temperature. However, this is true only for particles larger than roughly 2 nm, as for particles with smaller sizes the molecular-like behavior starts dominating and size-induced gaps appear in the density of states of these systems. More on this can be found in the work of Prof. El-Sayed and Prof. Whetten and their research groups at Georgia Tech. For example see Ref. 81.

The "hot electrons" further lose their kinetic energy due to collisions with the ionic crystal lattice of the NP. This process, usually referred to as electron-phonon relaxation, leads to the lowering of the Fermi level and thermalization of the crystal lattice of the nanoparticle.[64] Hodak et al. showed that the electron-phonon-relaxation time constant in gold NPs did not depend on the size of nanoparticles for samples within the 2.5 nm to 120 nm size range,[74] and that its value (ca. 0.7 ps) was very similar to that measured for bulk gold films.[82] Since higher laser power causes a higher temperature jump of the electrons after electron-electron relaxation the electron-phonon-relaxation time constant depends on the power of the excitation beam, as shown experimentally by various researchers.[64,74,78] A spectacular phenomenon related to the heating of the crystal lattice of gold NPs due to the electron-phonon relaxation has been demonstrated by Hodak et al.[83] The researchers observed coherent oscillations in the signal of the surface-plasmon-resonance-band bleach in a femtosecond transient absorption experiment. The oscillations showed a frequency of ca. 6 cm^{-1} and coherence time of ca. 15 ps, which was limited by the polydispersity of the sample. The authors attributed the observed phenomenon to a vibrational "breathing mode" of gold nanoparticles with the hot lattice induced coherently by the photoexcitation followed by electron-phonon relaxation.[83] The expanding – shrinking lattice of a nanoparticle causes shifts in the surface plasmon resonance band, thus causing the measured bleaching signal to show an oscillatory behavior.[64,83]

The final process that leads to the equilibration of a gold nanoparticle after the photoexcitation with the surroundings is sometimes called "phonon-phonon relaxation". This process is responsible for the energy exchange between the hot crystal lattice of the

nanoparticle with the surroundings. Dependent on the nature of the matrix in which the nanoparticles are embedded, the phonon-phonon relaxation time constants are usually on the order of tens to several hundreds of picoseconds.[64,84] The time constant for this process does not depend on the excitation beam power (i.e. on the initial electron temperature after photoexcitation), but it depends on the square of the radius of the particles, which is in agreement with it being a mechanism of energy transfer through the nanoparticle surface.[84]

As described above, the rather complicated cascade of processes leading to the excited-state deactivation of gold nanoparticles is mostly non-radiative, implying fast and efficient heating of the close surroundings of the nanoparticle right after photoexcitation.[k] This behavior has been exploited for a variety of potential applications including information storage,[85] and cancer diagnostics and therapy.[10]

1.2.4. Noble Metal Nanoparticles – Local Field Effects

The induced collective electron oscillations associated with the surface plasmon resonance give rise to induced local electric fields near the nanoparticle surface. The induced electric field originating from the charge separation in the nanoparticle during the plasmon resonance oscillations is very large at very small distances from the surface. For silver nanoparticles the values of the induced field can be tens of times larger than the incident electric field values. Hao and Schatz performed calculations for a silver sphere with a 20 nm diameter and found that due to the surface plasmon resonance the incident electric field is enhanced by ca. 13 times at the immediate particle surface.[86] This

[k] This heating can be so efficient that it can actually cause irreversible changes in the nanoparticle morphology due to melting.

enhancement factor quickly drops to smaller values as the distance from the surface increases.[86,87] These enhanced local fields are responsible for increased rates of field-dependent processes at surfaces of nanostructured metals.

While phenomena in which the local field effect plays a crucial role include surface-enhanced photochemistry[88] and second-harmonic generation,[89,90] perhaps the most celebrated analytical technique based on the local electric-field enhancement by metal surfaces is Surface-Enhanced Raman Spectroscopy. Jeanmaire and Van Duyne found in the late 1970s that pyridine molecules physisorbed onto a rough silver electrode exhibit an unusually strong Raman signal.[91] It is agreed today that the enhanced intensity of the Raman scattering signal of molecules adsorbed on rough metal surfaces is largely due to the enhanced local field effects in the close proximity of the nanostructured metal surface. These signal enhancements can be as large as 10^{14}, of which a factor of 10^{7} - 10^{8} is attributed to the local field effects.[92,93] The large improvement in the detectability afforded by the signal enhancement resulted in a number of analytical techniques, including methods allowing one to probe single molecules.[92,93]

Wenseleers et al. demonstrated that two-photon absorption (TPA) induced fluorescence of an organic dye underwent very large enhancements when the dye was deposited onto a surface composed of silver islands with a fractal geometry.[94] The authors rationalized this behavior in terms of the presence of so-called hot-spots on the surface of the silver film, at which the local field enhancements could be as large as 1.6×10^{5}. The local field effects on TPA were also demonstrated by Cohanoschi and Hernandez. They used Z-scan measurements to show that combining an organic dye in

solution with aggregates of gold nanoparticles resulted in an enhancement of the TPA cross section by a factor of 480 times.[11]

The potentially important consequences of the enhancements in nonlinear spectroscopic response of molecules due to the proximity of metallic nanostructures form one of the points of motivation for the work on gold nanoparticles presented in this thesis.

1.2.5. Gold Nanoparticle / Organic Dye Systems and their Photophysics

The unique photophysical properties of gold nanoparticles, which include the efficient absorption characteristics and the local field effects discussed in the previous sections, offer many opportunities for sensing, photothermal, or nonlinear-optical applications. In addition, combining the properties of gold nanoparticles with those of known organic dyes has already led to interesting applications including mercury sensing,[95] and sensing of biologically relevant molecules.[8,9] Because of their chemistry, gold nanoparticles are an excellent platform for studying the influence of a metallic core on organic dyes in close proximity to it.

To date there are numerous reports on the study of the influence of gold nanoparticles on the photophysics and photochemistry of organic dyes anchored to the nanoparticle surface. The scientific questions dominating the developments in this field are related to the radiative and non-radiative deactivation pathways of the excited state of organic dyes immobilized on the surface of nanoparticles. Considering the geometry and photophysical properties of gold nanoparticles, three major processes leading to the deactivation of a photoexcited dye in close proximity to the nanoparticle surface should be considered. First, the efficient absorption by gold nanoparticles throughout the UV-

Vis spectrum (see Figure 1.14) can lead to a fast *energy transfer* from the photoexcited dye to the nanoparticle. Related to the energy transfer is the modification of the natural luminescence lifetime, or radiative rate, of dyes by the proximal gold nanoparticle.[96] Second, the photoexcited dye can undergo an *electron transfer* to the continuum of energy levels in the metallic core. Finally, the high local density of organic dyes anchored to the nanoparticle surface facilitates dye – dye interactions, which can manifest themselves through the formation of *intermolecular excited species* such as excimers.[97]

Figure 1.15 shows a schematic of the three possible mechanisms of deactivation of excited states of organic dyes by gold nanoparticles. Another process, not shown in Figure 1.15, that can play a role in the excited-state deactivation of dyes in close proximity to gold nanoparticles is connected with the change of the natural fluorescent lifetime, or radiative decay rate, of fluorophores and it will be discussed later on.[96]

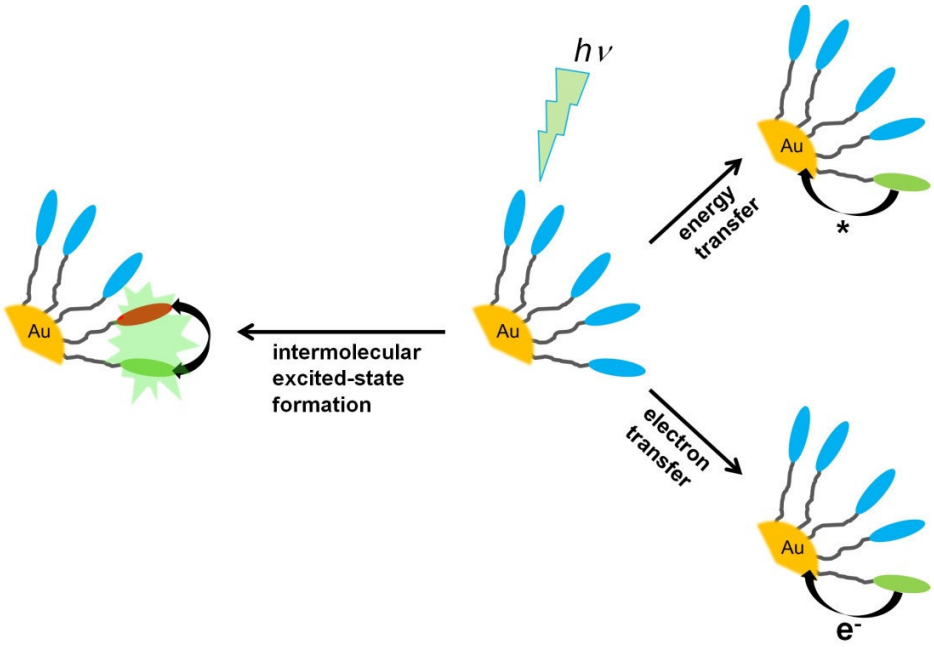

Figure 1.15. Schematic representation of the possible processes leading to excited-state deactivation of an organic dye anchored to the surface of a gold nanoparticle. Based on ref. 97.

1.2.5.1. Energy Transfer to the Nanoparticle and Radiative Rate Modification

Energy transfer from fluorescent organic dyes to gold nanoparticles is generally considered to be the major process leading to the excited-state deactivation of the dyes.[97] Before introducing examples of published reports on the energy transfer involving gold nanoparticles, it is useful to discuss the mechanisms by which the process is likely to occur. Perhaps the most familiar mechanism is that of energy transfer via dipole-dipole interactions. Named after the scientist who described the mechanism mathematically, the rate of Förster resonance energy transfer (FRET) from an energy donor to an energy acceptor, k_{FRET}, depends on: the fluorescence quantum yield of the donor, Φ_D^{fl}; its excited state lifetime, τ_D; refractive index, n; the distance between the donor and the acceptor, r_{D-A}; and the spectral overlap of the fluorescence of the donor, $f_D(v)$ with the molar

extinction coefficient of the acceptor, $\varepsilon_A(\nu)$. The rate constant is described by the following equation:[73]

$$k_{FRET} = \frac{c\,\Phi_D^{fl}\,k^2}{n^4\,\tau_D\,r_{D-A}^6}\int_0^\infty f_D(\nu)\varepsilon_A(\nu)\frac{d\nu}{\nu^4}\,, \qquad \textbf{Equation 1.5}$$

where c is speed of light, k is an orientational factor defining the projection of angles between the transition dipole moment of a donor and that of an acceptor, and ν is frequency. As already mentioned, the fact that gold nanoparticles have very large molar extinction coefficients makes them potentially excellent energy acceptors, according to Equation 1.5. A sizeable effort has been directed at studying promising fluorescent energy donor – gold nanoparticle systems in order to understand the process of energy transfer in these hybrid systems.

Aguila and Murray showed that the fluorescence of dansyl cadaverine – a green-fluorescent dye – attached to the surface of small gold nanoparticles (1.6 nm in diameter) is quenched with respect to isolated dyes in solution.[98] The authors reported that the intensity of the fluorescence emission of the dye attached to the nanoparticles is two orders of magnitude less intense than the fluorescence of the free dye at same concentration.[98] This behavior was explained in terms of energy transfer from the photoexcited fluorophore to the metallic core of the gold nanoparticle. Additionally, the authors pointed out that the length of the alkyl-chain linker between the dansyl moiety and the nanoparticle surface had an influence on the fluorescence quenching efficiency, a more efficient quenching being observed when the linker was shorter, qualitatively consistent with the FRET model.[98]

Gu et al. studied the photophysics of UV-fluorescent fluorene-based dyes covalently attached to gold nanoparticles. Using nanosecond flash photolysis the authors

showed that the triplet-triplet absorption of the fluorene moiety was suppressed in the presence of gold nanoparticles, suggesting that the rate of energy transfer from the photoexcited dye to the gold core had to be much faster than the intersystem-crossing rate of the dye.[99]

Huang and Murray studied the effect of gold nanoparticles on the emissive properties of a cationic dye – $[Ru(bpy)_3]^{2+}$; bpy = 2,2'-bipyridine.[100] The phosphorescence of the dye in aqueqous solution, observed around 610 nm, was quenched after addition of gold nanoparticles with anion-rich surface ligands. This behavior suggested that the electrostatic binding of the cationic dye to the anion-rich surface of the nanoparticles resulted in energy transfer from the photoexcited $[Ru(bpy)_3]^{2+}$ to the nanoparticle core. Additionally, the researchers showed that the quenching of the phosphorescence was 20 times more efficient for gold nanoparticles with 2.2 nm diameter than for those with 1.8 nm diameter.[100] Considering that the larger nanoparticles exhibit molar extinction coefficient larger than that for the smaller particles, the energy transfer to the particles with 2.2 nm diameter should be more efficient than that for nanoparticles with 1.8 nm diameter, in qualitative accordance to Equation 1.5 and the experimental findings.

Phosphorescence of $[Ru(bpy)_3]^{2+}$ attached to gold nanoparticles was also studied by Glomm et al.[101] The authors used the time-correlated single-photon counting technique to measure excited stated lifetimes in these systems and observed more than two orders of magnitude suppression for the lifetime of the dye after attaching it to the surface of gold nanoparticles with 10 nm diameter. In this case, energy transfer as a mechanism leading to the deactivation of the excited state was argued against on the basis

of the spectral properties of the studied systems and the spin-conservation principle, as the studied excited state was a triplet state.[101] Instead, the authors pointed out that an electron transfer mechanism was a more likely candidate for the excited-state deactivation. It should be noted, however, that the argument there was mostly speculative and the experimental techniques used by the authors did not and could not provide a direct evidence for a photoinduced electron transfer from the photoexcited $[Ru(bpy)_3]^{2+}$ to the gold nanoparticle.

Traditionally, Equation 1.5 has been used to successfully describe dipole – dipole energy transfer between molecules. However, an interaction between an organic fluorophore and a gold nanoparticle – a rather exotic species – may follow a different dependence on the relevant system parameters. One of the reports in which the authors attempted to describe the nature of the energy transfer from an organic fluorophore to a gold nanoparticle was published by Yun et al.[102] In particular, the researchers addressed the question of the distance dependence between the fluorophore and the surface of a gold nanoparticle on the rate of energy transfer. A series of samples of DNA-bound fluorescein covalently attached to small, 1.4 nm in diameter, gold nanoparticles was studied in terms of the fluorescence lifetime of the organic dye. The systems were designed in such a way that the DNA strands of different length acted as rigid spacers between the nanoparticle surface and fluorescein moiety, thus allowing preparation of systems with different distance between the dye and the nanoparticle surface. The fluorescence intensities were measured for different samples and the fluorescence quenching efficiencies compared using the parameter $Q_{eff} = 1 - \frac{I'}{I_0}$, where I' is the fluorescence intensity of the dye attached to nanoparticles and I_o is the fluorescence

intensity of the dye in the absence of nanoparticles.[102] Within the tested dye – nanoparticle distance range (6 nm – 23 nm) the quenching efficiency followed a $\frac{1}{r_{Dye-NP}^4}$ dependence, where r_{Dye-NP} is the distance between the dye and the nanoparticle. This behavior is different from that expected for the FRET mechanism, from which a $\frac{1}{r_{Dye-NP}^6}$ dependence would be expected. Yun et al. pointed out that the observed distance dependence of the fluorescence-quenching efficiency is in agreement with the existing description of a mechanism of energy transfer between fluorophores and metal surfaces: surface energy transfer (SET).[102,103] These observations are rather surprising as the nanoparticles studied by Yun were very small and the description of the SET mechanism was developed for infinite metal surfaces.[102] Subsequently, Jennings et al. reported fluorescence lifetime measurements of similar systems to those studied by Yun, including two different fluorophores – one with green fluorescence and one with red fluorescence – and demonstrated that the fluorescence quenching efficiency followed $\frac{1}{r_{Dye-NP}^4}$ dependence, consistent with the findings of Yun.[104]

Dulkeith et al. studied the effects of gold nanoparticles on both radiative and nonradiative rates of excited-state deactivation of lissamine dye molecules.[96] The researchers examined fluorescence lifetimes and quantum yields of a series of systems incorporating lissamine molecules attached to gold nanoparticles of different sizes. It was concluded that the fluorescence quenching, i.e. the reduction of the fluorescence quantum yield, observed in the studied systems was caused not only by an efficient energy transfer from the photoexcited dye to the gold nanoparticle but also by the suppression of the

radiative rate, k_{rad}, of the dye after attaching them to a gold particle. The quantum yield of fluorescence, Φ_{fl}, is defined as:

$$\Phi_{fl} = \frac{k_{rad}}{k_{rad}+k_{nr}}, \qquad \textbf{Equation 1.6}$$

where k_{nr} is a combined rate of all processes leading to a nonradiative deactivation of the excited state of the dye. For simple solutions of fluorescent molecules the radiative rate, k_{rad}, remains more or less unchanged, thus usually fluorescence quenching is not attributed to the changes in the natural fluorescence lifetime, $\tau_{rad} = 1/k_{rad}$. Dulkeith et al. showed that depending on the size of the gold nanoparticles, 1 – 30 nm in diameter in their studies, the radiative rate of particle-attached lissamine molecules was decreased by as much as two orders of magnitude with respect to free dye molecules.[96] At the same time the nonradiative decay rate, k_{nr} in Equation 1.6, increased by almost two orders of magnitude for the studied systems. Thus, according to Equation 1.6 the decrease in the fluorescence quantum yield was caused by both the suppression of the radiative rate and the increase of the nonradiative rate.[96] Dulkeith et al. later investigated the photophysics of a red-fluorescent cyanine molecule (Cy5) attached to gold nanoparticles with a diameter of 6 nm via rigid DNA linkers.[105] Again, fluorescence quenching of the dye was observed after attaching it to the surface on nanoparticles via linkers of different lengths, and the radiative rates of the dye were suppressed in all of the studied systems. In the studied range of dye-nanoparticle distances, 2 nm to 16 nm, the nonradiative rate, which was most likely dominated by energy transfer, seemed to be increased only for systems incorporating the shortest DNA linkers. For systems with the dye-nanoparticle distance larger than 4 nm the nonradiative rate seemed to be the same as that for free dye and the

fluorescence quenching was governed solely by radiative rate suppression, according to Equation 1.6.[105]

The radiative rate modification by metal spheres has been described theoretically by Gersten and Nitzan.[106] Using a purely classical description of an oscillating point dipole placed in close proximity of a metallic sphere with a known dielectric function, the authors calculated the effective radiative and nonradiative rate of the radiating dipole. Dipole – particle distance, particle diameter, dipole orientation with respect to the particle surface, and the dipole-oscillation frequency were found to be important parameters influencing the final values of the radiative and nonradiative rates.[106]

The Gersten-Nitzan (G-N) theory was used for comparison with experimental data for systems incorporating gold nanoparticles, with 10 nm and 20 nm diameters, and covalently attached dyes – $[Ru(bpy)_3]^{2+}$ and a substituted Pd-porphyrin (PdCS3P). Soller et al. prepared such systems and studied the effects of the gold nanoparticles on the phosphorescence of the dyes with the use of the time-correlated single-photon counting technique.[107] At the distance of ca. 4 nm between the luminescent dye and the nanoparticle both $[Ru(bpy)_3]^{2+}$ and PdCS3P showed very similar radiative rates to those measured for free dyes in solution. The nonradiative rates of the dyes on gold nanoparticles were measured to be higher by an order of magnitude than those for the free dyes. The values of radiative and nonradiative rates calculated from the G-N theory were in very good agreement with the measured data when the authors made the assumption of a random orientation of the transition dipoles of the molecules with respect to the particle surface.[107]

It should be noted that the G-N theory fails to describe systems in which the distance between the luminescent dye and the nanoparticle surface is small (i.e. on the order of a nanometer). For example the experimental data of Dulkeith et al., which was previously mentioned, showed much smaller nonradiative rates than those calculated from G-N theory.[96,105] Also, radiative rates calculated for a cyanine molecule (Cy5) at different distances from a gold nanoparticle surface were overestimated when compared to the measured values.[105]

1.2.5.2. Electron Transfer to the Nanoparticle

The possibility that electron transfer is the main channel of deactivation of excited states of organic dyes attached to gold nanoparticles has been suggested by a number of researchers and several studies addressing this hypothesis have been performed.[108,109] The work of Glomm et al. regarding $[Ru(bpy)_3]^{2+}$ on gold nanoparticles was already mentioned.[101] The expectation that gold nanoparticles may be good electron acceptors is supported by a variety of reports on their electrochemical properties. In particular it was demonstrated that gold nanoparticles can accept multiple electrons and the potential for consecutive reduction processes is dictated by the capacitance of the stabilizing alkyl ligand layer.[110,111]

Ipe et al. proposed that in systems involving pyrene – a UV-fluorescent dye – covalently attached to the surface of gold nanoparticles (ca. 2.5 nm in diameter) electron transfer was one of the major processes leading to the deactivation of the excited state of pyrene moiety.[112] The authors used nanosecond flash photolysis in order to study the transient absorption spectra of the hybrid systems. A rather subtle change in the transient

spectrum was observed when examining a solution of free pyrene and a solution of the dye attached to the surface of a nanoparticle. Based on this, the authors suggested that the change in the spectrum originated from the formation of the pyrene radical cation, which is a product in the process of photoinduced electron transfer to the gold nanoparticle.[112]

Barazzouk et al. found that fluorescence of chlorophyll *a* (Chl*a*) is quenched in the presence of gold nanoparticles (8 nm diameter).[113] Even though nanosecond transient absorption of the hybrid system showed no evidence of a radical cation of Chl*a*, the authors favored the photoinduced electron transfer from Chl*a* to the gold nanoparticle as the main deactivation channel of the excited state of the dye. The following experiment, showing results consistent with photoinduced electron transfer, was performed and used to support the interpretation. The authors prepared an indium tin oxide electrode coated with gold nanoparticles onto which Chl*a* molecules were deposited. The authors showed that upon applying a negative potential to the electrode the quenching of the emission of Chl*a* by gold nanoparticles was reduced. It was concluded that this behavior was consistent with the suppression of the photoinduced electron transfer by negatively charging of the gold nanoparticles.[113]

van Herrikhuyzen et al. used a femtosecond transient absorption setup to study the effect of gold nanoparticles (ca. 1.6 nm and 4.1 nm in diameter) on the photophysics of oligo(phenylene-vinylene) (OPV) covalently attached to the nanoparticle surface.[114] Even though the signal from the metallic core of the particles dominated the measured transient absorption traces the authors, were able to conclude that the measured traces were consistent with ultrafast energy transfer, which limited the lifetime of the organic dye to 2 ps. The authors demonstrated no measurable electron transfer taking place in the studied

system, thus limiting the number of processes of the excited-state deactivation of the organic dye to the energy transfer.[114]

1.2.5.3. Intermolecular Interactions

As shown in Figure 1.15, intermolecular interactions may play a role in the deactivation of excited state of dyes attached to gold nanoparticles.[97] The high local density of dyes packed on the metal surface can in principle facilitate such interactions.

Ipe and Thomas prepared a series of gold nanoparticles coated with pyrene-based ligands with alkyl spacers of different chain length as shown in Figure 1.16.[115]

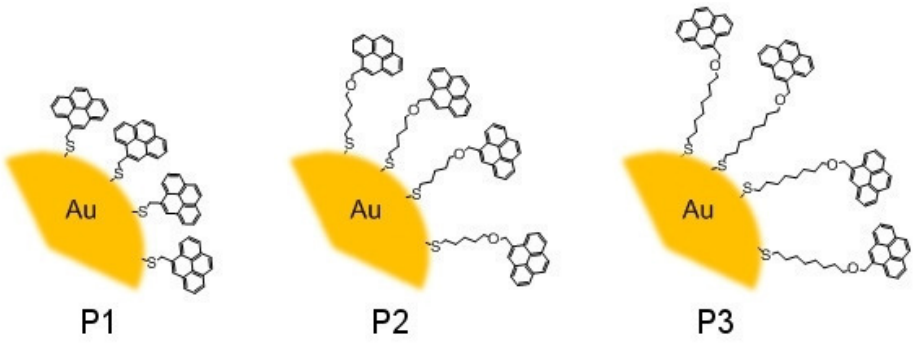

Figure 1.16. Schematic representation of the systems studied by Ipe and Thomas. Based on ref. [115].

Fluorescence spectra of toluene solutions of **P2** and **P3** showed a feature characteristic of the excimer emission of the pyrene moiety. Additionally systems similar to **P2** and **P3** in which pyrene-thiols were used in mixtures with dodecanethiol as the stabilizing ligands of gold nanoparticles showed a decreased signal from pyrene excimers. This was interpreted as being consistent with the formation of pyrene excimers on the surface of nanoparticles, by invoking the dilution of pyrene moieties on the surface

in the pyrene-thiol / dodecanethiol systems. The authors further argued that the structural ability of the pyrene moieties in **P2** and **P3** to align themselves after the photoexcitation to the geometry that allows for excimer formation makes this process efficient on the surface of gold nanoparticles. On the other hand, the researchers concluded, due to a relatively more rigid linker between the anchoring sulfur atom and the pyrene moiety than in **P2** and **P2**, **P1** showed no excimer formation.[115] Interestingly, fluorescence decay data showed that the pyrene-fluorescence lifetimes in the studied nanoparticle systems were not changed appreciably when compared to the fluorescence decay of the corresponding free pyrene-thiol dyes in toluene solution. Based on that observation the authors ruled out a possibility of pyrene-excited-state quenching due to energy or electron transfer.[115]

It is interesting to compare the data of Ipe and Thomas to another report on fluorescence studies of pyrene-thiol coated gold nanoparticles. Werts et al. showed that adsorption of a disulfide bearing two pyrene moieties, showing efficient intramolecular excimer formation, onto the surface of gold nanoparticles (the representation of the reaction is shown in Figure 1.17) causes a decrease of the excimer emission relative to the monomer emission of pyrene.[116] This implies that the pyrene-excimer formation on the surface of gold nanoparticles is less efficient than its formation in the case of the pyrene moieties bound in the form of a disulfide.

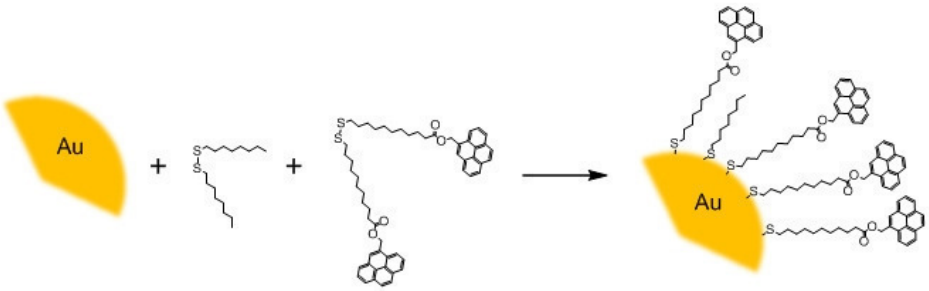

Figure 1.17. Representation of the reaction studied by Werts et al.[l] Based on ref. 116.

Comparison of the data of Werts et al. and the findings of Ipe and Thomas, especially the unchanged fluorescence lifetime of the hybrid systems in Ipe's work, suggests it is possible that Ipe and Thomas inadvertently probed the fluorescence emission of pyrene disulfides, which do show pyrene-excimer emission, as demonstrated by Werts.[115,116] This of course poses the question of the origin of pyrene disulfides in **P2** and **P3** studied by Ipe and Thomas. Actually, the first step of the preparation of gold nanoparticles followed by Ipe, the so-called Brust synthesis,[72] involves reduction of a Au(III) salt to a Au(I) compound with a portion of the thiols used in the synthesis being oxidized to disulfides.[117] Perhaps after the synthesis of the nanoparticles small amounts of pyrene-disulfide impurities were still present in the samples that Ipe and Thomas studied and the observed fluorescence was dominated by the signal from these disulfides.[m]

[l] The starting gold nanoparticles were stabilized with tetraoctylammonium bromide (TOAB) which is not shown in the scheme. Such nanoparticles are commonly referred to as "naked nanoparticles" as TOAB is readily displaced by thiol ligands.

[m] This would be possible only if the fluorescence from particle-bound pyrene moieties was greatly quenched. The fluorescence quantum yield contrast between the surface-bound pyrene and pyrene disulfide would result in the latter dominating the fluorescence signal. This may well be the case as Ipe and Thomas mentioned the existence of a small fraction of fluorescence signal with greatly reduced fluorescence lifetime in the studied hybrid systems.

This alternative interpretation of the published data is of course only speculative, but it opens a question about the usefulness of the widely-used fluorescence-based techniques in the studies of the excited-state deactivation of organic dyes attached to gold nanoparticles. The presence of small amounts of highly fluorescent impurities in samples which possibly have minimal fluorescence quantum yields, because the fluorescence of dyes is quenched by gold nanoparticles, can in principle lead to the measured signal being dominated by emission from the impurities rather than by emission from the systems of interest.

1.2.6. Gold Nanoparticles – Thesis Motivation

In light of the reports described in the previous sections it is still unclear what role the energy and electron transfer and intermolecular interactions play in the context of excited-state deactivation of organic dyes attached to gold nanoparticles. Most of the experimental evidence seems to favor energy transfer coupled with radiative rate suppression as the main processes of quenching of excited states of dyes in close proximity to gold nanoparticles. As to the role of electron transfer and intermolecular interactions, the understanding is rather vague and more work is needed.

One of the goals for the work described in this thesis was to prepare systems incorporating an organic dye, bis(diarylamino)biphenyl (TPD), covalently linked to gold nanoparticles via an alkyl chain or varying length and to investigate the photophysics of these hybrid systems (Figure 1.18).

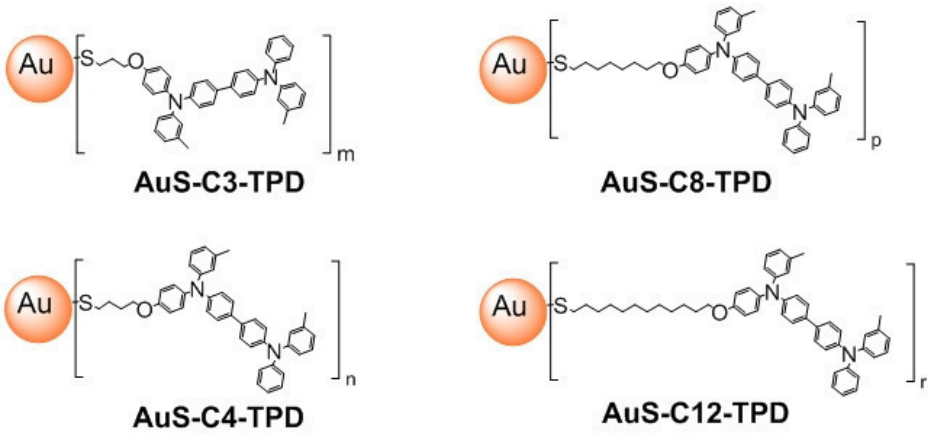

Figure 1.18. Schematic representation of the systems described in this thesis.

There are a few reasons for the choice of the TPD moiety as the dye of interest. First, as mentioned before, there are electric-field enhancement effects in close proximity of metal nanoparticles with a frequency of the oscillating field roughly the same as the surface plasmon resonance frequency.[87] TPD exhibits a sizeable two-photon absorption band for excitation wavelengths from 500 nm to 600 nm,[118] which overlaps with the surface plasmon resonance band of gold nanoparticles. Placing TPD moiety in close proximity of the nanoparticle may result in enhancement of two-photon cross section due to the local field effects. While the nonlinear spectroscopy of the systems shown in Figure 1.18 is not a part of thesis, the findings on the basic photophysics described here are potentially valuable for designing future experiments addressing the influence of gold nanoparticles on TPA characteristics of TPD or similar compounds. Second, TPD is an electron-rich dye, i.e. its oxidation potential is rather low (0.26 V vs $FeCp_2^+$/ $FeCp_2$)[119], which may facilitate an electron transfer from the photoexcited TPD to the nanoparticle. Third, the dye exhibits rather efficient fluorescence (quantum yield of ca. 70 % in dioxane solution),[120] thus, showing relatively straightforward intrinsic photophysics,

which makes TPD a good model for studying the effects of nanoparticles on dye photophysics.

The designed structures, in particular the varying alkyl-spacer length between the TPD moiety and the sulfur atom, in principle allow one to study the effects of the distance between the dye and the nanoparticle on the photophysical characteristics of organic ligand. Also, systems involving gold nanoparticles stabilized with mixed-thiol monolayers, where dodecanethiol was used as a spectroscopically inert ligand, were prepared in order to address the question of the impact of intermolecular interactions on the deactivation of nanoparticle-bound TPD excited state.

1.3. References

(1) Love, J. C.; Estroff, L. A.; Kriebel, J. K.; Nuzzo, R. G.; Whitesides, G. M. *Chem. Rev.* **2005**, *105*, 1103-1170.
(2) Daniel, M. C.; Astruc, D. *Chem. Rev.* **2004**, *104*, 293-346.
(3) Porter, M. D.; Bright, T. B.; Allara, D. L.; Chidsey, C. E. D. *J. Am. Chem. Soc.* **1987**, *109*, 3559-68.
(4) Bain, C. D.; Troughton, E. B.; Tao, Y. T.; Evall, J.; Whitesides, G. M.; Nuzzo, R. G. *J. Am. Chem. Soc.* **1989**, *111*, 321-35.
(5) Whitesides, G. M.; Laibinis, P. E. *Langmuir* **1990**, *6*, 87-96.
(6) Jennings, G. K.; Yong, T.-H.; Munro, J. C.; Laibinis, P. E. *J. Am. Chem. Soc.* **2003**, *125*, 2950-2957.
(7) Chaki, N. K.; Vijayamohanan, K. *Biosens. Bioelectron.* **2002**, *17*, 1-12.
(8) Griffin, J.; Singh, A. K.; Senapati, D.; Rhodes, P.; Mitchell, K.; Robsinson, B.; Yu, E.; Ray, P. C. *Chem. Eur. J.* **2009**, *15*, 342-351.
(9) Shang, L.; Qin, C.; Wang, T.; Wang, M.; Wang, L.; Dong, S. *J. Phys. Chem. C* **2007**, *111*, 13414-13417.
(10) Huang, X.; Jain, P. K.; El-Sayed, I. H.; El-Sayed, M. A. *Nanomedicine* **2007**, *2*, 681-693.
(11) Cohanoschi, I.; Hernandez, F. E. *J. Phys. Chem. B* **2005**, *109*, 14506-14512.
(12) Cahen, D.; Kahn, A. *Adv. Mater.* **2003**, *15*, 271-277.
(13) Ishii, H.; Sugiyama, K.; Ito, E.; Seki, K. *Adv. Mater.* **1999**, *11*, 605-625.
(14) Heimel, G.; Romaner, L.; Zojer, E.; Bredas, J.-L. *Acc. Chem. Res.* **2008**, *41*, 721-729.
(15) Murphy, E. L.; Good, R. H. *Phys. Rev.* **1956**, *102*, 1464.
(16) Hölzl, J.; Schulte, F. K.; Wagner, H. *Solid surface physics*; Springer-Verlag: Berlin, 1979; Vol. 85.
(17) Eastman, D. E. *Phys. Rev. B: Condens. Matter* **1970**, *2*, 1.
(18) Bock, C.; Pham, D. V.; Kunze, U.; Kafer, D.; Witte, G.; Woll, C. *J. Appl. Phys.* **2006**, *100*, 114517/1-114517/7.
(19) Santato, C.; Cicoira, F.; Cosseddu, P.; Bonfiglio, A.; Bellutti, P.; Muccini, M.; Zamboni, R.; Rosei, F.; Mantoux, A.; Doppelt, P. *Appl. Phys. Lett.* **2006**, *88*, 163511/1-163511/3.
(20) Campbell, I. H.; Rubin, S.; Zawodzinski, T. A.; Kress, J. D.; Martin, R. L.; Smith, D. L.; Barashkov, N. N.; Ferraris, J. P. *Phys. Rev. B: Condens. Matter* **1996**, *54*, R14321.
(21) De Boer, B.; Hadipour, A.; Mandoc, M. M.; Van Woudenbergh, T.; Blom, P. W. M. *Adv. Mat.* **2005**, *17*, 621-625.
(22) Nieuwenhuys, B. E.; Bouwman, R.; Sachtler, W. M. H. *Thin Solid Films* **1974**, *21*, 51-8.
(23) Nieuwenhuys, B. E.; Van Aardenne, O. G.; Sachtler, W. M. H. *Chem. Phys.* **1974**, *5*, 418-28.
(24) Huckstadt, C.; Schmidt, S.; Hufner, S.; Forster, F.; Reinert, F.; Springborg, M. *Phys. Rev. B: Condens. Matter* **2006**, *73*, 075409/1-075409/10.
(25) Cornil, D.; Olivier, Y.; Geskin, V.; Cornil, J. *Adv. Funct. Mater.* **2007**, *17*, 1143-1148.

(26) Romaner, L.; Heimel, G.; Ambrosch-Draxl, C.; Zojer, E. *Adv. Funct. Mater.* **2008**, *18*, 3999-4006.
(27) Laibinis, P. E.; Whitesides, G. M.; Allara, D. L.; Tao, Y. T.; Parikh, A. N.; Nuzzo, R. G. *J. Am. Chem. Soc.* **1991**, *113*, 7152-67.
(28) Schreiber, F. *Prog. Surf. Sci.* **2000**, *65*, 151-257.
(29) Laibinis, P. E.; Nuzzo, R. G.; Whitesides, G. M. *J. Phys. Chem.* **1992**, *96*, 5097-105.
(30) Duan, L.; Garrett, S. J. *J. Phys. Chem. B* **2001**, *105*, 9812-9816.
(31) Kang, J. F.; Ulman, A.; Liao, S.; Jordan, R.; Yang, G.; Liu, G. y. *Langmuir* **2001**, *17*, 95-106.
(32) Azzam, W.; Fuxen, C.; Birkner, A.; Rong, H.-T.; Buck, M.; Woell, C. *Langmuir* **2003**, *19*, 4958-4968.
(33) Laibinis, P. E.; Bain, C. D.; Whitesides, G. M. *J. Phys. Chem.* **1991**, *95*, 7017-7021.
(34) Bumm, L. A.; Arnold, J. J.; Cygan, M. T.; Dunbar, T. D.; Burgin, T. P.; Jones, L., II; Allara, D. L.; Tour, J. M.; Weiss, P. S. *Science (Washington, D. C.)* **1996**, *271*, 1705-07.
(35) Zangmeister, C. D.; Robey, S. W.; Van Zee, R. D.; Yao, Y.; Tour, J. M. *J. Phys. Chem. B* **2004**, *108*, 16187-16193.
(36) Houseman, B. T.; Gawalt, E. S.; Mrksich, M. *Langmuir* **2003**, *19*, 1522-1531.
(37) Lee, J. K.; Lee, K.-B.; Kim, D. J.; Choi, I. S. *Langmuir* **2003**, *19*, 8141-8143.
(38) Collman, J. P.; Devaraj, N. K.; Chidsey, C. E. D. *Langmuir* **2004**, *20*, 1051-1053.
(39) Evans, S. D.; Ulman, A. *Chem. Phys. Lett.* **1990**, *170*, 462-466.
(40) Evans, S. D.; Urankar, E.; Ulman, A.; Ferris, N. *J. Am. Chem. Soc.* **1991**, *113*, 4121-4131.
(41) Lu, J.; Delamarche, E.; Eng, L.; Bennewitz, R.; Meyer, E.; Guntherodt, H. J. *Langmuir* **1999**, *15*, 8184-8188.
(42) Alloway, D. M.; Hofmann, M.; Smith, D. L.; Gruhn, N. E.; Graham, A. L.; Colorado, R.; Wysocki, V. H.; Lee, T. R.; Lee, P. A.; Armstrong, N. R. *J. Phys. Chem. B* **2003**, *107*, 11690-11699.
(43) Wold, D. J.; Frisbie, C. D. *J. Am. Chem. Soc.* **2001**, *123*, 5549-5556.
(44) Fuxen, C.; Azzam, W.; Arnold, R.; Witte, G.; Terfort, A.; Woell, C. *Langmuir* **2001**, *17*, 3689-3695.
(45) Dhirani, A.-A.; Zehner, R. W.; Hsung, R. P.; Guyot-Sionnest, P.; Sita, L. R. *J. Am. Chem. Soc.* **1996**, *118*, 3319-3320.
(46) Yang, G.; Qian, Y.; Engtrakul, C.; Sita, L. R.; Liu, G. y. *J. Phys. Chem. B* **2000**, *104*, 9059-9062.
(47) Richter, L. J.; Yang, C. S. C.; Wilson, P. T.; Hacker, C. A.; van Zee, R. D.; Stapleton, J. J.; Allara, D. L.; Yao, Y.; Tour, J. M. *J. Phys. Chem. B* **2004**, *108*, 12547-12559.
(48) Arnold, R.; Terfort, A.; Woell, C. *Langmuir* **2001**, *17*, 4980-4989.
(49) Frey, S.; Stadler, V.; Heister, K.; Eck, W.; Zharnikov, M.; Grunze, M.; Zeysing, B.; Terfort, A. *Langmuir* **2001**, *17*, 2408-2415.
(50) Campbell, I. H.; Kress, J. D.; Martin, R. L.; Smith, D. L.; Barashkov, N. N.; Ferraris, J. P. *Appl. Phys. Lett.* **1997**, *71*, 3528-3530.

(51) Zehner, R. W.; Parsons, B. F.; Hsung, R. P.; Sita, L. R. *Langmuir* **1999**, *15*, 1121-1127.
(52) Chen, W.; Huang, C.; Gao, X. Y.; Wang, L.; Zhen, C. G.; Qi, D.; Chen, S.; Zhang, H. L.; Loh, K. P.; Chen, Z. K.; Wee, A. T. S. *J. Phys. Chem. B* **2006**, *110*, 26075-26080.
(53) Zangmeister, C. D.; Picraux, L. B.; van Zee, R. D.; Yao, Y.; Tour, J. M. *Chem. Phys. Lett.* **2007**, *442*, 390-393.
(54) Risko, C.; Zangmeister, C. D.; Yao, Y.; Marks, T. J.; Tour, J. M.; Ratner, M. A.; van Zee, R. D. *J. Phys. Chem. C* **2008**, *112*, 13215-13225.
(55) Heimel, G.; Romaner, L.; Bredas, J.-L.; Zojer, E. *Phys. Rev. Lett.* **2006**, *96*, 196806/1-196806/4.
(56) Romaner, L.; Heimel, G.; Zojer, E. *Phys. Rev. B: Condens. Matter* **2008**, *77*, 045113-9.
(57) Cyganik, P.; Buck, M.; Wilton-Ely; James D. E. T.; Woell, C. *J. Phys. Chem. B* **2005**, *109*, 10902-10908.
(58) Ruivo, A.; Gomes, C.; Lima, A.; Botelho, M. L.; Melo, R.; Belchior, A.; Pires de Matos, A. *J. Cult. Herit.* **2008**, *9*, e134-e137.
(59) Wagner, F. E.; Haslbeck, S.; Stievano, L.; Calogero, S.; Pankhurst, Q. A.; Martinek, P. *Nature* **2000**, *407*, 691-692.
(60) Carbert, J. *Gold Bull.* **1980**, *13*, 144-50.
(61) Hunt, L. *Gold Bull.* **1976**, *9*, 134-39.
(62) Ware, M. *Gold Bull* **2006**, *39*, 124-131.
(63) Faraday, M. *Philos. Trans. R. Soc. London* **1857**, *147*, 145-181.
(64) Link, S.; El-Sayed, M. A. *Annu. Rev. Phys. Chem.* **2003**, *54*, 331-366.
(65) Zsigmondy, R. *Liebigs Ann.* **1898**, *301*, 361-87.
(66) http://nobelprize.org/.
(67) Garnett, J. C. M. *Philos. Trans. R. Soc. London, Ser. A* **1904**, *203*, 385-420.
(68) Garnett, J. C. M. *Philos. Trans. R. Soc. London, Ser. A* **1906**, *205*, 237-288.
(69) Mie, G. *Ann. Physik* **1908**, *25*, 377-445.
(70) Underwood, S.; Mulvaney, P. *Langmuir* **1994**, *10*, 3427-30.
(71) Mulvaney, P. *Langmuir* **1996**, *12*, 788-800.
(72) Brust, M.; Walker, M.; Bethell, D.; Schiffrin, D. J.; Whyman, R. *J. Chem. Soc., Chem. Commun.* **1994**, 801-2.
(73) Suppan, P. *Chemistry and Light*; The Royal Society of Chemistry: Cambridge, 1994.
(74) Hodak, J. H.; Henglein, A.; Hartland, G. V. *J. Phys. Chem. B* **2000**, *104*, 9954-9965.
(75) Kelly, K. L.; Coronado, E.; Zhao, L. L.; Schatz, G. C. *J. Phys. Chem. B* **2003**, *107*, 668-677.
(76) Berlman, I. B. *Handbook of fluorescence spectra of aromatic compounds*; 2nd ed.; Academic Press: New York, 1971.
(77) Liu, X.; Atwater, M.; Wang, J.; Huo, Q. *Colloid. Surface. B* **2007**, *58*, 3-7.
(78) Link, S.; El-Sayed, M. A. *J. Phys. Chem. B* **1999**, *103*, 8410-8426.
(79) Alvarez, M. M.; Khoury, J. T.; Schaaff, T. G.; Shafigullin, M. N.; Vezmar, I.; Whetten, R. L. *J. Phys. Chem. B* **1997**, *101*, 3706-3712.

(80) Dulkeith, E.; Niedereichholz, T.; Klar, T. A.; Feldmann, J.; von Plessen, G.; Gittins, D. I.; Mayya, K. S.; Caruso, F. *Physical Review B* **2004**, *70*, 205424.
(81) Logunov, S. L.; Ahmadi, T. S.; El-Sayed, M. A.; Khoury, J. T.; Whetten, R. L. *J. Phys. Chem. B* **1997**, *101*, 3713-3719.
(82) Sun, C. K.; Vallée, F.; Acioli, L. H.; Ippen, E. P.; Fujimoto, J. G. *Physical Review B* **1994**, *50*, 15337.
(83) Hodak, J. H.; Martini, I.; Hartland, G. V. *The Journal of Chemical Physics* **1998**, *108*, 9210-9213.
(84) Hu, M.; Hartland, G. V. *J. Phys. Chem. B* **2002**, *106*, 7029-7033.
(85) Zijlstra, P.; Chon, J. W. M.; Gu, M. *Nature* **2009**, *459*, 410-413.
(86) Hao, E.; Schatz, G. C. *J. Chem. Phys.* **2004**, *120*, 357-366.
(87) Zeman, E. J.; Schatz, G. C. *J. Phys. Chem.* **1987**, *91*, 634-643.
(88) Chen, C. J.; Osgood, R. M. *Appl. Phys. A* **1983**, *A31*, 171-82.
(89) Chen, C. K.; de Castro, A. R. B.; Shen, Y. R. *Phys. Rev. Lett.* **1981**, *46*, 145.
(90) Boyd, G. T.; Rasing, T.; Leite, J. R. R.; Shen, Y. R. *Phys. Rev. B* **1984**, *30*, 519.
(91) Jeanmaire, D. L.; Van Duyne, R. P. *J. Electroanal. Chem.* **1977**, *84*, 1-20.
(92) Kneipp, K.; Kneipp, H.; Itzkan, I.; Dasari, R. R.; Feld, M. S. *Chem. Rev.* **1999**, *99*, 2957-2975.
(93) Kudelski, A. *Surf. Sci.* **2009**, *603*, 1328-1334.
(94) Wenseleers, W.; Stellacci, F.; Meyer-Friedrichsen, T.; Mangel, T.; Bauer, C. A.; Pond, S. J. K.; Marder, S. R.; Perry, J. W. *J. Phys. Chem. B* **2002**, *106*, 6853-6863.
(95) Huang, C.-C.; Chang, H.-T. *Anal. Chem.* **2006**, *78*, 8332-8338.
(96) Dulkeith, E.; Morteani, A. C.; Niedereichholz, T.; Klar, T. A.; Feldmann, J.; Levi, S. A.; van Veggel, F. C. J. M.; Reinhoudt, D. N.; Moller, M.; Gittins, D. I. *Phys. Rev. Lett.* **2002**, *89*, 203002/1-203002/4.
(97) Thomas, K. G.; Kamat, P. V. *Acc. Chem. Res.* **2003**, *36*, 888-898.
(98) Aguila, A.; Murray, R. W. *Langmuir* **2000**, *16*, 5949-5954.
(99) Gu, T.; Whitesell, J. K.; Fox, M. A. *Chem. Mater.* **2003**, *15*, 1358-1366.
(100) Huang, T.; Murray, R. W. *Langmuir* **2002**, *18*, 7077-7081.
(101) Glomm, W. R.; Moses, S. J.; Brennaman, M. K.; Papanikolas, J. M.; Franzen, S. *J. Phys. Chem. B* **2004**, *109*, 804-810.
(102) Yun, C. S.; Javier, A.; Jennings, T.; Fisher, M.; Hira, S.; Peterson, S.; Hopkins, B.; Reich, N. O.; Strouse, G. F. *J. Am. Chem. Soc.* **2005**, *127*, 3115-3119.
(103) Persson, B. N. J.; Lang, N. D. *Phys. Rev. B* **1982**, *26*, 5409.
(104) Jennings, T. L.; Singh, M. P.; Strouse, G. F. *J. Am. Chem. Soc.* **2006**, *128*, 5462-5467.
(105) Dulkeith, E.; Ringler, M.; Klar, T. A.; Feldmann, J.; Munoz Javier, A.; Parak, W. J. *Nano Lett.* **2005**, *5*, 585-589.
(106) Gersten, J.; Nitzan, A. *J. Chem. Phys.* **1981**, *75*, 1139-52.
(107) Soller, T.; Ringler, M.; Wunderlich, M.; Klar, T. A.; Feldmann, J.; Josel, H. P.; Markert, Y.; Nichtl, A.; Kuerzinger, K. *Nano Lett.* **2007**, *7*, 1941-1946.
(108) Kotiaho, A.; Lahtinen, R.; Lehtivuori, H.; Tkachenko, N. V.; Lemmetyinen, H. *J. Phys. Chem. C* **2008**, *112*, 10316-10322.
(109) Kotiaho, A.; Lahtinen, R. M.; Tkachenko, N. V.; Efirnov, A.; Kira, A.; Imahori, H.; Lemmetyinen, H. *Langmuir* **2007**, *23*, 13117-13125.

(110) Hicks, J. F.; Templeton, A. C.; Chen, S.; Sheran, K. M.; Jasti, R.; Murray, R. W.; Debord, J.; Schaaff, T. G.; Whetten, R. L. *Anal. Chem.* **1999**, *71*, 3703-3711.
(111) Hicks, J. F.; Miles, D. T.; Murray, R. W. *J. Am. Chem. Soc.* **2002**, *124*, 13322-13328.
(112) Ipe, B. I.; Thomas, K. G.; Barazzouk, S.; Hotchandani, S.; Kamat, P. V. *J. Phys. Chem. B* **2002**, *106*, 18-21.
(113) Barazzouk, S.; Kamat, P. V.; Hotchandani, S. *J. Phys. Chem. B* **2005**, *109*, 716-723.
(114) van Herrikhuyzen, J.; Janssen, R. A. J.; Schenning, A. P. H. J.; Meskers, S. C. J. *Chem. Phys. Lett.* **2007**, *433*, 340-344.
(115) Ipe, B. I.; Thomas, K. G. *J. Phys. Chem. B* **2004**, *108*, 13265-13272.
(116) Werts, M. H. V.; Zaim, H.; Blanchard-Desce, M. *Photochem. Photobiol. Sci.* **2004**, *3*, 29-32.
(117) Chen, S.; Templeton, A. C.; Murray, R. W. *Langmuir* **2000**, *16*, 3543-3548.
(118) Martineau, C.; Anemian, R.; Andraud, C.; Wang, I.; Bouriau, M.; Baldeck, P. L. *Chem. Phys. Lett.* **2002**, *362*, 291-295.
(119) Sasaki, Y.; Araki, Y.; Fujitsuka, M.; Ito, O.; Hirao, A.; Nishizawa, H. *Photochem. Photobiol. Sci.* **2003**, *2*, 136-141.
(120) Philip, R.; Holzer, W.; Penzkofer, A.; Tillmann, H.; Horhold, H. H. *Synth. Met.* **2003**, *132*, 297-308.

CHAPTER 2

MATERIALS AND METHODS

2.1 Materials

2.1.1 General

All solvents and reagents were purchased and were used without further purification with the exception of THF and toluene, which were dried by passing through columns of activated alumina in a manner similar to that described in the literature.[1] Toluene used for the preparation of solutions of gold nanoparticles was purchased from Aldrich (spectroscopic grade) and purified in order to remove sulfur-containing impurities according to a standard procedure.[a,2] Dodecanethiol-d_{25} was prepared by reacting the commercially available dodecyl bromide-d_{25} with potassium thioacetate and further hydrolysis of the resulting ester. The final product was purified by column chromatography.[b] Preparation of 3-(4-bromo-phenoxy)-propan-1-ol and 4'-bromo-4-iodo-biphenyl was described elsewhere.[3] **P1** was prepared from 4-(methylthio)benzyl alcohol according to a slightly modified published procedure.[4] 3-(4-Bromo-phenoxy)-propan-1-ol, 4'-bromo-4-iodo-biphenyl, **1**, **2**, **3**, **4**, and **5** were prepared according to procedures reported in ref. 3, and **7** was prepared according to the procedure described in ref. 5. NMR spectra were recorded using Bruker DRX-500, Bruker AM-250, or Varian Gemini-300 spectrometers. Elemental analysis was performed by Atlantic Microlabs.

---

[a] Fluorescence analysis of diluted toluene (Aldrich, spec. grade) solutions of TPD-coated gold nanoparticles revealed that the fluorescence signal of the dye was growing in time, consistent with the dyes detaching from the surface of nanoparticles. Solutions prepared with the purified toluene showed much smaller changes in the fluorescence signal in time.

[b] The resulting material consisted of 95 % of the thiol and small amount of the corresponding disulfide as measured by GC-MS.

2.1.2 *Synthesis*

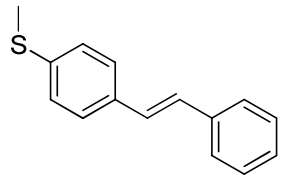

E-4-(Methylthio)stilbene[c] (**M1**)

To a mixture of dimethyl 4-(methylthio)benzylphosphonate (**P1**, 5.54 g, 22.5 mmol)[d] and benzaldehyde (4.78 g, 45.1 mmol) in dry THF (80 mL) at 0 °C potassium *tert*-butoxide (5.95 g, 53.0 mmol) in dry THF (75 mL) was added dropwise under a nitrogen atmosphere. The reaction mixture was then allowed to warm to room temperature and it was stirred under a nitrogen atmosphere for 2 h. The flask was then opened to air and water (5 mL) was added. THF was evaporated under reduced pressure. Then, 150 mL of dichloromethane were added to the remaining crude product and the mixture was washed with water (3 × 50 mL). The organic phase was then dried over magnesium sulfate and filtered. The solvent was evaporated under reduced pressure. The isolated solid material was then recrystallized from ethanol to yield a white solid (4.23 g, 83 %). ^{1}H NMR (500 MHz, CD_2Cl_2) δ (ppm) 7.52 (d, J = 8.4 Hz, 2H), 7.46 (d, J = 8.5 Hz, 2H), 7.36 (t, J = 7.6 Hz, 2H), 7.23-7.28 (m, 3H), 7.09 (s, 2H), 2.50 (s, 3H); ^{13}C{^{1}H} NMR (125 MHz, CD_2Cl_2) δ (ppm) 138.49, 137.70, 134.49, 129.03, 128.25, 128.23, 127.90, 127.19, 126.79, 126.71, 15.81; Anal. Calcd for $C_{15}H_{14}S$: C, 79.60; H, 6.23, Found C, 79.68; H, 6.17; HRMS-EI (*m/z*): calcd for $C_{15}H_{14}S$ (M^+), 226.08162; found, 226.08267.

[c] It is not possible to identify which isomer was synthesized according to the characterization data. However, based on the knowledge of the mechanism of Horner-Wadsworth-Emmons reaction that was used to synthesize **M1**, and the fact that the following reaction leading to the substitution at the sulfur atom yields **Ac1** as *E* isomer, it is most likely that **M1** was obtained as the pure *E* isomer.

[d] **P1** was prepared from 4-(methylthio)benzyl alcohol according to a slightly modified published procedure (Xue, C.; Luo, F.-T. *J. Org. Chem.* **2003**, 68, 4417-4421).

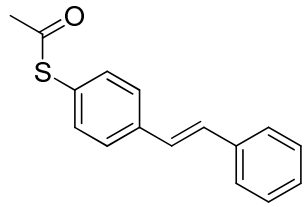

E-4-(Acetylthio)stilbene (**Ac1**)

Compound **M1** (4.0 g, 17.7 mmol) and sodium thio-*tert*-butoxide (5.05 g, 45.0 mmol) in dry DMF (50 mL) were heated to reflux for 24 h under a nitrogen atmosphere. The flask was then cooled to 0 °C and acetyl chloride (10 mL) was added at once to the mixture under a strong nitrogen gas flow. The mixture was then allowed to warm to room temperature and it was stirred under a nitrogen flow for an additional 30 min. The flask was then opened to air and the mixture was poured into water (500 mL). The product was extracted with dichloromethane (200 mL) followed by washing the organic phase with water (4 × 100 mL). The organic phase was then dried over magnesium sulfate, filtered, and the solvent was evaporated under reduced pressure. The crude product was purified by column chromatography using dichloromethane / hexanes (1:1) as eluent, followed by recrystallization from ethanol. This afforded pale greenish needles (2.89 g, 64%). ^{1}H NMR (500 MHz, CD_2Cl_2) δ (ppm) 7.58 (d, J = 8.3 Hz, 2H), 7.55 (d, J = 7.3 Hz, 2H), 7.41 (d, J = 8.3 Hz, 2H), 7.38 (t, J = 7.8 Hz, 2H), 7.29 (t, J = 7.4 Hz, 1H), 7.20 (d, J = 16.4 Hz, 1H), 7.14 (d, J = 16.4 Hz, 1H), 2.42 (s, 3H); ^{13}C{^{1}H} NMR (125 MHz, CD_2Cl_2) δ (ppm) 193.63, 138.17, 136.56, 134.44, 129.77, 128.36, 127.65, 127.08, 126.69, 126.67, 126.26, 29.68; Anal. Calcd for $C_{16}H_{14}OS$: C, 75.55; H, 5.55, Found C, 75.44; H, 5.49; HRMS-EI (*m/z*): calcd for $C_{16}H_{14}OS$ (M^+), 254.07654; found, 254.07653.

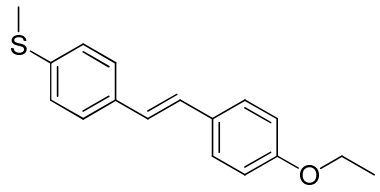

E-4-Methylthio-4'-(ethoxy)stilbene (**M2**)

Compound **P1** (5.51 g, 22.4 mmol) and 4-(ethoxy)benzaldehyde (5.02 g, 33.4 mmol) were dissolved in dry THF (60 mL) under a nitrogen atmosphere. The solution was cooled in an ice-bath and potassium *tert*-butoxide (6.72 g, 59.9 mmol) in dry THF (70 mL) was added dropwise. The reaction mixture was then allowed to allow to warm to room temperature and it was stirred under a nitrogen atmosphere for 1.5 h. After that time the flask was opened to air and poured into methanol (500 mL). The mixture was then cooled to –6 °C for 24 h. The solid was collected by filtration, washed with methanol, and recrystallized from ethanol to give white flakes (4.30 g, 71%). ^{1}H NMR (500 MHz, CD_2Cl_2) δ (ppm) 7.44 (d, J = 8.7 Hz, 2H), 7.42 (d, J = 8.4 Hz, 2H), 7.23 (d, J = 8.4 Hz, 2H), 7.04 (d, J = 16.3 Hz, 1H), 6.94 (d, J = 16.3 Hz, 1H), 6.88 (d, J = 8.8 Hz, 2H), 4.04 (q, J = 7.0 Hz, 2H), 2.49 (s, 3H), 1.40 (t, J = 7.0 Hz, 3H); ^{13}C{^{1}H} NMR (125 MHz, CD_2Cl_2) δ (ppm) 159.18, 137.86, 134.97, 130.27, 127.97, 127.93, 126.95, 126.92, 126.01, 115.01, 63.94, 15.95, 15.04; Anal. Calcd for $C_{17}H_{18}OS$: C, 75.51; H, 6.71, Found C, 75.39; H, 6.65; HRMS-EI (*m/z*): calcd for $C_{17}H_{18}OS$ (M^+), 270.10784; found, 270.11040.

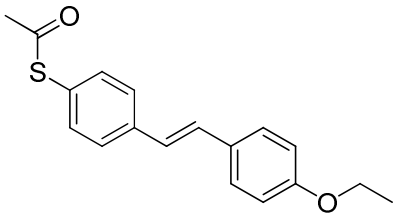

E-4-(Acetylthio)-4'-(ethoxy)stilbene (**Ac2**)

Compound **M2** (4.1 g, 15.2 mmol) and sodium thio-*tert*-butoxide (4.41 g, 39.3 mmol) were heated to reflux in dry DMF (60 mL) for 24 h under a nitrogen atmosphere. The flask then was cooled down to 0 °C and acetyl chloride (10 mL) was added at once to the mixture under a strong nitrogen gas flow. The mixture was then allowed to warm to room temperature and it was stirred under nitrogen gas atmosphere for 1 h. Next the mixture was poured into dichloromethane (200 mL). It was then washed with water (3 × 100 mL). Next the organic phase was dried over magnesium sulfate, filtered, and evaporated under reduced pressure. The crude product was purified by column chromatography using dichloromethane / hexanes (1:1) as eluent, followed by recrystallization from ethanol to give a yellow solid (1.82 g, 40%). ^{1}H NMR (500 MHz, CD_2Cl_2) δ (ppm) 7.54 (d, J = 8.2 Hz, 2H), 7.47 (d, J = 8.7 Hz, 2H), 7.38 (d, J = 8.3 Hz, 2H), 7.14 (d, J = 16.3 Hz, 1H), 6.99 (d, J = 16.3 Hz, 1H), 6.90 (d, J = 8.8 Hz, 2H), 4.05 (q, J = 7.0 Hz, 2H), 2.41 (s, 3H), 1.41 (t, J = 7.0 Hz, 3H); ^{13}C{^{1}H} NMR (125 MHz, CD_2Cl_2) δ (ppm) 193.78, 158.76, 138.60, 134.43, 129.41, 129.09, 127.54, 126.38, 126.07, 124.76, 114.28, 63.21, 29.66, 14.26; Anal. Calcd for $C_{18}H_{18}O_2S$: C, 72.45; H, 6.08, Found C, 72.45; H, 6.08; HRMS-EI (*m/z*): calcd for $C_{18}H_{18}O_2S$ (M^+), 298.10275; found, 298.10333.

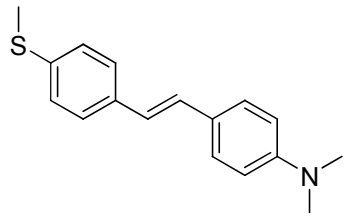

E-4-Methylthio-4'-(dimethylamino)stilbene (**M3**)

Compound **P1** (5.52 g, 22.4 mmol) and 4-dimethylamino-benzaldehyde (6.51 g, 43.6 mmol) were dissolved in dry THF (80 mL) under a nitrogen atmosphere. The mixture was cooled down to 0 °C and potassium *tert*-butoxide (5.99 g, 53.4 mmol) in dry THF (75 mL) was added dropwise. The reaction mixture was then allowed to warm to room temperature and it was stirred under nitrogen gas atmosphere for 24 h. After that time, the flask was opened to air and water (5 mL) was added. The mixture then was poured into methanol (600 mL) and it was stirred for 30 min. The mixture was then cooled down to 6 °C for 1 h. The solid was filtered and washed with methanol to give a white solid (5.52 g, 91%). ^{1}H NMR (500 MHz, CD_2Cl_2) δ (ppm) 7.37-7.42 (m, 4H), 7.22 (d, J = 8.4 Hz, 2H), 7.01 (d, J = 16.3 Hz, 1H), 6.87 (d, J = 16.3 Hz, 1H), 6.71 (d, J = 8.9 Hz, 2H), 2.97 (s, 6H), 2.49 (s, 3H); ^{13}C{^{1}H} NMR (125 MHz, CD_2Cl_2) δ (ppm) 150.59, 137.03, 135.54, 128.55, 127.75, 127.05, 126.65, 125.80, 123.67, 112.67, 40.56, 16.04; Anal. Calcd for $C_{17}H_{19}NS$: C, 75.79; H, 7.11; N, 5.20, Found C, 75.52; H, 7.09; N, 5.21; HRMS-EI (*m/z*): calcd for $C_{17}H_{19}NS$ (M^+), 269.12382; found, 269.12537.

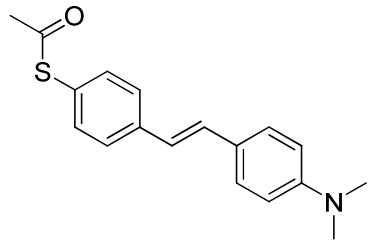

E-4-(Acetylthio)-4'-(dimethylamino)stilbene (**Ac3**)

Compound **M3** (4.13 g, 15.3 mmol) and sodium thio-*tert*-butoxide (3.81 g, 34.0 mmol) were heated to reflux in dry DMF (50 mL) under a nitrogen atmosphere for 24 h. Next the flask was cooled down to 0 °C and acetyl chloride (10 mL) was added at once to the mixture under a strong nitrogen flow. The mixture was then allowed to warm to room temperature and it was stirred under nitrogen flow for 1 h. The flask was then opened to air and the mixture was poured into water (100 mL). The product was extracted with dichloromethane (100 mL) followed by washing the organic phase with water (4 × 100 mL). The organic phase was dried over magnesium sulfate, filtered, and evaporated under reduced pressure. The solid product was recrystallized twice from ethanol to give a yellow solid (2.11 g, 46%). ^{1}H NMR (500 MHz, CD_2Cl_2) δ (ppm) 7.52 (d, J = 8.4 Hz, 2H), 7.42 (d, J = 8.9 Hz, 2H), 7.36 (d, J = 8.3 Hz, 2H), 7.11 (d, J = 16.3 Hz, 1H), 6.92 (d, J = 16.3 Hz, 1H), 6.72 (d, J = 8.8 Hz, 2H), 2.99 (s, 6H), 2.40 (s, 3H); ^{13}C{^{1}H} NMR (125 MHz, CD_2Cl_2) δ (ppm) 194.05, 150.29, 139.31, 134.53, 130.18, 127.50, 126.20, 125.46, 124.70, 122.47, 111.97, 39.89, 29.73; Anal. Calcd for $C_{18}H_{19}NOS$: C, 72.69; H, 6.44; N, 4.71, Found C, 72.55; H, 6.41; N, 4.74; HRMS-EI (*m/z*): calcd for $C_{18}H_{19}NOS$, (M^+), 297.11874; found, 297.11983.

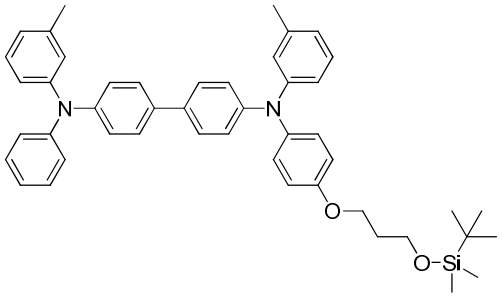

N^4-(4-(3-(tert-Butyldimethylsilyloxy)propoxy)phenyl)-$N^{4'}$-phenyl-N^4,$N^{4'}$-di(m-tolyl)biphenyl-4,4'-diamine (**4**)

Dry toluene (75 mL), **2** (9.10 g, 24.50 mmol), and **3** (8.82 g, 21.30 mmol) were added to a dry round bottomed flask. The mixture was bubbled with an argon gas for 20 min and then $Pd_2(dba)_3$ (0.28 g, 0.31 mmol) and DPPF (0.34 g, 0.60 mmol) were added. After stirring under an argon atmosphere for 10 minutes NaO^tBu (2.32 g, 24.50 mmol) was added. The mixture was heated to 120 °C and was stirred under reflux for 48 h. The solvent was then evaporated under reduced pressure and the solid residue was dissolved in 100 mL of dichloromethane. The solution was washed with water (3 × 200 mL), dried over magnesium sulfate and filtered. Then dichloromethane was evaporated under reduced pressure. The product was purified by column chromatography using hexane / dichloromethane (1:1). After evaporating the solvent under reduced pressure the pure product was obtained (10.11 g, 67%). ^{1}H NMR (300 MHz, CD_2Cl_2) δ (ppm) 7.38-7.52 (m, 4H), 6.75-7.33 (m, 21H), 4.05 (t, J = 6.0 Hz, 2H), 3.80 (t, J = 6.0 Hz, 2H), 2.26 (s, 3H), 2.25 (s, 3H), 1.96 (quint, J = 6.0 Hz, 2H), 0.89 (s, 9H), 0.05 (s, 6H); ^{13}C{^{1}H} NMR (200 MHz, $CDCl_3$) δ (ppm) 155.69, 147.85, 147.68, 147.22, 146.66, 140.55, 139.08, 138.91, 134.77, 133.67, 129.17, 129.04, 128.90, 127.31, 127.14, 127.09, 125.05, 124.15, 124.09, 123.84, 123.77, 122.96, 122.69, 122.57, 121.62, 120.41, 115.35, 112.98, 64.82, 59.61, 32.52, 25.94, 21.44, 18.33, -5.34; Anal. Calcd for $C_{47}H_{52}N_2O_2Si$: C, 80.07; H,

7.43; N, 3.97, Found C, 80.17; H, 7.44; N, 3.96; HRMS-FAB+ (*m/z*): calcd for $C_{47}H_{52}N_2O_2Si$ (M^+), 704.3798; found, 704.3787.

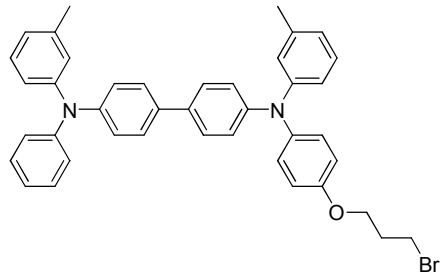

N^4-(4-(3-Bromopropoxy)phenyl)-$N^{4'}$-phenyl-N^4,$N^{4'}$-di(m-tolyl)biphenyl-4,4'-diamine

(**TPD-C3-bromide**)

5 (6.48 g, 11.0 mmol) was added to a dry round bottomed flask containing 60 mL of dry THF. The mixture was stirred and bubbled with argon gas for 20 minutes. Then triphenylphosphine (5.64 g, 21.5 mmol) and carbon tetrabromide (7.13 g, 21.5 mmol) were added and the mixture was stirred at room temperature for 1 h. The flask was then opened to air and THF was evaporated under reduced pressure. The product was purified by column chromatography using hexane / dichloromethane (7:3). Evaporating the solvent under reduced pressure yielded pure product (6.1 g, 85.1%). ^{1}H NMR (250 MHz, acetone-d_6) δ (ppm) 7.39-7.47 (m, 4H), 6.77-7.27 (m, 21H), 4.08 (t, J = 5.8 Hz, 2H), 3.64 (t, J = 6.5 Hz, 2H), 2.27 (quint, J = 6.0 Hz, 2H), 2.19 (s, 3H), 2.18 (s, 3H); ^{13}C{^{1}H} NMR (62.5 MHz, acetone-d_6) δ (ppm) 155.49, 147.89, 147.75, 147.62, 147.21, 146.66, 140.68, 138.95, 138.75, 134.47, 133.38, 129.22, 129.14, 129.00, 127.19, 126.95, 126.91, 124.88, 123.99, 123.81, 123.11, 122.69, 122.44, 121.51, 120.44, 115.41, 65.48, 32.33, 30.07, 20.59, 20.54;[e] Anal. Calcd for $C_{41}H_{37}BrN_2O$: C, 75.34; H, 5.71; N, 4.29, Found C, 75.30;

[e] Two aromatic carbon signals are missing most likely due to an overlap.

H, 5.68; N, 4.22; HRMS-EI (*m/z*): calcd for $C_{41}H_{37}BrN_2O$ (M^+), 652.2089; found, 652.2078.

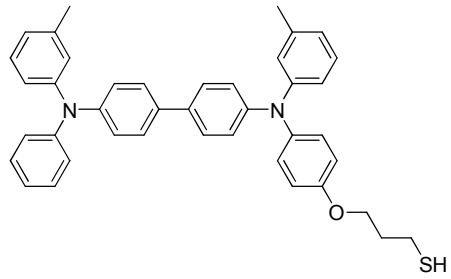

3-(4-{[4'-(Phenyl-m-tolyl-amino)-biphenyl-4-yl]-m-tolyl-amino}-phenoxy)-propane-1-thiol (**TPD-C3-thiol**)

TPD-C3-bromide (4.84 g, 7.41mmol) was dissolved in 100 mL of DMF in a round bottomed flask under an argon atmosphere. Thiourea (1.41 g, 18.5 mmol) was added and the mixture was heated to 90 °C and stirred for 4 h. Then potassium hydroxide (15.0 g, 230 mmol) in 50 mL of water was added and the reaction mixture was stirred for additional 10 h. After that time, the reaction mixture was neutralized by addition of 1 M sulfuric acid and the product was extracted with diethyl ether. The organic phase was washed with diluted hydrochloric acid after which ether was evaporated under reduced pressure and the solid residue was dissolved in dichloromethane (150 mL). The solution was dried over magnesium sulfate and filtered. The product was purified by column chromatography on silica gel, using dichloromethane / hexane (2:3). Evaporating the solvent under reduced pressure yielded the desired product (3.06 g, 68%). ^{1}H NMR (500 MHz, acetone-d_6) δ (ppm) 7.52 (d, J = 8.7 Hz, 2H), 7.50 (d, J = 8.7 Hz, 2H), 7.26-7.30 (m, 2H), 7.18 (t, J = 7.7 Hz, 1H), 7.14 (t, J = 7.8 Hz, 1H), 6.98-7.08 (m, 9H), 6.81-6.95 (m, 8H), 4.10 (t, J = 6.1 Hz, 2H), 2.72 (app. q, J = 7.1 Hz, 2H), 2.24 (s, 3H), 2.23 (s, 3H),

2.06 (app. quint, J = 6.9 Hz, 2H), 1.81 (t, J = 8.1 Hz, 1H); $^{13}C\{^{1}H\}$ NMR (125 MHz, acetone-d_6) δ (ppm) 157.72, 149.86, 149.71, 149.58, 149.22, 148.63, 142.42, 140.93, 140.72, 136.46, 135.30, 131.17, 131.08, 130.92, 129.22, 128.88, 128.83, 126.83, 125.93, 125.80, 125.73, 125.69, 125.02, 124.66, 124.27, 123.44, 122.32, 117.31, 67.79, 35.36, 22.53, 22.47, 22.42; Anal. Calcd for $C_{41}H_{38}N_2OS$: C, 81.15; H, 6.31; N, 4.62; S, 5.28, Found C, 81.06; H, 6.22; N, 4.61; S, 5.04; HRMS-EI (*m/z*): calcd for $C_{41}H_{38}N_2OS$ (M^+), 606.2705; found, 606.2702.

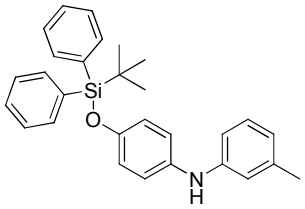

N-[4-(tert-Butyldiphenylsilyloxy)phenyl]-3-methylaniline (**8**)

7 (15.00 g, 36.5 mmol) was added to a Schlenk tube containing anhydrous toluene (10 mL), $Pd_2(dba)_3$ (0.57 g, 0.62 mmol), DPPF (0.69 g, 1.24 mmol), and NaO^tBu (8.76 g, 91.2 mmol). *m*-Toluidine (5.5 mL, 51.3 mmol) was then slowly added to the stirring reaction mixture. The reaction was sealed under inert atmosphere, heated to 95 °C, and stirred for 20 h. The product was purified by column chromatography on silica gel using hexanes / diethyl ether (30:1) as eluent. Evaporating the solvent under reduced pressure yielded the desired product as a viscous liquid (13.00 g, 82%). ^1H NMR (500 MHz, CD_2Cl_2) δ (ppm) 7.79 (d, J = 6.6 Hz, 4H), 7.50 (t, J = 7.4 Hz, 2H), 7.44 (dd, J = 7.5 Hz, 6.9 Hz, 4H), 7.10 (t, J = 7.8 Hz, 1H), 6.90 (d, J = 8.8 Hz, 2H), 6.76 (d, J = 8.9 Hz, 2H), 6.75 (br s, 1H), 6.72 (br d, J = 8.0 Hz, 1H), 6.68 (br d, J = 8.0 Hz, 1H), 5.52 (br s, 1H), 2.30 (s, 3H), 1.16 (s, 9H); $^{13}C\{^{1}H\}$ NMR (125 MHz, CD_2Cl_2) δ (ppm) 151.0, 145.1,

139.5, 136.8, 136.0, 133.5, 130.3, 129.4, 128.1, 121.3, 120.9, 120.6, 116.9, 113.3, 26.7, 21.6, 19.7; Anal. Calcd for $C_{29}H_{31}NOSi$: C, 79.59; H, 7.14; N, 3.20, Found C, 79.41; H, 7.24; N, 3.37; HRMS-EI (*m/z*): calcd for $C_{29}H_{31}NOSi$ (M^+), 437.21749; found, 437.21606.

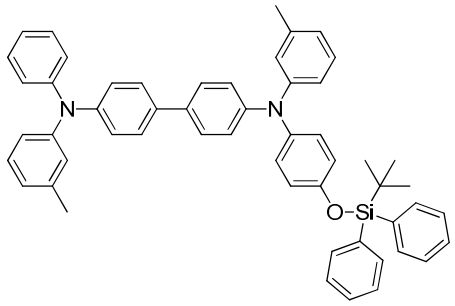

N^4-(4-(tert-Butyldiphenylsilyloxy)phenyl)-$N^{4'}$-phenyl-N^4,$N^{4'}$-di(m-tolyl)biphenyl-4,4'-diamine (**9**)

8 (9.03 g, 20.6 mmol) and **3** (7.24 g, 17.5 mmol) were dissolved in 50 mL of dry toluene. Next the solution was transferred under an nitrogen atmosphere to a Schlenk tube containing $Pd_2(dba)_3$ (0.28 g, 0.30 mmol) and DPPF (0.33 g, 0.60 mmol). Sodium *tert*-butoxide (4.18 g, 43.5 mmol) was then added and the mixture was heated up to 100 °C. The mixture was stirred under a nitrogen atmosphere for 23 h. At this time, the tube was opened to air and toluene was evaporated under reduced pressure. The mixture was then dissolved in diethyl ether (100 mL), washed with water (2 × 200 mL), dried over magnesium sulfate and filtered. The solvent was evaporated under reduced pressure. The product was purified by column chromatography using hexane / toluene (4:1). Evaporating the solvent under reduced pressure yielded the desired product as glassy solid (7.11 g, 53%). ^{1}H NMR (500 MHz, CD_2Cl_2) δ (ppm) 7.79 (d, J = 6.6 Hz, 4 H), 7.52 – 7.41 (m, 10 H), 7.31 (d, J = 7.4 Hz, 1 H), 7.29 (d, J = 7.4 Hz, 1 H), 7.20 (t, J = 7.8 Hz,

1 H), 7.16 – 7.10 (m, 5 H), 7.06 (t, *J* = 7.3 Hz, 1 H), 7.02 (d, *J* = 8.7 Hz, 2 H), 6.99 (br s, 1H), 6.94 (d, *J* = 8.1 Hz, 1 H), 6.94 (d, *J* = 8.1 Hz, 1 H), 6.92 (d, *J* = 8.8 Hz, 2 H), 6.89 (br s, 1 H), 6.85 (d, *J* = 8.1 Hz, 1 H), 6.83 (d, *J* = 7.6 Hz, 1 H), 6.77 (d, *J* = 8.9 Hz, 2 H), 2.31 (s, 3 H), 2.28 (s, 3 H), 1.17 (s, 9 H); $^{13}C\{^{1}H\}$ NMR (125 MHz, CD_2Cl_2) δ (ppm) 152.5, 148.2, 148.0, 147.6, 147.1, 141.4, 139.7, 139.4, 136.0, 135.0, 134.0, 133.4, 129.6, 129.4, 129.2, 128.1, 127.4, 127.3, 127.2, 125.5, 124.5, 124.4, 124.2, 123.5, 123.0, 122.0, 121.0, 120.9, 26.7, 21.5, 19.7; Anal. Calcd for $C_{54}H_{50}N_2OSi$: C, 84.11; H, 6.54; N, 3.63, Found C, 83.97; H, 6.64; N, 3.56; HRMS-EI (*m/z*): calcd for $C_{54}H_{50}N_2OSi$ (M^+), 770.36924; found, 770.37509.

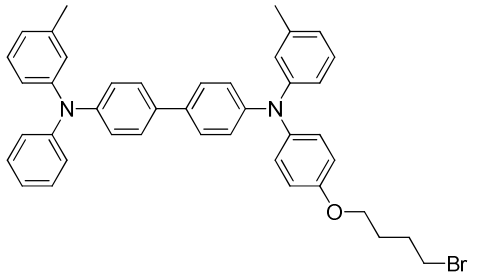

N^4-(4-(12-Bromobutyloxy)phenyl)-$N^{4'}$-phenyl-N^4,$N^{4'}$-di(m-tolyl)biphenyl-4,4'-diamine

(**TPD-C4-bromide**)

1,4-dibromobutane (4.3 g; 19.9 mmol), **9** (1.35 g; 1.8 mmol), and 10 mL of dry, oxygen-free THF were placed together in a Schlenk ampule. The solution was then degassed by three freeze-pump-thaw cycles and 4 mL of 1 M tetrabutylammonium fluoride in THF were added to the cold solution under a nitrogen gas flow. The ampule was then placed under reduced pressure, sealed and the reaction mixture was heated up to 65 ^{o}C and stirred for 15 h. The solvent was then evaporated under reduced pressure. The desired product was purified with a silica plug using hexane / toluene (3:2) as eluent. Evaporating

the solvent under reduced pressure yielded the product as a colorless solid (0.68 g, 58%). ^{1}H NMR (500 MHz, CD_2Cl_2) δ (ppm) 7.45 (d, J = 8.6 Hz, 2H), 7.43 (d, J = 8.7 Hz, 2H), 7.24-7.28 (m, 2H), 6.98-7.19 (m, 11H), 6.79-6.95 (m, 8H), 3.99 (t, J = 6.1 Hz, 2H), 3.52 (t, J = 6.7 Hz, 2H), 2.27 (s, 3H), 2.25 (s, 3H), 2.07 (app. quint, J = 6.9 Hz, 2H), 1.93 (m, 2H); ^{13}C{^{1}H} NMR (125 MHz, CD_2Cl_2) δ (ppm) 156.00, 148.26, 148.19, 147.99, 147.63, 147.10, 141.01, 139.61, 139.43, 134.97, 133.91, 129.53, 129.38, 129.25, 127.68, 127.38, 127.34, 125.45, 124.47, 124.33, 124.26, 124.19, 123.42, 122.98, 122.92, 121.96, 120.79, 115.65, 67.58, 34.12, 29.96, 28.35, 21.52, 21.48; Anal. Calcd for $C_{42}H_{39}BrN_2O$: C, 75.55; H, 5.89; N, 4.20, Found C, 75.49; H, 5.95; N, 4.14; HRMS-EI (*m/z*): calcd for $C_{42}H_{39}BrN_2O$ (M^+), 666.22458; found, 666.22262.

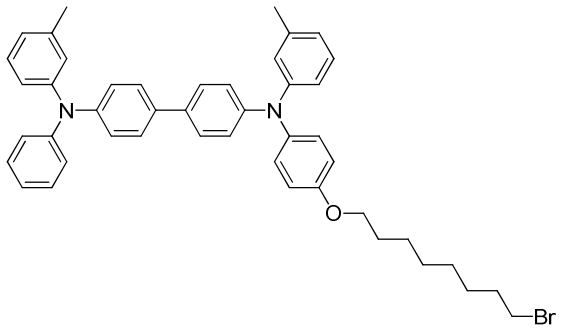

N^4-(4-(12-Bromooctyloxy)phenyl)-$N^{4'}$-phenyl-N^4,$N^{4'}$-di(m-tolyl)biphenyl-4,4'-diamine

(**TPD-C8-bromide**)

1,8-dibromooctane (7.0 g; 25.7 mmol) and **9** (2.0 g; 2.6 mmol) were placed together in a Schlenk ampule. The vessel was degassed by three freeze-pump-thaw cycles. Next 10 mL of dry, oxygen-free THF were added under nitrogen gas flow. 5.5 mL of 1 M solution of tetrabutylammonium fluoride in THF were added to the mixture. The reaction mixture was placed under reduced pressure, heated up to 60 ^{o}C and stirred for 24 h. The solvent

was then evaporated under reduced pressure. The product was purified by chromatography on a silica gel column with a mixture of toluene and hexanes (2:3) as eluent. The solvent was evaporated under reduced pressure and the resulting viscous residue was dried under vacuum overnight yielding the desired product as a glassy solid (0.70 g, 38%). ^{1}H NMR (500 MHz, acetone-d_6) δ (ppm) 7.53 (d, J = 8.7 Hz, 2H), 7.51 (d, J = 8.8 Hz, 2H), 7.26-7.31 (m, 2H), 7.12-7.21 (m, 2H), 7.02-7.08 (m, 7H), 7.00 (d, J = 8.7 Hz, 2H), 6.79-6.94 (m, 8H), 3.99 (t, J = 6.5 Hz, 2H), 3.49 (t, J = 6.8 Hz, 2H), 2.25 (s, 3H), 2.23 (s, 3H), 1.86 (app. quint, J = 7.0 Hz, 2H), 1.78 (app. quint, J = 7.0 Hz, 2H), 1.34-1.55 (m, 8H); ^{13}C{^{1}H} NMR (125 MHz, acetone-d_6) δ (ppm) 158.01, 149.89, 149.73, 149.59, 149.27, 148.63, 142.19, 140.94, 140.71, 136.49, 135.25, 131.17, 131.08, 130.91, 129.29, 128.88, 128.83, 126.83, 125.93, 125.81, 125.74, 125.66, 124.98, 124.67, 124.21, 123.44, 122.28, 117.26, 69.72, 35.80, 34.60, 31.23, 31.08, 30.91, 29.74, 27.70, 22.47, 22.42; Anal. Calcd for $C_{46}H_{47}BrN_2O$: C, 76.33; H, 6.55; N, 3.87, Found C, 76.34; H, 6.72; N, 3.83; HRMS-EI (*m/z*): calcd for $C_{46}H_{47}BrN_2O$ (M^+), 722.28718; found, 722.28859.

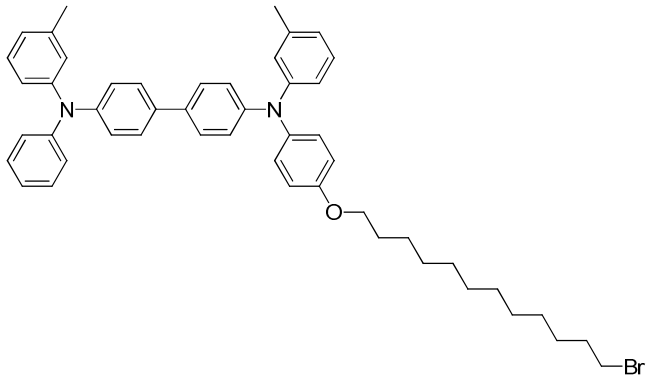

N^4-(4-(12-Bromododecyloxy)phenyl)-$N^{4'}$-phenyl-N^4,$N^{4'}$-di(m-tolyl)biphenyl-4,4'-diamine (**TPD-C12-bromide**)

1,12-Dibromododecane (8.5 g, 25.9 mmol) and **9** (2.0 g, 2.6 mmol) were placed together in a Schlenk ampule. The vessel was degassed by three freeze-pump-thaw cycles. 20 mL of dry, oxygen-free THF were then added under nitrogen gas flow and the ampule was placed in an ice bath. 5.2 mL of 1 M solution of tetrabutylammonium fluoride in THF were added to the mixture. The reaction mixture was placed under reduced pressure and stirred for 20 h at room temperature and additional 20 h at 50 °C. After that time the ampule was opened to air and the solvent was evaporated under reduced pressure. The product was purified by column chromatography on silica gel, using toluene / hexane (2:3) as eluent. Removing the solvent under reduced pressure gave pure desired product as glassy solid (0.96 g, 48%). ^{1}H NMR (500 MHz, acetone-d_6) δ (ppm) 7.55 (d, J = 8.6 Hz, 2H), 7.52 (d, J = 8.7 Hz, 2H), 7.27-7.32 (m, 2H), 7.13-7.22 (m, 2H), 6.99-7.09 (m, 9H), 6.81-6.95 (m, 8H), 3.99 (t, J = 6.4 Hz, 2H), 3.48 (t, J = 6.8 Hz, 2H), 2.25 (s, 3H), 2.24 (s, 3H), 1.85 (app. quint, J = 7.2 Hz, 2H), 1.78 (app. quint, J = 7.1 Hz, 2H), 1.28-1.53 (m, 16H); ^{13}C{^{1}H} NMR (125 MHz, acetone-d_6) δ (ppm) 158.04, 149.90, 149.74, 149.60, 149.28, 148.65, 142.19, 140.96, 140.72, 136.51, 135.27, 131.18, 131.08, 130.91, 129.31, 128.89, 128.83, 126.84, 125.94, 125.82, 125.74, 125.66, 124.99, 124.68, 124.21, 123.45, 122.28, 117.28, 69.75, 35.81, 34.62, 31.07, 30.44, 29.79, 27.79, 22.47, 22.41;[f] Anal. Calcd for $C_{50}H_{55}BrN_2O$: C, 77.00; H, 7.11; N, 3.59, Found C, 77.08; H, 7.15; N, 3.60; HRMS-EI (*m/z*): calcd for $C_{50}H_{55}BrN_2O$ (M^+), 778.34978; found, 778.34884.

[f] Five aliphatic carbon signals are missing most likely due to an overlap.

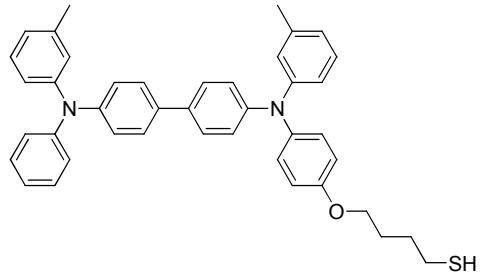

N-[4-(12-Mercaptobutyloxy)phenyl]-N'-phenyl-N,N'-di(m-tolyl)-biphenyl-4,4'-diamine

(**TPD-C4-thiol**)

TPD-C4-bromide (0.56 g; 0.84 mmol) and thiourea (0.22 g; 2.9 mmol) were placed together in a Schlenk ampule which was then degassed by three freeze-pump-thaw cycles. 15 mL of dry DMF were then added under nitrogen flow to the ampule. The solution was then placed under reduced pressure, heated up to 100 ^{o}C and stirred for 6 h. TLC of the reaction mixture showed that the starting bromide was all consumed. 1.55 g of KOH in 10 mL of deoxygenated DI water was added to the cooled reaction mixture under nitrogen flow. The mixture was then placed under reduced pressure, heated up to 100 ^{o}C and stirred for 14 h. Next the mixture was cooled to 4 ^{o}C and ca. 3 M HCl was added dropwise under nitrogen flow until pH reached value of about 4. The product was extracted with 100 mL of dichloromethane, washed with water (3 × 100 mL), and dried over sodium sulfate. Next the solution was filtered and the solvent was removed under reduced pressure. The crude product was purified by silica flash chromatography on silica gel, using hexane / toluene (1:1). Evaporating the solvent under reduced pressure yielded slightly yellow solid (0.49 g, 94%). ^{1}H NMR (500 MHz, acetone-d_6) δ (ppm) 7.55 (d, J = 8.8 Hz, 2H), 7.52 (d, J = 8.8 Hz, 2H), 7.27-7.32 (m, 2H), 7.19 (t, J = 7.8 Hz, 1H), 7.15 (t, J = 7.8 Hz, 1H), 6.99-7.09 (m, 9H), 6.81-6.95 (m, 8H), 4.02 (t, J = 6.2 Hz, 2H), 2.62 (app. quart, J = 7.5 Hz, 2H), 2.25 (s, 3H), 2.24 (s, 3H), 1.86-1.93 (m, 2H),

1.77-1.83 (m, 2H), 1.74 (t, J = 7.9 Hz, 1H); $^{13}C\{^{1}H\}$ NMR (125 MHz, CD_2Cl_2) δ (ppm) 157.89, 149.89, 149.73, 149.59, 149.27, 148.65, 142.30, 140.96, 140.73, 136.49, 135.29, 131.18, 131.09, 130.92, 129.29, 128.89, 128.84, 126.84, 125.94, 125.81, 125.74, 125.68, 125.01, 124.68, 124.23, 123.45, 122.30, 117.29, 69.28, 32.49, 29.77, 25.63, 22.46, 22.41; Anal. Calcd for $C_{42}H_{40}N_2OS$: C, 81.25; H, 6.49; N, 4.59, Found C, 81.51; H, 6.61; N, 4.51; HRMS-EI (*m/z*): calcd for $C_{42}H_{40}N_2OS$ (M^+), 620.28613; found, 620.28893.

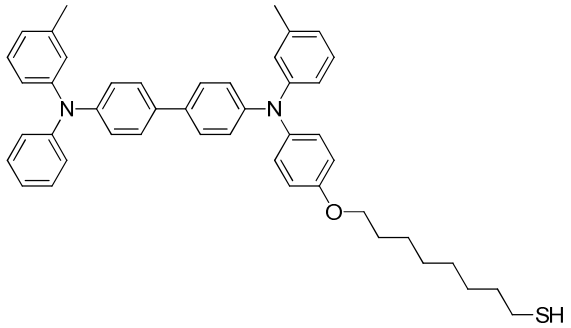

N-[4-(12-Mercaptooctyloxy)phenyl]-N'-phenyl-N,N'-di(m-tolyl)-biphenyl-4,4'-diamine (**TPD-C8-thiol**)

TPD-C8-bromide (0.66 g; 0.9 mmol) and thiourea (0.24 g; 3.1 mmol) were placed together into a Schlenk ampule. 20 mL of DMF were added and the mixture was deaerated by bubbling nitrogen gas through for 30 min followed by degassing by three freeze-pump-thaw cycles. The mixture was sealed under static vacuum and stirred at 100 ^{o}C overnight. TLC analysis revealed that the starting bromide was consumed and was consistent with the formation of the corresponding thiouronium salt. The hydrolysis of the salt was performed as follows. Potassium hydroxide (1.53 g; 27.3 mmol) was dissolved in 10 mL of water. The solution was bubbled with nitrogen gas for 40 min. The base solution was then transferred to the reaction mixture under inert atmosphere. Then

the reaction mixture was sealed under reduced pressure and stirred at 100 ^{o}C overnight. The vessel was then cooled to 4 ^{o}C and opened to nitrogen gas flow. HCl (ca. 3 M) was added to the mixture until pH reached 5. The product was extracted with 100 mL of dichloromethane. The organic phase was collected and washed with water (3 × 100 mL). Next the organic phase was dried over sodium sulfate and filtered. The solvent was removed under reduced pressure. The product was purified by chromatography on a silica gel column, using toluene / hexane (1:1) as eluent. After removing the solvent under reduced pressure the product was dried under vacuum to yield colorless solid (0.45 g, 73 %). ^{1}H NMR (500 MHz, acetone-d_6) δ (ppm) 7.54 (d, J = 8.7 Hz, 2H), 7.51 (d, J = 8.8 Hz, 2H), 7.27-7.31 (m, 2H), 7.19 (t, J = 7.8 Hz, 1H), 7.15 (t, J = 7.8 Hz, 1H), 6.98-7.07 (m, 9H), 6.80-6.94 (m, 8H), 3.99 (t, J = 6.5 Hz, 2H), 2.51 (q, J = 7.4 Hz, 2H), 2.24 (s, 3H), 2.23 (s, 3H), 1.74-1.80 (m, 2H), 1.66 (t, J = 7.8 Hz, 1H), 1.56-1.63 (m, 2H), 1.45-1.52 (m, 2H), 1.30-1.44 (m, 6H); ^{13}C{^{1}H} NMR (125 MHz, acetone-d_6) δ (ppm) 157.97, 149.85, 149.68, 149.55, 149.23, 148.60, 142.15, 140.93, 140.70, 136.43, 135.20, 131.16, 131.06, 130.90, 129.27, 128.85, 128.79, 126.78, 125.90, 125.79, 125.70, 125.61, 124.97, 124.67, 124.17, 123.39, 122.23, 117.25, 69.72, 35.78, 31.23, 29.91, 27.69, 25.76, 22.43, 22.38;[g] Anal. Calcd for $C_{46}H_{48}N_2OS$: C, 81.61; H, 7.15; N, 4.14, Found C, 81.36; H, 7.25; N, 4.07; HRMS-EI (*m/z*): calcd for $C_{46}H_{48}N_2OS$ (M^+), 676.34783; found, 676.35180.

[g] Two aliphatic carbon signals are missing most likely due to an overlap.

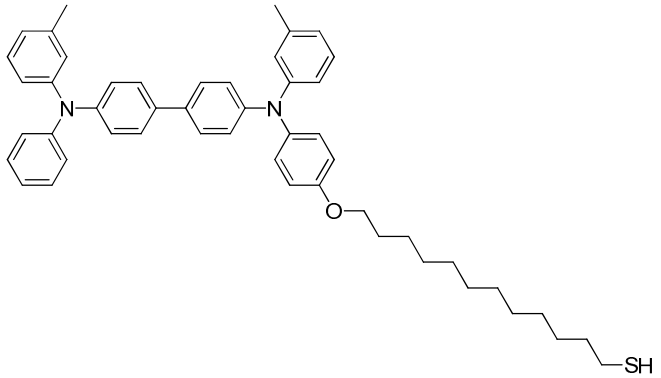

N-[4-(12-Mercaptododecyloxy)phenyl]-N'-phenyl-N,N'-di(m-tolyl)-biphenyl-4,4'-diamine (**TPD-C12-thiol**)

TPD-C12-bromide (0.90 g, 1.2 mmol) and thiourea (0.30 g, 3.9 mmol) were placed together into a Schlenk ampule. 15 mL of DMF were added and the mixture was deoxygenated by bubbling with nitrogen gas for 30 min followed by degassing by three freeze-pump-thaw cycles. The mixture was sealed under static vacuum and stirred at 100 °C for 20 h. TLC revealed that the starting bromide was consumed and was consistent with the formation of the corresponding thiouronium salt. The hydrolysis of the salt was performed as follows. Potassium hydroxide (1.96 g, 35.0 mmol) was dissolved in 10 mL of water. The solution was bubbled with nitrogen gas for 40 min. Then the hydroxide solution was transferred to the reaction mixture under inert atmosphere. The reaction vessel was then placed under static vacuum and stirred at 100 °C for 20 h. The ampule was then placed in an ice bath and it was opened to nitrogen gas flow. 1 M HCl was added to the mixture until pH reached ca. 5 and the product was extracted with 100 mL of dichloromethane. The organic phase was washed with water (3 × 100 mL), dried over sodium sulfate and filtered. The solvent was removed under reduced pressure. The product was purified by column chromatography on silica gel using toluene / hexane mixture (1:1) as eluent. After removing the solvent under reduced pressure the pure

desired product was collected (0.58 g, 69%). ^{1}H NMR (500 MHz, acetone-d_6) δ (ppm) 7.52 (d, J = 8.7 Hz, 2H), 7.50 (d, J = 8.8 Hz, 2H), 7.26-7.30 (m, 2H), 7.18 (t, J = 7.8 Hz, 1H), 7.14 (t, J = 7.8 Hz, 1H), 7.02-7.07 (m, 6H), 7.00 (d, J = 8.7 Hz, 2H), 6.79-6.93 (m, 9H), 3.98 (t, J = 6.5 Hz, 2H), 2.49 (app. q, J = 7.4, 2H), 2.24 (s, 3H), 2.22 (s, 3H), 1.77 (app. quint, J = 7.1 Hz, 2H), 1.63 (t, J = 7.8 Hz, 1H), 1.58 (app. quint, J = 7.4 Hz, 2H), 1.48 (app. quint, J = 7.3 Hz, 2H), 1.25-1.41 (m, 14H); ^{13}C{^{1}H} NMR (125 MHz, $CDCl_3$) δ (ppm) 157.96, 149.85, 149.68, 149.55, 149.22, 148.59, 142.15, 140.92, 140.68, 136.43, 135.20, 131.15, 131.06, 130.89, 129.26, 128.85, 128.79, 126.79, 125.90, 125.78, 125.71, 125.62, 124.96, 124.66, 124.18, 123.40, 122.24, 117.25, 69.73, 35.82, 31.26, 31.23, 31.06, 31.03, 30.77, 29.99, 27.76, 25.79, 22.46, 22.40;[h] Anal. Calcd for $C_{50}H_{56}N_2OS$: C, 81.92; H, 7.70; N, 3.82, Found C, 81.85; H, 7.78; N, 3.82; HRMS-EI (*m/z*): calcd for $C_{50}H_{56}N_2OS$ (M^+), 732.41134; found, 732.40701.

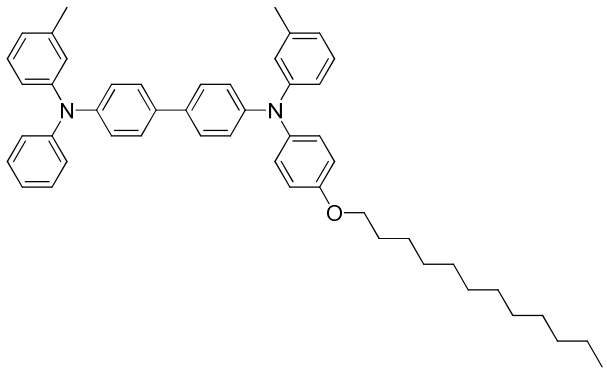

N-[4-(Dodecyloxy)phenyl]-N'-phenyl-N,N'-di(m-tolyl)-biphenyl-4,4'-diamine (**C12-TPD**)

1-Bromododecane (1.25 g, 5.0 mmol) and **9** (1.00 g, 1.3 mmol) were placed together in a Schlenk ampule. The vessel was degassed by three freeze-pump-thaw cycles. Dry, oxygen-free THF (8 mL) was then added under nitrogen gas flow. The ampule was

[h] Two aliphatic carbon signals are missing most likely due to an overlap.

placed in an ice bath and tetrabutylammonium fluoride (3 mL of a 1 M solution in THF) was added to the mixture. The reaction mixture was pumped down, sealed under static vacuum and stirred for 20 h at 60 °C. The solvent was then evaporated under reduced pressure and the crude product was loaded onto a short silica plug. The unreacted bromide was washed off with hexanes. This was followed by a wash with hexanes / toluene mixture (1:1), which eluted the desired product. Removing the solvent under reduced pressure yielded the product as a glassy solid (0.71 g, 78%). ^{1}H NMR (500 MHz, acetone-d_6) δ (ppm) 7.55 (d, J = 8.6 Hz, 2H), 7.52 (d, J = 8.7 Hz, 2H), 7.26-7.32 (m, 2H), 7.12-7.22 (m, 2H), 6.98-7.09 (m, 9H), 6.80-6.95 (m, 8H), 4.00 (t, J = 6.3 Hz, 2H), 2.25 (s, 3H), 2.24 (s, 3H), 1.78 (app. quint, J = 6.9 Hz, 2H), 1.45-1.53 (m, 2H), 1.21-1.42 (m, 16H), 0.87 (app. t, J = 6.9 Hz, 3H); ^{13}C{^{1}H} NMR (125 MHz, acetone-d_6) δ (ppm) 158.04, 149.91, 149.74, 149.60, 149.29, 148.65, 142.19, 140.96, 140.72, 136.51, 135.27, 131.18, 131.09, 130.92, 129.31, 128.89, 128.83, 126.84, 125.94, 125.82, 125.74, 125.67, 124.99, 124.68, 124.21, 123.45, 122.29, 117.28, 69.76, 33.63, 31.38, 31.35, 31.33, 27.80, 24.32, 22.47, 22.41, 15.35;[i] Anal. Calcd for $C_{50}H_{56}N_2O$: C, 85.67; H, 8.05; N, 4.00, Found C, 85.61; H, 8.06; N, 3.99; HRMS-EI (*m/z*): calcd for $C_{50}H_{56}N_2O$ (M^+), 700.43926; found, 700.43933.

Preparation of gold nanoparticles in the presence of oleylamine

Hydrogen tetrachloroaurate(III) trihydate (0.66 g, 1.68 mmol) was dissolved in a mixture of 6 mL of toluene and 6 mL of freshly distilled oleylamine (Acros). The solution was then added into a mixture of 50 mL of toluene and 12 mL of oleylamine. While the

[i] Four aliphatic carbon signals are missing most likely due to an overlap.

mixture was stirred at room temperature 6 mL of methanol were added. Then sodium borohydride (0.12 g, 3.2 mmol) was added at once to the stirred solution resulting in an immediate appearance of a dark color. The mixture was stirred for additional 2 h followed by pouring the reaction mixture into 100 mL of acetonitrile. The formed precipitate was washed twice with acetonitrile and twice with methanol. The procedure usually yields 0.32 g of nanoparticles with size distribution 3 ± 1.1 nm.

General procedure for reacting OA-coated gold nanoparticles with thiols

A known amount of OA-coated gold nanoparticles was dissolved in toluene (concentration ca. 15 mg/mL). Next the thiol of choice or mixture of thiols of choice (with 40% of dodecanethiol by mole in the mixture of two thiols) was added at once in 2× excess,[j] and the mixture was stirred in dark for 20 h. After that the particles were precipitated with addition of methanol and the resulting precipitate was washed with methanol / toluene mixture (1:1) until no fluorescence was observed in the supernatant upon UV-irradiation.

[j] The stoichiometry of the reaction was calculated assuming the thiol footprint (F_{thiol}) of 22 Å^2 and the total mass of starting NP's (m_{NP}) coming from metallic gold with density d_{Au} = 19.3 g/cm^3. The total surface of particles (S) was computed according to $S = \frac{3m_{NP}}{rd_{Au}}$ where r is particle radius (1.5 nm). The needed amount of moles of the thiol (n_{thiol}) was calculated according to $n_{thiol} = \frac{S}{N_A F_{thiol}}$.

2.2. Experimental Methodology

2.2.1. Sample Preparation and Manipulation

2.2.1.1. SAMs on Flat Gold

Infrared reflection-absorption spectroscopy (IRRAS), X-ray photoelectron spectroscopy (XPS), and ellipsometry measurements were carried out on monolayers prepared on 100 nm thick polycrystalline gold on titanium-primed glass purchased from EMF Corporation. X-ray diffraction of these substrates in Bragg-Brentano geometry is dominated by reflections from the Au(111) surface as shown in Figure 2.1.

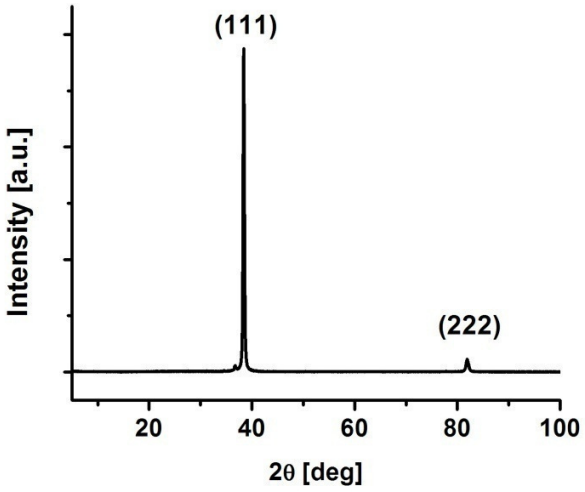

Figure 2.1. X-ray diffraction of the gold substrates acquired from EMF Corporation. The measurements were performed on a Scintag X1 powder diffractometer.

All gold substrates were stored under a nitrogen atmosphere and were cleaned with freshly prepared piranha solution followed by a thorough rinse with distilled water immediately before adsorption of thiolates. SAMs were prepared by immersing freshly cleaned gold substrates into ca. 0.5 mM ethanolic solutions of the appropriate 4-(acetylthio)stilbene and allowing the adsorption to continue for 20 h at room temperature

under a nitrogen atmosphere. Each sample was then washed copiously with ethanol, dried under a stream of nitrogen gas, and stored under nitrogen for later analysis. Ultraviolet photoelectron spectroscopy (UPS) and Scanning Tunneling Microscopy (STM) measurements were performed on atomically flat Au(111) on mica acquired from Agilent. The substrates were received under an argon atmosphere, were unpacked in a glove box, and placed directly into ca. 0.5 mM ethanolic solution of the appropriate acetylthio-stilbene for 20 h. Next each sample was washed copiously with ethanol, dried under a stream of nitrogen, and stored under nitrogen for later analysis. All samples of SAMs on flat gold were performed under inert gas atmosphere except for the ellipsometry measurements, which were performed under ambient conditions, and for the transfer of the samples into the XPS airlock, during which the samples were exposed to the atmosphere for less than 3 min.

2.2.1.2. Gold Nanoparticle Samples

Immediately after preparation and purification, gold NP samples were dissolved either in sulfur-residue-free toluene or in $CDCl_3$ and were stored in solution at room temperature. No steps were taken to remove air from the NP solutions. Neat films of NPs for Fourier-transform infrared spectroscopy (FT-IR) analysis were prepared by drop casting from $CDCl_3$ solutions onto a NaCl disk.

2.2.2. Measurement Details

2.2.2.1. FT-IR

A nitrogen-purged Digilab FTS-600 FT-IR instrument equipped with an MCT detector was used for measuring IR absorption spectra of solutions. A KBr window cell was used for the measurements. 256 scans were collected for each spectrum with 2 cm^{-1} resolution. Each solution transmission spectrum was referenced to the transmission spectrum of pure solvent and the baseline was corrected manually using the spline function approach.

A grazing-angle accessory (80° angle of incidence, from Pike) was employed in the IRRAS studies of the monolayers on gold. The light was p-polarized with a gold grid polarizer from Perkin-Elmer. The resolution was 2 cm^{-1} and the mirror speed used was 1.28 cm/s. 20000 scans were collected for each sample. A gold slide coated with dodecanethiol-d_{25} was used as a reference.[6,7] The resulting absorption spectra generally contained either positive or negative signals due to varying amounts of water vapor present in the optical path. These signals were removed by a careful subtraction of a prerecorded high-quality water vapor spectrum with an appropriate scaling factor. The baseline of the water-vapor-free spectrum was corrected manually using the spline function approach.

FT-IR spectra of the Au NP films on NaCl disk were acquired with the use of a Perkin Elmer Spectrum 1000 spectrometer. 32 scans were acquired for each sample at 4 cm^{-1} resolution. The spectrum of a clean NaCl disk was used as a reference. A spline function baseline correction, included in the instrument's software, was used to correct the baseline.

2.2.2.2. XPS

XPS analysis of the monolayers on flat gold was performed with the use of a Surface Science SSX-100 with an Al Kα X-ray source. The pressure was typically around 3×10^{-9} Torr. The photoelectron take-off angle was 35° with respect to the surface plane and the spot size was chosen to be 0.8 mm in diameter. The uncertainty of the monolayer thicknesses obtained from XPS data was calculated from the error propagation of the double standard deviations for the Au($4f_{7/2}$) peak intensities, which were obtained from measurements of four different spots for each sample. For the calculations of coverage, each S(2p) peak was fitted with two mixed Gaussian-Lorenzian functions with an assumed spin-orbit splitting of 1.18 eV and with a Shirley-type background correction.[8] The fitted function was then numerically integrated and the square root of the sum of squares of the residuals was propagated as the error in the integrated area of the S(2p) peak. Each measured Au(4f) peak was integrated numerically after subtracting Shirley-type backgrounds. The double standard deviation was then calculated from the data for four spots for each sample and propagated in the error analysis. Fitting and background correction were done using the free fitting software XPSPeak 4.1.

2.2.2.3. UPS

UPS measurements of the stilbene-thiol monolayers on gold were performed with the help of Dr. Zelei Guan in Prof. Antoine Kahn's laboratory at Princeton University. An ultra-high vacuum system (base pressure $<1 \times 10^{-10}$ Torr), consisting of a main analysis chamber and a sample preparation chamber was used for the measurements. The analysis chamber was equipped with a He discharge lamp (photon energy 21.2 eV and

40.8 eV) and a double-pass cylindrical mirror analyzer. The sample was negatively biased at -3 V to overcome the contact potential between the sample and the detector. The double standard deviation based on the low kinetic energy photoelectron onset measurements of three spots for each sample was chosen as the error bar for the extracted work function value.

2.2.2.4. Ellipsometry

A Woollam M-2000 spectroscopic ellipsometer was used for the determination of the ellipsometric thickness of monolayers on flat gold. All the measurements were performed at 70 ° angle of incidence in the spectral range of 370–1000 nm. Three spots were measured for each sample and a mean value of thickness and a standard deviation were calculated. The uncertainty in the measurement is assumed to be the sum of the standard deviation in the measurement and a typical error of the fitting procedure given by the fitting software (0.1 Å). It has been demonstrated that upon thiol adsorption on gold a new optical transition is present in the reflection spectrum of gold, which has to be included in the model for fitting ellipsometric data.[9] In order to include the effects of the gold–thiol layer, a substrate model was created as follows. Ellipsometric parameters were measured for a gold slide cleaned with piranha solution as well as for a gold slide coated with octadecanethiol (ODT). An initial model was built, which consisted of 1000 Å of gold with optical constants measured for the cleaned gold slide, 2 Å of a Au-S adlayer with unknown optical constants, and 21.4 Å of octadecane monolayer with the index of refraction from reference 10. By fitting the model with the ellipsometric parameters measured for the ODT-coated gold slide, the optical constants of the Au-S adlayer were

obtained. The substrate model was then built consisting of 1000 Å of gold with the adlayer of 2 Å of Au-S, with the optical constant obtained as described above, on top. In order to find the thickness of an unknown adlayer on the substrate a new model was created consisting of the substrate model described above with a Cauchy adlayer with known index of refraction on top. The model was then tested by fitting ellipsometric parameters measured for a gold slide coated with dodecanethiol (DDT). Assuming that the index of refraction of the dodecyl chain is identical to that of the octadecyl chain, the extracted thickness of the DDT monolayer was calculated to be 15 ± 1.5 Å, which is consistent with literature values.[9,11]

2.2.2.5. STM

STM measurements were performed by Mr. Sieu Ha in the laboratory of Prof. Antoine Kahn at Princeton University. A STM from Omicron Nanotechnologies was operated at room temperature in ultra-high vacuum (4×10^{-11} Torr). Images were recorded in constant-current mode in which the tip-sample distance is varied and recorded for the conditions of the fixed tunneling current and sample bias (U = –1.8 V; I = 30 pA). STM tips were electrochemically etched from 0.25 mm tungsten wire in a 2 M NaOH solution and annealed in situ by electron bombardment. The STM image showed minimal drift and distortion effects when calibrated with a Si(111)-7 × 7 sample and compared to literature.[12] Topographic images were analyzed with the WSxM software available from Nanotec Electronica.[13]

2.2.2.6. Calculations

Calculations of the molecular geometry, dipole moments, vibrational frequencies, and IR transition dipoles of isolated 4'-substituted-4-stilbene thiols in vacuum were performed by Dr. Georg Heimel at the Humboldt University of Berlin. The calculations were performed within the framework of Density-Functional Theory (DFT), using the modified Perdew-Wang (mPW) exchange,[14] and the Lee-Yang-Parr (LYP) correlation functional,[15] in conjunction with a 4-31G** basis set as implemented in Gaussian98.[16]

2.2.2.7. Steady-state UV-Vis-NIR absorption and fluorescence spectroscopy

Absorption spectra of solutions in quartz cuvettes were recorded on a Varian Cary 5E UV-Vis-NIR spectrometer. Fluorescence spectra of solutions in quartz cuvettes were acquired on a Fluorolog 3 spectrofluorimeter from Horiba Jobin Yvon and were corrected for instrument response.

2.2.2.8. NMR experiments for establishing T_1 and T_2 relaxation times

Measurements of T_1 and T_2 relaxation times of $CDCl_3$ solutions of Au NPs were performed with the use of a Bruker DRX-500. T_1 relaxation time measurements were performed using the conventional population-inversion recovery method, and the Carr-Purcell-Meiboom-Gill (CPMG) pulse sequence was employed in T_2 relaxation time measurements.

2.2.2.9. Transmission Electron Microscopy (TEM)

A toluene solution of each NP sample was drop casted onto a holey carbon-coated copper grid substrate. The analysis was performed using a JEOL 100 CX-II system at 100 kV acceleration voltage. The instrument is equipped with a calibrated CCD camera that was used to acquire the images. More than 400 particles were analyzed for each sample using the freeware ImageJ to obtain particle size distribution.

2.2.2.10. Electrochemical Measurements

Electrochemical measurements were carried out under nitrogen in dry deoxygenated dichloromethane solutions of ca. 10^{-4} M analyte and 0.1 M tetrabutylammonium hexafluorophosphate using a BAS potentiostat, a glassy carbon working electrode, a platinum auxillary electrode, and, as a pseudo-reference electrode, a silver wire anodized in 1 M aqueous potassium chloride. Potentials were referenced to ferrocenium / ferrocene by using ferrocene as an internal reference. Cyclic voltammograms were recorded at a scan rate of 50 mV s^{-1}.

2.2.2.11. Time-Correlated Single Photon Counting (TC-SPC)

Fluorescence lifetimes of solutions were measured using the time-correlated single-photon counting technique. A schematic representation of the optical setup is shown in Figure 2.2. A femtosecond mode-locked Ti:Sapphire laser (Tsunami, Spectra-Physics) pumped by a 5W diode laser (Millennia, Spectra-Physics) was used as the excitation source. The laser generated pulses of mean power ~0.5 W with the repetition rate of ~81 MHz at 730 nm. The laser beam was split (BS2) and a small fraction of the

light was directed to a spectrum analyzer. The rest of the beam was split again (BS2) and ca. 5% of the beam was focused onto the timing photodiode (Newport 818-BB-21A, PD1). The photodiode signal was used to drive a constant-fraction discriminator (Tennelec TC455 Quad, CFD2). The rate of the discriminator output pulses was reduced sixteen times with the use of a frequency divider (FD, Pulse Research Lab, PRL-256N). The divided signal was sent through another constant fraction discriminator (CFD4) to the stop input of a time to amplitude converter (Ortec 457, TAC). The majority of the laser beam was focused onto a BBO crystal and frequency doubled. The resulting second harmonic (365 nm) and the fundamental beams were separated after passing a quartz prism and a half-wave plate. The fundamental beam was blocked and the frequency doubled beam was sent through a pinhole to a Glan-Thompson polarizer (POL1) with the transmitted polarization direction oriented perpendicularly to the surface of the table. The power at the sample was controlled by rotating the polarization plane of the half-wave plate. The beam was passed through a beam splitter (BS3) and the reflected light was focused onto a DC-coupled photodiode (Thorlabs DET210, PD2) connected to a series RC circuit with a time constant of 0.22 sec. The output of the RC circuit was connected to an input of a DAQ board (National Instruments, USB-6221 BNC) connected via a USB port to a PC. This electronic setup was used as the "signal integrator", effectively measuring the relative energy dose at the sample. The transmitted beam was focused on the sample by a quartz lens with a 30 cm focal length. The sample holder was masked so only a small portion of the fluorescence light was collected. The fluorescence was detected at 90^{o} with respect to the excitation beam. The fluorescence light was collimated by a quartz lens and sent through a sheet polarizer (POL2) with its polarization plane at

the magic angle (54.7^{o}) to the normal of the surface of the table. The light was then sent through a depolarizer (DEPOL) and focused onto the entrance slit of a monochromator (Instruments SA H10, 1200 grooves/mm, 100 mm path length, Mono). The monochromatic light was then sent to a photomultiplier tube (Hammamatsu R1564U-01, PMT) biased at 3250 V. The pulses from the photomultiplier were amplified by a 1 GHz amplifier (Ortec 9306, Amp) and sent to a constant fraction discriminator (CFD3) and then to the start input of the time-to-amplitude converter (TAC). The output of the time-to-amplitude converter was directed to a pulse height analyzer (Ortec-Norland 5600 Multichannel Analyzer, PHA), and transferred to a personal computer (PC). The PHA channel width was determined for each experiment from the distance between two consecutive laser pulses and the repetition rate of the laser (measured by the timing photodiode PD2 and a pulse counter (Protek B-808)). The Instrument Response Function (IRF) was measured before each decay experiment using silica particles suspended in water (Ludox, Aldrich). The full width at half maximum (FWHM) of the response function was between 50 and 70 ps. The system was optimized by checking the goodness of the fit (χ^2, randomness of residual function) and the extracted value of the fluorescence lifetime of the fitted decay function of 1,4-bis(5-phenyloxazol-2-yl) benzene (POPOP) in degassed cyclohexane.[17,18] Generally values of χ^2 lower than 1.20 indicated good fits. In order to ensure operation in the linear regime of the electronics, the count rate at the Start input of TAC was kept below 10 kcps. Both IRFs and decays were collected until the number of counts at maximum reached 10,000, although for unstable NP samples only 5,000 counts at maximum were collected. The experimental data were fitted using the FAST software from Edinburgh Instruments.

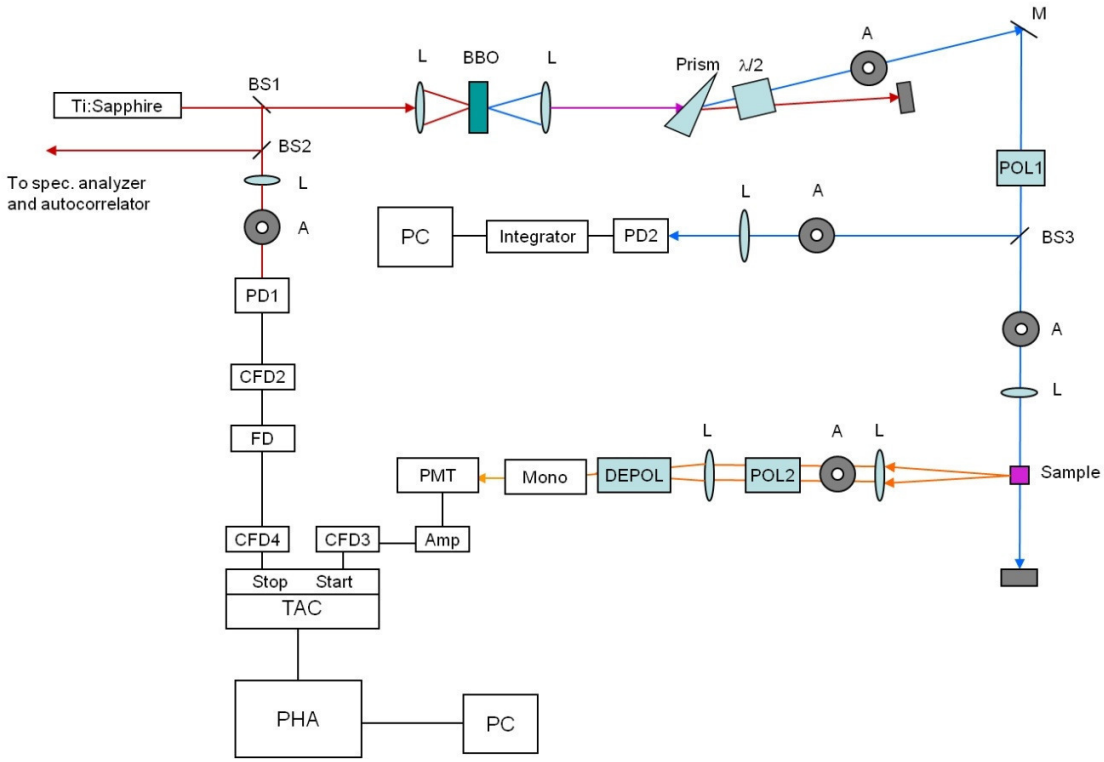

Figure 2.2. Scheme of the optical layout of TC-SPC experiment; L = lens, A = aperture, λ/2 = Half-wave plate. See text for the details.

2.2.2.12. Nanosecond Transient Absorption (TA)

The measurement of the NIR transient absorption spectrum of ca. 1×10^{-5} M toluene solution of **TPD-C12** was performed with the help of Mr. Matteo Cozzuol (the Perry group). The solution was degassed by the freeze-pump-thaw technique and kept in a sealed quartz cuvette with a 1 cm optical path. Figure 2.3 shows a schematic of the optical setup for the TA measurement. The 355 nm excitation beam in the nanosecond transient absorption setup was generated by a nanosecond Q-switched laser (Newport Spectra Physics Quanta-Ray PRO-250-10) with 8 ns pulse duration. The energy of the pulse was measured using a PE25BB pyroelectric head connected to an Ophir Nova II

power meter and the power stability was constantly monitored during the measurement. This was done by placing a glass slide along the propagation path of the excitation beam and redirecting ca. 4 % of the excitation beam to an amplified silicon PIN detector (Newport 818-BB-21A). The collected signal was converted to a DC output in the range from 0 to 10 Volts by a gated integrator (SRS SR250). A National Instrument BNC-2110 data acquisition interface was used to save the data into a personal computer. A white-light source (Newport, 250 W tungsten lamp, driven by a 300 W radiometric power supply, model 69931) was used as the probe. The angle between the pump and the probe light was about 15 ° and it was kept as small as possible to maximize the pump-probe spatial overlap. After passing through the sample, the probe light was sent to a monochromator (PI SP150) and then to an InGaAs PIN detector (HCA-S-200M-IN). The electric signal from the photodiode was detected with an oscilloscope (Tektronix TDS 3034b), triggered by the Quanta-Ray Q-switch pulse, and recorded into a personal computer memory via a GPIB interface. Changes in optical density as a function of time, $\Delta OD(t)$, were calculated according to: $\Delta OD(t) = -\log (I(t) / I_0)$, where I_0 is an averaged signal from the photodiode measured before the laser pulse, and $I(t)$ is the photodiode signal measured at a delay t from the excitation pulse.

In order to find the profile of a transient spectrum decay traces at different wavelengths were fitted globally in Origin 7.5 software with a monoexponential decay function: $\Delta OD(t, \lambda) = A(\lambda) \times \exp(-kt) + const(\lambda)$, in which the decay rate k was used as a global parameter. The wavelength-dependent preexponential amplitudes, $A(\lambda)$, from the best fit of the data were then used to plot the spectral profile of the transient species.

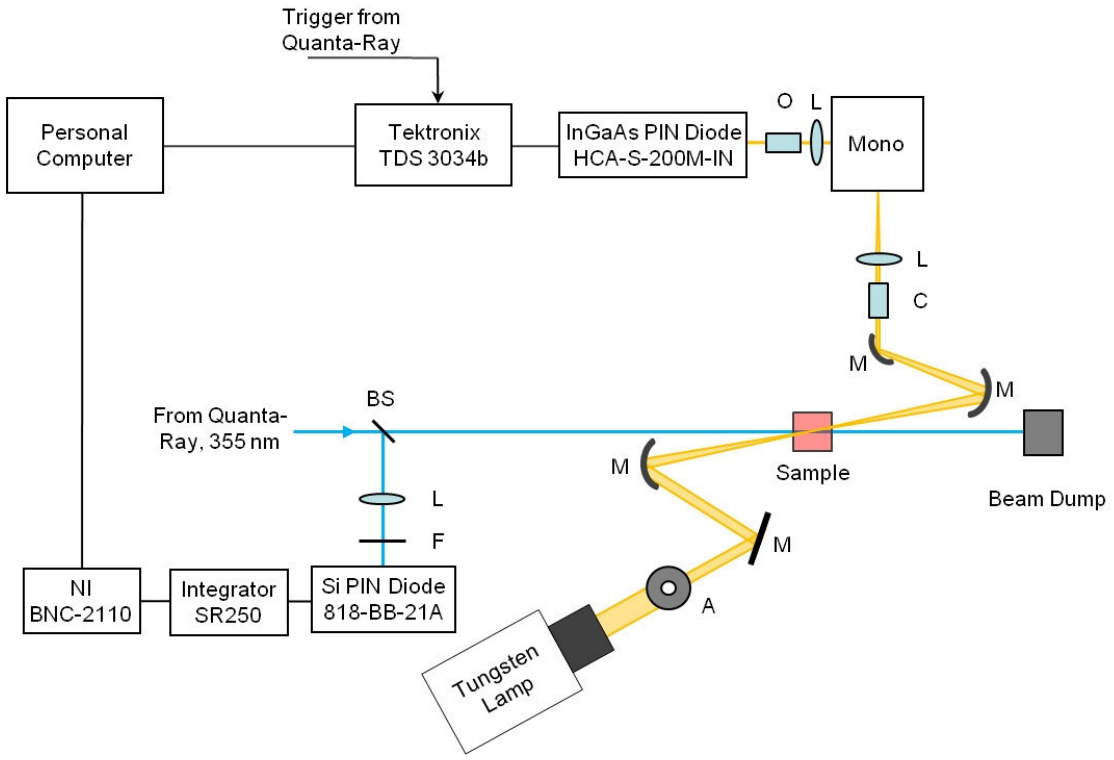

Figure 2.3. Scheme of the optical layout of the nanosecond TA experiment; BS = beam splitter, L = lens, F = filter, M = mirror, A = aperture, C = collimator, O = microscope objective, Mono = monochromator. See text for the details.

2.2.2.13. *Femtosecond Broad-Band-NIR Transient Absorption*

Femtosecond transient absorption spectra were acquired using a commercially available transient absorption spectroscopy system (Newport, Helios). This system accepts two input laser beams, one of variable wavelength used as the pump beam and one of a fixed wavelength (800 nm) used to generate the probe beam in a proprietary nonlinear optical crystal. For the pump beam, the light source was an ultrafast optical parametric amplifier (Newport, TOPAS) running at a repetition rate of 1 kHz, pumped by a Ti:Sapphire regenerative amplifier (Newport, Spitfire). The TOPAS output was set to 700 nm with a pulse width of approximately 120 fs (FWHM) and frequency doubled

using a BBO crystal, resulting in the excitation wavelength of 350 nm. Approximately 5% of the Spitfire fundamental at 800 nm was used for NIR white-light continuum (WLC) generation (850 – 1650 nm) in the Helios nonlinear crystal to provide the experimental probe beam. The polarization of the excitation beam was set to the magic angle with respect to the polarization of the probe beam in order to sample pure depopulation dynamics. With these specifications, the instrument response function (IRF) was approximately 300 – 400 fs (FWHM).[k] The temporal window that can be studied is 3200 ps wide. At each temporal delay point, data were averaged for 4 s. The Helios pump beam was chopped at 500 Hz to obtain pumped (signal) and non-pumped (reference) absorption spectra of the sample. The data were stored as 3-D Wavelength-Time-Absorbance matrices that were exported for use with the fitting software.

An optical Kerr effect (OKE) experiment on a sample of CCl_4 was performed in order to measure the temporal chirp of the signal. Briefly, the sample was pumped with a 350 nm light with polarization vertical to the optical table surface. The WLC probe light was also vertically polarized and passed through the irradiated sample. The probe beam was sent to the detector through a polarizer which was set to horizontal polarization. The OKE signal was then collected for different pump-probe delay time. As can be seen in Figure 2.4, the normalized OKE signals at different wavelengths do not show significant temporal shift with respect to each other. This illustrates no appreciable temporal chirp of the WLC probe in the NIR region and therefore chirp correction of the acquired transient spectra was unnecessary.

[k] IRF was assumed to have a Gaussian profile and its width (FWHM) was estimated based on fitting of time resolved data of various samples in the software provided by the manufacturer of Helios (Surface Xplorer Pro from Newport, Spectra Physics). The fitting procedure takes into account IRF with its width as one of the parameters. Allowing IRF width to be a floating parameter returned values between 300 and 400 fs for transient absorption data in the NIR range.

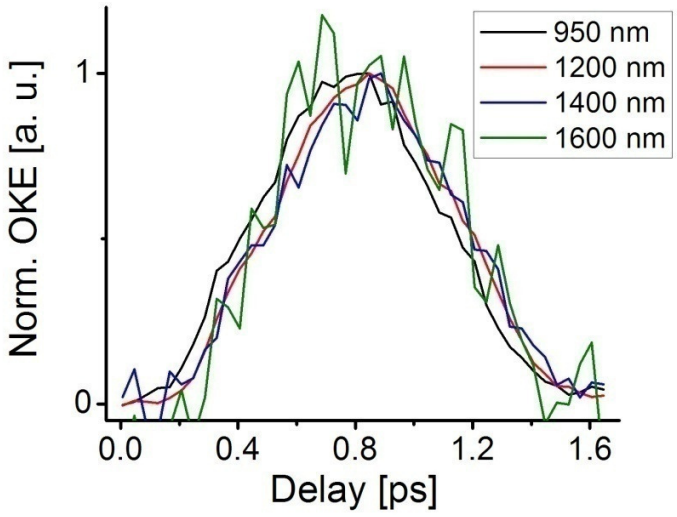

Figure 2.4. Normalized OKE signal as a function of pump-probe delay measured at different wavelengths.

The studied solutions of NPs had OD_{350} of between 3 and 4 in a 2 mm path length quartz cuvette, and were stirred continuously throughout the data acquisition. A neat film of **C12-TPD** was prepared by drop casting from a toluene solution. Slow solvent evaporation resulted in a film of very good optical quality. All samples were photostable under the applied excitation conditions (subsequent measurements showed no change of the transient signal after ca. 10 minutes of signal acquisition). Excitation beam power values of 2.1 mW, 1.1 mW and 0.4 mW at the sample were used for the measurements of the NP solutions, a 0.1 M toluene solution of **C12-TPD** and the neat film of **C12-TPD**, respectively. The excitation beam spot size at the sample was determined to be 312 μm (HW1/e).

In order to avoid instrument response-related artifacts, the usable temporal delay range for single wavelength kinetic traces was determined to begin about one width of the IRF, ca. 350 fs, after the rising edge of the signal. This point was defined as zero delay

time for all fitting procedures. In general, the transient kinetic signal response for metallic NPs can be quite strong in the spectral region close to that of the surface-plasmon absorption band.[19,20] However, due to the large spectral separation between the Au NP surface-plasmon band (ca. 520 nm) and the NIR probe wavelengths used here, only a small contribution to the overall transient ΔOD signals in the samples containing Au NPs comes from the metallic core of the NPs. Nonetheless, for completeness, the contribution to the overall transient signal from the metal NP was appropriately subtracted as detailed in the following. Figure 2.5 shows a few transient spectra measured for a toluene solution of gold NPs coated with dodecanethiol (**AuS-C12**). Since in this sample the metallic core is the only species giving rise to the measured signal, the gathered data can be used to subtract the contribution of the Au NP core to the ΔOD in the other NP samples. The subtraction was performed under the following assumptions. Firstly, the ground-state absorption cross sections at the excitation wavelength (350 nm) of both the metallic core (σ_{Au}) and the TPD moiety (σ_{TPD}) were assumed to be the same from sample to sample. We used $\sigma_{Au} = 6.3 \times 10^{-15}$ cm^2/particle, which is a value based on a literature report on the molar extinction coefficient established for Au NPs (diameter ca. 3 nm) in toluene solutions.[21] The value of $\sigma_{TPD} = 1.5 \times 10^{-16}$ cm^2/molecule was obtained from the molar extinction coefficient at 350 nm established from absorption measurements of a series of toluene solutions of **C12-TPD** of known concentration ($\varepsilon_{C12\text{-}TPD} = 3.97 \times 10^4$ Lmol^{-1}cm^{-1}). Secondly, the decay dynamics of the excited state of the metallic core was assumed to be the same for each NP sample. The third assumption was that the excited states of the Au NP metallic core and of the TPD moiety each have negligible absorption cross sections at 350 nm.

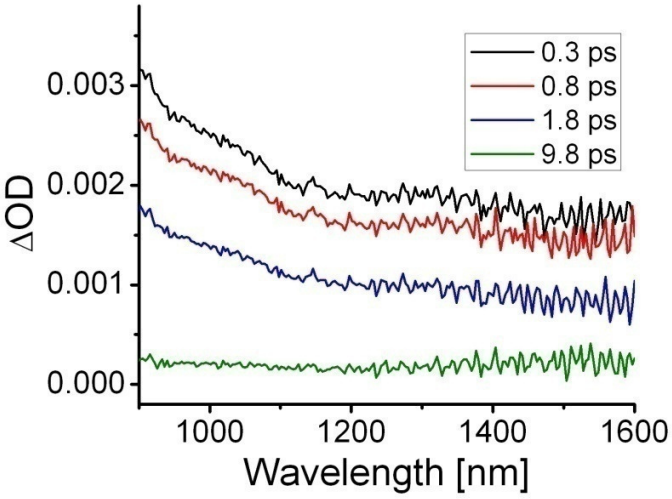

Figure 2.5. Transient spectra measured for a toluene solution of Au NPs coated with dodecanethiol. The delay values are shown in the legend.

In order to subtract the contribution from the metallic core of Au NPs from the measured ΔOD signal, the excited-state populations of Au NPs in **AuS-C12** and in the samples containing TPD moieties were calculated as follows. The excitation beam with photon fluence $\Phi_0 = 7.2 \times 10^{14}$ photons/cm^2 at the front face of the sample[1] was propagated through the 2 mm path length of a sample containing known concentrations of Au NP metallic cores and TPD moieties (as estimated from the absorbance of the samples), describing the system as a series of thin slabs with planes perpendicular to the

[1] The fluence was calculated using the measured power of the excitation (pump) beam at the front face of the sample (2.1 mW), repetition rate of the laser (1 kHz), the photon energy (5.7×10^{-19} J), and the overlap of the pump and probe beams, both of which were measured to have a Gaussian function spatial distribution with parameters σ_{pump} = 312 μm (HW1/e) and σ_{probe} = 168 μm (HW1/e). Only overlap in the circular area with the radius of $2\sigma_{probe}$ was taken into account for fluence calculations. For further calculations the intensity profiles of the overlapped beams were assumed to be constant over the overlap region.

direction of beam propagation.[m] In the calculation the sample was divided into 5000 slabs.[n] Excitation beam attenuation and ground-state population depletion of both the metallic core and the TPD moiety in each slab were computed according to the following equations and then used as input for the following slab:

- $\Phi_n = \Phi_{n-1} e^{-[(N_{Au}^0 - N_{Au}^{*n})\sigma_{Au} + (N_{TPD}^0 - N_{TPD}^{*n})\sigma_{TPD}]\Delta l}$,
- $N_{Au}^{*n} = N_{Au}^0(1 - e^{-\sigma_{Au}\Phi_n})$,
- $N_{TPD}^{*n} = N_{TPD}^0(1 - e^{-\sigma_{TPD}\Phi_n})$,

where Φ_n, Φ_{n-1} are the excitation beam fluence values at the *n*'th slab and in the slab immediately before respectively, N_{Au}^0, N_{TPD}^0 are the ground-state populations of the Au NP metallic core and the TPD moiety respectively, N_{Au}^{*n}, N_{TPD}^{*n} are the excited-state populations of the Au NP metallic core and the TPD moiety in the *n*'th slab respectively, σ_{Au}, σ_{TPD} are the ground-state cross sections at 350 nm for the Au NP metallic core and the TPD moiety respectively, and Δl is the path length of the slab. Such computation was repeated for each slab until the end of the path length was reached (n = 5000). The output of the calculation was the value of fluence of the excitation beam after passing through the sample, and the total initial excited-state populations of both the Au NP metallic core ($N_{Au}^* = \sum_{n=0}^{5000} N_{Au}^{*n}$) and the TPD moiety ($N_{TPD}^* = \sum_{n=0}^{5000} N_{TPD}^{*n}$).[o]

The kinetic profiles of ΔOD measured at different wavelengths for AuS-C12 were then multiplied by a factor $\frac{N_{Au}^{S*}}{N_{Au}^{ref*}}$, where N_{Au}^{S*} and N_{Au}^{ref*} are the total initial excited-state

[m] This approach was taken in order to account for both the ground-state depletion of the two-component system (TPD moiety and Au NP metallic core) and the excitation beam attenuation through the sample as the studied solutions had high absorbance values at the excitation wavelength.

[n] It was found that a change in the number of slabs above 4000 had negligible effect on the output values.

[o] In all of the samples the calculated fraction of photoexcited TPD moiety population was less than 10% of the total population.

populations of Au NP metallic core calculated as discussed above for the sample of interest and **AuS-C12**, respectively. The scaled kinetic traces of **AuS-C12** were then subtracted from the kinetic traces of the sample of interest, thus removing the contribution of Au NP metallic core to the measured ΔOD. Figure 2.6 shows an example of the kinetic traces measured for toluene solution of Au NPs coated with TPD-C12-thiol (**AuS-C12-TPD**) at a few wavelengths before and after subtraction of the scaled traces of **AuS-C12**.

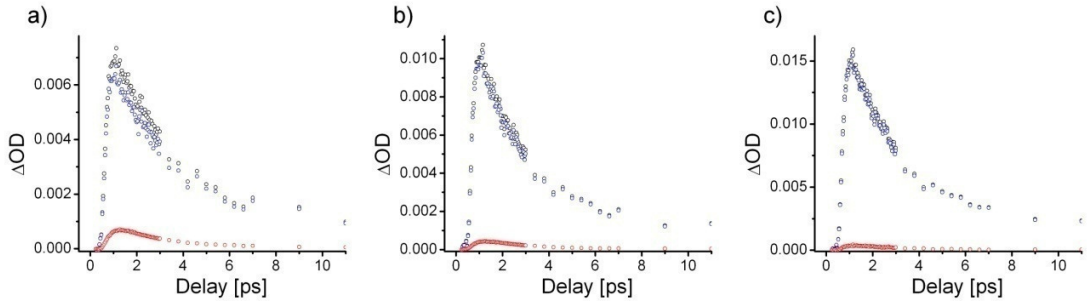

Figure 2.6. Kinetic traces before (black circles) and after (blue circles) subtraction of scaled trace of **AuS-C12** (red circles) from traces measured for **AuS-C12-TPD** at a) 900 nm, b) 1200 nm, and c) 1600 nm.

The kinetic traces at different wavelengths treated as described above were analyzed using a global fitting routine where the fitting function was a sum of exponential functions of the form: $\Delta OD = A_1 e^{-\frac{t}{\tau_1}} + A_2 e^{-\frac{t}{\tau_2}} + \cdots + y_0$, where t is the variable temporal delay of each data point, A_1, A_2, ... are the preexponential amplitudes, and τ_1, τ_2, … are the decay lifetimes. This was implemented in the Origin 7.5 software. The only global parameters used in the fitting routine were the decay lifetimes. The

fitting routine returned these constants as well as a corresponding set of preexponential amplitudes for each wavelength.

2.3. References

(1) Pangborn, A. B.; Giardello, M. A.; Grubbs, R. H.; Rosen, R. K.; Timmers, F. J. *Organometallics* **1996**, *15*, 1518-1520.
(2) Perrin, D. D.; Armarego, L. F. *Purification of Laboratory Chemicals*; 3rd ed.; Butterworth-Heinemann: Oxford, 1988.
(3) Xue, C.; Luo, F.-T. *J. Org. Chem.* **2003**, *68*, 4417-4421.
(4) Hreha, R. D.; Zhang, Y.-D.; Domercq, B.; Larribeau, N.; Haddock, J. N.; Kippelen, B.; Marder, S. R. *Synthesis* **2002**, 1201-1212.
(5) Andersen, N. G.; Maddaford, S. P.; Keay, B. A. *J. of Org. Chem.* **1996**, *61*, 9556-9559.
(6) Laibinis, P. E.; Nuzzo, R. G.; Whitesides, G. M. *J. Phys. Chem.* **1992**, *96*, 5097-105.
(7) Arnold, R.; Terfort, A.; Woell, C. *Langmuir* **2001**, *17*, 4980-4989.
(8) Shaporenko, A.; Terfort, A.; Grunze, M.; Zharnikov, M. *J. Electron Spectrosc. Relat. Phenom.* **2006**, *151*, 45-51.
(9) Shi, J.; Hong, B.; Parikh, A. N.; Collins, R. W.; Allara, D. L. *Chem. Phys. Lett.* **1995**, *246*, 90-94.
(10) Richter, L. J.; Yang, C. S. C.; Wilson, P. T.; Hacker, C. A.; van Zee, R. D.; Stapleton, J. J.; Allara, D. L.; Yao, Y.; Tour, J. M. *J. Phys. Chem. B* **2004**, *108*, 12547-12559.
(11) Porter, M. D.; Bright, T. B.; Allara, D. L.; Chidsey, C. E. D. *J. Am. Chem. Soc.* **1987**, *109*, 3559-68.
(12) Binnig, G.; Rohrer, H.; Gerber, C.; Weibel, E. *Phys. Rev. Lett.* **1983**, *50*, 120-123.
(13) Horcas, I.; Fernandez, R.; Gomez-Rodriguez, J. M.; Colchero, J.; Gomez-Herrero, J.; Baro, A. M. *Rev. Sci. Instrum.* **2007**, *78*, 013705.
(14) Adamo, C.; Barone, V. *J. Chem. Phys.* **1998**, *108*, 664-675.
(15) Lee, C.; Yang, W.; Parr, R. G. *Phys. Rev. B: Condens. Matter Mater. Phys.* **1988**, *37*, 785-789.
(16) M. J. Frisch et al., Gaussian 98, Revision A.11, Gaussian Inc., Pittsburgh PA, 2001.
(17) Lampert, R. A.; Chewter, L. A.; Phillips, D.; O'Connor, D. V.; Roberts, A. J.; Meech, S. R. *Anal. Chem.* **1983**, *55*, 68-73.
(18) O'Connor Desmond V., P. D. *Time-correlated Single Photon Counting*; Academic Press Inc.: London, 1984.
(19) Logunov, S. L.; Ahmadi, T. S.; El-Sayed, M. A.; Khoury, J. T.; Whetten, R. L. *J. Phys. Chem. B* **1997**, *101*, 3713-3719.
(20) Link, S.; El-Sayed, M. A. *Annu. Rev. Phys. Chem.* **2003**, *54*, 331-366.
(21) Rance, G. A.; Marsh, D. H.; Khlobystov, A. N. *Chem. Phys. Lett.* **2008**, *460*, 230-236.

CHAPTER 3

PREPARATION AND CHARACTERIZATION OF SELF ASSEMBLED MONOLAYERS OF STILBENE THIOLATES ON FLAT GOLD SURFACES

3.1. Introduction

Self-Assembled Monolayers (SAMs) of organic molecules on metals have received considerable attention over the last two decades.[1-4] Proposed applications of SAMs include their use as agents for improving the wettability of surfaces,[5] anticorrosive layers,[6] biosensors,[7] and resists for lithography.[4] From a purely scientific standpoint these structurally ordered systems offer a great opportunity for studying structure–property relationships of organic-inorganic interfaces. Studies of the influence of the molecular structure on the packing of thiols on noble metal surfaces have led to important insights into the molecular scale morphology of the monolayers. It is now understood that the thiol group binds to gold leading often to formation of long-range order in the resulting organic adlayer.[2-4,8-11] This understanding has further led to studies of the influence of synthetically accessible adsorbate structures on a variety of surface characteristics including wetting properties,[5,8] electronic characteristics,[12-14] and chemical reactivity.[15-17]

This chapter describes the preparation and characterization of self-assembled monolayers of three different substituted stilbene thiolates on gold (Figure 3.1), which were prepared for studies of the influence of the organic thin films on the electronic properties of the underlying gold substrate. This work constitutes the first report on the

preparation of monolayers composed of conjugated stilbene thiolates. Hence, the monolayers were characterized in detail using infrared reflection-absorption spectroscopy (IRRAS), X-ray photoelectron spectroscopy (XPS), ellipsometry, and scanning tunneling microscopy (STM) studies.

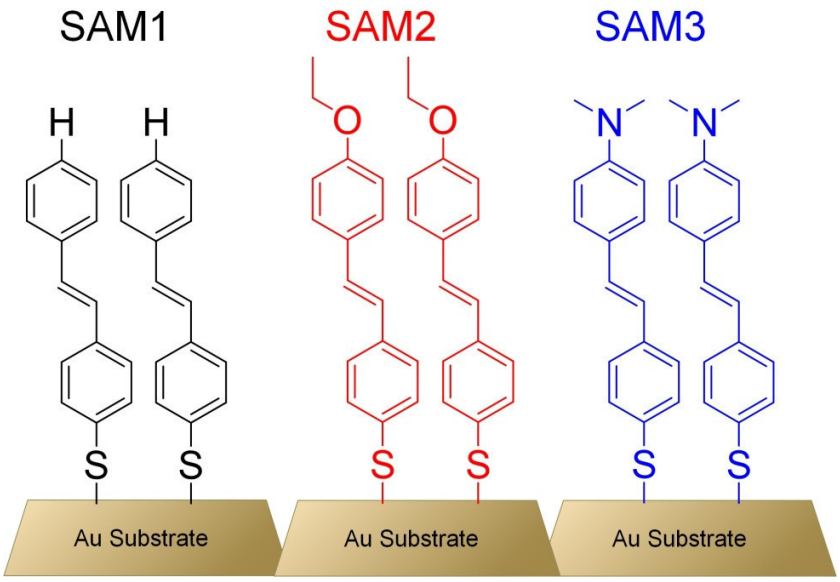

Figure 3.1. Schematic representation of SAMs studied herein. The color coding will be used throughout Chapters 2 and 3.

3.2. Synthesis and Monolayer Preparation

3.2.1. Synthesis of S-thioacetyl Protected Stilbenes

For this study, three stilbene thiol derivatives were synthesized, two containing a π-electron-donating group in the 4'-position. In order to avoid the known issue of air oxidation of aromatic thiols to form disulfides, which are often insoluble, acetyl-protected thiols were prepared.[18,19] Figure 3.2 shows the general synthetic scheme describing the preparation of the protected stilbene thiols, **Ac1-3**. The Horner-

Wadsworth-Emmons reaction between dimethyl 4-(methylthio)benzylphosphonate (**P1**) and commercial 4-substituted benzaldehydes was utilized to prepare the *S*-methylated stilbene thiols, **M1-3**, in good yields.[20,21] The acetyl group was introduced by treating each thiomethylated stilbene with sodium thio-*tert*-butoxide in refluxing DMF and quenching the resulting thiolate anion with acetyl chloride.[22] This approach gave moderate yields of 40-64 %.

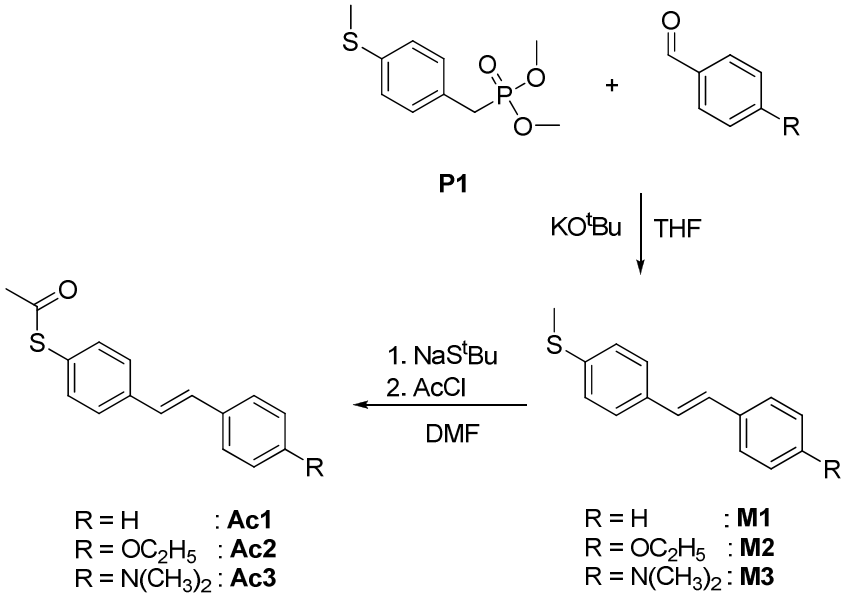

Figure 3.2. Synthesis of 4'-substituted-4-(acetylthio)stilbenes.

3.2.2. Preparation of Monolayers

The acetyl-protected stilbene thiols were used in the preparation of monolayers directly without deprotection from ethanol solutions as described in detail in Chapter 2 (section 2.2.1.1).[19,23,24] Figure 3.3 shows a comparison of FT-IR spectra of $CDCl_3$ solutions of **Ac1**, **Ac2**, and **Ac3** with IRRAS spectra of the corresponding monolayers (**SAM1**, **SAM2**, and **SAM3**, respectively) on gold. The major IR modes associated with

the stilbene π-conjugated systems are present in the IRRAS spectra of the monolayers confirming the adsorption of the molecules on gold. However, the carbonyl stretching mode (~1700 cm^{-1}) present in the spectra of $CDCl_3$ solutions of the acetyl-protected molecules is absent in the IRRAS spectra of the SAMs indicating that the adsorbed species do not contain the carbonyl group, consistent with the formation of thiolate monolayers. The IRRAS spectra are discussed in more detail in section 3.3.3.

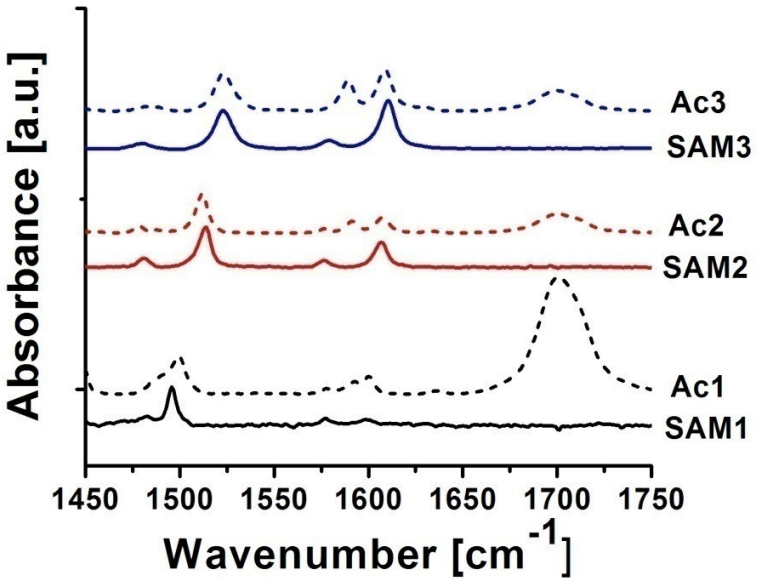

Figure 3.3. Comparison of IR spectra of $CDCl_3$ solutions of compounds **Ac1**, **Ac2**, and **Ac3** and IRRAS spectra of the corresponding monolayers.

3.3. Characterization of SAMs

3.3.1. XPS

3.3.1.1. Elemental Composition

XPS provides additional evidence for the adsorption of the thiolates on gold. Figure 3.4 shows XPS spectra of **SAM1** – **SAM3**. The data in the S(2p) region confirm the presence of sulfur with the peak maximum around 162.7 eV, consistent with the literature for other conjugated thiolate monolayers.[25,26] Additionally, no oxidized sulphur species was observed in the spectra.[27] All SAMs show the main C(1s) peak around 284.2 eV, which is in agreement with literature values obtained for biphenyl thiolate SAMs.[25,26] There is a pronounced shoulder on the high-binding-energy side in the case of **SAM2** and **SAM3**. This is consistent with the presence of carbon attached to an electronegative atom (O and N for **SAM2** and **SAM3**, respectively).[28] As expected, only **SAM3** shows signal from nitrogen core electrons. The spectra in the binding energy region of O(1s) core electrons are also presented in Figure 3.4. **SAM2** shows a strong signal around 533.1 eV, which can be attributed to the oxygen attached to a phenyl ring.[29] Additionally, **SAM3** shows a signal around 532.3 eV; this signal is also discernible, although weak, in the spectrum of **SAM1**. There are a few literature reports that reveal oxygen presence in amine-terminated SAMs on gold.[27,30-32] In a comprehensive study Baio *et al*. showed that, in the case of amine-terminated alkylthiolate SAMs on gold, the major source of oxygen signal in XPS is hydrogen-bound water molecules.[31] Even though the molecular structure of **SAM3** differs from that of amine-terminated alkylthiolate SAMs, it is not implausible that the dimethylamino group in **SAM3** is a sufficiently good hydrogen bond acceptor to facilitate the formation of a high-vacuum-stable water adlayer. Additionally, the position

of the O(1s) signal in the XPS spectrum of **SAM3** is very close to O(1s) signal reported for SAMs composed of 4-(4-mercaptophenyl)pyridine.[33] Those SAMs were shown to facilitate adsorption of a water adlayer that was stable under ultra-high vacuum conditions at room temperature.[33] Thus, the observed oxygen signal in the XPS spectrum of **SAM3** suggests water adsorption on top of the monolayer.

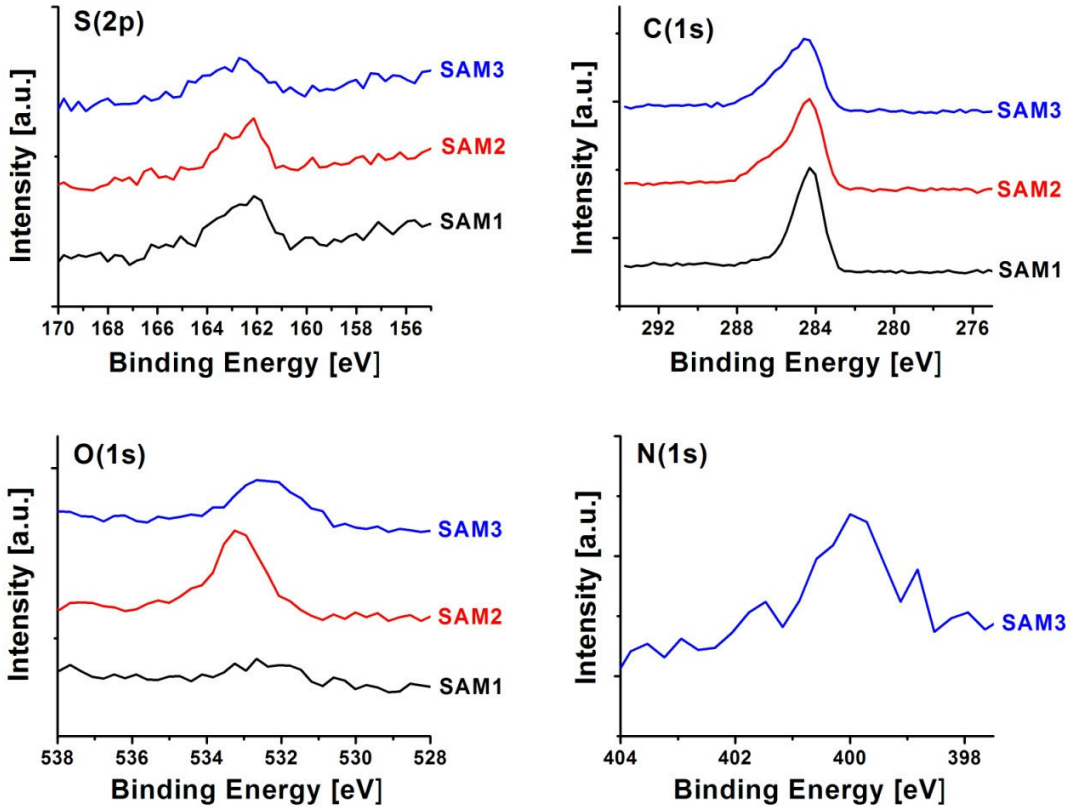

Figure 3.4. XPS spectra of stilbene thiolate SAMs in different spectral regions. The spectra are displaced vertically for clarity.

3.3.1.2. Monolayer Thickness and Coverage

XPS data can be used to establish the thickness of the monolayers. The relative attenuation of photoelectrons originating from the photoionization of the substrate is a measure of the thickness of an adlayer residing above the substrate as described by:

$$\ln \frac{I_1}{I_2} = \frac{d_2 - d_1}{\lambda \sin \phi} \qquad \textbf{Equation 3.1}$$

where I_1 and I_2 are measured Au($4f_{7/2}$) photoelectron intensities of sample 1 and sample 2, d_1 and d_2 are the thickness of the adlayer in sample 1 and sample 2, λ is the attenuation length of Au($4f_{7/2}$) photoelectrons caused by the organic adlayer,[a] and ϕ is the photoelectron take-off angle with respect to the sample surface.[12,35,36] Table 3.1 shows the thickness values obtained from XPS results on **SAM1**, **SAM2**, and **SAM3** using a gold slide coated with dodecanethiol (DDT) as a reference with the assumed thickness of DDT monolayer of 15.2 Å.[b,12] The extracted XPS thickness values are slightly smaller than the DFT calculated long molecular axis lengths for all three monolayers (Figure 3.6). This is consistent with the existence of dense monolayers with the molecules slightly tilted from the surface normal.[c]

Additional data confirming the existence of dense monolayers is the surface coverage that can be extracted from the XPS data comparing the ratio of S(2p) and Au(4f) peak areas of the samples of interest with the same ratio measured for a well-defined reference.[37-39] The coverage is then calculated according to:

---

[a] The equation assumes the same attenuation length of photoelectrons for sample 1 and sample 2. Value of λ = 42 Å was used, according to ref. 34.

[b] Octadecanethiol coated gold slide was also measured. The calculated thickness of octadecanethiol monolayer was 21.1 +/- 0.4 Å.

[c] An alternative interpretation is a slightly less dense non-tilted layer. However, analysis of the surface coverage supports the explanation given in the main text.

$$\theta_s = \theta_{ref} \frac{A^s_{S(2p)} A^{ref}_{Au(4f)}}{A^s_{Au(4f)} A^{ref}_{S(2p)}} \qquad \textbf{Equation 3.2}$$

where θ_s and θ_{ref} are the coverages in the sample and reference, respectively, $A^s_{S(2p)}, A^{ref}_{S(2p)}$ are the areas of the S(2p) peak measured for the sample and the reference respectively, and $A^s_{Au(4f)}, A^{ref}_{Au(4f)}$ are the areas of the Au(4f) peak measured for the sample and the reference respectively. As in the case of XPS thickness measurements, a dodecanethiol-coated gold slide was used as a reference. The coverage of the dodecanethiol coated gold slide was assumed to be 4.6×10^{14} molecules / cm^2, which is a value based on a literature report by Schreiber.[3] Following the procedure described above, a coverage of $4.6 \times 10^{14} \pm 0.4 \times 10^{14}$ molecules / cm^2 was extracted from the measurement of an octadecanethiol-coated gold slide. The coverage values for the monolayers studied here are summarized in Table 3.1. The obtained values are similar to those obtained for other conjugated thiol monolayers on gold,[37-40] with the polar substituents in **SAM2** and **SAM3** not having a large effect on the coverage in the monolayers.

3.3.2. Ellipsometry

Ellipsometry has been successfully used to establish the thickness of monolayers on noble metals,[1,10,28,41] and thus, to measure the quality of the monolayers. The technique was used to obtain an independent estimate of the monolayer thicknesses in the case of **SAM1-3**. The collected ellipsometric parameters of stilbene thiolate monolayers were used to fit the thickness values of the films using the model described in Chapter 2 (section 2.2.2.4). Only data in the spectral range of 600 – 1000 nm were used for fitting.[41]

Each stilbene adlayer was assumed to be a Cauchy layer with optical constants A = 1.63,[42] and B = 0.01 μm^2,[43] where $n(\lambda) = A + B/(\lambda^2)$. The only parameter that was allowed to vary in the fitting procedure was the adlayer thickness. The total thickness of the monolayer is then given by the sum of the Au-S layer thickness (2 Å, see Chapter 2 section 2.2.2.4) and the thickness of the stilbene adlayer.

It is not possible to extract both thickness and refractive index of a monolayer from ellipsometry measurements. Thus, the value of the refractive index of the monolayer must be assumed in order to extract the film thickness from the fit of the experimental data. The similarity of the assumed refractive index value to the actual refractive index value of the monolayer is crucial for obtaining an accurate determination of the thickness value of the thin film. The influence of the assumed refractive index on the extracted thickness of each monolayer is shown in Figure 3.5. The range of A values in the figure are similar to those discussed for oligo(phenylene-ethynylene) thiolate monolayers on gold in a report by Richter *et al*.[41] While including the uncertainty of A would increase the error bars on the extracted thickness values, but all of the comparisons and trends discussed here would remain valid.

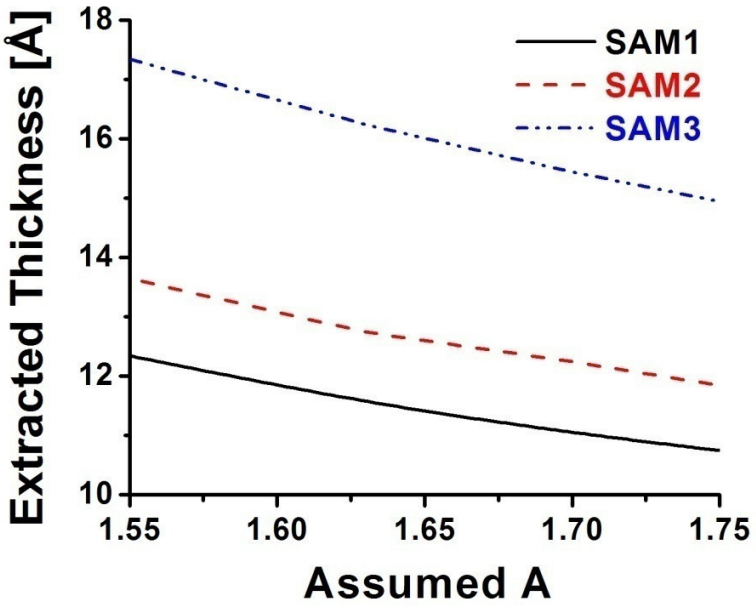

Figure 3.5. Influence of the assumed refractive index of the monolayer on the extracted thickness values of the stilbene SAMs on gold from the ellipsometry measurements.

Table 3.1. Thickness and coverage data of stilbene thiolate monolayers on gold. The coverage was obtained from XPS measurements.

Sample	XPS thickness [Å]	Ellipsometric thickness [Å]	Coverage [10^{14} molecules / cm^2]
SAM1	12.1 ± 0.6	11.1 ± 0.5	3.5 ± 0.24
SAM2	13.7 ± 0.5	12.7 ± 0.1	3.2 ± 0.23
SAM3	12.8 ±0.7	15.7 ± 0.7	3.1 ± 0.23

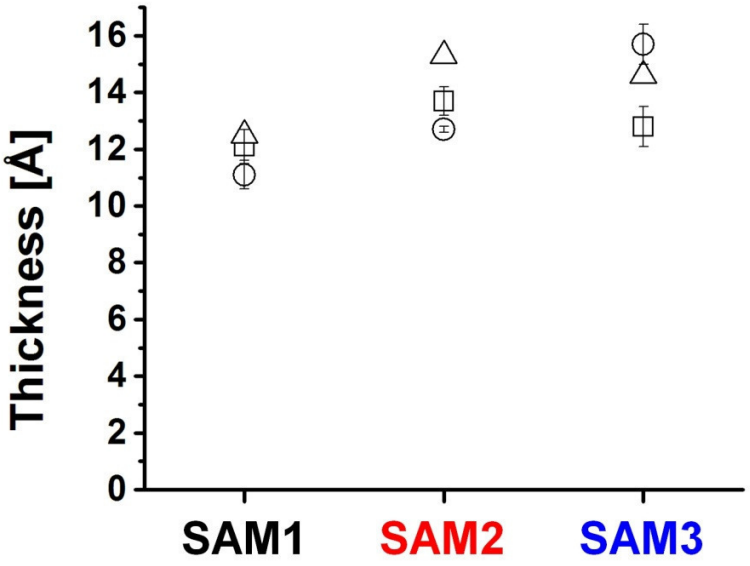

Figure 3.6. Summary of the thickness values extracted from ellipsometry (○) and XPS measurements (□). The triangles correspond to the DFT calculated distance from sulfur atom to terminal hydrogen along the long molecular axis for the relaxed geometry.

The ellipsometric thicknesses for **SAM1** and **SAM2** are slightly smaller than the calculated molecular lengths and consistent with the XPS estimates of the thickness (Figure 3.6). However, **SAM3** appears somewhat thicker. This may be due to adsorption of water onto the monolayer under the ambient conditions used for the ellipsometry measurements. Moreover, this is consistent with the presence of oxygen in the XPS spectrum of **SAM3** (see section 3.3.1.1).

3.3.3. Infrared Reflection-Absorption Spectroscopy Analysis

Infrared Reflection Absorption Spectroscopy (IRRAS) has proven to be very useful in the characterization of monolayers on metals.[1,10,44,45] It is, in principle, possible

to establish the molecular orientation of the constituents of a self-assembled monolayer by comparing the IR spectrum of adsorbate-like free molecules with the IRRAS spectrum of the monolayer.[10,44,45] The selection rule for light absorption by molecules on metallic surfaces states that only transitions with transition dipole moments (TDMs) that have nonzero projection onto the surface normal are allowed.[44] There are two main assumptions one must make in order to extract the molecular orientation from comparison of relative intensities in the FT-IR spectrum of the bulk adsorbate-like species and the IRRAS spectrum of the monolayer: firstly, that the TDMs of the vibrational modes of interest are the same for the adsorbate and the adsorbate-like species, and, secondly, that the free adsorbate-like sample is isotropic.[10] The second assumption is, of course, valid if one uses liquid solutions of the adsorbate-like species.

*3.3.3.1. IRRAS of **SAM1***

The comparison of IRRAS spectrum of **SAM1** and FT-IR spectra of solutions of the corresponding thiomethylated stilbene (**M1**) is presented in Figure 3.7.

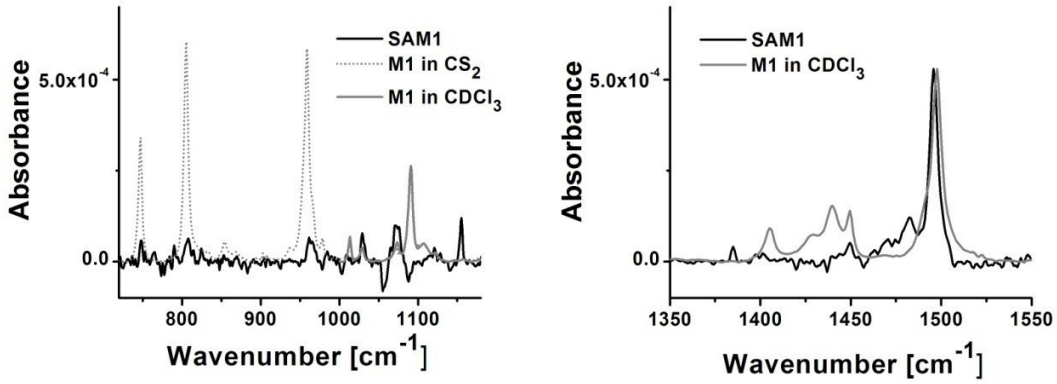

Figure 3.7. Comparison of IRRAS spectrum of **SAM1** and FT-IR spectra of solutions of **M1**. The absorbance of solutions of **M1** was scaled to match the absorbance measured for **SAM1** at 1496 cm^{-1}.

The $CDCl_3$ solution spectrum of **M1** was scaled to match the intensity of the phenyl ring semicircle stretch at 1496 cm^{-1} with that of the signal in the IRRAS spectrum of **SAM1**. TDM of this mode is oriented along the long axis of the molecule.[46] The corresponding semicircle stretches along the short axis of the molecule are located at 1450 cm^{-1} and 1406 cm^{-1}.[46] The IRRAS spectrum of **SAM1** shows that these signals are greatly reduced when compared to the solution FT-IR spectrum of **M1**. The mode at 1090 cm^{-1} can be attributed to a semicircle phenyl ring stretch involving the C-S bond stretching.[10] Even though TDM of this mode is oriented along the long axis of the molecule, the IRRAS spectrum of **SAM1** does not show strong signal in this spectral region. This might be due to a change of the resonant frequency of this vibrational mode upon binding of sulfur to gold. In fact, there is a new band in the IRRAS spectrum around 1155 cm^{-1} which is not present in solution spectrum of **M1**. The out-of-plane modes involving C-H wagging (959 cm^{-1}, 805 cm^{-1}, and 747 cm^{-1}) are all greatly reduced in IRRAS spectrum. The large reduction in intensity of both out-of-plane modes as well as

the in-plane modes along the short axis of the molecule is consistent with the long molecular axis being very close to the surface normal.[10] Table 3.2 shows a comparison of positions and intensities of the most prominent IR modes measured for **SAM1** and for **M1** solutions. Due to a very low signal to noise ratio, the attempts to extract the tilt angle of the molecular axis have not been made.

*3.3.3.2. IRRAS of **SAM2***

SAM2 exhibits much stronger IRRAS signal than that of **SAM1** (Figure 3.8). This is due to the substitution of the phenyl ring with the electronegative oxygen atom, which leads to larger changes in dipole moment during vibrations.[10]

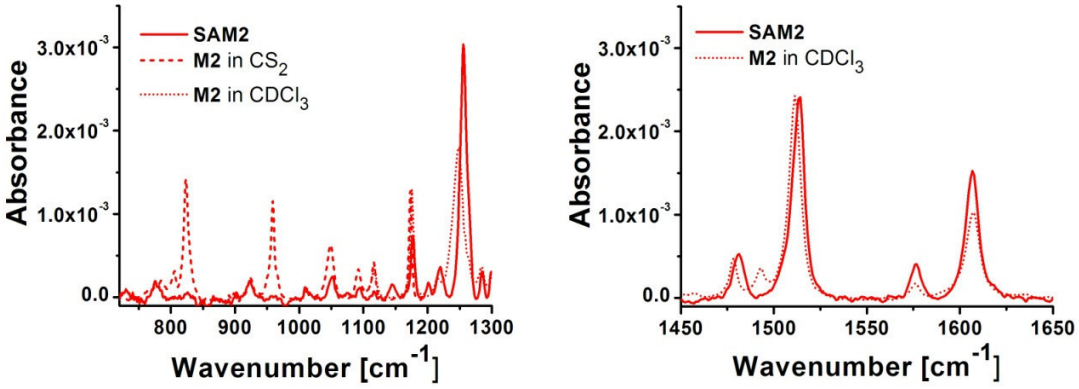

Figure 3.8. Comparison of IRRAS spectrum of **SAM2** and FT-IR spectra of solutions of **M2**. The absorbance of solutions of **M2** was scaled to match the absorbance measured for **SAM2** at 1511 cm^{-1}.

The $CDCl_3$ solution spectrum of **M2** was scaled to match the intensity of the semicircle stretch mode at 1511 cm^{-1} (TDM along the long molecular axis). The phenyl quadrant stretch modes at 1607 cm^{-1} and 1577 cm^{-1} (TDM along the long molecular axis),

as well as the Aryl-O stretch mode at 1256 cm^{-1} show higher relative signal in the monolayer IRRAS spectrum than in the FT-IR spectrum of solution of **M2**.[46] The changes in the relative intensities of the modes with parallel TDMs suggest that the adsorbed species exhibits different magnitudes of TDMs than **M2**. The only mode with TDM along the in-plane short molecular axis which could be identified is the aromatic C-H in-plane bending mode at 1118 cm^{-1}.[46] The relative intensity of the transition is dramatically decreased in the case of **SAM2** when compared with FT-IR spectrum of CS2 solution of **M2**. The out-of-plane C-H wagging modes (959 cm^{-1}, and 824 cm^{-1}) are practically absent in the IRRAS spectrum of **SAM2**. The large decrease of signal from modes with TDMs perpendicular to the long molecular axis in **SAM2** suggests that the long molecular axis of 4'-(ethoxy)stilbenethiolate is very close to parallel to the surface normal in the monolayer. Table 3.2 shows a comparison of positions and intensities of the most prominent IR modes measured for **SAM2** and for **M2** solutions.

*3.3.3.3. IRRAS of **SAM3***

The FT-IR spectrum of solutions of **M3** and the IRRAS spectrum of **SAM3** are compared in Figure 3.9. The mode at 1610 cm^{-1} (assigned to the phenyl quadrant stretching, with TDM along the long molecular axis) and the mode at 1523 cm^{-1} (assigned to the phenyl semicircle stretch mode, also with TDM along the long molecular axis) show practically the same relative intensity in the FT-IR spectrum of $CDCl_3$ solution of **M3** and in the IRRAS spectrum of **SAM3**. The second phenyl semicircle stretch mode with TDM along the long molecular axis was assigned to the band at 1483 cm^{-1}.[10] The relative intensity of this mode in the spectrum of the monolayer is the same as

in the spectrum of the $CDCl_3$ solution of **M3**. Interestingly, the peak observed at 1493 cm^{-1} in the solution spectrum of **M3** appears to be completely extinguished in the spectrum of **SAM3**. This vibration is most likely the asymmetric H-C-H bending mode of the methyl group, the TDM of which is perpendicular to the long molecular axis.[46] The Aryl-N stretching mode at 1354 cm^{-1} shows very similar relative intensities in the solution and monolayer spectra. The relative intensities of the out-of-plane C-H wagging modes (958 cm^{-1} and 820 cm^{-1}), with TDMs perpendicular to the long molecular axis, are greatly reduced in the monolayer spectrum with respect to the solution (see also Table 3.2); a similar behavior is observed in the case of **SAM1** and **SAM2**. At the same time, the symmetric C-N-C stretching mode with peak at 950 cm^{-1} (TDM along the long molecular axis) shows an intense signal in the spectrum of the monolayers. These observations suggest that the orientation of the long molecular axis of the adsorbate in **SAM3** is very close to parallel to the surface normal.

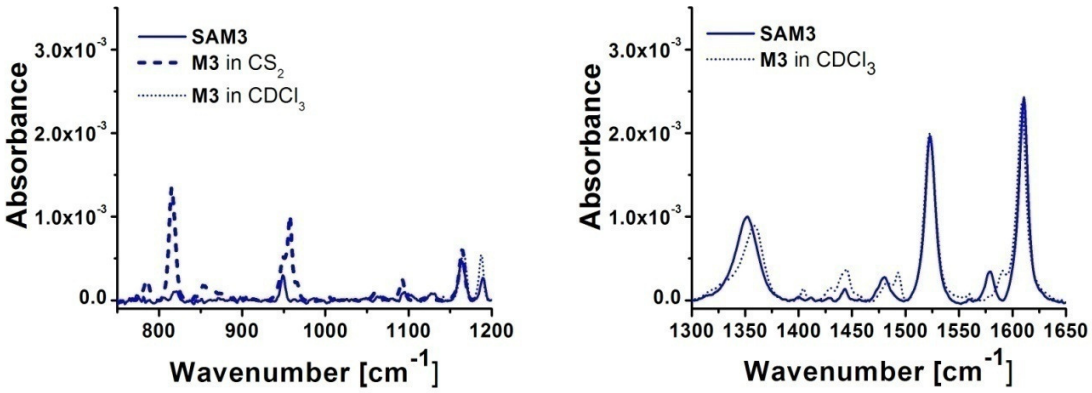

Figure 3.9. Comparison of IRRAS spectrum of **SAM3** and FT-IR spectra of solutions of **M3**. The absorbance of solutions of **M3** was scaled to match the absorbance measured for **SAM3** at 1523 cm^{-1}.

Table 3.2. Vibrational Frequencies (in cm^{-1}) of the Most Prominent IR Modes Measured for Solutions of 4'-Substituted-4-(Methylthio)stilbenes and the Corresponding SAMs.

Solution M1	SAM 1	I_{SAM1}/I_{M1} **	Solution M2	SAM 2	I_{SAM2}/I_{M2} **	Solution M3	SAM 3	I_{SAM3}/I_{M3} **	Assignment *
			1608	1607	1.5	1610	1610	1	Phenyl quadrant str., ip par
			1577	1577	2.3	1591	1579	1	Phenyl quadrant str., ip par
1497	1496	1	1514	1511	1	1523	1523	1	Phenyl semicircle str., ip par
						1493	-	<0.01	Methyl H-C-H bend., ip perp
			1478	1481	1.1	1484	1483	1.2	Phenyl semicircle str., ip par
1450	1450	<0.2							Phenyl semicircle str., ip perp
						1359	1352	1.1	Aryl-N str., ip par
			1247	1256	1.6				Aryl-O str., ip par
			1117	1118	0.15				Arom. C–H bend., ip perp
959	962	<0.08	959	-	<0.01	958	-	<0.01	C–H wag, op
						950	950	>0.8	C–N–C symm. str., ip par
805	808	0.1	826	824	<0.05	815	820	<0.08	C–H wag, op

* Assignment is based on literature[46] and DFT calculated vibrational modes of the isolated molecules; str. - stretching mode, bend. - bending mode, wag - wag mode, ip - in plane, op - out of plane, par – TDM parallel to the long molecular axis, perp – TDM perpendicular to the long molecular axis. ** Ratios of experimental intensities for a given mode in a SAM and in the solution of the corresponding free molecule

As can be seen in Table 3.2, modes assigned to vibrations with TDM perpendicular to the long molecular axis show a large depletion of intensity also in the IRRAS spectra of **SAM1-3** with respect to solution measurements, which is consistent with the orientation of the long molecular axes being close to the surface normal in all three monolayers. This behavior is similar to that previously observed in biphenyl thiolate SAMs, for which a tilt angle from the surface normal of ca. 20 degrees has been reported.[4]

3.3.4. Scanning Tunneling Microscopy

STM studies of thiol monolayers with molecular backbone similar to that of stilbene (i.e. biphenyl backbone) have shown that conjugated thiols can form a variety of ordered structures upon adsorption to gold.[11,47,48] Figure 3.10 shows a molecular resolution STM image of **SAM1**. The monolayer is characterized by a hexagonal close-packed array of molecules with a unit-cell lattice constant of 5.3 ± 0.3 Å which, given the experimental uncertainties, is indistinguishable from that of the unit cell of the densest phase observed for 4'-methyl-4-mercaptobiphenyl SAMs on gold, which was obtained after long immersion times.[11] It should be noted Figure 3.10 does not provide clear information on the molecular orientation in the cell and thus it is not possible to determine if there exists a superstructure with more than one non-equivalent molecule per unit cell or if there is orientational disorder within the domain. Taking into consideration the size of the molecule (~12 Å along the long molecular axis), the STM data are consistent with the molecules "standing up" on the surface with their long molecular axes being only slightly tilted from the surface normal. Based on the established unit cell size, the maximum molecular coverage possible for this monolayer on a perfectly flat surface is calculated to be $4.1 \pm 0.46 \times 10^{14}$ molecules / cm^2. When compared to this value, the XPS-estimated coverages (Table 3.1) suggest that the stilbene thiolates form dense monolayers. It was not possible to establish the maximum domain size of the stilbene thiolate monolayer due to the relatively small size of the terraces on the gold substrate used.

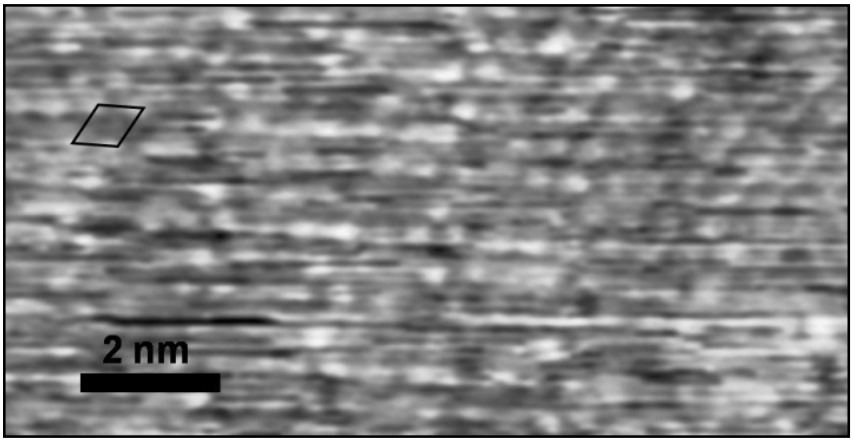

Figure 3.10. STM image of **SAM1** on gold. The rhombus in the upper left represents the unit cell of the hexagonal lattice.

3.4. Conclusions

A series of π-conjugated 4'-substituted-4-stilbene acetylthio derivatives was successfully synthesized. These protected thiol molecules react to form dense self-assembled monolayers of stilbene thiolates on gold when deposited from ethanolic solutions. These conclusions have been supported by evidence obtained by a variety of surface-sensitive techniques - XPS, IRRAS, ellipsometry and STM. Furthermore, it was found that the long axes of the molecules in the SAMs are oriented almost perpendicularly to the surface, consistent with the reports of a tilt from the surface normal of ca. 20° for biphenyl thiolate SAMs.[4] These systems were further used to study the effects of the π-electron-donating substituents on the electronic properties of the obtained monolayers and the underlying gold substrate. Those will be discussed in Chapter 4.

3.5. References

(1) Porter, M. D.; Bright, T. B.; Allara, D. L.; Chidsey, C. E. D. *J. Am. Chem. Soc.* **1987**, *109*, 3559-68.
(2) Laibinis, P. E.; Whitesides, G. M.; Allara, D. L.; Tao, Y. T.; Parikh, A. N.; Nuzzo, R. G. *J. Am. Chem. Soc.* **1991**, *113*, 7152-67.
(3) Schreiber, F. *Prog. Surf. Sci.* **2000**, *65*, 151-257.
(4) Love, J. C.; Estroff, L. A.; Kriebel, J. K.; Nuzzo, R. G.; Whitesides, G. M. *Chem. Rev.* **2005**, *105*, 1103-1170.
(5) Whitesides, G. M.; Laibinis, P. E. *Langmuir* **1990**, *6*, 87-96.
(6) Jennings, G. K.; Yong, T.-H.; Munro, J. C.; Laibinis, P. E. *J. Am. Chem. Soc.* **2003**, *125*, 2950-2957.
(7) Chaki, N. K.; Vijayamohanan, K. *Biosens. Bioelectron.* **2002**, *17*, 1-12.
(8) Laibinis, P. E.; Nuzzo, R. G.; Whitesides, G. M. *J. Phys. Chem.* **1992**, *96*, 5097-105.
(9) Duan, L.; Garrett, S. J. *J. Phys. Chem. B* **2001**, *105*, 9812-9816.
(10) Kang, J. F.; Ulman, A.; Liao, S.; Jordan, R.; Yang, G.; Liu, G. y. *Langmuir* **2001**, *17*, 95-106.
(11) Azzam, W.; Fuxen, C.; Birkner, A.; Rong, H.-T.; Buck, M.; Woell, C. *Langmuir* **2003**, *19*, 4958-4968.
(12) Laibinis, P. E.; Bain, C. D.; Whitesides, G. M. *J. Phys. Chem.* **1991**, *95*, 7017-7021.
(13) Bumm, L. A.; Arnold, J. J.; Cygan, M. T.; Dunbar, T. D.; Burgin, T. P.; Jones, L., II; Allara, D. L.; Tour, J. M.; Weiss, P. S. *Science* **1996**, *271*, 1705-07.
(14) Zangmeister, C. D.; Robey, S. W.; Van Zee, R. D.; Yao, Y.; Tour, J. M. *J. Phys. Chem. B* **2004**, *108*, 16187-16193.
(15) Houseman, B. T.; Gawalt, E. S.; Mrksich, M. *Langmuir* **2003**, *19*, 1522-1531.
(16) Lee, J. K.; Lee, K.-B.; Kim, D. J.; Choi, I. S. *Langmuir* **2003**, *19*, 8141-8143.
(17) Collman, J. P.; Devaraj, N. K.; Chidsey, C. E. D. *Langmuir* **2004**, *20*, 1051-1053.
(18) Witt, D.; Klajn, R.; Barski, P.; Grzybowski, B. A. *Curr. Org. Chem.* **2004**, *8*, 1763-1797.
(19) Tour, J. M.; Jones, L., II; Pearson, D. L.; Lamba, J. J. S.; Burgin, T. P.; Whitesides, G. M.; Allara, D. L.; Parikh, A. N.; Atre, S. *J. Am. Chem. Soc.* **1995**, *117*, 9529-34.
(20) Horner, L.; Hoffmann, H.; Wippel, H. G. *Chem. Ber.* **1958**, *91*, 61-3.
(21) Wadsworth, W. S., Jr.; Emmons, W. D. *J. Am. Chem. Soc.* **1961**, *83*, 1733-8.
(22) Pinchart, A.; Dallaire, C.; Van Bierbeek, A.; Gingras, M. *Tetrahedron Lett.* **1999**, *40*, 5479-5482.
(23) Cai, L.; Yao, Y.; Yang, J.; Price, D. W.; Tour, J. M. *Chem. Mater.* **2002**, *14*, 2905-2909.
(24) Kang, Y.; Won, D.-J.; Kim, S. R.; Seo, K.; Choi, H.-S.; Lee, G.; Noh, Z.; Lee, T. S.; Lee, C. *Mater. Sci. Eng., C* **2004**, *C24*, 43-46.
(25) Heister, K.; Zharnikov, M.; Grunze, M.; Johansson, L. S. O. *J. Phys. Chem. B* **2001**, *105*, 4058-4061.

(26) Shaporenko, A.; Terfort, A.; Grunze, M.; Zharnikov, M. *J. Electron Spectrosc. Relat. Phenom.* **2006**, *151*, 45-51.
(27) Wang, H.; Chen, S.; Li, L.; Jiang, S. *Langmuir* **2005**, *21*, 2633-2636.
(28) Bain, C. D.; Troughton, E. B.; Tao, Y. T.; Evall, J.; Whitesides, G. M.; Nuzzo, R. G. *J. Am. Chem. Soc.* **1989**, *111*, 321-35.
(29) Stoycheva, S.; Himmelhaus, M.; Fick, J.; Kornviakov, A.; Grunze, M.; Ulman, A. *Langmuir* **2006**, *22*, 4170-4178.
(30) Wang, H.; Castner, D. G.; Ratner, B. D.; Jiang, S. *Langmuir* **2004**, *20*, 1877-1887.
(31) Baio, J. E.; Weidner, T.; Brison, J.; Graham, D. J.; Gamble, L. J.; Castner, D. G. *J. Electron Spectrosc. Relat. Phenom.* **2009**, *172*, 2-8.
(32) Chuang, W.-H.; Lin, J.-C. *J. Biomed. Mater. Res., Part A* **2007**, *82A*, 820-830.
(33) Zubavichus, Y.; Zharnikov, M.; Yang, Y.; Fuchs, O.; Umbach, E.; Heske, C.; Ulman, A.; Grunze, M. *Langmuir* **2004**, *20*, 11022-11029.
(34) Laibinis, P. E.; Bain, C. D.; Whitesides, G. M. *J. Phys. Chem.* **1991**, *95*, 7017-7021.
(35) Whelan, C. M.; Smyth, M. R.; Barnes, C. J. *Langmuir* **1999**, *15*, 116-126.
(36) Frey, S.; Stadler, V.; Heister, K.; Eck, W.; Zharnikov, M.; Grunze, M.; Zeysing, B.; Terfort, A. *Langmuir* **2001**, *17*, 2408-2415.
(37) Whelan, C. M.; Barnes, C. J.; Walker, C. G. H.; Brown, N. M. D. *Surf. Sci.* **1999**, *425*, 195-211.
(38) Pugmire, D. L.; Tarlov, M. J.; van Zee, R. D.; Naciri, J. *Langmuir* **2003**, *19*, 3720-3726.
(39) Zangmeister, C. D.; Picraux, L. B.; van Zee, R. D.; Yao, Y.; Tour, J. M. *Chem. Phys. Lett.* **2007**, *442*, 390-393.
(40) Tao, Y.-T.; Wu, C.-C.; Eu, J.-Y.; Lin, W.-L.; Wu, K.-C.; Chen, C.-h. *Langmuir* **1997**, *13*, 4018-4023.
(41) Richter, L. J.; Yang, C. S. C.; Wilson, P. T.; Hacker, C. A.; van Zee, R. D.; Stapleton, J. J.; Allara, D. L.; Yao, Y.; Tour, J. M. *J. Phys. Chem. B* **2004**, *108*, 12547-12559.
(42) *CRC Handbook of Chemistry and Physics*; 63 ed.; Weast, R. C., Ed.; CRC Press: Boca Raton, Florida, 1982.
(43) Cooper, P. R. *Appl. Opt.* **1983**, *22*, 3070-3072.
(44) Dubois, L. H.; Zegarski, B. R.; Nuzzo, R. G. *J. Am. Chem. Soc.* **1990**, *112*, 570-9.
(45) Arnold, R.; Terfort, A.; Woell, C. *Langmuir* **2001**, *17*, 4980-4989.
(46) Lin-Vien, D.; Colthup, N. B.; Fataley, W. G.; Grasselli, J. G. *The Handbook of Infrared and Raman Characteristic Frequencies of Organic Molecules*; Academic Press, Inc.: New York, 1991.
(47) Dhirani, A.-A.; Zehner, R. W.; Hsung, R. P.; Guyot-Sionnest, P.; Sita, L. R. *J. Am. Chem. Soc.* **1996**, *118*, 3319-3320.
(48) Yang, G.; Qian, Y.; Engtrakul, C.; Sita, L. R.; Liu, G. y. *J. Phys. Chem. B* **2000**, *104*, 9059-9062.

CHAPTER 4

ELECTRONIC PROPERTIES OF STILBENE THIOLATE MONOLAYERS ON GOLD

4.1. Introduction

One of the interesting effects induced by SAMs is the modification of the work function of the metallic substrate, which is of great importance in organic electronic applications, since it is one of the parameters determining the barrier for charge-carrier injection from the metal into the organic overlayer.[1,2] Although any adsorbate can potentially modify the work function of a metal,[1,3] SAMs offer the opportunity to systematically investigate the influence of molecular structure on the work function. This has been described in detail in Chapter 1.

While most studies on the influence of thiol-based organic adsorbates on the work function of gold focused on alkyl thiol-based monolayers, a limitation on the use of monolayers consisting of long-chain alkyl thiols for modifying injection barriers between metals and organics is the intrinsic electrically insulating characteristics of the alkyl chains. Monolayers consisting of conjugated thiols, which have been shown to exhibit considerably enhanced conductivity,[4,5] may be more promising for this type of application. Although the work function modification by conjugated thiols has been studied both theoretically[6] and experimentally,[7-10] and monolayers of phenylene-ethynylene thiol derivatives on gold have been shown to exhibit the anticipated effects as a function of dipole moments,[11] it should be stressed that reports on the influence of the

end group substituents in monolayers of conjugated thiol molecules on the work function of the underlying metal are scarce and the understanding is still rather inchoate.

4.2. Work Function of Gold Coated with Stilbene Thiolate SAMs

4.2.1. UPS Measurements

As described in Chapter 1 (section 1.1.2), UPS allows for a direct measurement of the work function of surfaces. The stilbene thiolate SAMs on gold, whose preparation and characterization were described in Chapter 3, were analyzed with this technique and the work functions of the chemically-modified gold surfaces were determined. Figure 4.1 shows the low kinetic energy portion of UPS spectra of the stilbene thiolate monolayers on gold. This spectral region is often referred to as the secondary photoelectron cutoff and the position of the sharp rise of the signal (characterized by an electron kinetic energy of E_{min}) is used to establish the position of the vacuum level of the sample and its work function, Φ_m, according to the relation: $\Phi_m = E_{min} + h\nu - E_{max}$, where $h\nu$ is the photon energy (21.2 eV in this study), and E_{max} is the kinetic energy of photoelectrons originating from the Fermi level, as described in Chapter 1 (section 1.1.2).[1,8,12,13]

The work functions obtained from these measurements (Figure 4.2) for all three monolayers are significantly smaller than values reported for Au(111), which are typically in the range 5.2–5.3 eV.[1,3,8] The work function of 4.30 eV measured for the unsubstituted stilbene thiolate monolayer, **SAM1**, is very close to the values measured for monolayers of other conjugated thiolates without polar substituents; for example, values of 4.20 and 4.30 eV have been reported for the work function of Au(111) coated with 4,4'-(ethynylphenyl)-1-benzenethiolate (OPET)[14] and 4-terphenylthiolate (TPT),[8]

respectively (Figure 4.2). Substitution of the terminal phenyl ring of the stilbene backbone with a π donor group in the *para* position leads to further drop in the work function, as shown in Figure 4.2.

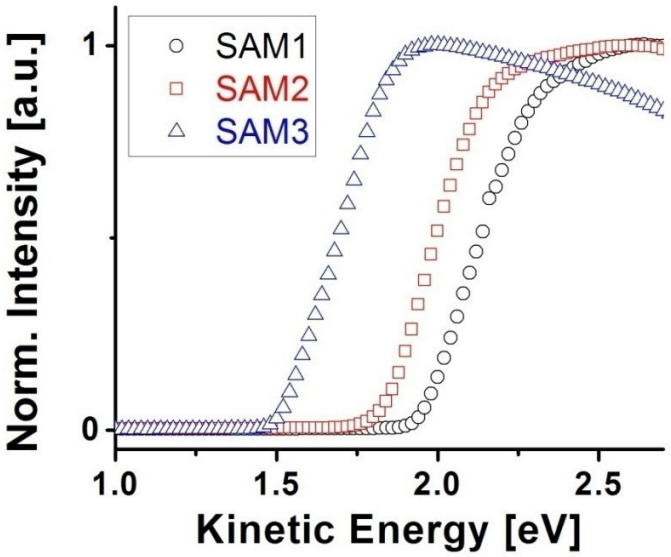

Figure 4.1. Secondary-photoelectron cutoff regions of the UPS spectra of stilbene thiolate monolayers on gold.

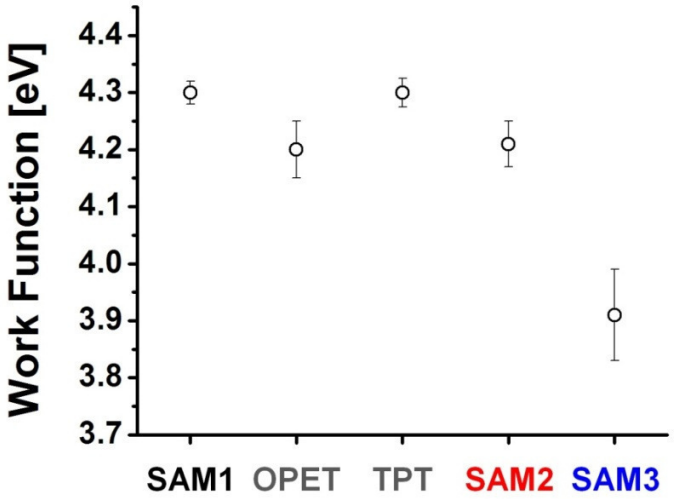

Figure 4.2. Work function values measured for **SAM1-3** on gold in this study and literature values found for OPET[14] and TPT[8] on gold.

4.2.2. Analysis of the Work-Function Changes

4.2.2.1. Comparison of the Experimental Work-Function Changes with Theoretical Predictions

It is interesting to compare the experimental modifications of the work function with those anticipated on a purely electrostatic basis. The work function change, $\Delta\Phi_m$, caused by a sheet of dipoles residing on the surface can be estimated using the projection of the molecular dipole moment onto the surface normal, μ_{mono}, and the coverage of the surface, θ, employing the Helmholtz equation, which was described in Chapter 1 (section 1.1.4):[7,15,16]

$$\Delta\Phi_m = \frac{\theta}{\varepsilon_0}\left(\frac{\mu_{mono}}{\kappa_{mono}} + \frac{\mu_{BD}}{\kappa_{BD}}\right) \qquad \textbf{Equation 4.3}$$

where μ_{BD} is the dipole moment induced by binding to the surface (Bond Dipole, BD),[17-19] κ_{mono} and κ_{BD} are the depolarization factors of the molecular dipole layer and BD layer respectively,[20] and ε_0 is the vacuum permittivity.[a] If μ_{BD} is assumed to be independent of the substitution pattern of the stilbene thiolate, and the coverage is assumed to be constant from sample to sample, the equation also implies that the y-intercept of a linear fit of the experimental values of $\Delta\Phi_m$ against the projection of the calculated molecular dipole moments onto the surface normal (Figure 4.3, solid line) is the measure of the work-function change originating solely from the BD layer. The value extracted in this way is $\Delta\Phi_m$ = –0.85 eV, which, assuming $\theta = 3.3 \times 10^{14}$ molecules / cm^2, which is the average value of the XPS estimated-coverages for the SAMs studied here (see Chapter 3, section 3.3.1.2), and a depolarization factor of BD layer, κ_{BD}, of 6.4,[7,21] corresponds to the projection of the dipole moment induced by adsorption onto the surface normal of around 4.4 D / molecule. To put this value into perspective, using the data of Alloway *et al.* for alkanethiol monolayers on gold one calculates μ_{BD} of ca. 1.9 D / molecule, assuming again κ_{BD} = 6.4 but a coverage of 4.6×10^{14} molecules / cm^2.[12] DFT calculations by Heimel *et al.* suggested the value of μ_{BD} induced upon adsorption of 4'-methyl-4-mercaptobiphenyl on gold to be around 4.5 D / molecule,[16] which is very similar to the experimental estimate obtained for the monolayers studied here.

Figure 4.3 also shows (dashed line) the work-function changes calculated for a sheet of dipoles on the surface representing only the molecular dipole (hence the assumed μ_{BD} is zero); the depolarization factor κ_{mono} of the molecular dipole sheet in the

[a] The version of the Helmholtz equation shown here is based on the assumption of the existence of two sheets of dipoles which additively influence the surface potential – one dipole originating from the intrinsic dipole moment of the adsorbed molecule, μ_{mono}, and one originating from the charge rearrangement upon binding of the thiol to gold, μ_{BD}.

calculations was assumed to be 3.0, which is a frequently cited value for conjugated thiol monolayers.[7,10,16,20] XPS-established coverage values were used for the calculations, and the DFT-calculated values of molecular dipole moment along the long molecular axis of the corresponding stilbene thiols were projected onto the surface normal assuming a tilt of the molecular long axis of 20°.[22]

Under these assumptions, the calculated data follow a linear trend with a slope 3.3 times larger than that of the linear fit of the experimental values. Also, analysis of the data of Alloway *et al.* reveals that the slope calculated for alkanethiols on gold is about 4 times larger than the slope found in this study.[12]

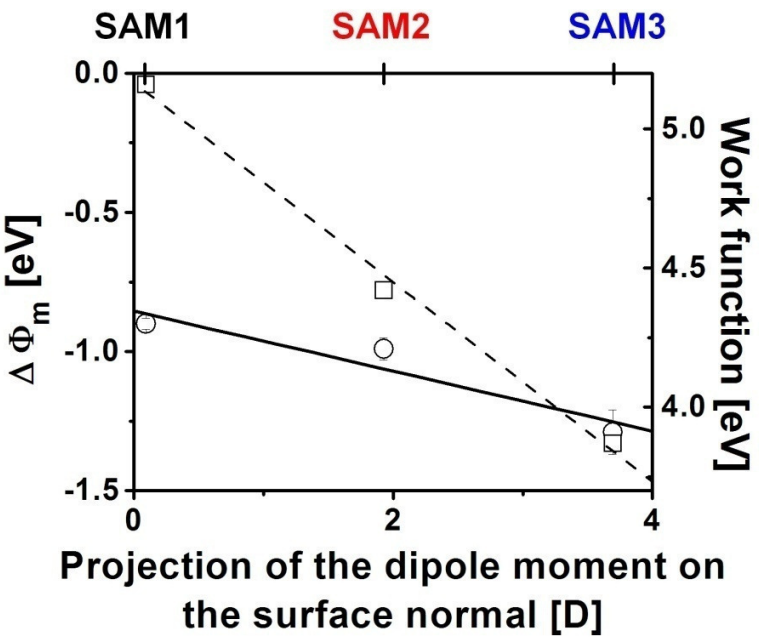

Figure 4.3. Work function changes caused by substituted stilbene thiolate monolayers on gold as a function of DFT-calculated dipole moments along the long molecular axis of the corresponding thiols projected on the surface normal: the circles are experimentally determined from UPS measurements and the squares are calculated from Equation 4.3 assuming $\mu_{BD} = 0$; the solid and dashed lines are the corresponding linear fits for each data set.

4.2.2.2. Factors Influencing the Measured Work-Function Changes

The possible contributions to the observed disparity between the theoretically-calculated and experimentally-measured values of work-function changes might include a depolarization factor of the dipole layer, κ_{mono}, much higher than the assumed value of 3.0, or dependence of μ_{BD} on the 4'-substituent in the stilbene thiolate molecules.

Another possibility, however, is the presence of other adsorbates on the surface, which have not been taken into account in the calculations based on Equation 4.3. In fact, as discussed earlier, XPS results indicate the presence of oxygen in the adsorbate, likely

arising from water, especially in the case of **SAM3**. Alignment or partial alignment of water molecules within this adlayer would give rise to an additional dipole layer, which, according to the Equation 4.3, could be anticipated to influence the work function. If a water adlayer indeed exists on top of **SAM3**, the alignment of water molecules with respect to the surface will most likely be dictated by the hydrogen bonds formed between the terminal dimethylamino group in **SAM3** and the water molecules.[23] Such simple analysis would only be valid if the adsorbed water does not form a multilayer. This may well be the case for **SAM3**, as the XPS-measured thickness of **SAM3** is close to the DFT-calculated molecular length of the corresponding thiol (see Figure 30), and the elemental composition of **SAM3** shows similar amounts of oxygen and nitrogen,[b] implying that the amount of the oxygen-containing species, i.e., most likely water, is close to the number of the terminal dimethylamino groups. Figure 4.4 shows the schematic of a possible arrangement of water molecules on top of **SAM3** as well as the projection of the dipole moments originating from different layers onto the surface normal. It should be stressed that due to the large dipole moment of a water molecule, ca. 1.85 D,[24] the alignment or partial alignment of the water molecules on top of **SAM3** would lead to a substantial increase of the work function, as the direction of the projection of the dipole moment of water molecules onto the surface normal would most

[b] The XPS-based relative amounts of the two elements with respect to each other were found by comparing the areas under the O(1s) and N(1s) signals in the XPS spectrum of **SAM3** and taking into account the different photoelectron-detection sensitivity in the different spectral regions (the detection sensitivity factor includes both the instrumental sensitivity and the photoionization cross section, i.e. the Scofield factor), which was provided by the manufacturer of the XPS spectrometer. Additionally, the found amounts of the two elements should not be strongly influenced by photoelectron-attenuation effects, as both oxygen and nitrogen should be located in the top portion of the SAM. The values of relative amounts of nitrogen and oxygen were found to be different by only ca. 5 % which, considering uncertainty of the measured values, suggests a 1 : 1 ratio of nitrogen to oxygen on the surface.

likely be opposite to the projection of the dipole moment of the 4'-dimethylamino-4-stilbene thiolate, as shown schematically in Figure 4.4.

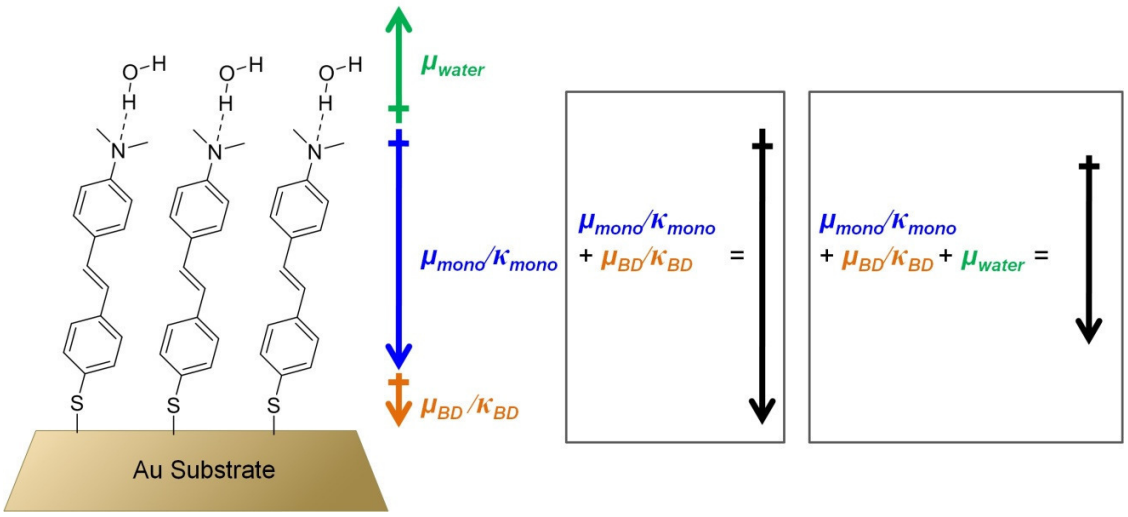

Figure 4.4. Schematic representation of a possible arrangement of water molecules hydrogen-bound on top of **SAM3**. Projections of the depolarized dipole moments of the monolayer, μ_{mono}/κ_{mono}, bond dipole, μ_{BD}/κ_{BD}, and the water-molecule dipole moment, μ_{water}, onto the surface normal are shown with the arrows.

In any case, the studied self-assembled monolayers of stilbene thiolates show the expected trend in the modification of the work function of the underlying metal with substituents of different π-electron-donating ability.

4.3. Molecular Energy Levels of Stilbene Thiolate Monolayers on Gold

4.3.1. UPS Measurements

UPS allows one to measure energy of electronic states of molecules on surfaces. An increased density of states localized on the surface-residing adsorbates results in the increased photoelectron intensity at the corresponding kinetic energy, i.e., in a peak with

its position determined by the energetics of the electronic state.[1,16] Figure 4.5 shows the measured UPS spectra for clean gold,[c] and for gold substrates covered with **SAM1-3**.

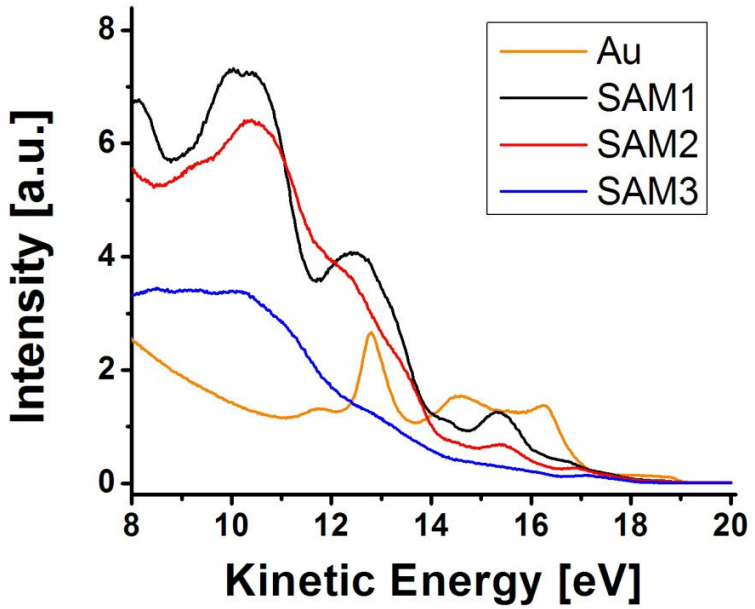

Figure 4.5. UPS spectra of clean gold (Au) and gold coated with stilbene thiolate monolayers (as measured).

The spectra measured for **SAM1-3** differ significantly from the spectrum measured for clean gold. This can be related to the attenuation of the photoelectrons originating from the gold surface by the organic adlayers and the significant contribution of the photoelectrons originating from the organic molecules to the observed spectra.[1,25]

A comparison of the UPS spectra of the monolayers with the spectrum of clean gold in the Fermi-level region (Figure 4.6) reveals that the position of the Fermi level is

[c] The clean gold sample was prepared by sputtering of the gold substrate with Ar^+ (0.5 kV, 2.0 $\times 10^{-5}$ Torr) in the UHV chamber and subsequent annealing of the sample (400 °C).

the same for all samples (18.90 eV),[d] and that the intensity of the signal around the Fermi level is significantly reduced in **SAM1-3** with respect to clean gold. This intensity reduction can be attributed to the attenuation of the Fermi-level photoelectrons, which originate from the gold surface, by the organic adlayers in the monolayer samples.[12,25]

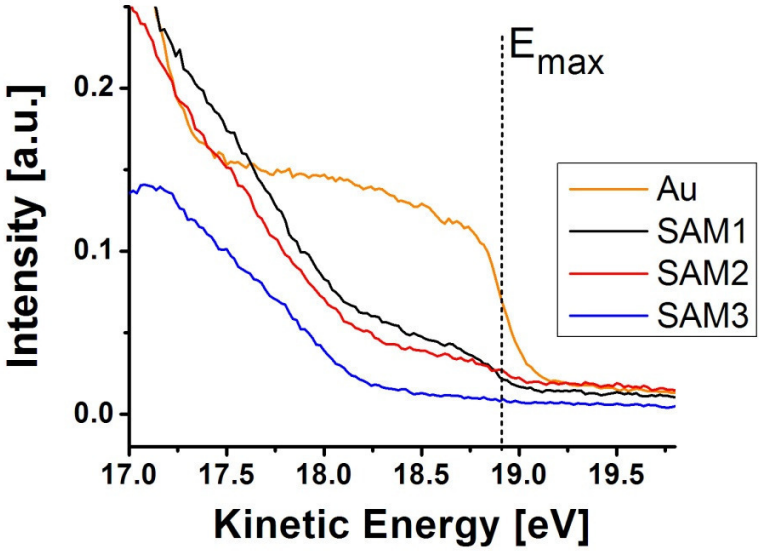

Figure 4.6. Fermi-level region of the UPS spectra measured for clean gold (Au) and for gold coated with stilbene thiolate monolayers. The vertical dashed line dissecting the abrupt signal-increase step represents the position of the Fermi level and can be related to E_{max} in Figure 1.2 (Chapter 1, section 1.1.2).

In order to establish the molecular contribution to the measured UPS spectra in **SAM1-3**, the photoelectrons originating from the gold surface, whose spectrum corresponds to that acquired in the case of clean gold, were subtracted. This was done by scaling the spectrum of clean gold to match its intensity around E_{max} with the

[d] A close-up of the curve measured for **SAM3** shows clearly that the position of the Fermi level is the same as for the other samples.

corresponding intensity in a spectrum measured for a monolayer sample, and then subtracting the scaled gold spectrum from the spectrum measured for the monolayer. This approach is based on the assumption that the attenuation length of the photoelectrons within the kinetic-energy range of interest is constant. Figure 4.7 shows normalized spectra of molecular contribution to the measured UPS signal for **SAM1-3** obtained in this fashion.

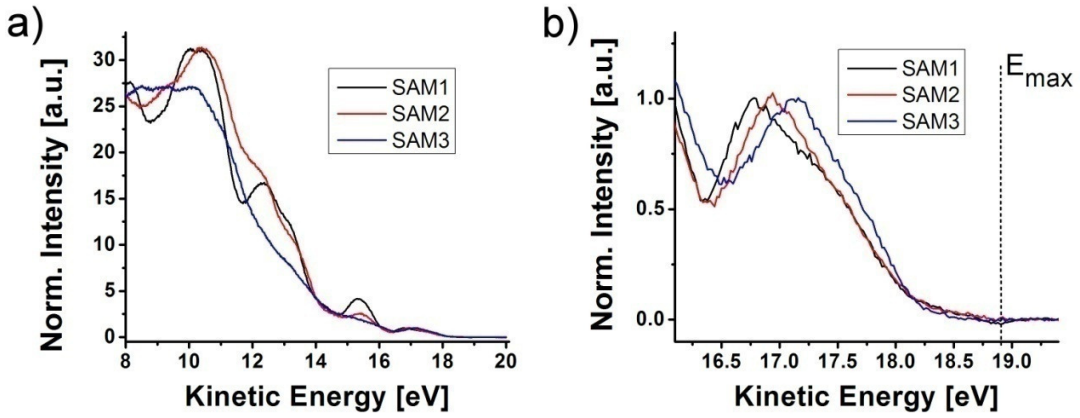

Figure 4.7. a) Molecular contribution to the UPS spectra measured for **SAM1-3**. b) High-kinetic-energy region of the UPS-measured molecular contributions for **SAM1-3**. The spectra were normalized at the maximum of the first feature below the Fermi level.

It is interesting to note that there is a clear progression of the position of the feature present around 17 eV with the different substituent on the 4' position of the stilbene thiolate molecular backbone. The observed maximum of the band shifts by as much as 0.35 eV towards the Fermi level when comparing the spectra of **SAM1** and **SAM3**. Additionally, the shape of the band seems to show significant asymmetry in all three spectra. Considering the fact that bands in UPS are often assumed to have a Gaussian function shape,[26,27] the observed asymmetry implies that in each monolayer the

observed band consists of at least two components. While it is not entirely clear what the origin of each of the observed features is, it is most likely that the asymmetric band seen in the spectrum of each SAM is a signature of at least two different electronic states. Fitting the experimental data for each SAM with a sum of two Gaussian functions with fixed width (full width at half maximum, FWHM) of 0.45 eV[e] yielded rather poor fits, which are presented in Figure 4.8.[27,f]

[e] The full width at half maximum of the Gaussian function was based on the measured width of the signal step at Fermi level. This approach was based on Ref. 27.

[f] The fitting was performed in Origin 7.5 software. Positions and amplitudes of the Gaussian functions were used as floating parameters while the width of the Gaussian function was set to be 0.45 eV. An offset was added as a constant fitting parameter; from the fits this was found to correspond to the value of the experimental point at the high-kinetic-energy limit of the data range used for fitting.

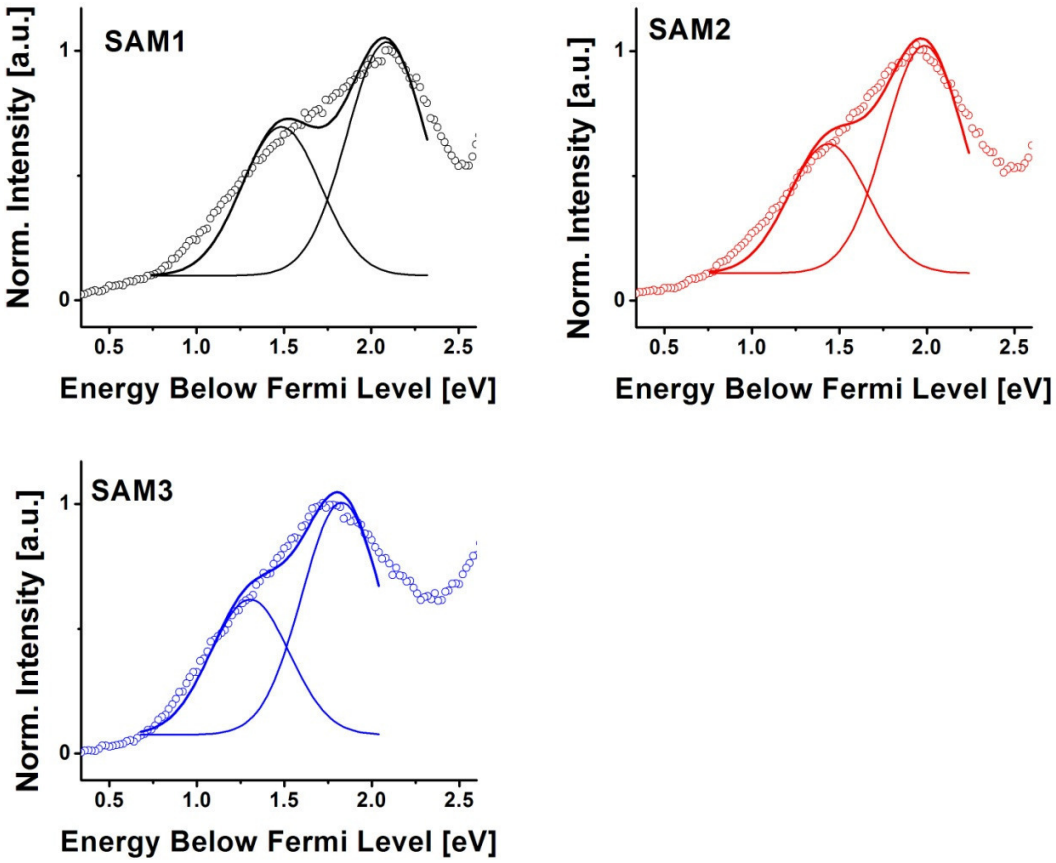

Figure 4.8. Experimentally measured UPS spectra (open circles) for **SAM1-3** and best fits obtained from fitting the band with a sum of two Gaussian functions (solid lines).

The fitting procedure gave much better agreement of the best-fit curves with the experimental data when a sum of three Gaussian functions with FWHM = 0.45 eV was used. This is shown in Figure 4.9 and the parameters of the Gaussian functions that gave the best fit for each SAM are listed in Table 4.1.

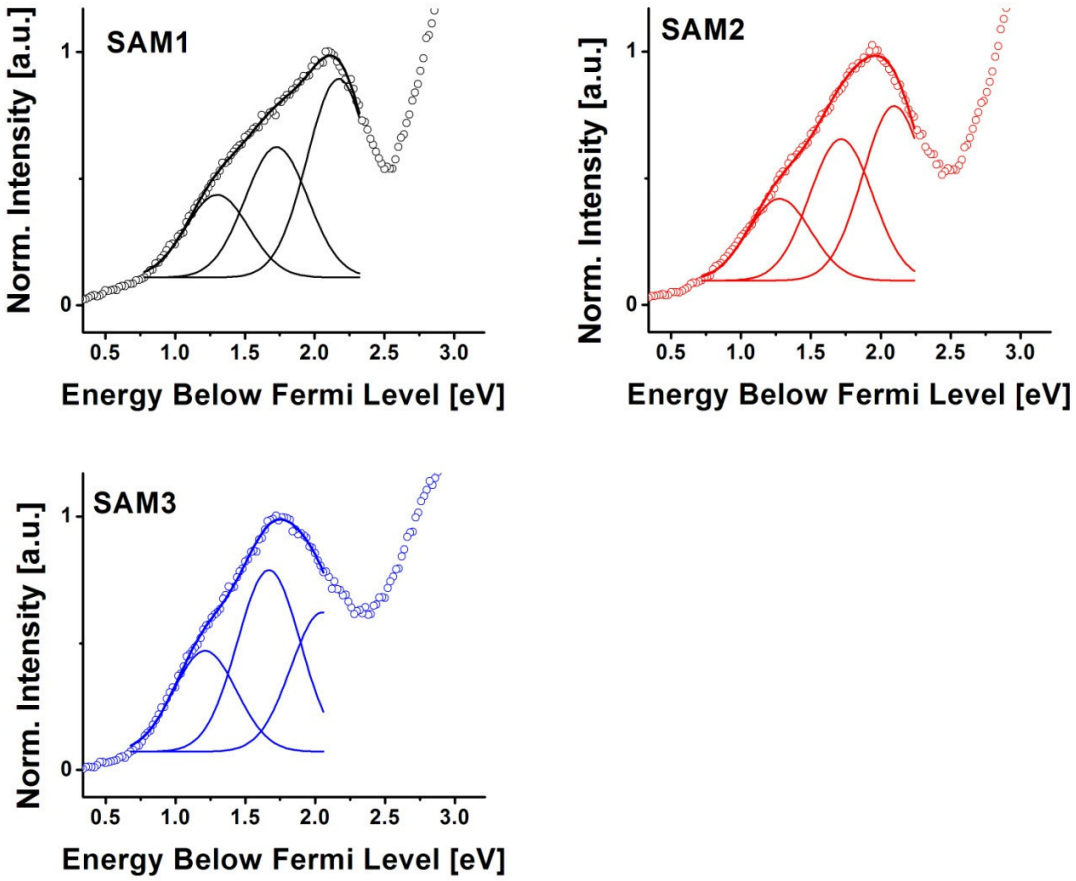

Figure 4.9. Comparison of the experimentally measured UPS spectra (open circles) for **SAM1-3** with the best fits obtained from fitting the band with a sum of three Gaussian functions (solid lines). Only the data range in which the fitted curve is drawn was used for fitting.

Table 4.1. Summary of the results obtained from the fitting of the experimentally measured asymmetric band in **SAM1-3** with a sum of three Gaussian functions with fixed FWHM of 0.45 eV. The energy at the peak of each of the three Gaussian functions with respect to Fermi level and their corresponding amplitudes are shown for all samples.[g]

Sample	1st position [eV]	1st amplitude [a.u.]	2nd position [eV]	2nd amplitude [a.u.]	3rd position [eV]	3rd amplitude [a.u.]
SAM1	1.3	0.2	1.7	0.3	2.2	0.4
SAM2	1.3	0.2	1.7	0.3	2.1	0.4
SAM3	1.2	0.2	1.7	0.4	2.0	0.3

Assuming that the three Gaussian functions obtained from the fitting procedure correspond to three different electronic states of the adsorbed molecules, it is possible to look at the influence of the different end-substituents in the constituents of **SAM1-3** on the position of the energy level closest to the Fermi level, i.e. the highest occupied molecular orbital (HOMO) of the adsorbed molecules.[6,16] Based on the fitting procedure the positions of HOMO with respect to the Fermi level in the studied monolayers, ΔE_{HOMO}(UPS), were found to be 1.3 eV, 1.3 eV, and 1.2 eV for **SAM1**, **SAM2**, and **SAM3**, respectively.

*4.3.2. Analysis of the Molecular Energy Levels in **SAM1-3***

4.3.2.1. Electrochemical Measurements

It is interesting to compare the position of the HOMO with respect to Fermi level in **SAM1-3** with the ionization potential (IP) of the corresponding adsorbate-like molecules in vacuum. From the perspective of organic electronics applications the choice of organic hole-transport material is dictated by its ionization potential, or position of

[g] While the error of the position of each Gaussian function from the fitting routine is rather small (ca. 1 %), the values given in Table 4.1 are shown with only two significant digits as additional factor are expected to contribute to the actual uncertainty for these parameters.

HOMO with respect to vacuum level, i.e., with the decrease of the IP of the material the hole-injection barrier decreases.[1,8] The SAMs studied here provide the opportunity to test whether the position of the HOMO with respect to the Fermi level, in this case this position is the same as the hole-injection barrier, of the SAM constituents correlates well with the measured gas-phase ionization potential of the corresponding adsorbate-like free molecules.

In order to estimate these ionization potentials, a series of electrochemical measurements were performed on dry dichloromethane solutions of **M1-3**. While electrochemical oxidation potentials do not exactly reflect the gas-phase ionization potentials of organic molecules, the changes in the electrochemical oxidation potential, $E_{ox}^{1/2}$, have been shown to correlate linearly with UHV-measured gas-phase ionization potentials, *IP*.[28-30] For a variety of organic molecules this correlation can be described with the following equation:[28,30]

$$E_{ox}^{1/2} = 0.9 \times IP + constant \qquad \textbf{Equation 4.1}$$

Thus, electrochemically measured oxidation potentials, and in particular the change in the electrochemical oxidation potential between different molecules, can be used as an estimate of the changes in the gas-phase IP between the molecules.

The cyclic voltammograms recorded for dichloromethane solutions of **M1-3** are shown in Figure 4.10. The oxidation potentials of the first reversible oxidation (quasi-reversible oxidation in the case of **M1**) for the three molecules were referenced to $FeCp_2^+$ / $FeCp_2$ and were found to be +0.69 V, +0.60 V, and +0.15 V for **M1**, **M2**, and **M3**, respectively. As expected, the first oxidation potential of the molecules decreased as the π-donating ability of the substituent in the 4' position of the stilbene backbone increased.

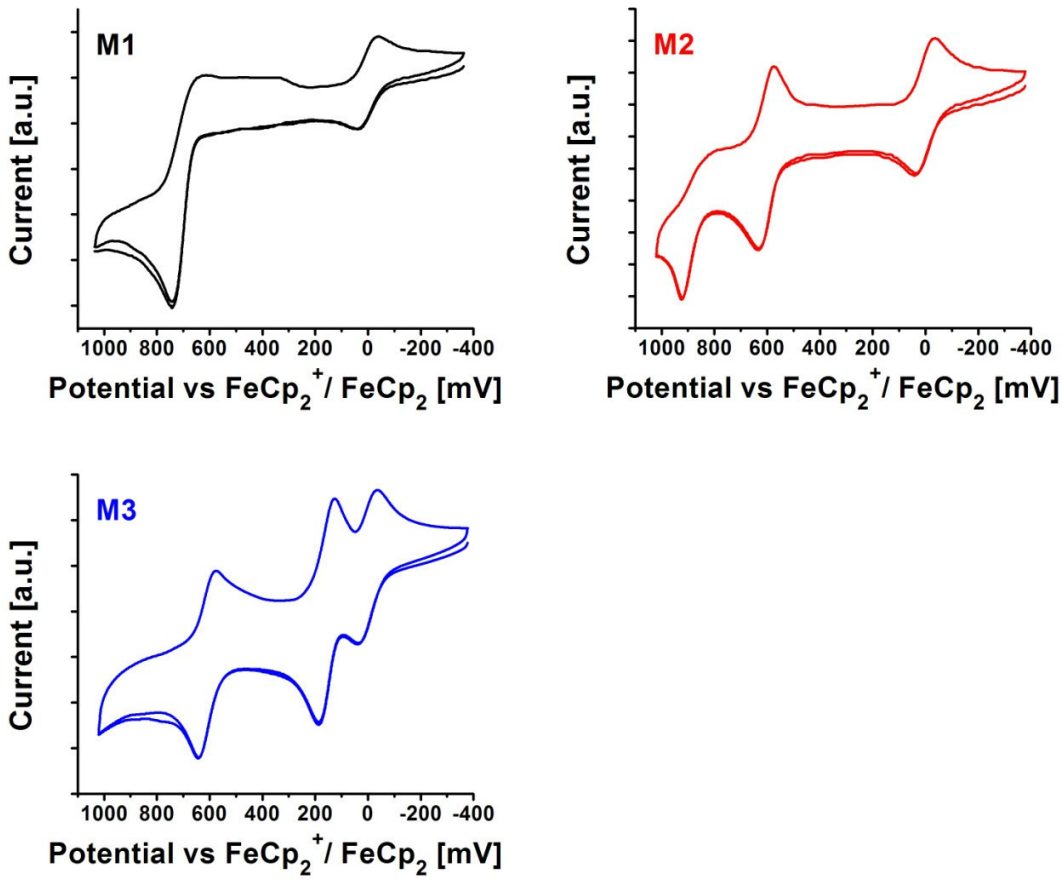

Figure 4.10. Cyclic voltammograms measured for dry dichloromethane solutions of **M1-3**. The wave corresponding to $FeCp_2^+$ / $FeCp_2$ redox process defines 0 V.

Taking into account the correlation between the electrochemical oxidation potential and the gas-phase IP (Equation 4.1), the gas-phase IPs offset from the real values by a constant were calculated to be 0.77 eV, 0.67 eV, and 0.17 eV for **M1**, **M2** and **M3**, respectively. Since the electrochemical oxidation potentials were calculated versus $FeCp_2^+$ / $FeCp_2$ as a reference, the constant by which the IP values calculated according to Equation 4.1 are offset from the actual gas-phase IPs for **M1-3** is simply the gas-phase ionization potential of ferrocene, for which the value of 6.52 eV based on He(I) UPS

measurements can be found in the literature.[31] The values of gas-phase IPs based on the CV measurements, Equation 4.1, and the gas-phase IP of ferrocene were found to be 7.29 eV, 7.19 eV, and 6.69 eV for **M1**, **M2**, and **M3**, respectively.

*4.3.2.2. Energy Diagram for **SAM1-3***

It is possible to calculate the position of the molecular HOMO with respect to the Fermi level, ΔE_{HOMO}, i.e. the hole-injection barrier in the case of SAMs, based on the gas-phase IP estimated in the previous section and the work function of the electrode, Φ_m:[1]

$\Delta E_{HOMO} = IP - \Phi_m$ **Equation 4.2**

Figure 4.11a shows a schematic diagram of the energetics of **SAM1-3** based on the gas-phase IPs of **M1-3** and the work function of clean gold (5.2 eV),[1,3,8] calculated according to Equation 4.2. Clearly in this case the changes in ΔE_{HOMO}(Au) for the three different systems simply follow the changes in the gas-phase IP of **M1-3**. However, when taking into account the changes in the work function caused by **SAM1-3** (see section 4.2 of this chapter) the differences between ΔE_{HOMO}(SAM) calculated according to Equation 4.2 for **SAM1-3** are greatly reduced, as can be seen in Figure 4.11b. In particular, this shows that the effect of the polar adsorbates on the work function of gold *suppresses the influence of the gas-phase IP difference between **M1-3** on the calculated ΔE_{HOMO}(SAM).*

The values of ΔE_{HOMO}(SAM): 3.0 eV, 3.0 eV, and 2.8 eV found from electrochemical data measured for **M1**, **M2**, and **M3**, respectively, show a rather large offset from the measured positions of HOMO with respect to the Fermi level, ΔE_{HOMO}(UPS): 1.3 eV, 1.3 eV, and 1.2 eV for **SAM1, SAM2,** and **SAM3,** respectively.

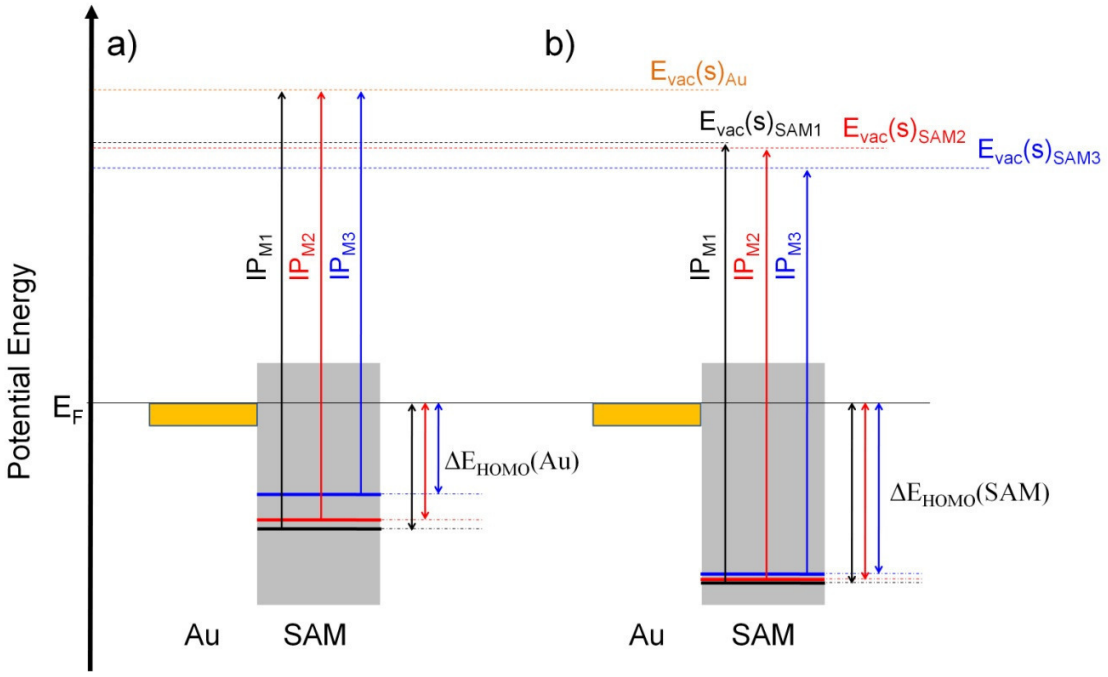

Figure 4.11. Plot of the position of HOMOs of stilbene thiolates in SAMs on gold with respect to the Fermi level calculated from Equation 4.2 for: a) a system in which the vacuum level close to the surface, $E_{vac}(s) = E_F + \Phi_m$, is governed by the work function of clean gold, $\Delta E_{HOMO}(Au)$, and b) a system in which the work function is altered by the adsorbed **SAM1-3**, $\Delta E_{HOMO}(SAM)$. The calculated gas-phase IPs for **M1-3** (vertical arrows) were used to position the HOMO of each system with respect to E_F (ΔE_{HOMO}, double-sided arrows) according to Equation 4.2.

The offset between calculated values of $\Delta E_{HOMO}(SAM)$ and the experimentally-measured values of $\Delta E_{HOMO}(UPS)$ is most likely due to the fact that the calculation of $\Delta E_{HOMO}(SAM)$ was based on gas-phase values and as such it did not take into account the depolarization effects present in the condensed phase, which the SAMs resemble. It has been demonstrated that for a variety of organic molecules the ionization potential in the gas phase is substantially higher than the corresponding IP in the solid state.[32,33] This IP difference is thought to be caused by polarization effects present in the solid with

polarization energies as high as 0.9 – 3.0 eV.[33] In particular, for a series of organic aromatic molecules it was found that the polarization energies were similar and showed the value of ca. 1.7 eV.[33] A rigid shift of ΔE_{HOMO}(SAM) by 1.7 eV to higher energy (i.e. to lower absolute values of the HOMO position with respect to the Fermi level) results in the values which are very close to the measured ΔE_{HOMO}(UPS) values (see Figure 4.12).

Figure 4.12 shows the plot of the positions of HOMO with respect to the Fermi level in **SAM1-3**, which were extracted from UPS measurements and the fitting procedure described in section 4.3.1, ΔE_{HOMO}(UPS), as a function of ΔE_{HOMO}(Au) calculated from Equation 4.2 using the work function of clean gold. As can be seen from the graph, the slope of the linear fit of the data is rather small, corresponding to a value of 0.18. This illustrates that the measured changes of ΔE_{HOMO}(UPS) for **SAM1-3** show the effect of the *suppression* (ca. 6 times) *of the influence of gas-phase IP on the position of the HOMO with respect to the Fermi level*, i.e. the hole-injection barrier, which is in qualitative agreement with Figure 4.11b. Additionally, a comparison of the positions of the HOMO with respect to the Fermi level based on UPS measurements of **SAM1-3**, ΔE_{HOMO}(UPS) (Figure 4.12), with the values of ΔE_{HOMO}(SAM) corrected for the solid-state polarization effects (i.e. shifted to higher energy by 1.7 eV) shows that the calculated values are in good agreement with the measured ones.

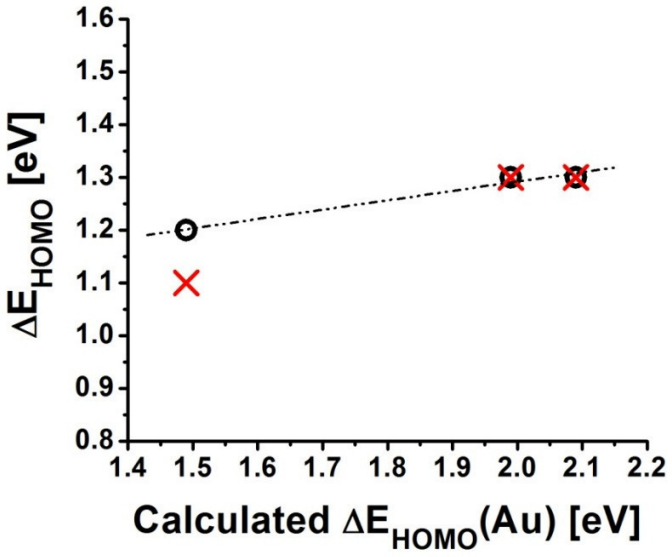

Figure 4.12. Plot of the position of (O) HOMO of **SAM1-3** with respect to the Fermi level extracted from UPS measurements, ΔE_{HOMO}(UPS), and (×) ΔE_{HOMO}(SAM) corrected for the solid-state polarization effects as a function of ΔE_{HOMO}(Au) (see Figure 4.11a). The slope of the linear fit of ΔE_{HOMO}(UPS) (dashed line) is 0.18.

4.4. Conclusions

SAMs of 4'-substituted stilbene thiolates on gold were studied in the context of their electronic properties. The studied systems showed the expected trend in the modification of the work function of the underlying metal with substituents of different π-electron-donating ability. While the qualitative dependence of the work function change on the substituents in the 4' position of the stilbene molecules could be rationalized in terms of a simple electrostatic model, the magnitude of the variation was smaller than expected by these electrostatic considerations, perhaps due to the effect of water adsorbed onto the monolayers. Nevertheless, it has been shown that the work function of gold can be lowered by as much as 1.3 eV using a conjugated thiolate

monolayer and that the degree to which it is lowered can be controlled by the substituents.[34]

The HOMOs of the series of stilbene thiolates on gold are located at approximately the same energy with respect to the Fermi level, which suggests a suppression of the effect of the changes in the gas-phase ionization potential of the corresponding adsorbate-like molecules on the position of the HOMO. It was found that the work-function changes brought about by the adsorbed stilbene thiolates caused the abovementioned suppression and that the positions of the HOMOs with respect to the Fermi level could be estimated using gas-phase IPs of the adsorbate-like molecules with rather good agreement with UPS results, when the work-function changes were taken into account and a polarization offset introduced. These findings are significant from the perspective of facilitating hole injection and / or suppressing electron injection from gold electrodes into organic charge-transport materials in organic electronics applications.

4.5. References

(1) Ishii, H.; Sugiyama, K.; Ito, E.; Seki, K. *Adv. Mater.* **1999**, *11*, 605-625.
(2) Kahn, A.; Koch, N.; Gao, W. *J. Polym. Sci., Part B: Polym. Phys.* **2003**, *41*, 2529-2548.
(3) Hölzl, J.; Schulte, F. K.; Wagner, H. *Solid surface physics*; Springer-Verlag: Berlin, 1979; Vol. 85.
(4) Bumm, L. A.; Arnold, J. J.; Cygan, M. T.; Dunbar, T. D.; Burgin, T. P.; Jones, L., II; Allara, D. L.; Tour, J. M.; Weiss, P. S. *Science* **1996**, *271*, 1705-07.
(5) Wold, D. J.; Frisbie, C. D. *J. Am. Chem. Soc.* **2001**, *123*, 5549-5556.
(6) Heimel, G.; Romaner, L.; Bredas, J.-L.; Zojer, E. *Phys. Rev. Lett.* **2006**, *96*, 196806/1-196806/4.
(7) Zehner, R. W.; Parsons, B. F.; Hsung, R. P.; Sita, L. R. *Langmuir* **1999**, *15*, 1121-1127.
(8) Chen, W.; Huang, C.; Gao, X. Y.; Wang, L.; Zhen, C. G.; Qi, D.; Chen, S.; Zhang, H. L.; Loh, K. P.; Chen, Z. K.; Wee, A. T. S. *J. Phys. Chem. B* **2006**, *110*, 26075-26080.
(9) Zangmeister, C. D.; Picraux, L. B.; van Zee, R. D.; Yao, Y.; Tour, J. M. *Chem. Phys. Lett.* **2007**, *442*, 390-393.
(10) Risko, C.; Zangmeister, C. D.; Yao, Y.; Marks, T. J.; Tour, J. M.; Ratner, M. A.; van Zee, R. D. *J. Phys. Chem. C* **2008**, *112*, 13215-13225.
(11) Campbell, I. H.; Kress, J. D.; Martin, R. L.; Smith, D. L.; Barashkov, N. N.; Ferraris, J. P. *Appl. Phys. Lett.* **1997**, *71*, 3528-3530.
(12) Alloway, D. M.; Hofmann, M.; Smith, D. L.; Gruhn, N. E.; Graham, A. L.; Colorado, R.; Wysocki, V. H.; Lee, T. R.; Lee, P. A.; Armstrong, N. R. *J. Phys. Chem. B* **2003**, *107*, 11690-11699.
(13) Cahen, D.; Kahn, A. *Adv. Mater.* **2003**, *15*, 271-277.
(14) Zangmeister, C. D.; Robey, S. W.; Van Zee, R. D.; Yao, Y.; Tour, J. M. *J. Phys. Chem. B* **2004**, *108*, 16187-16193.
(15) De Boer, B.; Hadipour, A.; Mandoc, M. M.; Van Woudenbergh, T.; Blom, P. W. M. *Adv. Mater.* **2005**, *17*, 621-625.
(16) Heimel, G.; Romaner, L.; Bredas, J.-L.; Zojer, E. *Surf. Sci.* **2006**, *600*, 4548-4562.
(17) Heimel, G.; Romaner, L.; Zojer, E.; Bredas, J.-L. *Nano Lett.* **2007**, *7*, 932-940.
(18) Heimel, G.; Romaner, L.; Zojer, E.; Bredas, J.-L. *Acc. Chem. Res.* **2008**, *41*, 721-729.
(19) Romaner, L.; Heimel, G.; Zojer, E. *Phys. Rev. B: Condens. Matter* **2008**, *77*, 045113-9.
(20) Romaner, L.; Heimel, G.; Ambrosch-Draxl, C.; Zojer, E. *Adv. Funct. Mater.* **2008**, *18*, 3999-4006.
(21) Evans, S. D.; Ulman, A. *Chem. Phys. Lett.* **1990**, *170*, 462-466.
(22) Love, J. C.; Estroff, L. A.; Kriebel, J. K.; Nuzzo, R. G.; Whitesides, G. M. *Chem. Rev.* **2005**, *105*, 1103-1170.
(23) Zubavichus, Y.; Zharnikov, M.; Yang, Y.; Fuchs, O.; Umbach, E.; Heske, C.; Ulman, A.; Grunze, M. *Langmuir* **2004**, *20*, 11022-11029.

(24) *CRC Handbook of Chemistry and Physics*; 63 ed.; Weast, R. C., Ed.; CRC Press: Boca Raton, Florida, 1982.
(25) Laibinis, P. E.; Bain, C. D.; Whitesides, G. M. *J. Phys. Chem.* **1991**, *95*, 7017-7021.
(26) Zahn, D. R. T.; Gavrila, G. N.; Gorgoi, M. *Chem. Phys.* **2006**, *325*, 99-112.
(27) Zahn, D. R. T.; Gavrila, G. N.; Salvan, G. *Chem. Rev.* **2007**, *107*, 1161-1232.
(28) Yanilkin, V.; Zverev, V. *Russ. Chem. Bull.* **1999**, *48*, 677-685.
(29) Mochida, K.; Itani, A.; Yokoyama, M.; Tsuchiya, T.; Worley, S. D.; Kochi, J. K. *Bull. Chem. Soc. Jpn.* **1985**, *58*, 2149-50.
(30) Miller, L. L.; Nordblom, G. D.; Mayeda, E. A. *J. Org. Chem.* **1972**, *37*, 916-918.
(31) Matsumura-Inoue, T.; Kuroda, K.; Umezawa, Y.; Achiba, Y. *J. Chem. Soc., Faraday Trans. 2* **1989**, *85*, 857-66.
(32) Nayak, P. K.; Periasamy, N. *Org. Electron.* **2009**, *10*, 532-535.
(33) Sato, N.; Seki, K.; Inokuchi, H. *J. Chem. Soc., Faraday Trans. 2* **1981**, *77*, 1621-33.
(34) Malicki, M.; Guan, Z.; Ha, S. D.; Heimel, G.; Barlow, S.; Rumi, M.; Kahn, A.; Marder, S. R. *Langmuir* **2009**, *25*, 7967-7975.

CHAPTER 5

PREPARATION AND CHARACTERIZATION OF BIS(DIARYLAMINO)BIPHENYL-FUNCTIONALIZED GOLD NANOPARTICLES

5.1. Introduction

Gold nanoparticles (Au NPs) have received considerable attention in the recent years. Due to their size many physical properties of Au NPs differ significantly from the properties of bulk gold, with optical properties being of major interest.[1,2] Owing to the development of synthetic methodology it has become possible to prepare Au NPs that can be dissolved in organic solvents and can be manipulated with standard organic chemistry techniques.[3-6] This has opened the possibility to study the influence of synthetically-accessible organic ligands on the physical properties of Au NPs, and vice versa.[1] Examples of interesting electrochemical,[7-9] and optical[10-12] properties of organic ligand-coated Au NPs have been reported and potential applications of the hybrid organic-metal systems have been identified.[1]

The systems studied here are shown in Figure 5.1. The choice of the organic fluorophore – bis(diarylamino)biphenyl (TPD) – was dictated by considerations discussed in Chapter 1, section 1.2.6. Briefly, TPD exhibits a sizeable two-photon absorption in the spectral region in which Au NPs generate local field enhancements,[13] thus, in principle, placing TPD moiety in close proximity of the nanoparticle may result in enhancement of two-photon cross section due to the local field effects.[10]

Understanding of the basic photophysics of the hybrid organic – metal system, which is addressed in this study, is crucial for future studies of its nonlinear optical properties. Additionally, the rather low oxidation potential of TPD,[14] which may facilitate an electron transfer from the photoexcited TPD to the nanoparticle, and its sizeable fluorescence quantum yield,[15] make this dye a good model compound to study the possible effects of energy and electron transfer from the photoexcited dye to a nanoparticle.

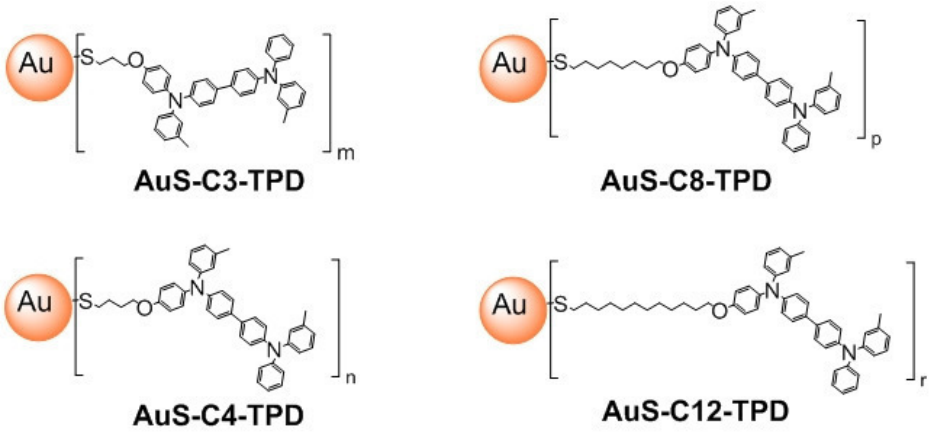

Figure 5.1. Schematic representation of the systems whose studies are described in this chapter.

This chapter describes the preparation of the hybrid organic – metal systems as well as the chemical characterization of the obtained TPD-coated Au NPs.

5.2. Synthesis of Organic Ligands and Preparation of Gold Nanoparticles

5.2.1. Synthesis of TPD-thiol molecules

Figure 5.2 shows a scheme of the preparation of **TPD-C3-thiol**, the key precursor to **AuS-C3-TPD**. Pd-catalyzed coupling of (*tert*-butyl)dimethylsilane-protected alcohol **1** and *m*-toluidine yielded the desired secondary amine **2**. The amine was then reacted with 4'-bromo-*N*-phenyl-*N*-*m*-tolylbiphenyl-4-amine (**3**), which was prepared via Ullmann coupling of 4-iodo-4'-bromobiphenyl and 3-methyl-*N*-phenylaniline, to yield the substituted bis(diarylamino)biphenyl **4**. The deprotection of **4** to the corresponding alcohol and further bromination yielded **TPD-C3-bromide** which was converted to the target **TPD-C3-thiol** via a reaction with thiourea and subsequent hydrolysis of the generated thiouronium salt. The preparations of **TPD-C4-thiol**, **TPD-C8-thiol**, **TPD-C12-thiol**, and the model compound **TPD-C12** were performed according to Figure 5.3. In this case the (*tert*-butyl)diphenylsilane-protected TPD-phenol **9**, which was prepared by Ms. LaKeisha McClary, was deprotected *in situ* and the resulting phenolate was reacted with an excess of an alkyl dibromide of choice (4, 8, and 12 methylene units in the chain) to yield the corresponding **TPD-Cx-bromide** (x = 4, 8, and 12). Each bromide was then reacted with thiourea and the corresponding thiouronium salts were hydrolyzed to yield **TPD-Cx-thiols** (x = 4, 8, and 12). **TPD-C12** was prepared by reacting the *in-situ* deprotected TPD-phenol **9** with 1-bromododecane. The yields of the reactions were generally good, in the range of 38 – 94%; the synthetic details and full characterization of the new compounds can be found in Chapter 2, section 2.1.2.

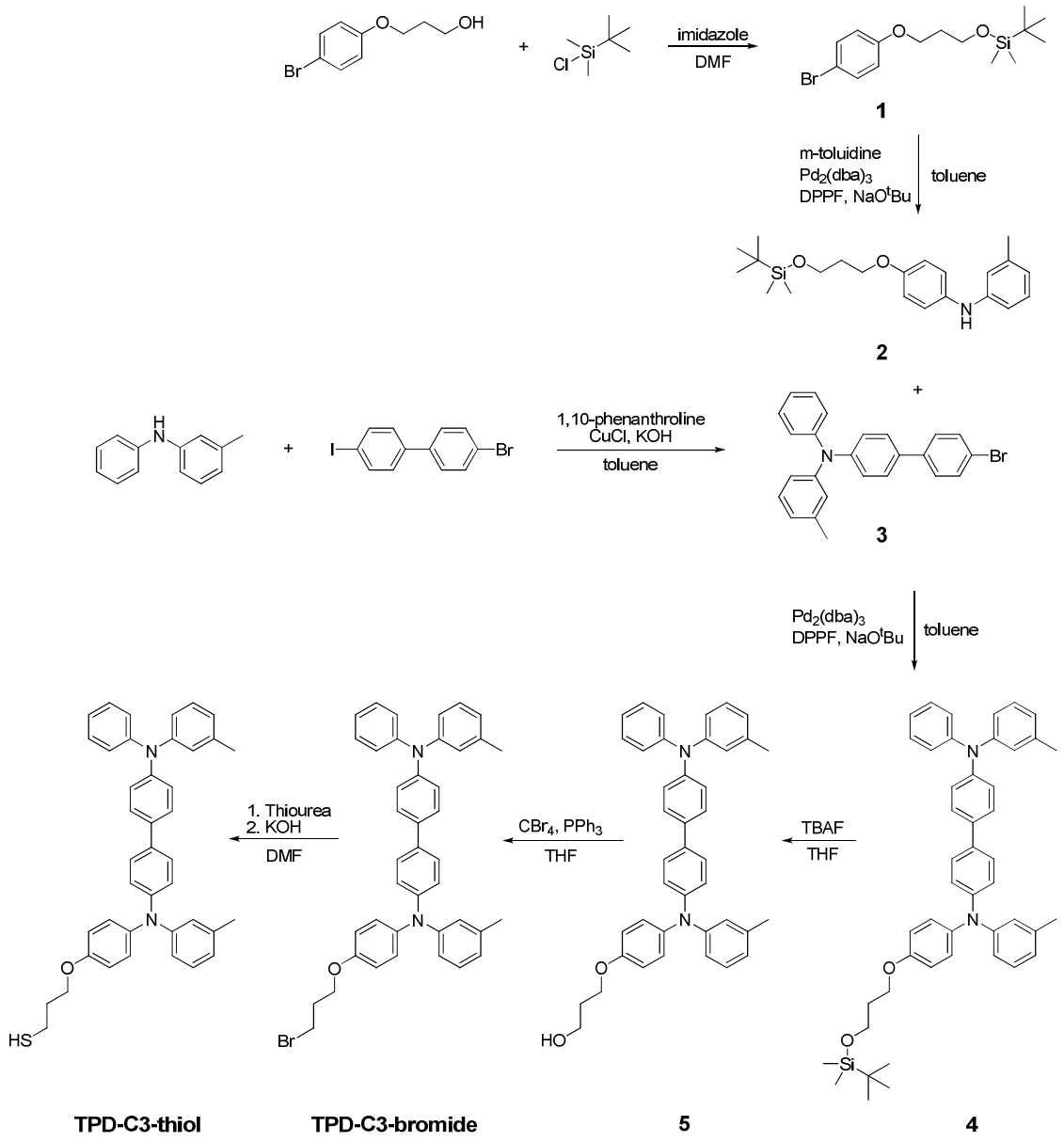

Figure 5.2. Synthesis of **TPD-C3-thiol**.

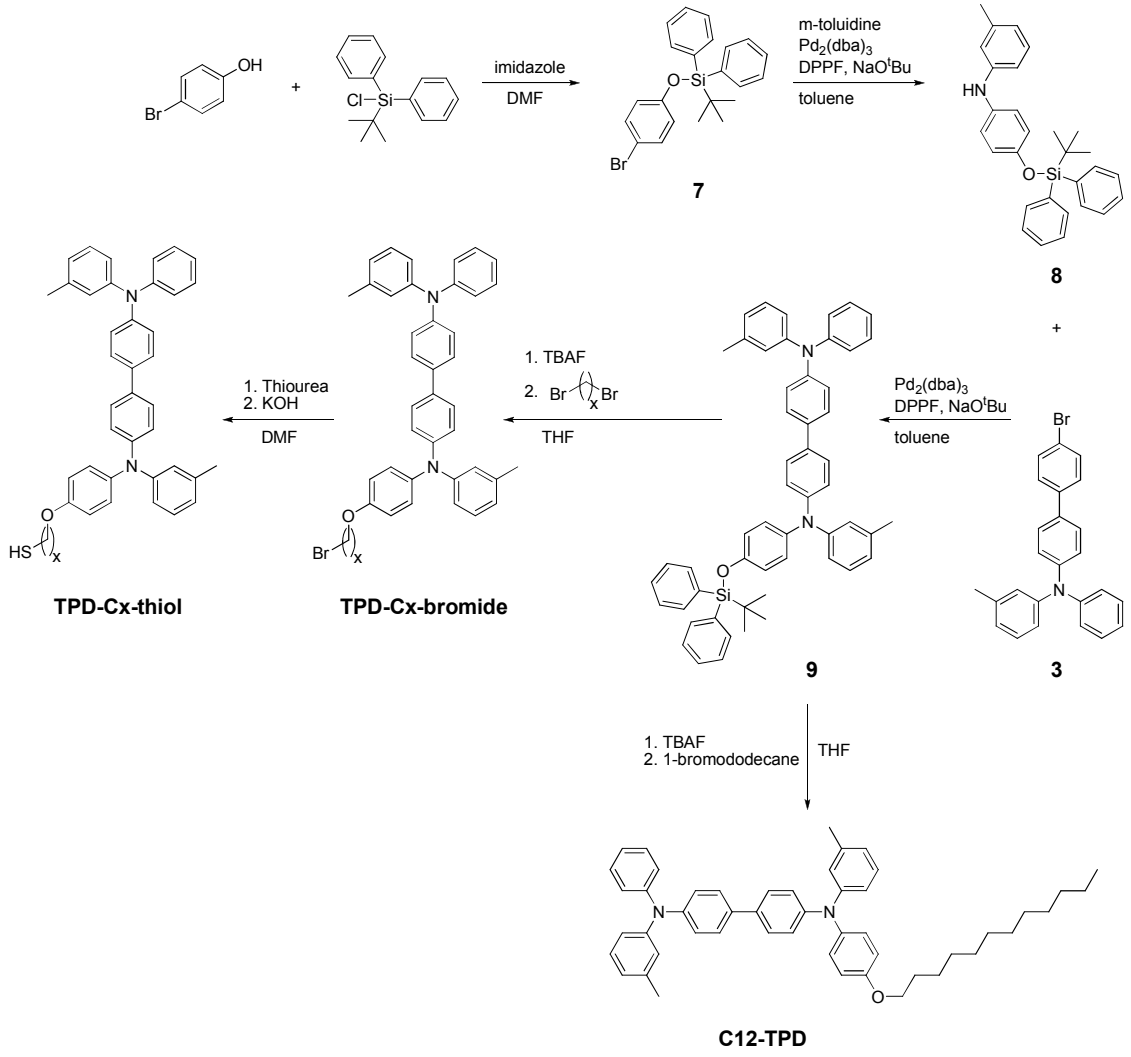

Figure 5.3. Synthesis of **TPD-C4-thiol** (x = 4), **TPD-C8-thiol** (x = 8), **TPD-C12-thiol** (x = 12), and **C12-TPD**.

5.2.2. Preparation of Gold Nanoparticles

Due to multistep syntheses of the TPD-thiols, the method of preparation of TPD-coated Au NPs had to meet the condition of high yield with respect to the TPD-thiol. The standard synthesis of thiol-coated Au NPs, the so-called Brust synthesis,[3] does not fulfill the requirement as it requires a rather large amount of the thiol ligand to be used during the synthesis; the amounts of dodecanethiol used in a typical synthesis are close to 1

equivalent with respect to the gold precursor.[5] In a report on the preparation of Au NPs stabilized with primary amines Leff *et al.* showed that primary amines are labile ligands, i.e., they can be readily displaced from the surface of Au NPs by thiols.[4] This approach was adapted for the preparation of Au NPs in this work as it allows one to use moderate amounts of thiol ligands. Figure 5.4 shows a scheme for the synthesis of oleylamine-coated Au NPs and the subsequent synthetic step in which the amine is displaced by TPD-thiol.

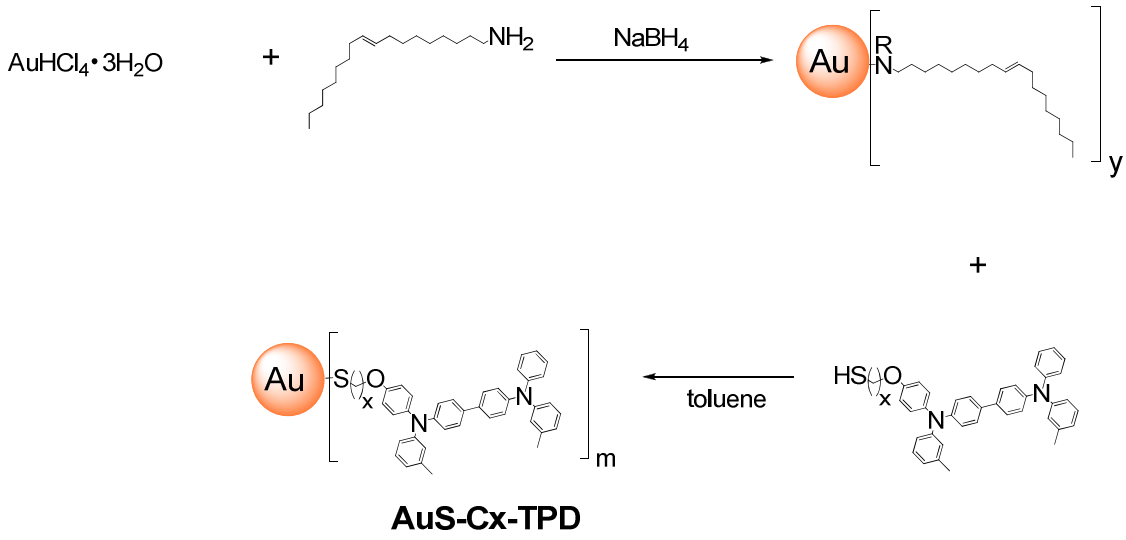

Figure 5.4. Synthesis of gold nanoparticles coated with **TPD-Cx-thiols** (x= 3, 4, 8, 12).

The obtained thiol-coated nanoparticles were stable and could be precipitated and redissolved multiple times without loss of solubility in common organic solvents, such as toluene and chloroform. The purification procedure included precipitation of the particles from toluene solutions by addition of methanol and further washing of the solid with toluene / methanol (1:1) mixture to remove unbound TPD-thiol molecules. This procedure gave nanoparticles that showed minimal blue fluorescence upon UV

irradiation, indicating that the majority of the unbound fluorescent TPD ligands were successfully removed.

Additionally, samples containing a mixture of thiol ligands – **TPD-Cx-thiol** (x = 3, 4, 8, 12) and dodecanethiol (DDT) – were prepared by reacting the OA-coated Au NPs with a mixture of **TPD-Cx-thiol** (x = 3, 4, 8, 12) and dodecanethiol with different percentages of dodecanethiol in the mixture (ca. 60% and 90% of DDT in the reaction mixtures were used). The preparation of the mixed-ligand Au NPs is illustrated in Figure 5.5.

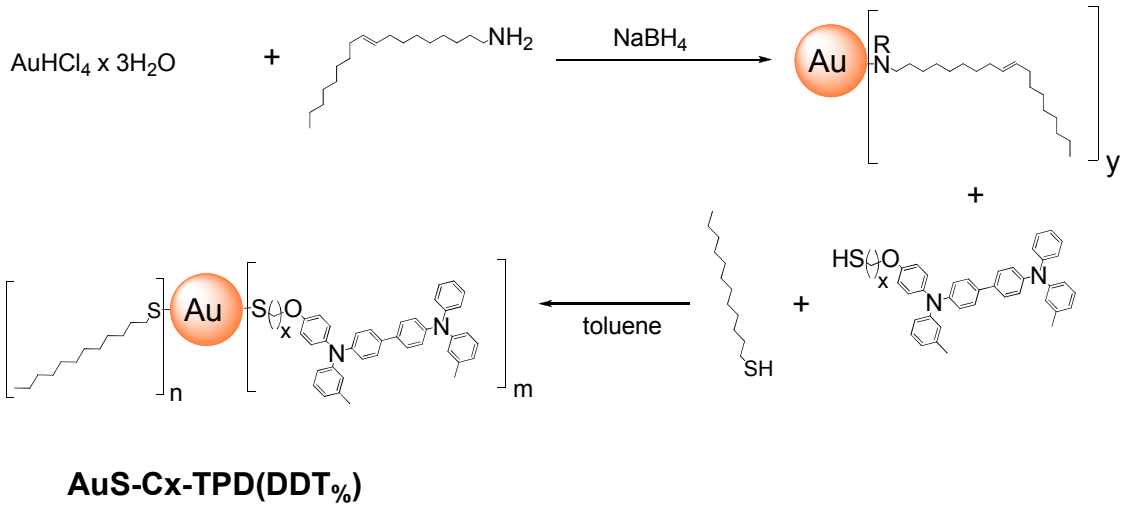

AuS-Cx-TPD(DDT%)

Figure 5.5. Synthesis of gold nanoparticles coated with a mixture of dodecanethiol and **TPD-Cx-thiols** (x = 3, 4, 8, 12). The relative amounts of **TPD-Cx-thiol** (x = 3, 4, 8, 12) and DDT relative to each other were varied.

The particles prepared in the manner described above were purified in a fashion similar to the purification procedure followed in the case of particles prepared with **TPD-Cx-thiols** (x = 3, 4, 8, 12) only. The naming of the samples – **AuS-Cx-TPD(DDT%)** (x = 3, 4, 8, 12) – reflects the composition of the organic ligands in the reaction mixture, i.e.

TPD-Cx-thiol and a molar percentage of DDT in the two-component mixture (e.g. the reaction mixture used for the preparation of **AuS-C3-TPD(DDT$_{60}$)** contained 60% of DDT and 40% of **TPD-C3-thiol**). A sample of Au NPs coated exclusively with DDT was also prepared (**AuS-C12**).

5.3. Characterization of Gold Nanoparticles Coated with TPD-Thiol Ligands

5.3.1. Transmission Electron Microscopy

TEM is a standard tool for characterization of Au NPs as it allows one to determine the shape and size distribution of the particles.[1,5] Figure 5.6 shows an example of TEM micrographs acquired for **AuS-C3-TPD**.

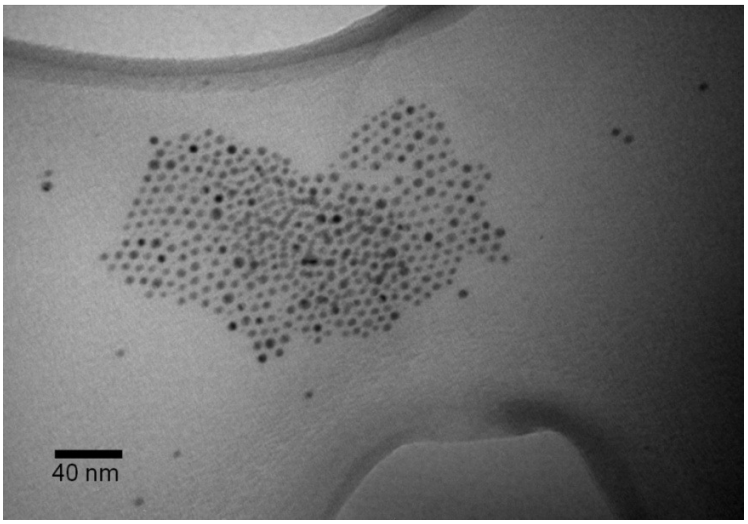

Figure 5.6. TEM micrograph of **Au-S-C3-TPD**.

Analysis of the micrographs recorded for all of the samples revealed that the majority of the particles were spherical, or nearly spherical, and allowed the distributions

of diameters of the nanoparticles to be determined. The histograms of diameters of the prepared nanoparticles as well as their average diameters with the corresponding standard deviations are shown in Figure 5.7. As can be seen from the figure the distributions of sizes were rather similar for all of the analyzed samples and the standard deviations from the average particle diameters were around 30% for most of the samples. These data show that the employed synthetic procedure generated nanoparticles that were characterized by rather similar size distributions, independently of the specific **TPD-Cx-thiol** used in the synthesis.

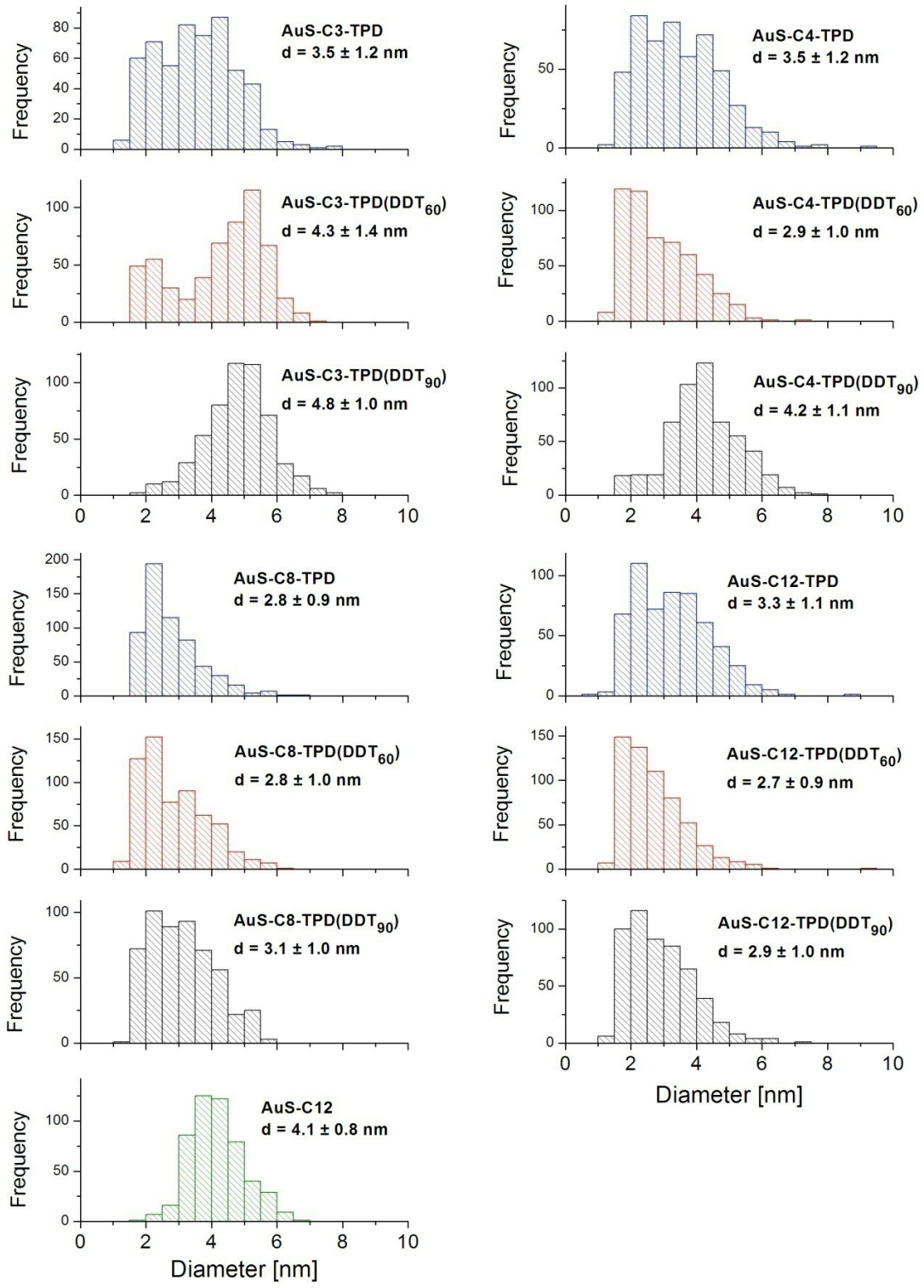

Figure 5.7. Histograms of diameters of Au NPs studied herein. Average diameters (**d**) and their standard deviations are shown .

5.3.2. FT-IR Spectroscopy

Infrared spectroscopy of Au NPs is routinely used in order to establish the composition and, to some extent, the structure of the organic ligand shell.[3,16-18] Figure 5.8 shows FT-IR spectra of neat films of TPD-coated Au NPs as well as the spectrum of a neat film of the model compound **TPD-C12**.

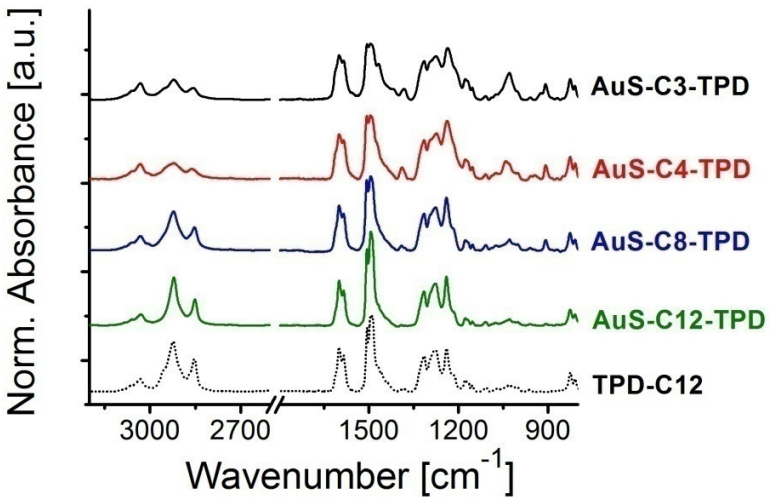

Figure 5.8. FT-IR spectra of neat films of **AuS-Cx-TPD** systems (x= 3, 4, 8, 12) and of **TPD-C12**. The spectra were normalized at 1600 cm^{-1} and displaced vertically for clarity.

The spectra of the NP samples shown in Figure 5.8 exhibit signals of the IR modes that are present in **TPD-C12**, thus confirming the presence of the TPD moiety on the surface of Au NPs. Additionally, the comparison of the signal intensity in the C-H stretching spectral region reveals that the while the intensity of the aromatic C-H stretching modes (above 3000 cm^{-1}) is approximately the same for all of the normalized spectra, the intensity of the signals originating from the C-H stretching modes in alkyl

groups (below 3000 cm^{-1}) increases from the smallest for **AuS-C3-TPD** to the largest for **AuS-C12-TPD**. This is consistent with the different lengths of the alkyl linkers between the thiol group and the TPD moiety in the studied systems.

The frequencies of the signals originating from C-H stretching modes have been often used to establish the degree of order in aliphatic chains.[18-23] In particular, it has been shown that it is possible to qualitatively establish the extent of order, i.e. the extent of the all-*trans* conformation, of aliphatic chains in SAMs on gold and in ligand-coated Au NPs.[18,19,22,23] According to a report on FT-IR studies of Au NPs coated with alkanethiol ligands of varying lengths, an all-*trans* conformation of the alkyl chains was found in NPs coated with alkanethiols containing six or more methylene groups in the chain and the position of the band of the C-H stretching symmetric mode in those systems was found at 2850 cm^{-1}.[18] In NP systems incorporating shorter alkanethiols there are generally substantial amounts of gauche defects which manifest themselves with the shift of the C-H stretching symmetric mode signal to higher energy.[18] Figure 5.9 shows the FT-IR spectra measured for neat films of **AuS-Cx-TPD** systems (x= 3, 4, 8, 12) in the spectral region of C-H stretching modes. Additionally, a spectrum of Au NPs coated with dodecanethiol (**AuS-C12**) is shown for comparison. As can be seen from the figure, the frequency of the signal of the C-H stretching symmetric mode in **AuS-C12** is 2850 cm^{-1}, consistent with all-*trans* conformation of the dodecanethiol chains in this system. A similar situation is observed in **AuS-C12-TPD**, suggesting that in this system the alkyl linkers between the thiol group and the TPD moieties are fully extended, i.e. their conformation is dominated by the all-*trans* form.[18,19] **AuS-C8-TPD** shows the signal of the symmetric C-H stretching mode at 2852 cm^{-1} suggesting still a fairly large proportion

of the all-trans conformations of the alkyl linkers.[18,19] However, in the case of **AuS-C4-TPD** and **AuS-C3-TPD** the signal of the symmetric C-H stretching mode is shifted to 2860 cm^{-1} and 2858 cm^{-1}, respectively. This indicates that the NP systems with the short alkyl linkers between the thiol group and the TPD moiety contain a substantial number of gauche defects present in the alkyl linkers. The alkyl-chain-length dependence of the extent of gauche defects, i.e. the extent of disorder, in the chains is consistent with the dependence observed by Hostetler et al. for simple alkanethiol ligands on Au NPs where, as mentioned above, alkyl chains with more than six methylene units showed negligible number of gauche defects.[18]

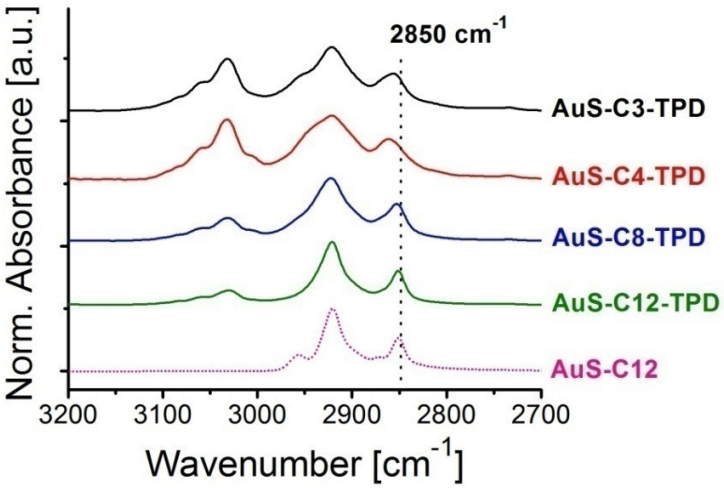

Figure 5.9. FT-IR spectra of neat films of **AuS-Cx-TPD** (x= 3, 4, 8, 12) systems and of **AuS-C12** in the spectral region of C-H stretching mode. The spectra were normalized at 2920 cm^{-1} and displaced vertically for clarity.

A comparison of Au NPs coated with different mixtures of TPD-thiols and dodecanethiol with the NPs coated exclusively with TPD-thiols is presented in Figure

5.10. It is clear from the graphs that the signal in the spectral region of alkyl of C-H stretching modes (2800 - 3000 cm^{-1}) in normalized spectra of the samples prepared in the presence of mixtures of **TPD-Cx-thiol** (x = 3, 4, 8, 12) and DDT is significantly higher than that seen for the NPs prepared with **TPD-Cx-thiols** (x = 3, 4, 8, 12) only. This supports the presence of mixed ligands on the surface of Au NPs that were prepared in the presence of mixtures of thiols.

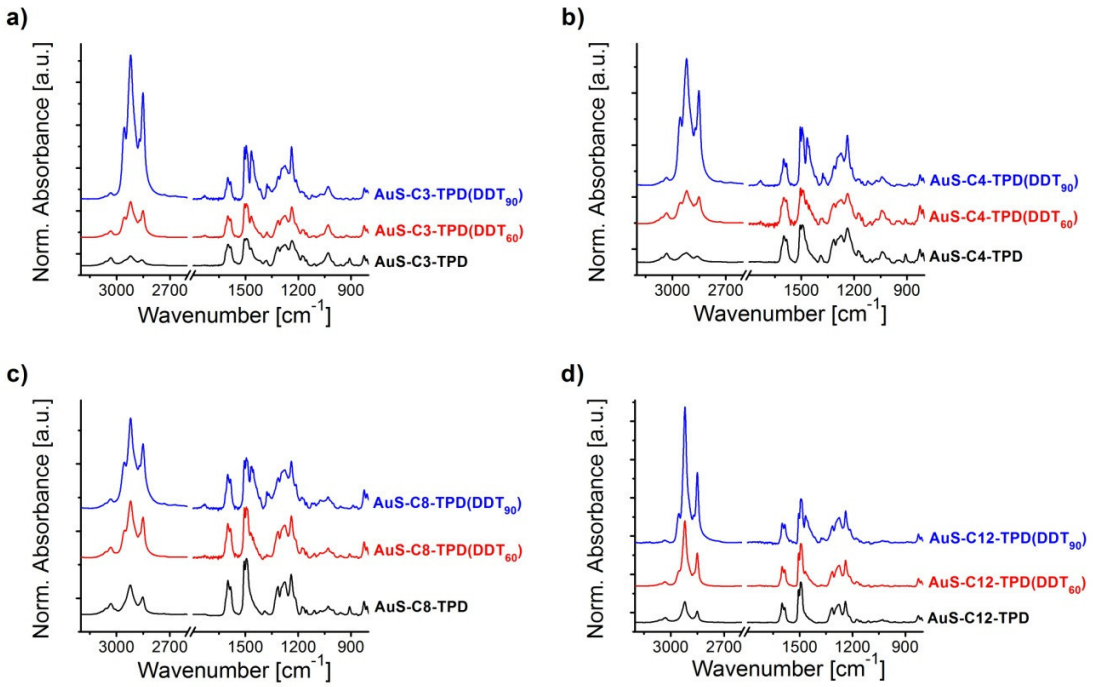

Figure 5.10. FT-IR spectra of neat films of Au NP samples coated with different mixtures of a) **TPD-C3-thiol** and dodecanethiol, b) **TPD-C4-thiol** and dodecanethiol, c) **TPD-C8-thiol** and dodecanethiol, and d) **TPD-C12-thiol** and dodecanethiol. All spectra were normalized at 1600 cm^{-1} and displaced vertically for clarity.

5.3.3. UV-Vis absorption spectroscopy

Figure 5.11 shows UV-Vis absorption spectra of toluene solutions of **AuS-Cx-TPD** systems (x = 3, 4, 8, 12) and **AuS-C12**. All spectra show the presence of the surface plasmon resonance (SPR) band around 520 nm, which is characteristic of Au NPs.[1,5,24] Additionally, it is clear that only NPs coated with **TPD-Cx-thiols** (x = 3, 4, 8, 12) show the absorption characteristic of the TPD moiety, i.e. the band around 350 nm. This further confirms the attachment of TPD moieties to Au NP surface in **AuS-Cx-TPD** systems (x = 3, 4, 8, 12).

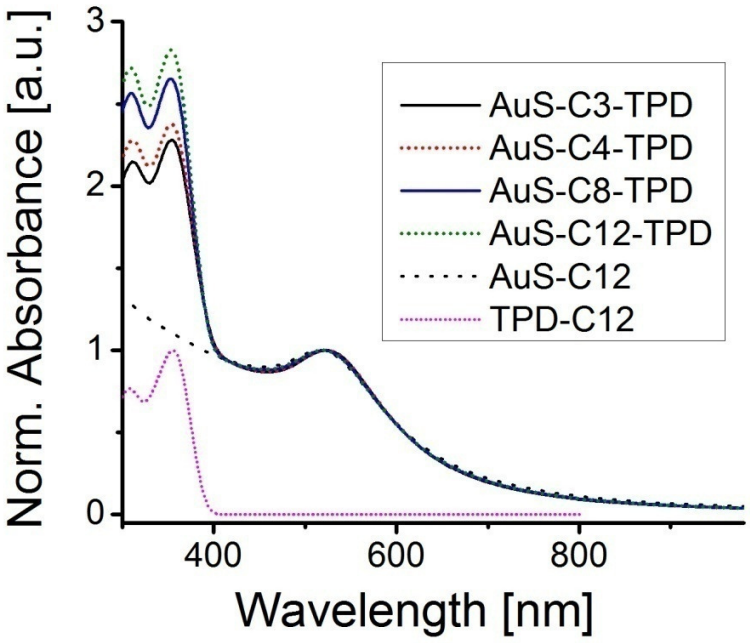

Figure 5.11. UV-Vis absorption spectra of toluene solutions of **AuS-Cx-TPD** (x = 3, 4, 8, 12), **AuS-C12**, and **TPD-C12**. Each spectrum of NPs was normalized at the maximum of the surface plasmon resonance band and the spectrum of **TPD-C12** was normalized at 353 nm.

An interesting trend can be observed in the position of the SPR band in the TPD-coated NP samples. As can be seen in Figure 5.12 the position of the maximum of the SPR band is most red-shifted in the case of **AuS-C3-TPD** and it becomes gradually less red-shifted as the alkyl chain between the thiol group and the TPD moiety becomes longer.

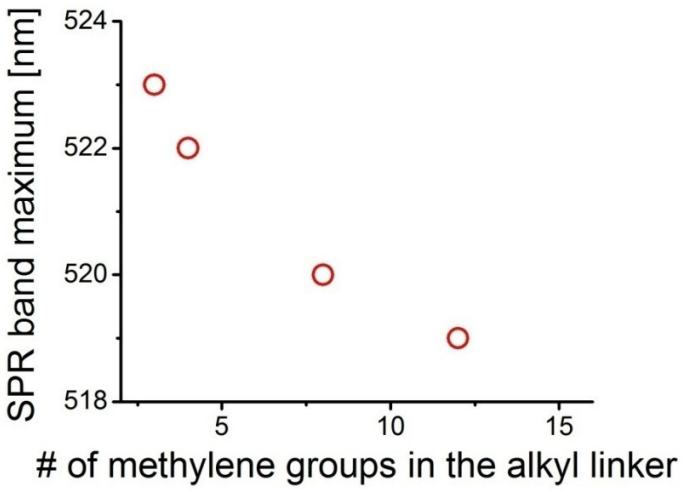

Figure 5.12. Position of the SPR band maximum as a function of the alkyl linker length in **AuS-Cx-TPD** (x = 2, 4, 8, 12)

This effect can be rationalized in terms of the effective dielectric constant around the nanoparticle.[25,26] The ligand shell around the NP surface contains the polarizable TPD moiety at a distance that should be largely dictated by the length of the alkyl linker between the thiol group and the TPD moiety. The dielectric function of the TPD-moiety shell, due to the TPD moiety's absorption with the onset at ca. 400 nm (see Figure 5.11), is most likely higher than that of toluene – the solvent, with its absorption onset around

280 nm – in the UV-Vis spectral region.[a] Thus, qualitatively, according to a model describing the SPR in Au NPs coated with a dielectric shell,[26,27] the decrease of the distance of the polarizable TPD moiety from the NP surface results in the red shift of the SPR band. In other words, the effective dielectric constant around the nanoparticle becomes larger as the TPD moiety is placed closer to the NP surface, which causes the SPR band to shift towards longer wavelengths.[25] The observed behavior is consistent with the expected variation in the TPD-Au NP distance with chain length.

UV-Vis absorption spectroscopy can be employed to estimate the TPD-moiety content in NPs coated with mixtures of thiols relative to that in NPs coated with **TPD-Cx-thiols** (x = 3, 4, 8, 12) only. Figure 5.13 shows normalized spectra of the NP systems studied herein. It can be seen, as expected, that the intensity of the signal originating from the TPD moiety (the band around 350 nm) is smaller for the samples prepared with the mixtures of thiols. Assuming the molar extinction coefficient of the TPD moiety is the same in both high TPD coverage and mixed monolayer systems, the values of absorbance due to the TPD moiety (band around 350 nm) can be used to estimate the fraction of TPD ligands present in the mixed monolayer systems (after subtraction of the contribution from the metal core). Figure 5.14 presents the residual optical density spectra after subtracting the normalized spectrum of **AuS-C12** from the normalized spectra of TPD-thiol containing NPs.

[a] This is based on the classical theory of electromagnetism. In particular, the Lorenz model of optical properties of materials gives the dependence of the real part of the dielectric function on the position of an absorption band. A detailed description can be found in Chapter 9 of ref. 27.

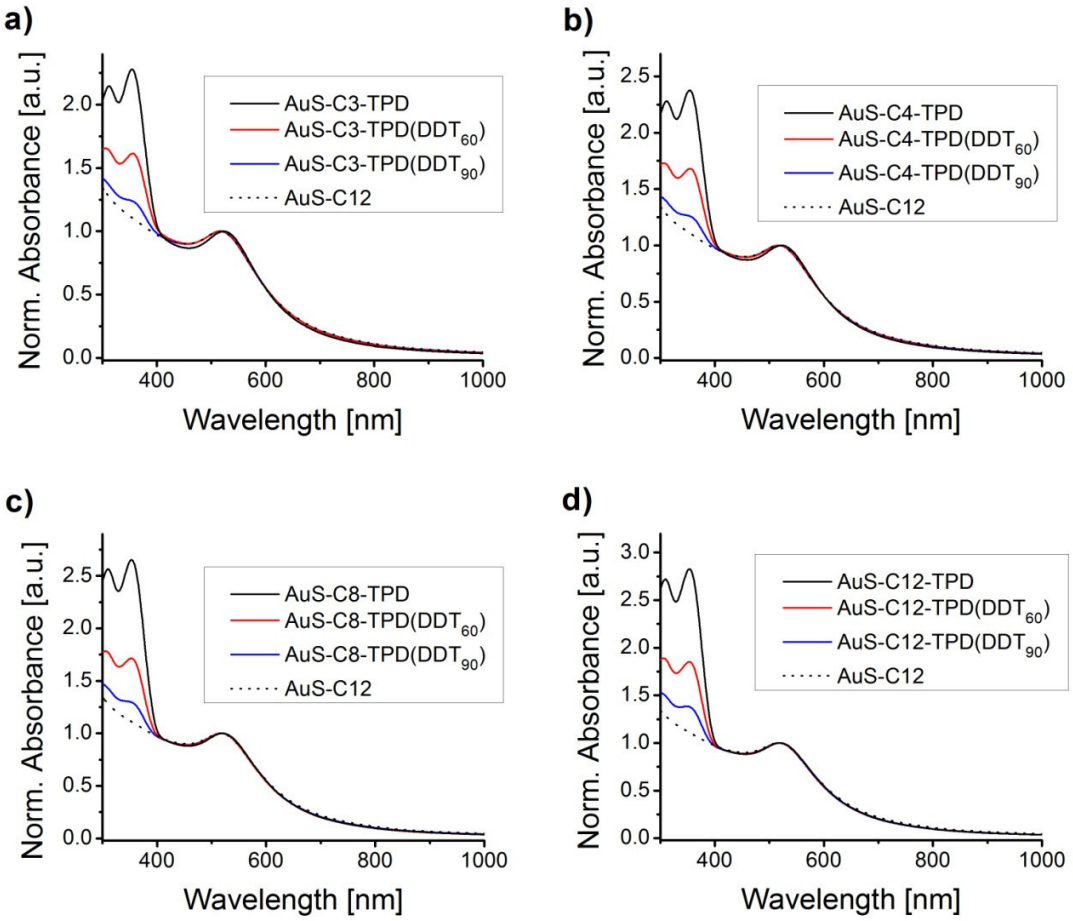

Figure 5.13. Comparison of UV-Vis absorption spectra of toluene solutions of **AuS-C12** with NP systems incorporating a) **TPD-C3-thiol**, b) **TPD-C4-thiol**, c) **TPD-C8-thiol**, and d) **TPD-C12-thiol** studied herein. Each spectrum was normalized at the maximum of the surface plasmon resonance band.

A comparison of the residual optical density at the maximum of the absorption band of the TPD moiety (355 nm) for NP samples, which were prepared with different relative amounts of the two-component mixtures of **TPD-Cx-thiol** (x = 3, 4, 8, 12) and DDT, allowed to calculate the amounts of TPD moiety in the mixed-ligand systems relative to the high TPD coverage sample within each series. This is summarized in Table 5.1.

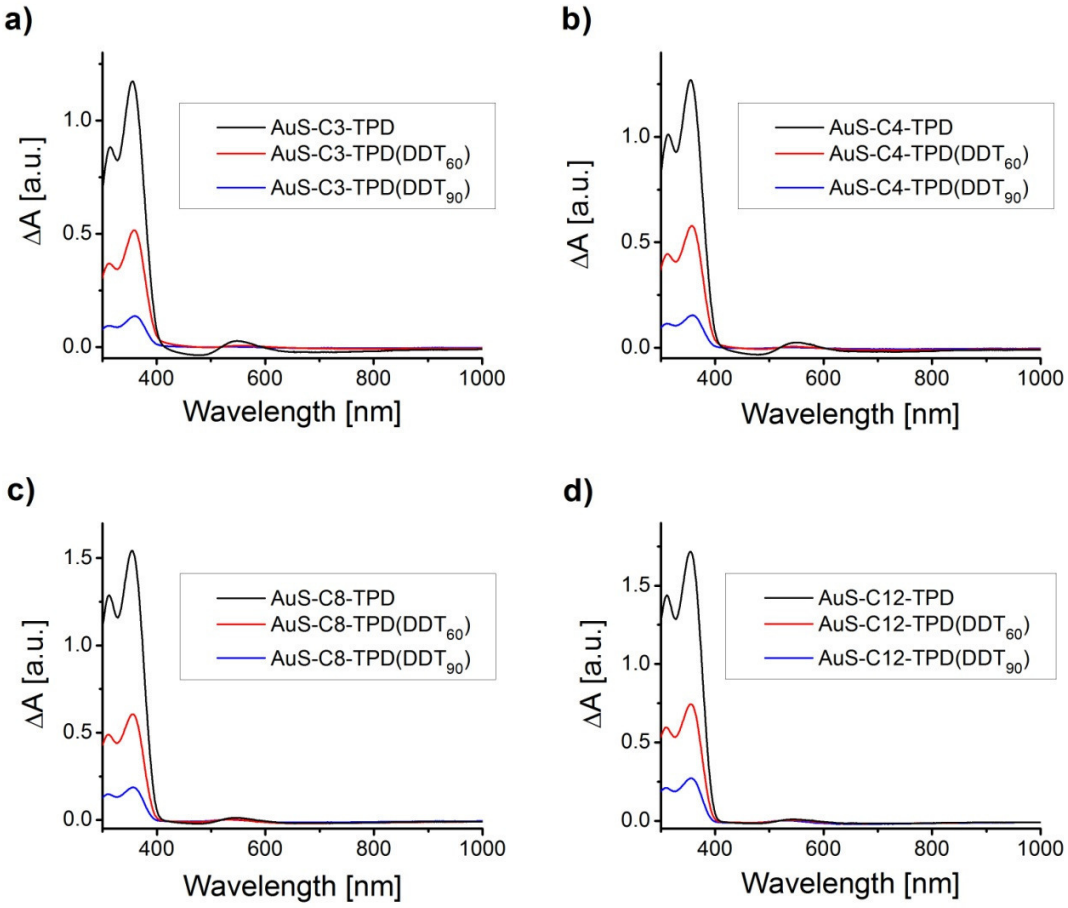

Figure 5.14. Spectra of residual optical density (ΔA) after subtracting a normalized UV-Vis absorption spectrum of toluene solution of **AuS-C12** from normalized spectra of NP systems incorporating a) **TPD-C3-thiol**, b) **TPD-C4-thiol**, c) **TPD-C8-thiol**, and d) **TPD-C12-thiol**.

Table 5.1. Comparison of the percentages of **TPD-Cx-thiols** (x = 3, 4, 8, 12) in the mixtures of two thiols used in the preparation of the Au NPs with the percentages of TPD moieties calculated from the UV-Vis analysis.

Sample	% **TPD-Cx-thiol** in NP synthesis*	% TPD moiety from UV-Vis analysis**
AuS-C3-TPD	100	100
AuS-C3-TPD(DDT_{60})	37	44
AuS-C3-TPD(DDT_{90})	12	12
AuS-C4-TPD	100	100
AuS-C4-TPD(DDT_{60})	40	46
AuS-C4-TPD(DDT_{90})	12	12
AuS-C8-TPD	100	100
AuS-C8-TPD(DDT_{60})	37	39
AuS-C8-TPD(DDT_{90})	13	12
AuS-C12-TPD	100	100
AuS-C12-TPD(DDT_{60})	38	43
AuS-C12-TPD(DDT_{90})	12	16

* The percentage of **TPD-Cx-thiol** used in the synthesis is based on the amount of the **TPD-Cx-thiol** in the mixture of two thiols
** The percentage of TPD moieties in the high TPD coverage samples was defined as 100%

Interestingly, according to the UV-Vis data in Table 5.1 the percentage of **TPD-Cx-thiol** (x = 3, 4, 8, 12) in the mixture of thiols used in the synthesis of Au NPs resulted in particles containing very similar percentages of TPD moieties. This finding is quite significant as it clearly shows that the synthetic method used in this work allows one to predict the composition of mixed-ligand NP systems based on the composition of the reaction mixture in the synthetic step involving the reaction with thiol ligands. For comparison, a typical procedure for a preparation of mixed-ligand Au NPs based on the Brust synthesis protocol is followed by a ligand-exchange reaction which, often, requires

the use of an excess of the ligands of interest during the synthesis in order to achieve a desired ligand composition in the NP samples.[28-30]

5.3.4. NMR analysis

^{1}H NMR analysis is frequently used to characterize the organic ligands attached to the surface of Au NPs.[5,8,31] Figure 5.15 shows ^{1}H NMR spectra of $CDCl_3$ solutions of **AuS-Cx-TPD** systems (x = 3, 4, 8, 12) and, for comparison, a spectrum of a $CDCl_3$ solution of **TPD-C4-thiol**.

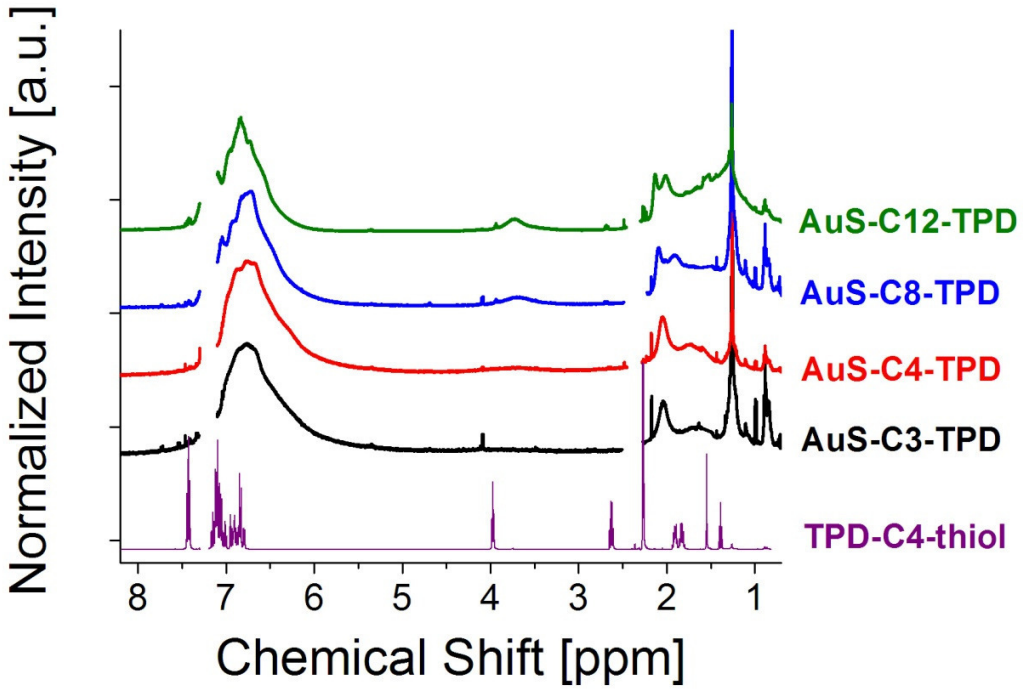

Figure 5.15. ^{1}H NMR spectra of $CDCl_3$ solutions of **AuS-Cx-TPD** systems (x = 3, 4, 8, 12) studied herein and of a $CDCl_3$ solution of **TPD-C4-thiol**. All spectra were normalized at the highest peak in the aromatic-proton region (6 – 8 ppm). The residual $CHCl_3$ and toluene solvent peaks were masked out.

As can be seen from Figure 5.15 neither of the NP samples shows peaks characteristic of free TPD-thiols in solution, which are shown in the spectrum of **TPD-C4-thiol**. Instead, very broad features are present, which are consistent with the attachment of TPD-thiols to the surface of Au NPs.[5,8] This is discussed in more detail below.

Since the preparation of the particles involved the reaction of TPD-thiols with oleylamine-coated Au NPs, ^{1}H NMR spectra of **AuS-Cx-TPD** systems (x = 3, 4, 8, 12) were used to estimate the residual amount of OA present in the samples. This was done according to two methods:

- *Method I*

  A spectrum was divided into two parts: an aliphatic part (0.0 – 4.5 ppm) and an aromatic part (4.5 – 8.0 ppm), and the total integrated signal in each part (not including signals from water and residual solvent) was measured, I_{aliph}, I_{arom}. If a mixture of **TPD-Cx-thiol** (x = 3, 4, 8, 12) and OA are present in the NP sample, the total signals expected for the aliphatic and aromatic protons are given by equations 5.1 and 5.2, respectively:

  $$I_{aliph} = (2x + 6)\times[\text{TPD-Cx-thiol}]_{\%} + 35\times[\text{OA}]_{\%} \qquad \textbf{Equation 5.1}$$

  $$I_{arom} = 25\times[\text{TPD-Cx-thiol}]_{\%} + 2\times[\text{OA}]_{\%} \qquad \textbf{Equation 5.2}$$

  For each type of NPs (x = 3, 12), the equations above can be solved for the two unknown percentage values $[\text{TPD-Cx-thiol}]_{\%}$ and $[\text{OA}]_{\%}$. The following values were obtained: $[\text{TPD-C3-thiol}]_{\%}$ = 88%, $[\text{TPD-C4-thiol}]_{\%}$ = 99%, $[\text{TPD-C8-thiol}]_{\%}$ = 89%, and $[\text{TPD-C12-thiol}]_{\%}$ = 100%.

- *Method II*

  Since neither of **TPD-Cx-thiols** has a methyl group attached to an alkyl chain the integrated signal from such methyl groups (ca. 0.9 ppm), I_{methyl}, can be attributed to the methyl group from residual oleylamine (Eq. 5.3). The total integrated signal I_{total} can be expressed by Eq. 5.4:

  $I_{methyl} = 3\times[OA]_{\%}$ **Equation 5.3**

  $I_{total} = (31 + 2x)\times[\text{TPD-Cx-thiol}]_{\%} + 37\times[OA]_{\%}$ **Equation 5.4**

  Again, for each NP sample, equations 5.3 and 5.4 can be solved for the two unknown percentage values $[\text{TPD-Cx-thiol}]_{\%}$ and $[OA]_{\%}$, using the experimental values for the integrations of I_{methyl} and I_{total}. The calculated values were $[\text{TPD-C3-thiol}]_{\%}$ = 95%, $[\text{TPD-C4-thiol}]_{\%}$ = 98%, $[\text{TPD-C8-thiol}]_{\%}$ = 92% and $[\text{TPD-C12-thiol}]_{\%}$ = 98%.

The results from the two methods for each sample were averaged, yielding: $[\text{TPD-C3-thiol}]_{\%}$ = 92%, $[\text{TPD-C4-thiol}]_{\%}$ = 99%, $[\text{TPD-C8-thiol}]_{\%}$ = 91%, and $[\text{TPD-C12-thiol}]_{\%}$ = 99%. Thus, it was concluded that the amount of residual oleylamine was below 10% in all **AuS-Cx-TPD** systems studied here.

Figure 5.16 shows a comparison of the ^{1}H NMR spectra of the NP systems studied herein.[b] As expected, the normalized spectra of mixed-ligand systems in each series of NPs, i.e., in each of the Au NP systems incorporating the same **TPD-Cx-thiol**, show higher intensity of signals in the aliphatic-proton region of the spectrum due to the presence of dodecanethiol. Additionally, within each series of NPs, there is a consistent downfield shift (i.e., a shift towards higher ppm values) of the aromatic-proton feature in

[b] The spectrum of **AuS-C4-TPD(DDT$_{60}$)** is not shown due to a technical issue with the data file.

the spectra of mixed-ligand systems when comparing them with the spectrum of the corresponding high-TPD-coverage NPs.

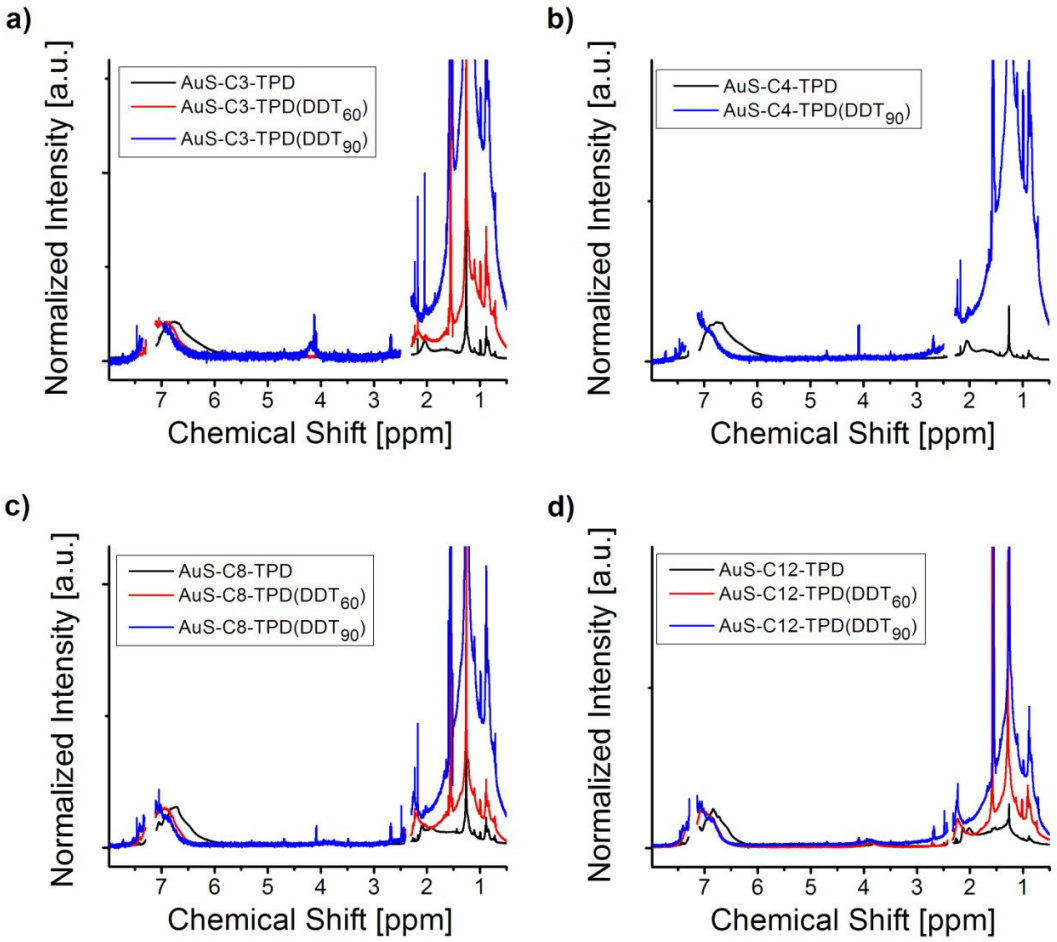

Figure 5.16. ^{1}H NMR spectra of $CDCl_3$ solutions of Au NP systems incorporating: a) **TPD-C3-thiol**, b) **TPD-C4-thiol**, c) **TPD-C8-thiol**, and d) **TPD-C12-thiol**. All spectra were normalized at the highest peak in the aromatic-proton region (6 – 8 ppm). The residual $CHCl_3$ and toluene solvent peaks were masked out.

This can be rationalized by invoking the concept of shielding and deshielding of protons by the magnetic field induced by the electric current in aromatic rings.[32] Protons which are positioned in plane of an aromatic ring are deshielded, i.e., the effective

magnetic field that the protons are immersed in is lowered, and this results in a downfield shift of the corresponding ^{1}H NMR signal.[32] On the other hand, protons which are positioned above the plane of an aromatic ring experience shielding, which, in effect, increases the magnetic field with which the protons are interacting, causing the ^{1}H NMR signal to shift upfield (towards smaller ppm values).[32] It is useful at this moment to go back to Figure 5.15. As can be seen there, the positions of the aromatic-proton features in all **AuS-Cx-TPD** systems are *shifted upfield* from the position of the envelope of the aromatic-proton signals of **TPD-C4-thiol**. The major chemical difference between TPD moieties in the $CDCl_3$ solution of **TPD-C4-thiol** and TPD moieties in $CDCl_3$ solutions of **AuS-Cx-TPD** systems (x = 3, 4, 8, 12) is that in the latter case the TPD moieties are most likely not solvated by $CDCl_3$ molecules to the extent they are in the solution of **TPD-C4-thiol**. Further, it is likely that in the NP systems TPD moieties are in fact surrounded by other TPD moieties that contain aromatic phenyl rings. Thus, the proximity of aromatic rings from neighboring TPD moieties in the NP systems would lead to *shielding* of the aromatic protons and an *upfield shift* of their NMR signal. The data presented in Figure 5.16 show that lowering the coverage of TPD-thiol ligands, i.e. lowering the number of TPD-thiol molecules attached to each nanoparticle, leads to the *downfield shift* of the aromatic-proton signal, bringing the signal closer to the envelope of the aromatic-proton signals of **TPD-C4-thiol** (see Figure 5.17). This is entirely consistent with the discussion above: the lower TPD-thiol coverage in the mixed-ligand systems would increase the average distance between TPD moieties and thus it would limit the effect of shielding of the aromatic protons by neighboring TPD moieties. Since this would be true only if the distribution of the TPD moieties on the surface in the mixed-ligand systems was

statistical, i.e., if there was no phase segregation of TPD-thiols and dodecanethiol on the surface of Au NPs, *the NMR data discussed here supports a more-or-less statistical distribution of TPD moieties on the surface of Au NPs in the mixed-ligand systems.*

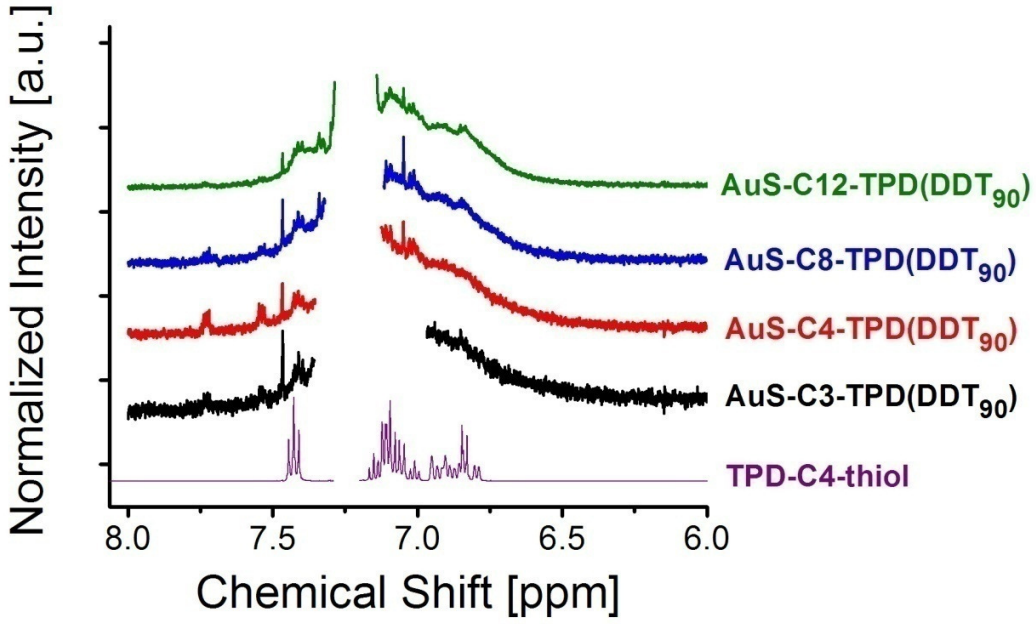

Figure 5.17. ^{1}H NMR spectra of $CDCl_3$ solutions of **AuS-Cx-TPD(DDT$_{90}$)** systems (x = 3, 4, 8, 12) studied herein and of a $CDCl_3$ solution of **TPD-C4-thiol**. All spectra were normalized at the highest peak in the aromatic-proton region (6 – 8 ppm). The residual $CHCl_3$ and toluene solvent peaks were masked out.

One particular feature of the ^{1}H NMR spectra presented here must be addressed. As mentioned before, the broadness of the signals seen in the NMR spectra of the NP systems studied here is an indication of the TPD-thiols have been attached to the surface of Au NPs.[5,8] According to the literature reports, there are two main reasons for such broadening. First, the distribution of chemical shifts caused by different adsorption sites on the NP surface can lead to inhomogenous broadening of ^{1}H NMR and ^{13}C NMR signals.[5,33-35] Second, a drastic shortening of the spin-spin relaxation time, T_2, has been

reported as a major cause for broadening of ^{1}H NMR and ^{13}C NMR signals of systems incorporating organic thiols bound to Au NPs.[31,33,34] The shortening of T_2 in ^{1}H NMR spectra of organic thiol-coated Au NPs is not accompanied by shortening of the spin-lattice relaxation, T_1, which excludes the shortening of relaxation times by interactions with unpaired electrons, i.e., it excludes interactions of protons with paramagnetic centers, if there are any, in the NP.[34] The main explanation concerning the abovementioned T_2 shortening in Au NP systems that can be found in the literature invokes the dependence of the nuclear magnetic dipole-dipole interaction relaxation mechanism, which, in this case of homonuclear dipole-dipole relaxation, involves magnetic interactions of two protons, on the rate of molecular motion.[5,34] Equation 5.5 shows this dependence:[34]

$$\frac{1}{T_2} \propto \frac{1}{R^6}\tau_c \qquad \textbf{Equation 5.5}$$

where R is the distance between the interacting nuclei and τ_c is the molecular motion correlation time, which is directly proportional to the viscosity of the environment.[5] Thus, the shortening of the spin-spin relaxation time, T_2, and the resulting broadening of ^{1}H NMR signals observed for organic ligand-coated Au NPs is believed to be caused by the increased viscosity of the microenvironment close to the surface of a NP.[5,34] Further, it has been shown that the observed broadening of signals in alkanethiol-coated Au NPs decreases, due to an increase in T_2, for protons that are further away from the surface of the NP.[5] This effect has been rationalized by taking into account the geometry of the alkanethiol-coated Au NP systems – due to the curvature of the surface the local density of the alkyl chains is highest in the close proximity to the metal surface and it gradually decreases as distance from the surface increases.[5,31] This implies that the local viscosity

also decreases with the increase of the distance from the NP surface which results in longer T_2 values, and narrower signals, for protons that are further away from the surface in alkanethiol-coated Au NPs.[5]

Figure 5.18 shows superimposed normalized ^{1}H NMR spectra of $CDCl_3$ solutions of **AuS-Cx-TPD** systems (x = 3, 4, 8, 12).[c] The observed signals are broad for all samples in the figure. As mentioned in the previous paragraph, this broadness may be caused by the distribution of chemical shifts[5,33-35] and by shortening of spin-spin relaxation time, T_2.[31,33,34] Further, it can be clearly seen that the broadness of the aromatic-proton feature decreases as the alkyl linker between the thiol group and the TPD moiety becomes longer.[d]

[c] These spectra were acquired and the following T_2 relaxation time experiments were performed for a different batch of **AuS-Cx-TPD** (x = 3, 4, 8, 12) than the batch discussed in the rest of this chapter. The average diameters of the second batch of these NPs were found from TEM analysis to be 2.8 ± 0.8 nm, 2.6 ± 0.7 nm, 2.7 ± 0.6 nm, and 3.2 ± 0.7 nm for **AuS-C3-TPD**, **AuS-C4-TPD**, **AuS-C8-TPD**, and **AuS-C12-TPD**, respectively.

[d] It should be noted that the regression of the broadness of the aromatic band with the length of the alkyl linker between the thiol group and the TPD moiety is similar in both batches of NPs.

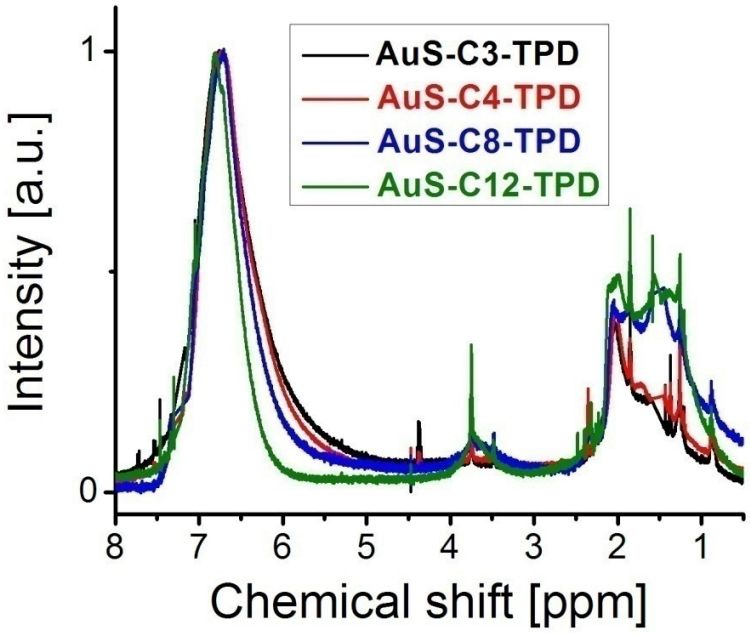

Figure 5.18. ^{1}H NMR spectra of $CDCl_3$ solutions of **AuS-Cx-TPD** systems (x = 3, 4, 8, 12) studied herein. All spectra were normalized at the highest peak in the aromatic-proton region (6 – 8 ppm). The residual $CHCl_3$ and toluene solvent peaks were masked out and the data points in these areas were then interpolated.

A series of measurements based on Carr-Purcell-Meiboom-Gill (CPMG) pulse sequence were performed on the samples whose spectra are shown in Figure 5.18. These experiments allow one to find T_2 relaxation times for ^{1}H NMR signals at different chemical shifts. Figure 5.19 shows CPMG-pulse-sequence-based decay traces of ^{1}H NMR signals originating from the tolyl methyl protons in the TPD moiety (2.05 ppm, Figure 5.19a) and from aromatic protons at 6.90 ppm (Figure 5.19b). It is clear that the signals decay much faster than typical organic molecules in solution, the T_2 relaxation times for which are usually on the order of seconds.[32] Also, there is a clear trend in the

decay dynamics for signals at both chemical shifts – the signal decay seems to be slower when the alkyl linker between the thiol group and the TPD moiety becomes longer.

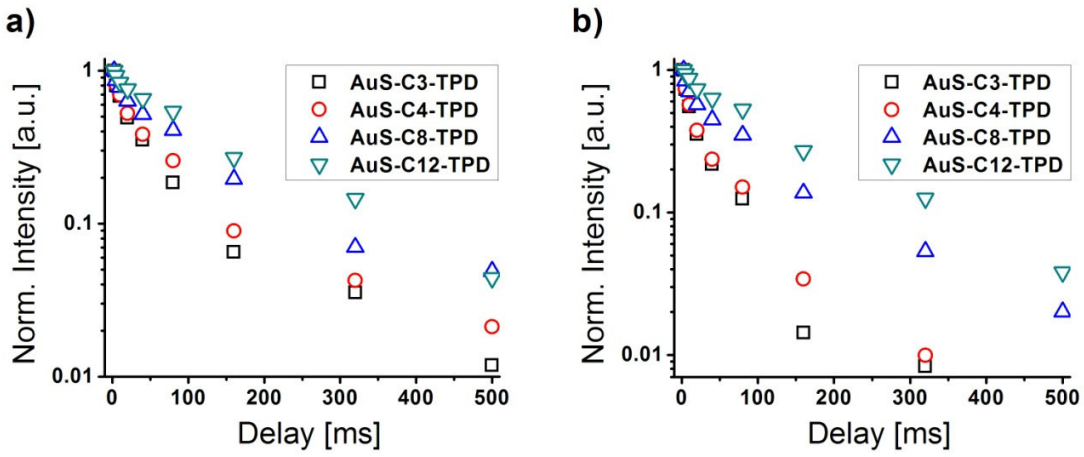

Figure 5.19. Decays of ^{1}H NMR signals as a function of delay between pulses in the CPMG pulse sequence measured at a) 2.05 ppm and b) 6.90 ppm, for $CDCl_3$ solutions of **AuS-Cx-TPD** systems (x = 3, 4, 8, 12).

Figure 5.20 presents the dependence of the found average T_2 relaxation times[e] on the number of methylene groups in the alkyl linkers between the thiol group and the TPD moiety. There is a clear trend showing the increase of the spin-spin relaxation time of the ^{1}H NMR signals corresponding to protons in TPD moieties with the increase of length of the alkyl linker between thiol group and the TPD moiety.

[e] Average T_2 relaxation time is defined as a time after which the signal decayed to 1/e of its original intensity

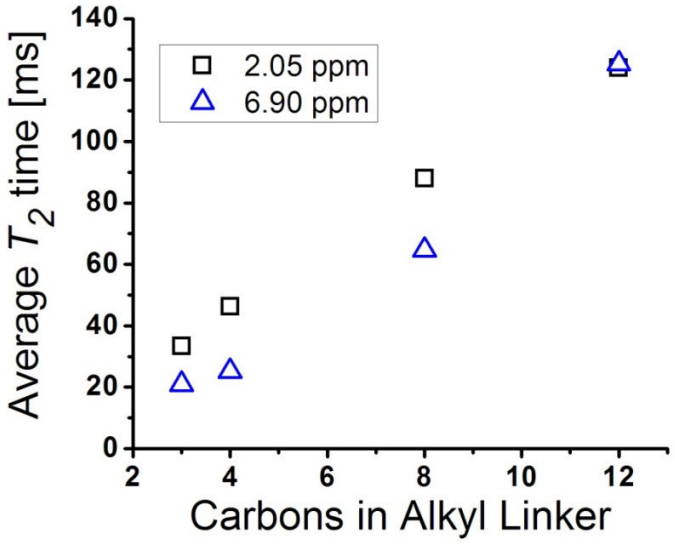

Figure 5.20. Average T_2 relaxation times as a function of the number of methylene groups in the alkyl linker between thiol group and the TPD moiety for $CDCl_3$ solutions of **AuS-Cx-TPD** systems (x = 3, 4, 8, 12).

Additionally, the spin-lattice relaxation time, T_1, relaxation time for all protons in $CDCl_3$ solution of **AuS-C3-TPD** was measured to be ca. 3 s, which is a typical value for an organic molecule in $CDCl_3$.[32] Considering that T_1 was not decreased in **AuS-C3-TPD**, the most likely reason for the shortening of T_2 in the studied systems is a homonuclear magnetic dipole-dipole relaxation and the effect of molecular motion on its efficiency (see Equation 5.5).[5,34] According to Equation 5.5, T_2 is inversely proportional to the molecular motion correlation time and thus to the local viscosity. Additionally, T_2 is directly proportional to the sixth power of the distance between interacting protons. According to this, the trend presented in Figure 5.20, i.e., the increase of the average T_2 with the number of methylene units in the alkyl linker between thiol group and the TDP moiety, is consistent with higher restrictions on molecular motion in the case of systems

incorporating shorter alkyl linkers. In other words, if the dominating mechanism of T_2 relaxation in **AuS-Cx-TPD** systems (x = 3, 4, 8, 12) is the homonuclear dipole-dipole interaction, the trend in Figure 5.20 can be explained by a progressive decrease of the local viscosity with a subsequent increase of the proton-proton distance for systems with increased length of the alkyl linker between the thiol group and the TPD moiety. This can be related to the geometry of **AuS-Cx-TPD** systems (x = 3, 4, 8, 12) (see Figure 5.21). Similarly to what has been described earlier for alkanethiol-coated Au NPs,[5] due to the surface curvature of Au NPs the molecular packing density drops as the TPD moiety is moved further away from the NP surface, resulting in lower local viscosity and larger intermolecular proton-proton distances and, according to Equation 5.5, leading to longer T_2 relaxation times. Thus, the T_2 data suggest that the average TPD-TPD distance in **AuS-Cx-TPD** systems (x = 3, 4, 8, 12) decreases, as expected from the structure, with the increased number of methylene groups in the alkyl linker between the thiol group and the TPD moiety (Figure 5.21).

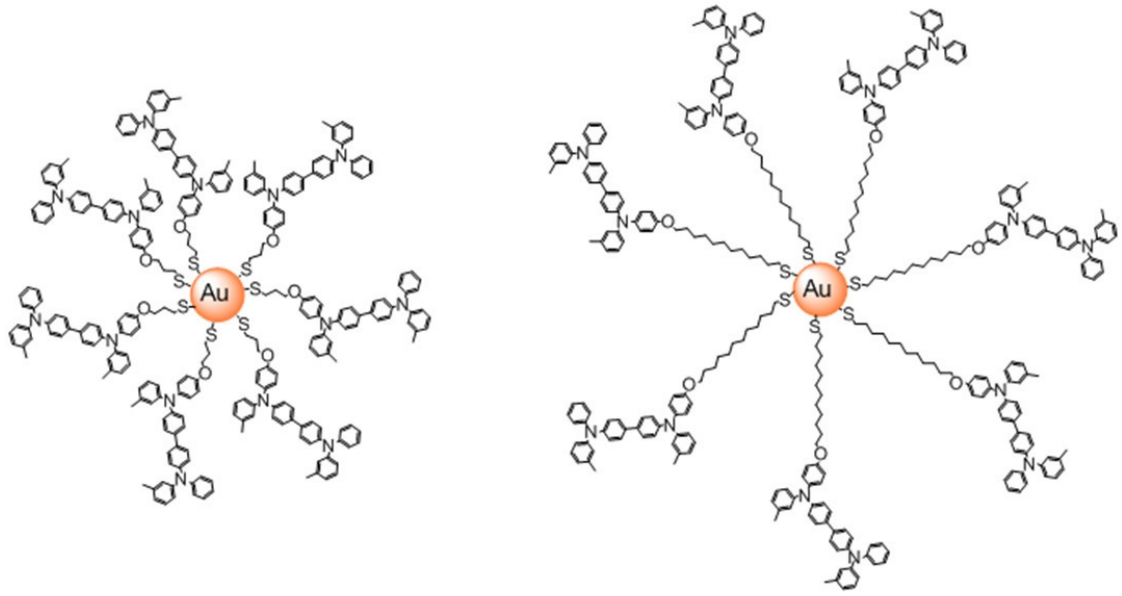

Figure 5.21. Schematic representations of the high-TPD-coverage systems: one with the shortest and one with the longest alkyl linker between the thiol group and the TPD moiety (the particle size and the organic ligand size are not to scale). Note the difference in the average distance between TPD moieties between both systems.

5.3.5. Thermogravimetric analysis (TGA)

Figure 5.22 shows thermogravimetric plots measured for AuS-Cx-TPD systems (x = 3, 4, 8, 12). The measurements were performed by Mr. Chun Huang. The mass loss for each sample was measured from the each plot at the plateau of the mass loss (ca. 700 ^{o}C). Mass-loss values of 32.5%, 33.9%, 34.3%, and 38.4% were found for **AuS-C3-TPD**, **AuS-C4-TPD**, **AuS-C8-TPD**, and **AuS-C12-TPD**, respectively. The increase of the mass loss for samples incorporating TPD-thiols with longer alkyl linkers is qualitatively consistent with the expectations based on the higher molecular weight of the TPD-thiols

with longer alkyl linkers, and on the assumption of similar TPD-thiol coverages for each NP system.

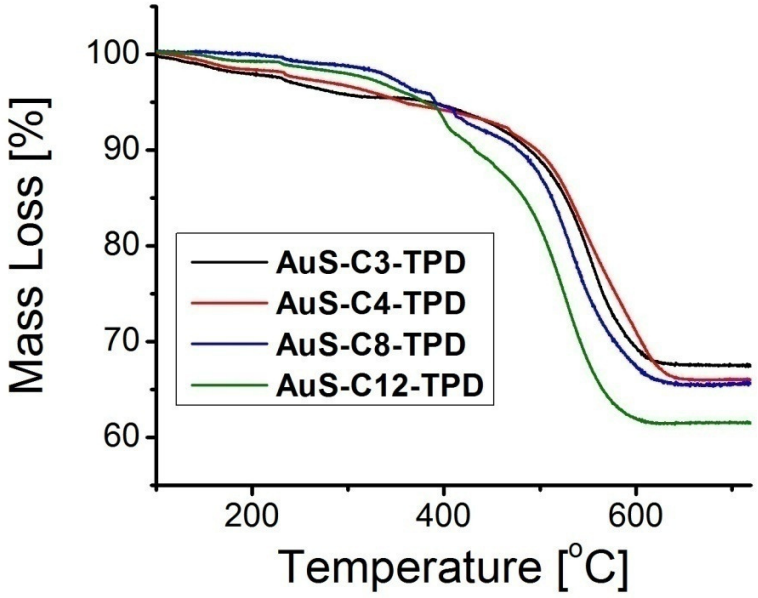

Figure 5.22. Thermogravimetric plots recorded for **AuS-Cx-TPD** systems (x = 3, 4, 8, 12) studied herein.

5.3.6. Calculations of TPD-thiol ligand coverages

5.3.6.1. Calculations based on UV-Vis absorption and TEM analysis

A combination of UV-Vis absorption and TEM data was used in order to establish the coverage of TPD-thiol ligands, i.e., the number of TPD-thiol molecules attached to each nanoparticle, and the molecular footprint of TPD-thiol (the surface area occupied by one TPD-thiol molecule) in the NP systems studied herein. In order to calculate the concentration of TPD-thiol molecules, concentration of Au NPs, and the total surface of Au NPs in each sample, the following approach was taken.

First, the concentration of TPD-thiols in each sample was calculated based on the residual optical density at 350 nm after subtraction of the contribution of Au NPs. The subtraction of the contribution of the metallic core of Au NPs to the optical density was performed in the same manner as was described in section 5.3.3 of this chapter (see Figure 5.13). The residual optical density at 350 nm, ΔA_{TPD}, is proportional to the concentration of the TPD moieties, c_{TPD}, according to Beer's law:

$$\Delta A_{TPD} = \varepsilon_{TPD}\, c_{TPD}\, b \qquad \textbf{Equation 5.6}$$

where ε_{TPD} is the molar extinction coefficient of TPD moiety at 350 nm (3.90×10^4 $Lmol^{-1}cm^{-1}$)[f], and b is the known pathway of light propagation through the sample in the UV-Vis absorption measurement.

Second, the concentration of Au NPs, c_{AuNP}, and the total NP surface, S_{AuNP}, in each sample were calculated according to both UV-Vis absorption and the TEM analysis as follows. The absorbance of the TPD-coated NP sample at the maximum of SPR band, A_{SPR}, arises from the contribution from NPs of different diameters, D_i, in each sample, which is characterized by a dispersion of particle diameters (known from the TEM analysis). This can be described by the following equation:

$$A_{SPR} = bc_n \sum_i \varepsilon_i \frac{c_i}{c_n} = bc_n \sum_i \varepsilon_i\, p_i \qquad \textbf{Equation 5.7}$$

where b is the known pathway of light propagation through the sample in the UV-Vis absorption measurement, ε_i is the molar extinction coefficient of Au NPs of diameter D_i in a toluene solution, c_i is the unknown concentration of Au NPs of diameter D_i in the sample, and c_n is an unknown constant. A normalized histogram of the NP diameters

[f] The molar extinction coefficient was calculated from a series of UV-Vis absorption measurements of the model compound **TPD-C12** in toluene solutions at different concentrations.

measured for each sample with the use of TEM gave the profile of the dependence of the NP concentration, p_i, on the diameter, D_i.[g] The values of ε_i for different diameters of NPs, D_i, were found from interpolation and extrapolation of literature values of molar extinction coefficients reported for DDT-coated Au NPs in toluene[36,37] and hexane[38] solutions.[h] Thus, based on the measured absorbance at the maximum of the SPR band for the NP sample, A_{SPR}, and on the known b, p_i, and the estimated ε_i, the unknown constant c_n for each sample was found. The concentration of NPs in each sample, c_{AuNP}, was then calculated according to:

$$c_{AuNP} = c_n \sum_i \frac{c_i}{c_n} = c_n \sum_i p_i \qquad \textbf{Equation 5.8}$$

where c_n is the constant calculated according to the above discussion and p_i is the TEM-based profile of the dependence of the NP concentration the diameter, D_i. The coverage of TPD-thiol ligands in each sample, $\chi_{TPD(Abs)}$, was then calculated by simply dividing the concentration of the TPD-thiol molecules by the concentration of Au NPs.

The total surface of the NPs in each sample, S_{AuNP}, was calculated according to:

$$S_{AuNP} = \pi N_A \sum_i c_i D_i^2 \qquad \textbf{Equation 5.9}$$

where N_A is Avogadro's number and c_i is the concentration of Au NPs with diameter D_i, which can be calculated from: $c_i = c_n \times p_i$. The footprint of the TPD-thiol molecule in each sample, $\theta_{TPD(Abs)}$, was then calculated by dividing the total surface area of Au NPs found for the sample by the number of TPD-thiol molecules. Table 5.2 summarizes the

[g] The center of ith bin in the histogram of diameters of NPs was chosen as the diameter D_i.

[h] This was done by fitting the literature data for particles of different diameters with a power function in the Origin 7.5 software. The best fit was obtained for $\varepsilon(D) = 9 \times 10^4 \times D^{2.8}$ Lmol^{-1}cm^{-1} where $\varepsilon(D)$ is the molar extinction coefficient of Au NPs with diameter D at the maximum of the SPR band. The obtained dependence was then used to find ε_i for particles with diameter D_i.

coverage of TPD-thiol ligands, $\chi_{TPD(Abs)}$, as well as the TPD-thiol footprints, $\theta_{TPD(Abs)}$, for the Au NP systems studied herein.

5.3.6.2. Calculations based on TGA and TEM analysis

Another method of establishing the TPD-thiol coverage and the footprint of TPD-thiol in Au NP samples involved the use of TGA data in conjunction with TEM analysis. This analysis was performed only for **AuS-Cx-TPD** systems (x = 3, 4, 8, 12) as TGA was performed only for those samples. Below is a brief description of the method.

The number of moles of **TPD-Cx-thiol** molecules (x = 3, 4, 8, 12) in each sample of interest, N_{TPD}, was calculated according to:

$$N_{TPD} = \frac{mm_{\%}}{100M_W^{TPD}} \qquad \textbf{Equation 5.10}$$

where m is the mass of the NP sample used for TGA, $m_{\%}$ is the percent mass loss found from TGA, and M_W^{TPD} is the molecular weight of **TPD-Cx-thiol**.

The number of moles of Au NPs in each sample, N_{AuNP}, was calculated as follows. First, the total volume of metallic gold in each sample, V_{Au}, can be expressed as:

$$V_{Au} = \frac{m(100-m_{\%})}{100d_{Au}} = \frac{4}{3}\pi n_n \sum_i \frac{n_i}{n_n}\left(\frac{D_i}{2}\right)^3 = \frac{4}{3}\pi n_n \sum_i p_i \left(\frac{D_i}{2}\right)^3 \qquad \textbf{Equation 5.11}$$

where m is the mass of the NP sample used for TGA, $m_{\%}$ is the percent mass loss found from TGA, d_{Au} is density of bulk gold (d_{Au} = 19.3 g / cm^3)[39], n_n is an unknown constant, n_i is the population of Au NPs with diameter D_i, and p_i is the known, TEM-based profile of the dependence of the NP population, n_i, on the diameter, D_i, the same quantity as in Equation 5.8. The unknown constant n_n was thus found for each of **AuS-Cx-TPD** systems (x = 3, 4, 8, 12) based on the experimental data according to:

$$n_n = \frac{3}{4}\frac{m(100-m_{\%})}{100 d_{Au}}\frac{1}{\pi \sum_i p_i \left(\frac{D_i}{2}\right)^3} \qquad \textbf{Equation 5.12}$$

The number of moles of Au NPs in each sample was further calculated according to:

$$N_{AuNP} = \frac{n_n}{N_A}\sum_i \frac{n_i}{n_n} = \frac{n_n}{N_A}\sum_i p_i \qquad \textbf{Equation 5.13}$$

where n_n is the constant calculated with the use of Equation 5.12 and N_A is Avogadro's number.

The total NP surface in each sample of interest, S_{AuNP}, was calculated according to:

$$S_{AuNP} = \pi \sum_i n_i D_i^2 \qquad \textbf{Equation 5.14}$$

where $n_i = n_n \times p_i$.

The coverage of TPD-thiol ligands in each sample, $\chi_{TPD}(TGA)$, was calculated by dividing the number of moles of TPD-thiol molecules by the number of moles of Au NPs. The footprint of TPD-thiol molecule in each sample, $\theta_{TPD}(TGA)$, was found by dividing the total surface of Au NPs found for the sample by the number of TPD-thiol molecules.

5.3.6.3. Summary and discussion of the TPD-thiol coverage and TPD-thiol footprint data

Table 5.2 summarizes and compares the UV-Vis absorption analysis based coverages of TPD-thiol ligands as well as the TPD-thiol footprints, $\chi_{TPD}(Abs)$ and $\theta_{TPD}(Abs)$, with the same quantities found from the TGA analysis, $\chi_{TPD}(TGA)$ and $\theta_{TPD}(TGA)$. As can be seen in the table, the UV-Vis-based TPD-thiol coverages, $\chi_{TPD}(Abs)$, for **AuS-Cx-TPD** systems are similar for x = 3, 4, and 12 with the much smaller value observed for **AuS-C8-TPD**. This is related to the fact that the average

diameter found for the latter sample was found to be smaller than for the other high-TPD-coverage systems. As expected, the calculated TPD-thiol coverage values for the systems incorporating mixtures of thiols are smaller than the corresponding **AuS-Cx-TPD** systems (x = 3, 4, 8, 12).

Table 5.2. Summary of the UV-Vis-based TPD-thiol coverages, $\chi_{TPD}(Abs)$, and TPD-thiol footprints, $\theta_{TPD}(Abs)$, calculated according to the discussion in sections 5.3.6.1 and 5.3.6.2 for NP samples studied herein. Also, TGA-based TPD-thiol coverages, $\chi_{TPD}(TGA)$, and TPD-thiol footprints, $\theta_{TPD}(TGA)$, calculated for **AuS-Cx-TPD** systems (x = 3, 4, 8, 12) are given.

Sample	TEM diameter [nm]	$\chi_{TPD}(Abs)$ [#/particle]	$\theta_{TPD}(Abs)$ [Å^2/molecule]	$\chi_{TPD}(TGA)$ [#/particle]	$\theta_{TPD}(TGA)$ [Å^2/molecule]
AuS-C3-TPD	3.5 ± 1.2	130	35	290	15
AuS-C3-TPD(DDT$_{60}$)	4.3 ± 1.4	88	69	-	-
AuS-C3-TPD(DDT$_{90}$)	4.8 ± 1.0	30	250	-	-
AuS-C4-TPD	3.5 ± 1.2	130	32	300	14
AuS-C4-TPD(DDT$_{60}$)	2.9 ± 1.0	32	91	-	-
AuS-C4-TPD(DDT$_{90}$)	4.2 ± 1.1	24	240	-	-
AuS-C8-TPD	2.8 ± 0.9	72	37	150	18
AuS-C8-TPD(DDT$_{60}$)	2.8 ± 1.0	32	88	-	-
AuS-C8-TPD(DDT$_{90}$)	3.1 ± 1.0	12	270	-	-
AuS-C12-TPD	3.3 ± 1.1	140	26	300	13
AuS-C12-TPD(DDT$_{60}$)	2.7 ± 0.9	35	74	-	-
AuS-C12-TPD(DDT$_{90}$)	2.9 ± 1.0	15	190	-	-

An interesting observation can be made when comparing the values of TPD-thiol coverage calculated according to the analysis of UV-Vis absorption, $\chi_{TPD}(Abs)$, with the values of TPD-thiol coverage based on TGA, $\chi_{TPD}(TGA)$. Values of $\chi_{TPD}(TGA)$ show ca.

2.2 times higher values than $\chi_{TPD(Abs)}$, consistently for all **AuS-Cx-TPD** systems. The opposite is true when comparing $\theta_{TPD(TGA)}$ with $\theta_{TPD(Abs)}$, i.e., TPD-thiol footprints found from UV-Vis absorption analysis are approximately 2.2 times larger than those based on TGA. This suggests that the values calculated from at least one of the two methods are not correct. It is interesting to consider the assumptions that were taken in order to perform the analyses described here. For the procedure which relied on the UV-Vis absorption data the main two assumptions were: firstly, the literature values of molar extinction coefficient for Au NPs of different sizes are the same as the molar extinction coefficients for TPD-thiol-coated NPs; secondly, the molar extinction coefficient of the TPD moiety does not change upon adsorption onto the NP surface. The first assumption is most likely not true as since there is an effect of the proximal polarizable TPD moiety on the SPR band position cross section (see section 5.3.3) there is most likely also an effect on the molar extinction coefficient of the SPR band.[24] The second assumption may or may not be true. In order to test if the two assumptions hold, a simple experiment was performed as follows. **AuS-C12-TPD** in a toluene solution was reacted with an excess of dodecanethiol that should displace the **TPD-C12-thiol** from the surface of Au NPs.[28-30] Evolution of UV-Vis absorption spectrum of the reaction mixture was monitored and the observed changes in UV-Vis absorption are presented in Figure 5.23. As can be seen in the figure the SPR band intensity dropped after the place exchange reaction. At the same time the absorbance in the region of a strong absorption of TPD moiety (ca. 355 nm) increased significantly. The ligand-exchange reaction that was carried out would not change the concentration of Au NPs and of TPD moieties, but it would result in the detachment of TPD moieties from the surface of Au NPs. Thus, the changes in the

absorption spectrum seen in Figure 5.23 must be related to the coupling between the TPD moiety and the Au NP. This clearly demonstrates that the assumptions of the invariance of molar extinction coefficients of both Au NPs and TPD moiety are incorrect.

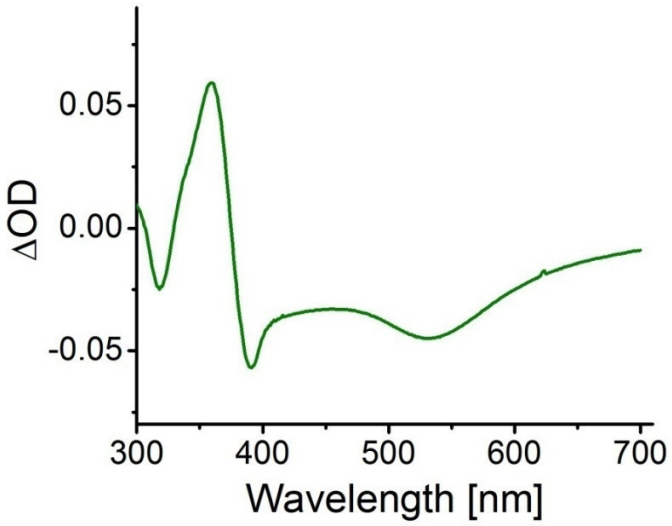

Figure 5.23. Changes in the optical density observed after 2 days of the reaction of **AuS-C12-TPD** with dodecanethiol in toluene.

In fact, as evidenced by the data presented in Figure 5.23, the presence of TPD moieties close to the surface of Au NPs causes an increase of the molar extinction coefficient of Au NPs and a decrease of the molar extinction coefficient of TPD moiety. These effects would give rise to an underestimation of the amount of TPD moieties and an overestimation of the amount of Au NPs based on UV-Vis absorption analysis. This, in turn, would lead to calculating *TPD-thiol coverages which are smaller than the actual values*, which is consistent with what was observed when comparing $\chi_{TPD}(Abs)$ with $\chi_{TPD}(TGA)$. The analysis of the data suggests that the TPD-thiol coverages based on the

UV-Vis analysis are most likely underestimated and the corresponding TPD-thiol footprints are overestimated.

The values of $\chi_{TPD}(TGA)$ and $\theta_{TPD}(TGA)$ should also be subject to critical evaluation. Based on ^{1}H NMR analysis (see section 5.3.4 of this chapter) TPD-thiol molecules in **AuS-Cx-TPD** systems (x = 3, 4, 8, 12) do not constitute 100% of the organic material present – some small amounts of residual oleylamine (< 10%) may be still present in these samples. Thus, the values of $\chi_{TPD}(TGA)$ are likely to be somewhat overestimated as the total mass loss measured in TGA did not arise solely from TPD-thiol molecules. Subsequently, the values of $\theta_{TPD}(TGA)$ are likely to be underestimated.

Since the UV-Vis-based TPD-thiol coverages are most likely underestimated and the TPD-thiol footprints overestimated, and the opposite can be said about the corresponding values based on TGA, the actual TPD-thiol coverages and footprints are probably lying somewhere in between the UV-Vis-based and TGA-based quantities. Table 5.3 shows average values of TPD-thiol coverages, $\chi_{TPD}(Av)$, and TPD-thiol footprints, $\theta_{TPD}(Av)$, calculated as the arithmetic mean value of the corresponding values found from UV-Vis analysis and TGA.

Table 5.3. Summary of the average TPD-thiol coverages, $\chi_{TPD}(Av)$, and TPD-thiol footprints, $\theta_{TPD}(Av)$, calculated according to the discussion in section 5.3.6.3 for **AuS-Cx-TPD** systems (x = 3, 4, 8, 12).

Sample	TEM diameter [nm]	$\chi_{TPD}(Av)$ [#/particle]	$\theta_{TPD}(Av)$ [Å^2/molecule]
AuS-C3-TPD	3.5 ± 1.2	210	25
AuS-C4-TPD	3.5 ± 1.2	220	23
AuS-C8-TPD	2.8 ± 0.9	110	28
AuS-C12-TPD	3.3 ± 1.1	220	20

The data in Table 5.3 can be compared to literature values found for alkanethiol-coated Au NPs. Hostetler *et al.* theoretically calculated and found experimentally the coverage of dodecanethiol on Au NPs of different sizes.[5] For Au NPs with ca. 3 nm diameters the number of dodecanethiol molecules on the surface of each NP, i.e., the dodecanethiol coverage, was found to be between 160 and 220 and for particles with diameters of ca. 4 nm the dodecanethiol coverage was found to be ca. 350.[5] Thus, the values found for **AuS-Cx-TPD** systems (x = 3, 4, 8, 12) are in rough agreement with the values found by Hostetler *et al.* for dodecanethiol-coated Au NPs.[5] The TPD-thiol footprints listed in table 5.3 are close to 22 $Å^2$, which is an often-quoted value for dodecanethiol footprint in SAMs on flat gold.[40]

5.4. Conclusions

A series of Au NP systems coated with organic ligands incorporating bis(diarylamino)biphenyl-based dye molecules with alkyl linkers of varying length between the dye and the surface-anchoring thiol group was successfully prepared. The synthetic methodology used for the preparation of these NPs involved a reaction between oleylamine-coated Au NPs and thiol ligand molecules (bis(diarylamino)biphenyl-based thiols and dodecanethiol) and resulted in displacement of oleylamine from the surface of NPs with subsequent binding of the thiol ligands to the surface, as evidenced by FT-IR and ^{1}H NMR spectroscopies. Almost complete exchange of oleylamine to the desired thiol ligands (> 90%) on the surface of NPs was evidenced by ^{1}H NMR spectroscopy. The metal-core diameters of the prepared NP systems were found, with the use of TEM, to be in the range 2.7 – 4.1 nm, with the standard deviations from the average diameters

of ca. 30%. FT-IR analysis of the particles coated solely with bis(diarylamino)biphenyl-based thiols revealed that in the case of the systems containing 8 and 12 methylene units between the bis(diarylamino)biphenyl moiety and the surface-anchoring thiol group, the alkyl chains were fully extended, i.e., all-*trans* conformations of the alkyl linkers were found. In contrast, the systems containing 3 and 4 methylene groups between the bis(diarylamino)biphenyl moiety and the surface-anchoring thiol group showed a substantial proportion of gauche defects in the alkyl linkers. ^{1}H NMR analysis revealed substantial shortening of the spin-spin relaxation time, T_2, which resulted in broadening of the proton signals in ^{1}H NMR spectra of the bis(diarylamino)biphenyl-based thiol ligands attached to Au NPs. The reduction of T_2 has been attributed to the restricted mobility of the dye molecules densely packed on the surface of the Au NPs. The measured dependence of T_2 on the number of methylene units between the bis(diarylamino)biphenyl moiety and the surface-anchoring thiol group suggested that the mobility of the dye molecules was larger in the systems incorporating longer alkyl linkers. A combined UV-Vis, TGA and TEM analysis of particles coated solely with bis(diarylamino)biphenyl-based thiols revealed that the number of bis(diarylamino)biphenyl dye molecules on the surface of each nanoparticle varied between 110 and 220 and that the footprints of the thiol dyes were similar to the footprint of dodecanethiol on flat gold surface. Furthermore, the analysis of Au NP systems coated with mixtures of two thiols (bis(diarylamino)biphenyl-based thiols and dodecanethiol) revealed that the proportions of the two thiols on the surface of the nanoparticles were practically the same as the proportions used during the synthesis.

Additionally, ^{1}H NMR analysis of the mixed-ligand NPs revealed that the distribution of the thiol molecules on the surface was more-or-less statistical.

The NP systems described in this chapter were further studied in the context of their photophysical properties. Those are described in Chapter 6.

5.5. References

(1) Daniel, M. C.; Astruc, D. *Chem. Rev.* **2004**, *104*, 293-346.
(2) Link, S.; El-Sayed, M. A. *Annu. Rev. Phys. Chem.* **2003**, *54*, 331-366.
(3) Brust, M.; Walker, M.; Bethell, D.; Schiffrin, D. J.; Whyman, R. *J. Chem. Soc., Chem. Commun.* **1994**, 801-2.
(4) Leff, D. V.; Brandt, L.; Heath, J. R. *Langmuir* **1996**, *12*, 4723-4730.
(5) Hostetler, M. J.; Wingate, J. E.; Zhong, C. J.; Harris, J. E.; Vachet, R. W.; Clark, M. R.; Londono, J. D.; Green, S. J.; Stokes, J. J.; Wignall, G. D.; Glish, G. L.; Porter, M. D.; Evans, N. D.; Murray, R. W. *Langmuir* **1998**, *14*, 17-30.
(6) Stoeva, S.; Klabunde, K. J.; Sorensen, C. M.; Dragieva, I. *J. Am. Chem. Soc.* **2002**, *124*, 2305-2311.
(7) Pietron, J. J.; Hicks, J. F.; Murray, R. W. *J. Am. Chem. Soc.* **1999**, *121*, 5565-5570.
(8) Lica, G. C.; Zelakiewicz, B. S.; Tong, Y. Y. *J. Electroanal. Chem.* **2003**, *554-555*, 127-132.
(9) Hicks, J. F.; Templeton, A. C.; Chen, S.; Sheran, K. M.; Jasti, R.; Murray, R. W.; Debord, J.; Schaaff, T. G.; Whetten, R. L. *Anal. Chem.* **1999**, *71*, 3703-3711.
(10) Wenseleers, W.; Stellacci, F.; Meyer-Friedrichsen, T.; Mangel, T.; Bauer, C. A.; Pond, S. J. K.; Marder, S. R.; Perry, J. W. *J. Phys. Chem. B* **2002**, *106*, 6853-6863.
(11) Thomas, K. G.; Kamat, P. V. *Acc. Chem. Res.* **2003**, *36*, 888-898.
(12) Cai, X.; Adhikari, R. M.; Anyaogu, K. C.; Palayangoda, S. S.; Estrada, L. A.; De, P. K.; Neckers, D. C. *J. Am. Chem. Soc.* **2009**, *131*, 1648-1649.
(13) Zeman, E. J.; Schatz, G. C. *J. Phys. Chem.* **1987**, *91*, 634-643.
(14) Sasaki, Y.; Araki, Y.; Fujitsuka, M.; Ito, O.; Hirao, A.; Nishizawa, H. *Photochem. Photobiol. Sci.* **2003**, *2*, 136-141.
(15) Philip, R.; Holzer, W.; Penzkofer, A.; Tillmann, H.; Horhold, H. H. *Synth. Met.* **2003**, *132*, 297-308.
(16) Zhang, H. L.; Evans, S. D.; Henderson, J. R.; Miles, R. E.; Shen, T. *J. Phys. Chem. B* **2003**, *107*, 6087-6095.
(17) Badia, A.; Cuccia, L.; Demers, L.; Morin, F.; Lennox, R. B. *J. Am. Chem. Soc.* **1997**, *119*, 2682-2692.
(18) Hostetler, M. J.; Stokes, J. J.; Murray, R. W. *Langmuir* **1996**, *12*, 3604-3612.
(19) Badia, A.; Singh, S.; Demers, L.; Cuccia, L.; Brown, G. R.; Lennox, R. B. *Chem. Eur. J.* **1996**, *2*, 359-363.
(20) Snyder, R. G.; Strauss, H. L.; Elliger, C. A. *J. Phys. Chem.* **1982**, *86*, 5145-5150.
(21) Snyder, R. G.; Maroncelli, M.; Strauss, H. L.; Hallmark, V. M. *J. Phys. Chem.* **1986**, *90*, 5623-5630.
(22) Porter, M. D.; Bright, T. B.; Allara, D. L.; Chidsey, C. E. D. *J. Am. Chem. Soc.* **1987**, *109*, 3559-68.
(23) Laibinis, P. E.; Nuzzo, R. G.; Whitesides, G. M. *J. Phys. Chem.* **1992**, *96*, 5097-105.
(24) Mulvaney, P. *Langmuir* **1996**, *12*, 788-800.
(25) Underwood, S.; Mulvaney, P. *Langmuir* **1994**, *10*, 3427-30.
(26) Templeton, A. C.; Pietron, J. J.; Murray, R. W.; Mulvaney, P. *J. Phys. Chem. B* **2000**, *104*, 564-570.

(27) Bohren, C. F.; Huffman, D. R. *Absorption and Scattering of Light by Small Particles*; Wiley-VCH: Weinheim, 2004.
(28) Donkers, R. L.; Song, Y.; Murray, R. W. *Langmuir* **2004**, *20*, 4703-4707.
(29) Hostetler, M. J.; Templeton, A. C.; Murray, R. W. *Langmuir* **1999**, *15*, 3782-3789.
(30) Gu, T.; Whitesell, J. K.; Fox, M. A. *Chem. Mater.* **2003**, *15*, 1358-1366.
(31) Terrill, R. H.; Postlethwaite, T. A.; Chen, C.-h.; Poon, C.-D.; Terzis, A.; Chen, A.; Hutchison, J. E.; Clark, M. R.; Wignall, G. *J. Am. Chem. Soc.* **1995**, *117*, 12537-12548.
(32) Silverstein, R. M.; Webster, F. X. *Spectrometric Identification of Organic Compounds*; 6th ed.; John Wiley & Sons, Inc.: New York, 1998.
(33) Badia, A.; Gao, W.; Singh, S.; Demers, L.; Cuccia, L.; Reven, L. *Langmuir* **1996**, *12*, 1262-1269.
(34) Kohlmann, O.; Steinmetz, W. E.; Mao, X.-A.; Wuelfing, W. P.; Templeton, A. C.; Murray, R. W.; Johnson, C. S. *J. Phys. Chem. B* **2001**, *105*, 8801-8809.
(35) Badia, A.; Demers, L.; Dickinson, L.; Morin, F. G.; Lennox, R. B.; Reven, L. *J. Am. Chem. Soc.* **1997**, *119*, 11104-11105.
(36) Liu, X.; Atwater, M.; Wang, J.; Huo, Q. *Colloids Surf. B* **2007**, *58*, 3-7.
(37) Rance, G. A.; Marsh, D. H.; Khlobystov, A. N. *Chem. Phys. Lett.* **2008**, *460*, 230-236.
(38) Maye, M. M.; Han, L.; Kariuki, N. N.; Ly, N. K.; Chan, W. B.; Luo, J.; Zhong, C. J. *Anal. Chim. Acta* **2003**, *496*, 17-27.
(39) *CRC Handbook of Chemistry and Physics*; 63 ed.; Weast, R. C., Ed.; CRC Press: Boca Raton, Florida, 1982.
(40) Schreiber, F. *Prog. Surf. Sci.* **2000**, *65*, 151-257.

CHAPTER 6

PHOTOPHYSICAL PROPERTIES OF BIS(DIARYLAMINO)BIPHENYL-FUNCTIONALIZED GOLD NANOPARTICLES

6.1. Introduction

The photophysical properties of systems incorporating metal nanoparticles (NPs) have received great attention in recent years. Of particular interest are the effects of metal nanostructures on the dynamics of both radiative and non-radiative processes leading to depopulation of excited states of dyes placed in close proximity to the metal.[1,2] Energy and electron transfer from the photoexcited organic dye to the metal NP, as well as intermolecular interactions such as excimer formation, have been proposed as possible non-radiative channels of deactivation of excited states of dyes attached to these nanostructures.[1-7] While deactivation of excited states of fluorescent organic dyes by metal NPs has already found applications,[8,9] fundamental questions, including the effects of the distance between the dye and the nanoparticle surface and between neighboring dyes on the non-radiative deactivation channels of the dye's excited state, have not been extensively studied.

The study described in this chapter addresses the influence of the linker length between a gold NP and a fluorescent organic dye on the excited-state deactivation dynamics of the fluorophore. The schematic structures of the Au NP systems containing bis(diarylamino)biphenyl (TPD) moieties, which were attached to the NP surface via

alkyl linkers of different lengths have been shown in Figure 5.1 and their characterization has been described in Chapter 5. The fluorescence of dyes anchored to NPs is often strongly quenched[1,5] and in the present systems it was found that employing a time-correlated single photon counting (TC-SPC) fluorescence technique, which is often used in the studies of metal NP – organic dye interactions,[2,6] resulted in signals dominated by traces of free ligand in solution, rather than by the strongly quenched NP-anchored dyes. Thus, in order to address the question of the influence of the alkyl spacer between the Au NP and TPD moiety on the deactivation dynamics of the TPD excited state, a fs near-infrared (NIR) broadband TA technique was employed. Furthermore, the use of the NIR probe allowed for preferential probing of the photoexcited TPD moiety as the contribution from the Au NP metallic core to the overall TA signal is minor (see Chapter 2 section 2.2.2.13).

6.2. Photophysical Properties of Gold Nanoparticles Coated with TPD-thiol Ligands

*6.2.1. The Photophysics of the Model Compound – **TPD-C12***

In order to understand the changes in the photophysics of the TPD moiety caused by the close proximity of a gold NP in the TPD-thiol-coated Au NP systems it is crucial to first describe the photophysical properties of NP-free TPD in solution and in the solid state. Thus, the TPD model compound – **TPD-C12** – was synthesized and its photophysical properties in toluene solutions as well as in the solid state were studied.

6.2.1.1. Solution Properties

Figure 6.1 shows the absorption spectrum as well as the fluorescence spectrum of **TPD-C12** in toluene solution. The absorption spectrum of **TPD-C12** in toluene solution shows a maximum at 355 nm with the molar extinction coefficient, ε, of 4.10 ± 0.06 L $mol^{-1}cm^{-1}$. The fluorescence spectrum of **TPD-C12** in toluene solution shows a maximum at 403 nm and the fluorescence quantum yield of the compound was measured to be 0.80 ± 0.07 for deoxygenated toluene solution.[a]

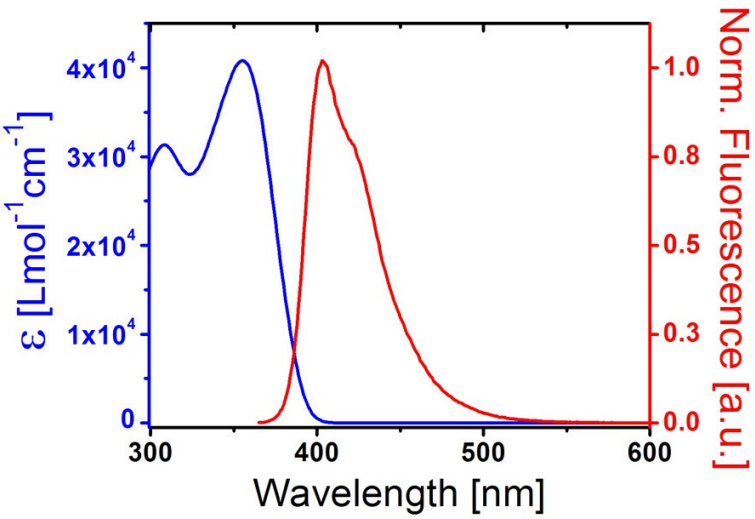

Figure 6.1. Spectral distribution of the molar extinction coefficient, ε, for **TPD-C12** in a toluene solution (blue line) and normalized fluorescence spectrum measured for a toluene solution of **TPD-C12** (red line). The excitation wavelength was 355 nm.

[a] The fluorescence quantum yield was measured using 1,4-bis(5-phenyloxazol-2-yl) benzene (POPOP) in degassed cyclohexane solution as a standard (quantum yield value of 0.97 was used based on ref. 10)

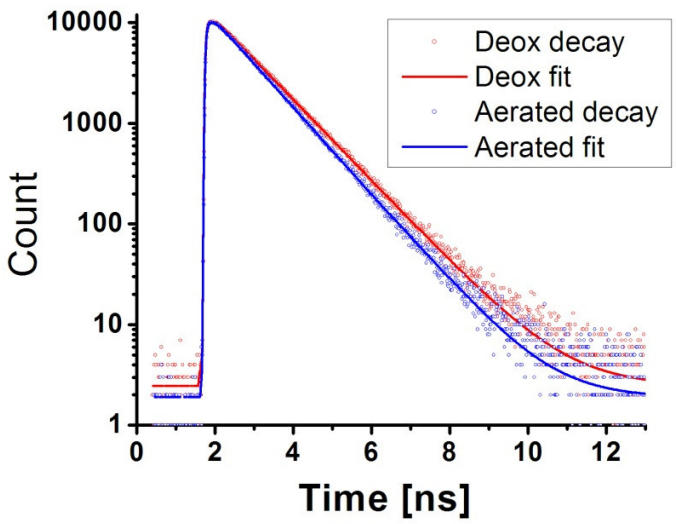

Figure 6.2. Fluorescence decays measured for deoxygenated (Deox decay, red circles) and air-equilibrated (Aerated decay, blue circles) toluene solutions of **TPD-C12**, and corresponding best-fit functions (solid lines). 365 nm was used as the excitation wavelength and the emission was collected at 420 nm.

Fluorescence decays of toluene solutions of **TPD-C12**, both degassed and air-equilibrated, measured with the use of a time-correlated single-photon counting setup (TC-SPC; see Section 2.2.2.11 for details), are presented in Figure 6.2. The fluorescence lifetimes found from fitting of the decay data with single exponential functions were found to be 1.07 ns and 0.98 ns for deoxygenated and air-equilibrated toluene solutions of **TPD-C12**, respectively. From these data it can be concluded that the excited singlet state of **TPD-C12** in an air-equilibrated toluene solution has a fluorescence lifetime of 0.98 ns.

A series of measurements were performed in order to measure a transient spectrum of the triplet state of **TPD-C12** in toluene solution (concentration ca. 1×10^{-5} M). The measurements were done with the help of Mr. Matteo Cozzuol, and a nanosecond transient absorption (TA) apparatus was employed for these studies (see

Section 2.2.2.12). Figure 6.3 shows transients of optical density at 1250 nm acquired for both deoxygenated and aerated toluene solutions of **TPD-C12**. As can be seen from the figure, there is a dramatic shortening of the lifetime of the transient species upon exposing the solution to air. This sensitivity towards air suggests that the transient species responsible for the observed optical density in the near-infrared (NIR) spectral region is the excited triplet state of **TPD-C12**.[11] Its transient spectrum is presented in Figure 6.4.

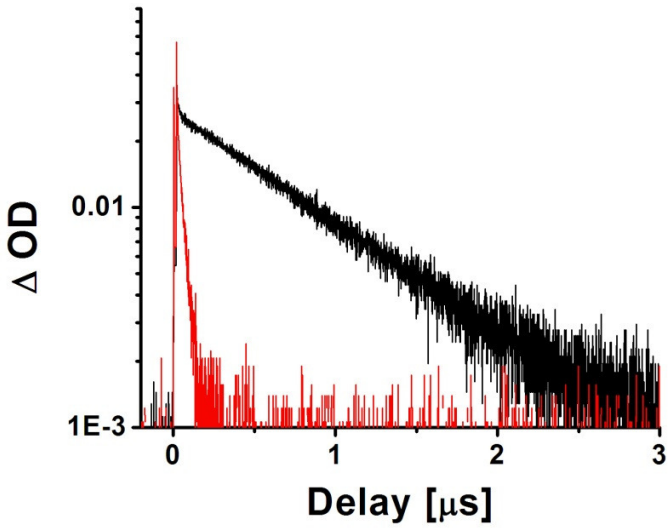

Figure 6.3. Optical density transients at 1250 nm acquired for deoxygenated (black line) and aerated (red line) toluene solutions of **TPD-C12**. 355 nm was used as the excitation wavelength.

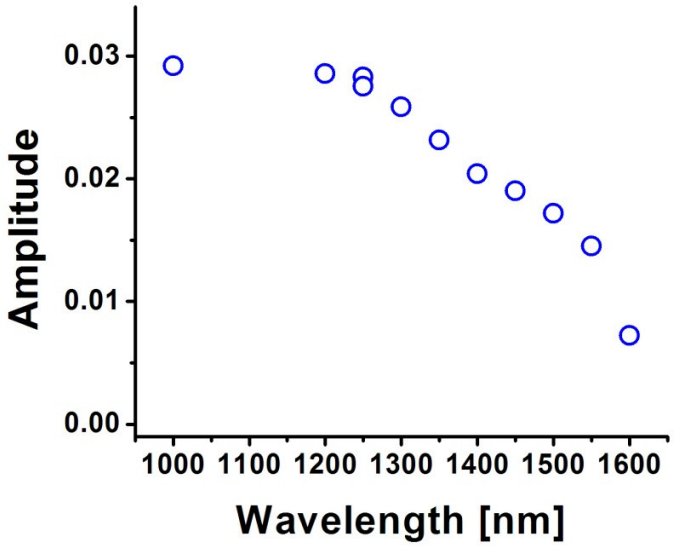

Figure 6.4. Transient NIR absorption spectrum of the excited triplet state of **TPD-C12** in degassed toluene solution calculated from fitting the transients measured at each individual wavelength (excitation wavelength: 355 nm).

Femtosecond broad-band transient absorption measurements in the NIR region (fs TA-NIR) were employed to study the ultrafast dynamics of ca. 0.1 M toluene solution of **TPD-C12**. Figure 6.5 shows selected transient spectra (Figure 6.5a) as well as transients at different wavelengths (Figure 6.5b) recorded for the solution.

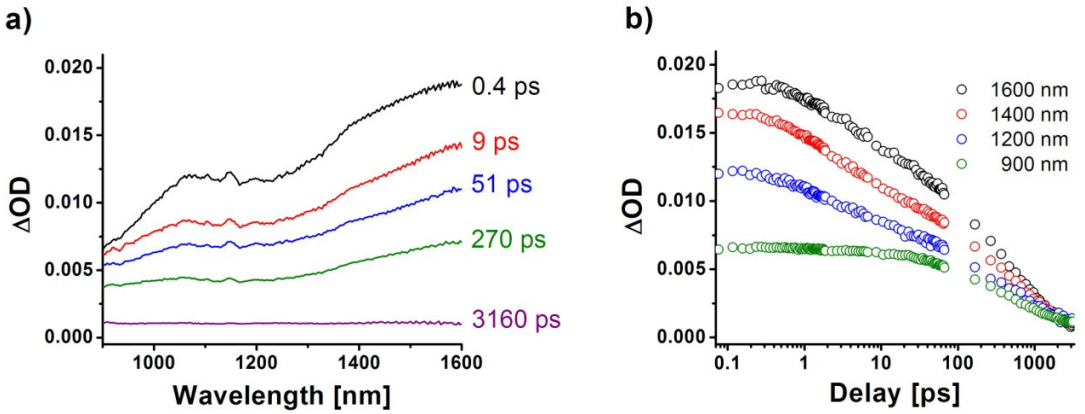

Figure 6.5. a) Transient spectra recorded at different pump-probe delays (given here as labels on the right-hand side of the spectra) measured for a 0.1 M toluene solution of **TPD-C12**; b) kinetic traces at different wavelengths, measured for the same sample as in a). The excitation wavelength was 350 nm and the average power of pump beam was 1.1 mW.

As can be seen in Figure 6.5a the excited state of **TPD-C12** in toluene solution shows a strong transient absorption signal in the NIR region and according to Figure 6.5b the majority of the ΔOD signal decays within 3 ns, consistent with fluorescence decay measurements (see Figure 6.2). The obtained data were fitted with a sum of three exponential functions (see Chapter 2, section 2.2.2.13) to yield three lifetime values, τ_1, τ_2, and τ_3, and three sets of corresponding preexponential amplitudes, $A_1(\lambda)$, $A_2(\lambda)$, and $A_3(\lambda)$. These are shown in Figure 6.6a and the transients at different wavelengths together with the best-fit functions are shown in Figure 6.6b.

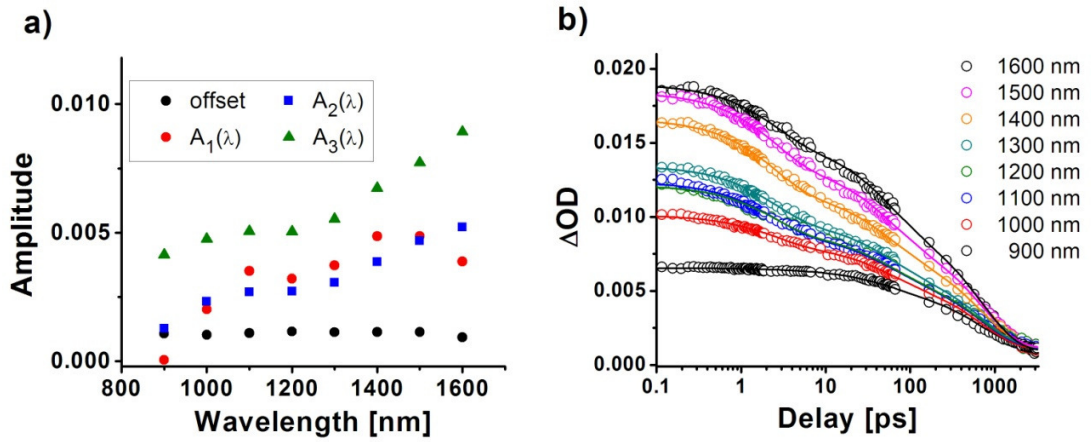

Figure 6.6. a) Spectral distribution of preexponential amplitudes obtained by fitting the data for a **C12-TPD** 0.1M toluene solution with a sum of three exponential functions. The corresponding lifetimes were: τ_1 = 2.4 ± 0.04 ps, τ_2 = 49 ± 2 ps, and τ_3 = 700 ± 12 ps ; b) kinetic traces (circles) and the corresponding curves from fitting the data (solid lines) with a sum of three exponential functions for the same sample as in a).

The results of the fitting presented in Figure 6.6 show that the dynamics of the initially-excited state of **TPD-C12** are rather complicated and involve an ultrafast (τ_1 = 2.4 ± 0.04 ps) process, perhaps conformational changes of the TPD moiety such as planarization of the biphenyl backbone,[12,13] and another, slower process (τ_2 = 49 ± 2 ps). The long decay component of the spectral evolution (τ_3 = 700 ± 12 ps) shows somewhat similar lifetime to that measured by TC-SPC (see Figure 6.2), suggesting that the spectral distribution of $A_3(\lambda)$ represents the spectral profile of the excited singlet state of **TPD-C12**.

Fs NIR-TA was also employed to measure the dynamics of the loss of polarization, i.e., the decay of the transient-absorption anisotropy in the photoexcited

TPD-C12 in toluene solution. Figure 6.7 presents the molecular origin of the transient anisotropy as well as the method of measurement of anisotropy dynamics.

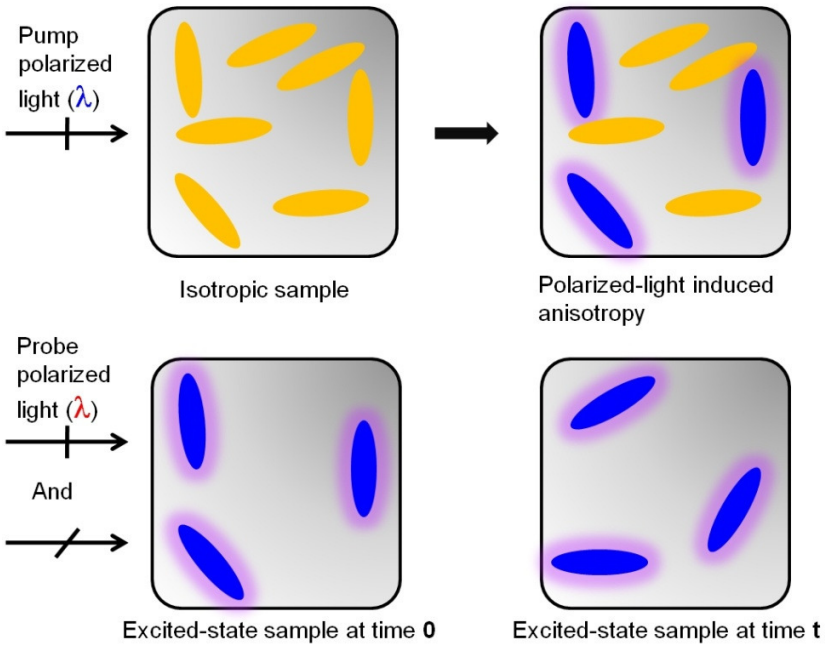

Figure 6.7. The molecular origin of photoinduced anisotropy. Top panel: the polarized laser pulse causes photoexcitation preferentially of molecules (yellow ellipsoids) with transition dipole moment vectors (along the long axis of the ellipsoid) aligned with the direction of polarization of the pump pulse (cross-mark on the arrow) to form excited-state species (blue ellipsoids). Bottom panel: only excited molecules are shown. A second beam is used to probe the ΔOD(t) of the initially anisotropic, i.e., polarized, photoexcited sample with two different probe pulses – one that has polarization parallel and the other perpendicular the pump pulse, and thus to follow the dynamics of depolarization of the sample. Over time, molecules can change their orientation due to various effects.

As shown in Figure 6.7, the initial pump pulse of linearly polarized light induces a polarization in the sample, according to:

$$P_{exc} \propto (\mu \cos \varphi)^2 \qquad \textbf{Equation 6.1}$$

where P_{exc} is the probability of excitation of a molecule, μ is the magnitude of the transition dipole moment (TDM) of the molecule and φ is the angle between the transition dipole moment of the molecule and the direction of polarization of light in the pump pulse.[11] At a given wavelength the $\Delta OD(t)$ of the polarized photoexcited sample can be monitored with a probe pulse that has parallel or perpendicular polarization with respect to the polarization of the pump pulse. The transient anisotropy, $R(t)$, is defined by:

$$R(t) = \frac{\Delta OD_{par}(t) - \Delta OD_{perp}(t)}{\Delta OD_{par}(t) + 2\Delta OD_{perp}(t)} \qquad \textbf{Equation 6.2}$$

where $\Delta OD_{par}(t)$ is the time-dependent change in the optical density measured by the probe pulse with parallel polarization with respect to the pump pulse and $\Delta OD_{perp}(t)$ is the time-dependent change in the optical density measured by the probe pulse with perpendicular polarization with respect to the pump pulse.[14,15]

A trace of anisotropy at 1500 nm measured for **TPD-C12** in toluene solution is presented in Figure 6.8. The large positive value of anisotropy present right after photoexcitation suggests that the TDM leading to the photoexcitation of the ground state of TPD moiety is roughly parallel to the TDM of the transitions of the excited state of the dye responsible for the observed signal in the NIR region.[14] The TDM leading to the excitation of the ground-state of the TPD moiety is oriented approximately along the long molecular axis of the molecule (i.e., the line connecting the two nitrogen atoms).[16] This and the large initial value of anisotropy measured for **TPD-C12** in toluene suggest that the TDM of the electronic transition of the excited state of the TPD moiety, which gives rise to ΔOD in the NIR region, is also oriented along the long molecular axis.

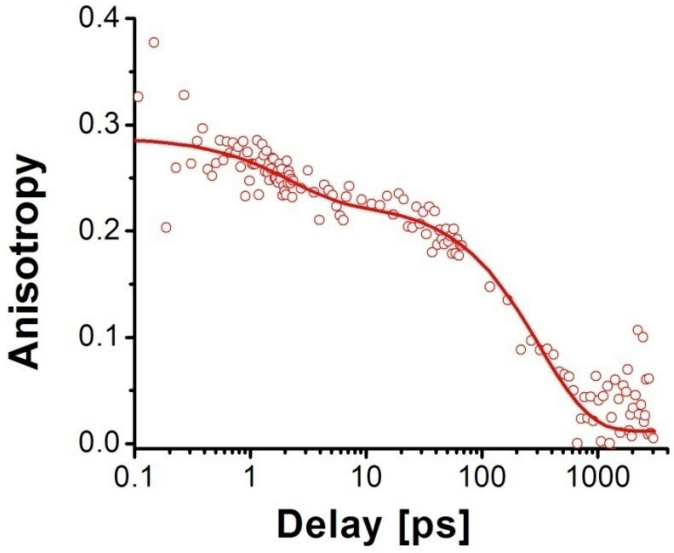

Figure 6.8. Anisotropy decay, $R(t)$, of photoexcited **TPD-C12** in toluene (circles) and the best-fit curve based on a sum of two exponential functions.

The TA anisotropy decay at 1500 nm shown in Figure 6.8 was fitted with a sum of two exponential functions. The lifetimes and the corresponding preexponential amplitudes of the best-fit function were found to be: $\tau_1 = 2.1 \pm 0.9$ ps ($A_1 = 0.06$), $\tau_2 = 320 \pm 40$ ps ($A_2 = 0.22$). The fast component, $\tau_1 = 2.1 \pm 0.9$ ps, is only a minor contribution ($A_1 = 0.06$) to the decay and it may be related to changes in conformation of the excited state of **TPD-C12**, as the lifetime of this component is similar to the fast component observed in the decay of ΔOD which was described earlier (see Figure 6.6, component with lifetime τ_1). The major component of the anisotropy decay ($A_2 = 0.22$) shows lifetime of ca. 320 ps. This is on the order of the timescale typically associated with depolarization via rotational diffusion for molecules of similar size.[17]

6.2.1.2. Solid-state properties

Figure 6.9 shows transient spectra recorded for a neat film of **TPD-C12** casted from toluene solution onto a glass slide using fs excitation at 350 nm. As shown with the red arrows, the spectrum of the initially excited state of TPD moiety (black line) evolves differently in different spectral regions – ΔOD around 1100 nm decays while the intensity of the signal around 1500 nm increases. The long lived signal, still present after 3 ns from the photoexcitation, with the spectral profile showing a maximum ΔOD around 1500 nm (purple line) was not present in the case of **TPD-C12** in toluene solution (see Figure 6.6). This suggests that after the photoexcitation the solid-state **TPD-C12** excited state decays fast but with the subsequent formation of a new, long-lived species with a distinct spectral profile represented by the purple line in Figure 6.9.

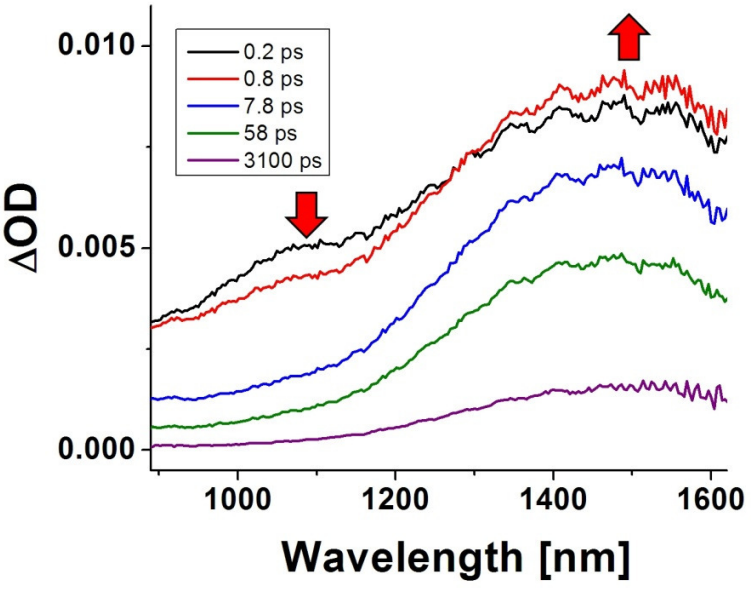

Figure 6.9. Transient spectra recorded at different pump-probe delays measured for a neat film of **TPD-C12**. The arrows show the direction of the evolution of ΔOD for the first two spectra.

The data recorded for the neat film of **TPD-C12** were fitted with a sum of three exponential functions. The spectral distributions of preexponential amplitudes of the best-fit function are shown in Figure 6.10a and the transients, together with the best-fit functions at different wavelengths, are presented in Figure 6.10b.

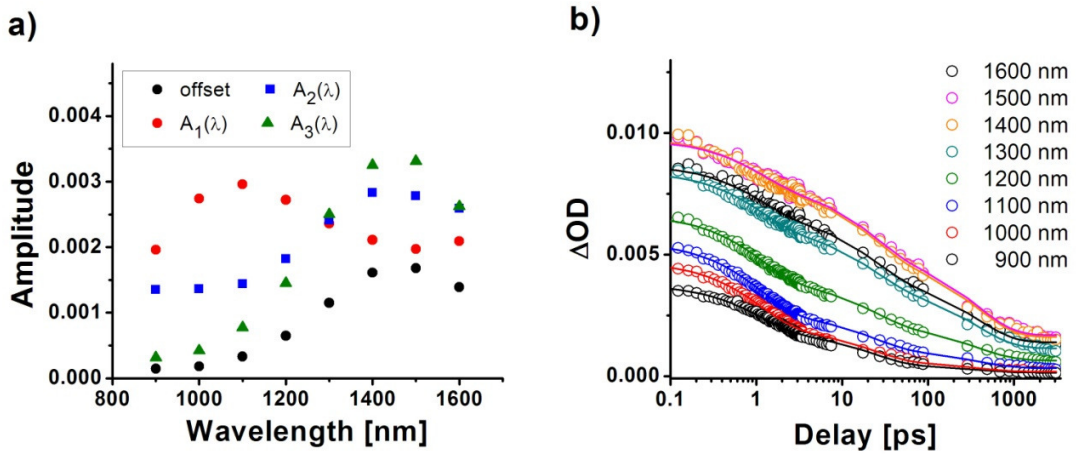

Figure 6.10. a) Spectral distribution of preexponential amplitudes obtained by fitting the data for a neat film of **TPD-C12** on glass with a sum of three exponential functions. The corresponding lifetimes were: τ_1 = 1.1 ± 0.02 ps, τ_2 = 22 ± 1 ps, and τ_3 = 370 ± 20 ps ; b) kinetic traces (circles) and the corresponding curves from fitting the data (solid lines) with a sum of three exponential functions for the same sample as in a).

The lifetimes and preexponential amplitudes found from fitting the data acquired for a **TPD-C12** neat film (Figure 6.10a) are different from those found for the toluene solution (Figure 6.6). The spectral signatures of the two long-lived components in the case of neat film of **TPD-C12**, $A_3(\lambda)$ and the offset in Figure 6.10a, are absent in the fitting results for **TPD-C12** in toluene solution (Figure 6.6a). Also, it is not clear what

process gives rise to the component with τ_2 = 22 ± 1 ps and with the amplitudes $A_2(\lambda)$ (blue squares in Figure 6.10a) in the case of the neat film.

The spectral distribution of preexponential amplitudes for the shortest-lived component ($A_1(\lambda)$, red circles in Figure 6.10a) looks different than the initially measured spectrum of the photoexcited **TPD-C12** in the neat film (black line in Figure 6.9). This requires a comment. Figure 6.9 shows that while ΔOD around 1100 nm rapidly decays, there is *a subsequent growth* of ΔOD in the 1500 nm region at early times after photoexcitation of the neat film of **TPD-C12**. Again, this suggests that while the initially-excited state of **TPD-C12** decays there is a subsequent formation of a new, spectrally-distinct species (X). The simplest process that can lead to such behavior can be described with:[b]

$$\textbf{TPD-C12*} \xrightarrow{k_1} \textbf{X} \xrightarrow{k_3} \textbf{TPD-C12}$$

where **TPD-C12*** is the initially excited state of **TPD-C12**,[c] which decays with a rate constant k_1 to form a spectrally-distinct species **X**. **X** decays to form the ground state of **TPD-C12** with a rate constant k_3. Equations describing the time-dependent concentrations of both **TPD-C12*** and **X** are shown below:

$$[TPD-C12^*](t) = [TPD-C12^*]_0 e^{-k_1 t} \qquad \textbf{Equation 6.3}$$

$$[X](t) = [TPD-C12^*]_0 \frac{k_1}{k_3-k_1}(e^{-k_1 t} - e^{-k_3 t}) \qquad \textbf{Equation 6.4}$$

where *[TPD-C12*]$_0$* is the initial concentration of the excited state of **TPD-C12**, i.e., the concentration of the excited states of **TPD-C12** right after the excitation pulse. Both

[b] While this model is oversimplified, additional branching of the decay channels of **TPD-C12*** leading to the formation of non-absorbing species would not change the conclusions of the discussion.

[c] Another oversimplification in the presented model is that it does not take into account the kinetics of the process leading to the population of the excited state, i.e., the absorption kinetics during the excitation pulse. Instead the population of excited states right after the excitation pulse, i.e., after the duration of the instrument response function (ca. 350 fs), is chosen as the starting point in the model.

TPD-C12* and **X** contribute to the measured ΔOD in the fs NIR-TA experiment. According to Beer's law, the total $\Delta OD(t, \lambda)$ can then be described by the following equation:

$$\Delta OD(t,\lambda) = \Delta OD_{TPD-C12*}(t,\lambda) + \Delta OD_X(t,\lambda) =$$

$$= b\varepsilon_{TPD-C12^*}(\lambda)[TPD - C12^*]_0 e^{-k_1 t} +$$

$$+b\varepsilon_X(\lambda)[TPD - C12^*]_0 \frac{k_1}{k_3 - k_1}(e^{-k_1 t} - e^{-k_3 t}) \qquad \textbf{Equation 6.5}$$

where $\Delta OD_{TPD\text{-}C12*}(t, \lambda)$ and $\Delta OD_X(t, \lambda)$ are the contributions to the total $\Delta OD(t, \lambda)$ from **TPD-C12*** and **X**, respectively, b is the optical path length, and $\varepsilon_{TPD\text{-}C12*}(\lambda)$and $\varepsilon_X(\lambda)$ are molar extinction coefficients of **TPD-C12*** and **X**, respectively.

Grouping the terms with the same time constant, Equation 6.5 can be rewritten as:

$$\Delta OD(t,\lambda) = b[TPD - C12^*]_0 \left(\varepsilon_{TPD-C12^*}(\lambda) + \varepsilon_X(\lambda)\frac{k_1}{k_3 - k_1}\right) e^{-k_1 t} +$$

$$+b[TPD - C12^*]_0 \varepsilon_X(\lambda)\frac{k_1}{k_1 - k_3} e^{-k_3 t} \qquad \textbf{Equation 6.6}$$

The coefficient of the exponential terms in equation 6.6 effectively describe the form of the preexponential amplitudes A_1 and A_2:

$$A_1(\lambda) = b[TPD - C12^*]_0 \left(\varepsilon_{TPD-C12^*}(\lambda) + \varepsilon_X(\lambda)\frac{k_1}{k_3 - k_1}\right) \qquad \textbf{Equation 6.7}$$

$$A_2(\lambda) = b[TPD - C12^*]_0 \varepsilon_X(\lambda)\frac{k_1}{k_1 - k_3} \qquad \textbf{Equation 6.8}$$

As can be seen from Equation 6.7, the wavelength-dependent preexponential amplitude $A_1(\lambda)$ does not have the same spectral distribution as the molar extinction coefficient of **TPD-C12***, $\varepsilon_{TPD\text{-}C12*}(\lambda)$. Instead, the molar extinction coefficient of **TPD-C12***, the rate constants k_1 and k_3, and the molar extinction coefficient of the species **X** all contribute to $A_1(\lambda)$. If $k_3 << k_1$, as seems to be the case for **TPD-C12** neat film (as $\tau_3 >> \tau_1$), Equation 6.7 takes the form:

$$A_1(\lambda) = b[TPD - C12^*]_0\left(\varepsilon_{TPD-C12^*}(\lambda) - \varepsilon_X(\lambda)\right)$$ **Equation 6.9**

Thus, the spectral distribution of the preexponential amplitude A_1 found from the fitting routine described for fs NIR-TA data of the neat film of **TPD-C12** (see Figure 6.10a, red circles) is not the same as the spectrum of the initially-excited **TPD-C12** (see Figure 6.9, black line). Rather, the spectral distribution of $A_1(\lambda)$ represents a difference in the molar extinction coefficients of **TPD-C12*** and **X**.

The spectrum of the molar extinction coefficient of **X** can be, in principle, estimated from $A_1(\lambda)$ and from the profile of $\varepsilon_{TPD\text{-}C12^*}(\lambda)$, which can be obtained from the early-time spectrum of the neat film of **TPD-C12**, according to:

$$\varepsilon_X(\lambda) = \varepsilon_{TPD-C12^*}(\lambda) - \frac{A_1(\lambda)}{b[TPD-C12^*]_0}$$ **Equation 6.10**

The spectral profile of preexponential amplitudes of the long-lived component ($A_3(\lambda)$, τ_3 = 370 ± 20 ps, green triangles in Figure 6.10a) found from the fitting of fs NIR-TA data for the neat film of **TPD-C12**, which in the above discussion corresponds to species **X**, shows negligible amplitude at 900 nm. This implies that at 900 nm the molar extinction coefficient of species **X**, $\varepsilon_X(900)$, is also negligible. Thus, from Equation 6.10, at 900 nm:

$$\varepsilon_X(900) = 0 = \varepsilon_{TPD-C12^*}(900) - \frac{A_1(900)}{b[TPD-C12^*]_0}$$ **Equation 6.11**

which implies:

$$A_1(900) = b[TPD - C12^*]_0\varepsilon_{TPD-C12^*}(900)$$ **Equation 6.12**

Additionally, for the early-time transient spectrum ($t << k_1^{-1}$) of the photoexcited neat film of **TPD-C12** (black line in Figure 6.9) equation 6.6 becomes:

$$\Delta OD(900) = b[TPD - C12^*]_0\varepsilon_{TPD-C12^*}(900)$$ **Equation 6.13**

Thus:

$$\Delta OD(900) = A_1(900) \qquad \textbf{Equation 6.14}$$

Figure 6.11 shows the early time spectrum of the photoexcited **TPD-C12** neat film (after 0.2 ps from the excitation pulse) as well as the spectral distribution of the preexponential amplitudes of the fast component found from the fitting routine, $A_1(\lambda)$, both normalized at 900 nm. Since the shape of the early-time spectrum of the photoexcited sample is the same as the shape of $\varepsilon_{TPD\text{-}C12^*}(\lambda)$, the normalized $A_1(\lambda)$ was subtracted from the normalized early-time spectrum of the photoexcited **TPD-C12** to yield the shape of $\varepsilon_X(\lambda)$, which is also shown in Figure 6.11 (black squares). It can be seen that the profile of $\varepsilon_X(\lambda)$, which was calculated based on the discussion above, overlaps well with the profile of the long-lived component $A_3(\lambda)$ found from the fitting routine of the data acquired for **TPD-C12** neat film. This implies that the initially excited state of **TPD-C12** in the neat film decays with a time constant k_1 = 1 / (1.1 ps), and a new species is generated at the same rate, which lives for 370 ± 20 ps and shows the spectral shape described by $A_3(\lambda)$ (green triangles in Figure 6.10a).

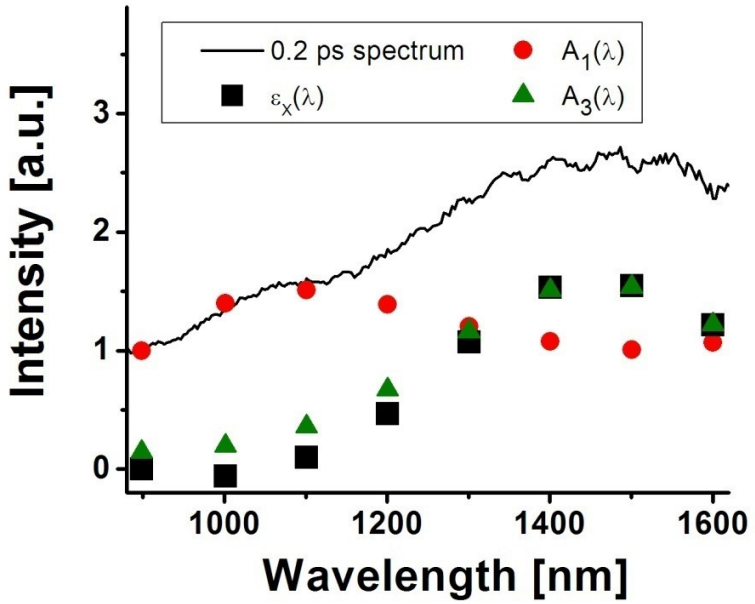

Figure 6.11. Spectral profiles of the early-time (0.2 ps) spectrum of photoexcited **TPD-C12** neat film (normalized at 900 nm), preexponential amplitudes $A_1(\lambda)$ (normalized at 900 nm) from the fitting routine on the data acquired for **TPD-C12** neat film, the result of the subtraction of the normalized $A_1(\lambda)$ from the normalized early-time spectrum of photoexcited **TPD-C12**, $\varepsilon_X(\lambda)$, and $A_3(\lambda)$ which was multiplied by a constant to match the value of $\varepsilon_X(\lambda)$ at 1500 nm. See text for details.

As mentioned before, the above discussion is oversimplified as the routine used for fitting the data acquired for the neat film of **TPD-C12** had to involve three exponential functions in order to find good fits. However, the data treatment based on the simple model described above resulted in calculating the spectrum of $\varepsilon_X(\lambda)$ with practically the same shape as the spectral distribution of preexponential amplitudes of the long-lived component found from fitting, $A_3(\lambda)$. This suggests that the long-lived species with the spectral profile described by $A_3(\lambda)$ was generated from the initial excited state of **TPD-C12** and that the component that persists for ca. 22 ps ($A_2(\lambda)$), the nature of which

is not clear, is perhaps formed right after photoexcitation and simply decays to the ground state.

It is important to address the question of the nature of the long-lived species generated from the initially-excited state of **TPD-C12** in the neat film. The fact that the spectrum of this species was not detected in the case of toluene solution of **TPD-C12** suggests that interactions between neighboring **TPD-C12** molecules may be involved in the excited-state dynamics in the neat film. The formation of an intermolecular excited-state complex involving two or more **TPD-C12** molecules, i.e., a formation of an excimer-like species, is thus probably responsible for the spectral signature seen only in **TPD-C12** neat film.

The spectrum of the unknown species is nearly identical to the spectrum of the radical cation of **TPD-C12**, which was chemically generated in toluene.[d] Figure 6.12 shows a comparison of the spectrum of **TPD-C12** radical cation (**TPD$^{\bullet+}$-C12**) and the spectral distribution of $A_3(\lambda)$ from Figure 6.10. The nearly perfect overlap of these spectra suggests that the photogenerated species in **TPD-C12** neat film may in fact be **TPD$^{\bullet+}$-C12**. Two major scenarios of the formation of **TPD$^{\bullet+}$-C12** in the photoexcited **TPD-C12** neat film can be envisioned. First, the excitation-pulse photon energy, 3.54 eV, facilitates two-photon photoionization of **TPD-C12**. The ionization potential of TPD in the solid state is ca. 5.5 eV[18] which is less energy than the sum of two excitation photons in the fs NIR-TA experiment. However, since the two-photon photoionization is a nonlinear process, pump-power dependence would be expected for the photoionization efficiency.

[d] A dry dichloromethane solution of a substoichiometric amount of $[(p\text{-}BrC_6H_4)_3N]^{\bullet+}[SbCl_6]^-$ was added to a dry toluene solution of **C12-TPD**. The absorption spectrum of the solution in the UV-Vis-NIR range was acquired in a 1 cm cuvette.

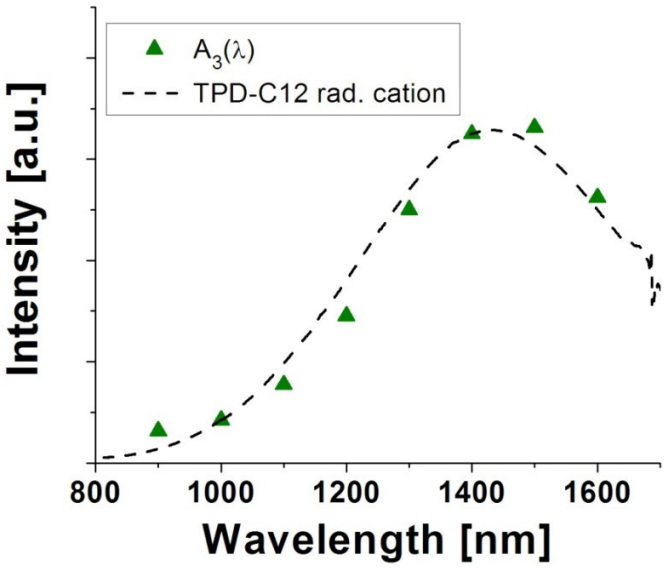

Figure 6.12. Preexponential amplitudes $A_3(\lambda)$ found from the fitting of the fs NIR-TA data acquired for neat film of **TPD-C12** and NIR absorption spectrum of a chemically-generated **TPD-C12** radical cation in toluene solution. Both spectra were multiplied by a constant to match their intensity at 1400 nm.

If two-photon photoionization took place in the **TPD-C12** neat film, a nonlinear pump-power dependence of the abundance of the long-lived species would be observed, i.e., the shapes of kinetic profiles of fs NIR-TA signals at different wavelengths would depend on the excitation power. However, a power dependence study of the neat film of **TPD-C12** showed no effect of the pump power on the shapes of kinetic profiles of ΔOD.[e] This suggests that the two-photon photoionization is not likely to take place in the studied system.

[e] It should be noted that the power range in which the experiments were performed was rather small, 0.14 - 0.42 mW, due to issues with sample stability at higher power values and low signal-to-noise at excitation power lower than 0.14 mW. It was observed that the early-time ΔOD at 1500 nm (close to the peak of the absorption spectrum of **TPD$^{\bullet+}$-C12**) scaled linearly with the excitation power thus suggesting that two-photon photoionization is not responsible for the formation of the TPD-cation-like species and that a one-photon excitation mechanism is instead involved.

Another scenario that could lead to the formation of **TPD$^{\bullet+}$-C12** in the neat film of **TPD-C12** is an electron transfer from a photoexcited **TPD-C12** molecule to an electron acceptor. Since the only component of the studied material is **TPD-C12**, the electron transfer would have to take place between two **TPD-C12** molecules. The resulting radical cation, **TPD$^{\bullet+}$-C12**, and the radical anion, **TPD$^{\bullet-}$-C12**, would be bound via Coulombic interactions and the resulting ion pair would persist until charge recombination takes place.[11]

While the possibility of the electron transfer between two **TPD-C12** molecules in the photoexcited neat film cannot be excluded, there is yet another potential explanation of the observed properties of the neat film of **TPD-C12**. As mentioned before, the excited state of **TPD-C12** can interact with a neighboring ground-state molecule, or molecules, to form an excited-state complex, an electronically coupled excimer-like species. If the electronic structure of such species involves charge transfer from the initially photoexcited **TPD-C12** molecule to the other electronically-coupled molecules, its spectral characteristics would be similar to **TPD$^{\bullet+}$-C12**. Such charge-transfer excitons have been proposed to contribute to transient absorption spectra of photoexcited crystalline pentacene[19] and photoexcited films of π-conjugated polymers.[20]

6.2.2. The Photophysics of TPD-coated Gold Nanoparticles

*6.2.2.1. Fs NIR-TA of **AuS-Cx-TPD** Systems (x = 3, 4, 8, 12)*

Figure 6.13 shows transient spectra and kinetic traces measured for toluene solutions of **AuS-Cx-TPD** systems (x = 3, 4). It can be seen that in both samples the initial transient spectrum (black lines in Figures 6.13a and c) shows similar shape to the

spectrum of the initially-excited state of **TPD-C12** (see Figure 6.5a). This suggests that the majority of the observed signal originates from the photoexcited TPD moieties, i.e., the contribution to ΔOD from the metallic core of Au NPs is small (see section 2.2.2.13 in Chapter 2 for more details).

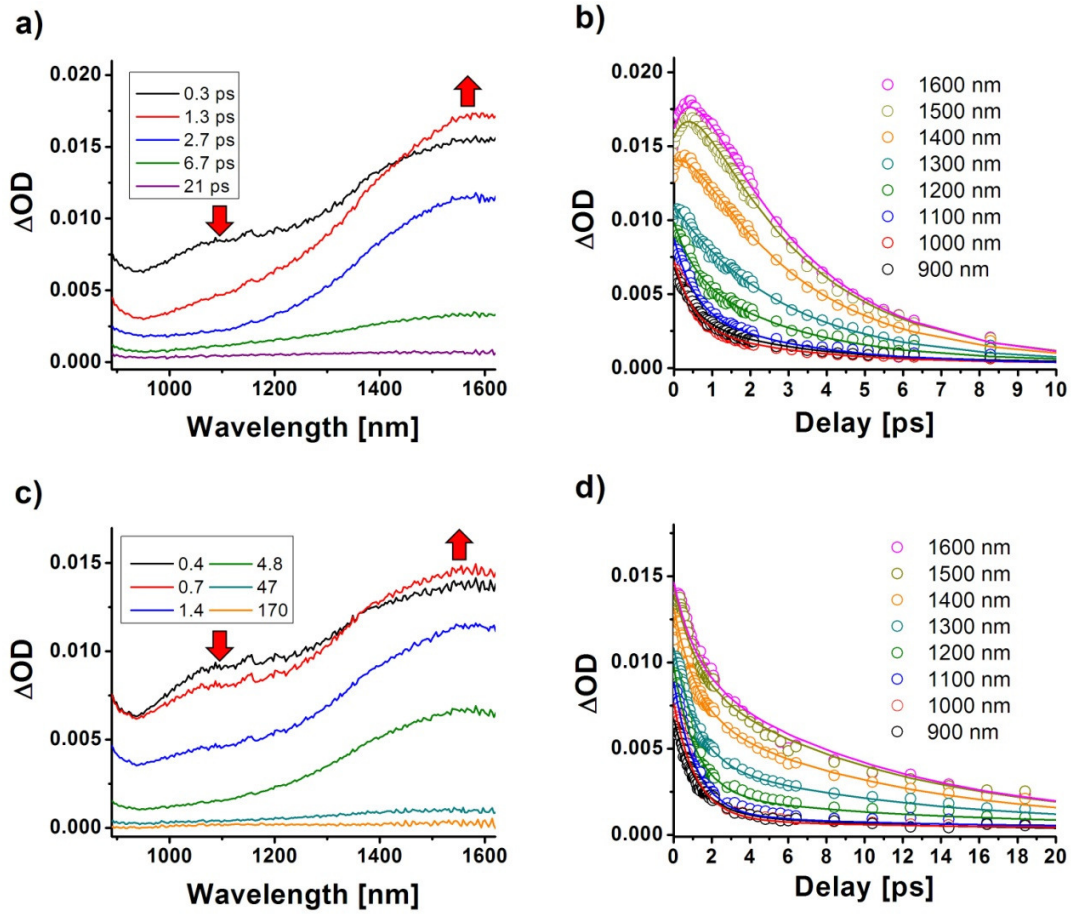

Figure 6.13. Transient spectra, as measured, at different pump-probe delays[f] for toluene solutions of a) **AuS-C3-TPD** and c) **AuS-C4-TPD**. Transients at different wavelengths after subtraction of the contributions to ΔOD from the metallic core of Au NPs[g] for: b) **AuS-C3-TPD** and d) **AuS-C4-TPD**. The solid lines in b) and d) represent the best-fit functions based on the fitting of the data with a sum of two exponential functions.

[f] The time-zero delay in graphs a) and c) is defined as the delay between the pump pulse and the probe pulse at which the rising edge of the signal was recorded. The time-zero delay in graphs b) and d) is the same as the time zero used for fitting the data (see section 2.2.13 in Chapter 2), i.e., one width of the instrument response function (ca. 350 fs) later than the delay between the pump pulse and the probe pulse at which the rising edge of the signal was recorded.

[g] See section 2.2.13 in Chapter 2 for details regarding the procedure of subtraction of the contribution of the metallic core of Au NPs to ΔOD.

The dynamics of ΔOD measured for toluene solutions of **AuS-C3-TPD** and **AuS-C4-TPD** and presented in Figure 6.13 are significantly different than those recorded for **TPD-C12** in toluene solution. First, the majority of the signal has disappeared after a just few tens of ps, in contrast to the hundreds of ps in the case of **TPD-C12** in toluene solution (see Figure 6.6). Second, the initial dynamics in both NP systems show similar behavior to that observed in **TPD-C12** neat film. In particular, there seems to be a decay of signal around 1100 nm with a subsequent growth of ΔOD around 1600 nm. This is shown with red arrows in Figures 6.13a and c.

Transient spectra and kinetic traces measured for toluene solutions of **AuS-C8-TPD** and **AuS-C12-TPD** are shown in Figure 6.14. As in the case of the two NP systems with shorter alkyl linkers, the shape of the initial transient spectra observed for **AuS-C8-TPD** and **AuS-C12-TPD** (black line in Figures 6.14a and c) is very similar to the shape of the initial transient spectrum recorded for **TPD-C12** in toluene solution, thus, suggesting that the majority of the observed signal originates from the photoexcited TPD moieties. Also, the decay of ΔOD is much faster than in the case of the toluene solution of **TPD-C12**. However, in contrast to the NP systems incorporating shorter alkyl linkers between the TPD moiety and the surface-anchoring thiol group, **AuS-C8-TPD** and **AuS-C12-TPD** show no ΔOD growth around 1500 nm. Thus, the systems incorporating longer alkyl linkers between the TPD moiety and the surface-anchoring thiol group do not show a behavior similar to that observed for the neat film of **TPD-C12**, as was the case for **AuS-C3-TPD** and **AuS-C4-TPD**.

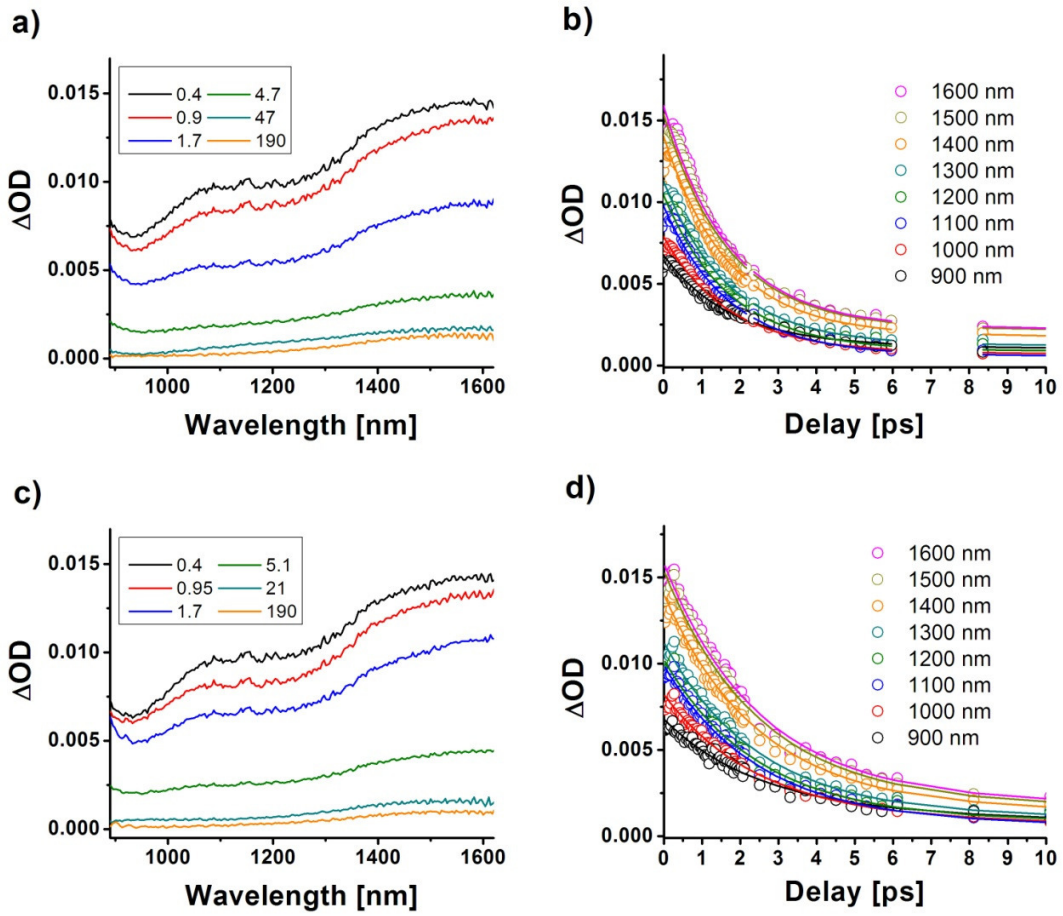

Figure 6.14. Transient spectra, as measured, at different pump-probe delays[h] for toluene solutions of a) **AuS-C8-TPD** and c) **AuS-C12-TPD**. Transients at different wavelengths after subtraction of the contributions to ΔOD from the metallic core of Au NPs[i] for: b) **AuS-C8-TPD** and d) **AuS-C12-TPD**. The solid lines in b) and d) represent the best-fit functions based on the fitting of the data with a sum of two exponential functions.

Each set of data obtained for toluene solutions of **AuS-Cx-TPD** systems (x = 3, 4, 8, 12) after subtracting contributions from the metallic core of NPs was fitted with a sum of two exponential functions, as described in section 2.2.2.13 of Chapter 2. The spectral

[h] See footnote to figure 6.13 for definition of time delay in the various graphs.
[i] See section 2.2.13 in Chapter 2 for details regarding the procedure of subtraction of the contribution of the metallic core of Au NPs to ΔOD.

distributions and the corresponding lifetimes obtained for the best fits are presented in Figure 6.15.

As can be seen in Figures 6.15c and d, only one major decay component was found for toluene solutions of **AuS-C8-TPD** and **AuS-C12-TPD**, with the respective lifetimes of 1.68 ps and 2.40 ps. In both cases, the spectral distributions of the preexponential amplitudes of the major decay component, $A_1(\lambda)$, overlap nearly perfectly with the early-time (ca. 1 ps delay) transient spectrum of **TPD-C12** in toluene solution (black solid lines in Figures 6.15c and d). This suggests that the excited-state deactivation of the TPD moieties in the abovementioned NP systems does not involve the generation of NIR-absorbing species and, most likely, proceeds via the channel of energy transfer from the photoexcited TPD to the metallic core of Au NPs.[1-3,5] For comparison, the excited-state lifetime of TPD in NP-free toluene solution was measured to be ca. 700 ps (see Figure 6.6). Thus, the TPD excited-state lifetimes in **AuS-C8-TPD** and **AuS-C12-TPD** are more than two orders of magnitude shorter than for the same, isolated chromophore in solution.

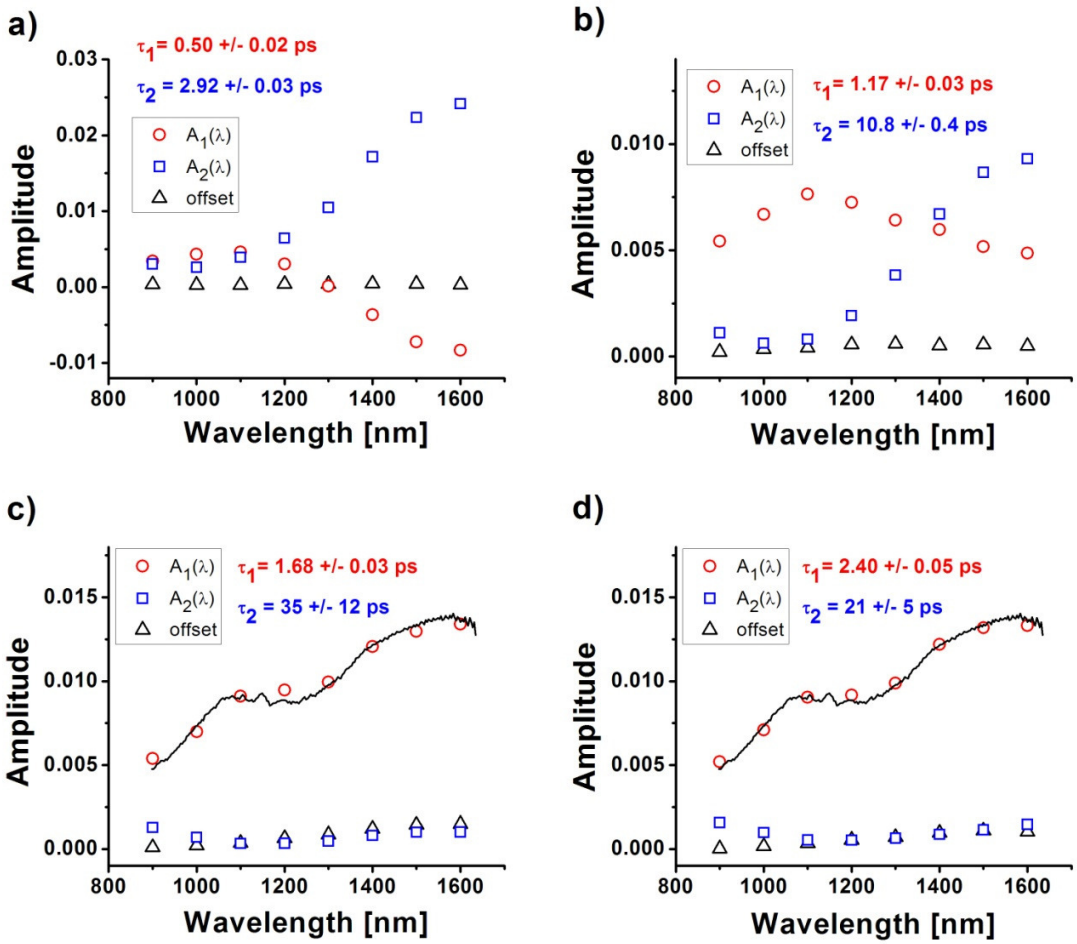

Figure 6.15. Spectral distributions of preexponential amplitudes and the corresponding lifetimes obtained by fitting the fs NIR-TA data obtained for toluene solutions of a) **AuS-C3-TPD**, b) **AuS-C4-TPD**, c) **AuS-C8-TPD**, and d) **AuS-C12-TPD**. A sum of two exponential functions was used in the fitting routine. The black solid lines in c) and d) correspond to a transient spectrum of photoexcited **TPD-C12** in 0.1 M toluene solution after pump-probe delay of ca. 1 ps.

Fitting the data for **AuS-C3-TPD** and **AuS-C4-TPD** gave two decay components for each NP sample with substantial values of preexponential amplitudes (Figures 6.15a and b). It can be seen that the spectral distributions of preexponential amplitudes of the fast decay components in both NP samples, $A_1(\lambda)$ in Figures 6.15 a and b, do not have the

same shape as the early-time spectra measured for the samples (black lines in Figures 6.13 a and c). In fact, in the case of **AuS-C3-TPD** the preexponential amplitudes $A_1(\lambda)$ show negative values in the spectral region 1300-1600 nm. This, together with the observed growth of ΔOD around 1500 nm presented in Figures 6.13a and c (red arrows), suggests that, as in the case of neat film of **TPD-C12** discussed in section 6.2.1.2, there is an ultrafast formation of a new, spectrally-distinct species subsequent to the decay of the excited state of TPD moiety, for both **AuS-C3-TPD** and **AuS-C4-TPD**. The lifetimes of the TPD excited state in the NP systems incorporating shorter alkyl linkers between the TPD moiety and the surface-anchoring thiol group are very short – 0.50 ps and 1.17 ps for **AuS-C3-TPD** and **AuS-C4-TPD**, respectively. The deactivation of the excited state of TPD most likely occurs via two channels in these systems – one involving energy transfer to the NP,[1-3,5] and another involving the formation of the new spectrally distinct species. Further, the generated species, the nature of which is not clear, shows lifetimes of 2.92 ps and 11 ps for **AuS-C3-TPD** and **AuS-C4-TPD**, respectively.

It is instructive to compare the spectral distributions of preexponential amplitudes found for the unknown, spectrally-distinct species in both **AuS-C3-TPD** and **AuS-C4-TPD**, $A_2(\lambda)$ with the NIR absorption spectrum measured for the **TPD-C12** radical cation in toluene solution (**TPD$^{\bullet+}$-C12**), and to the shape of the spectrum of the preexponential amplitudes found for the long-lived component in the neat film of **TPD-C12** (see Figure 6.12). Figure 6.16 shows such a comparison. It can be seen that the shapes of the spectral distributions $A_2(\lambda)$ found for **AuS-C3-TPD** and **AuS-C4-TPD** are nearly the same and, although red-shifted, they closely resemble the shapes of both the NIR absorption spectrum of **TPD$^{\bullet+}$-C12** and of the spectral distribution of the preexponential amplitudes

$A_3(\lambda)$ found for the long-lived component present in the photoexcited **TPD-C12** neat film.

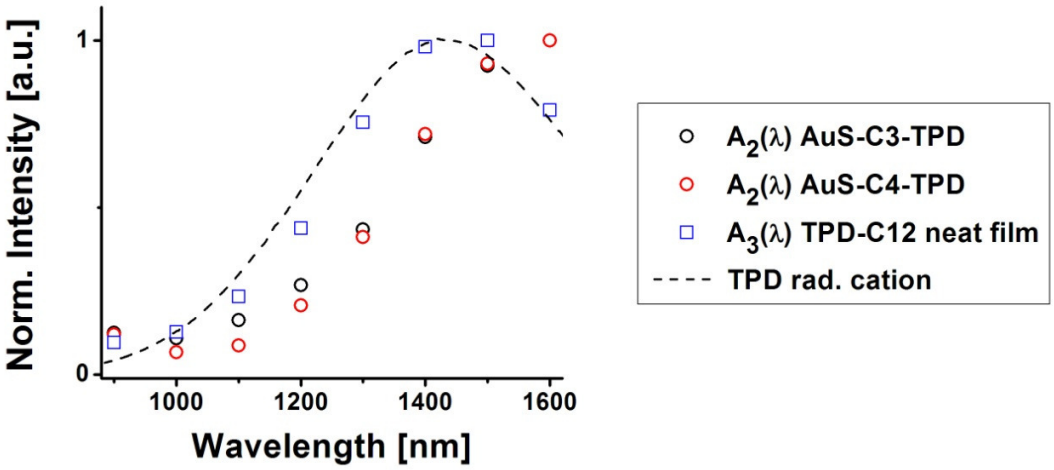

Figure 6.16. Normalized spectral distributions of preexponential amplitudes found for **AuS-Cx-TPD** (x = 3, 4), $A_2(\lambda)$, and for the long-lived component found for the neat film of **TPD-C12** ($A_3(\lambda)$ in Figure 6.10a). A normalized NIR absorption spectrum of the **TPD-C12** radical cation is shown for comparison.

The question arises regarding the nature of the new species present in **AuS-C3-TPD** and **AuS-C4-TPD**. The fact that the spectral distributions corresponding to these species are the nearly the same for the two NP samples suggests that in both cases the same species has been formed. Further, the close resemblance of its spectrum to the spectra of both **TPD$^{\bullet+}$-C12** and of the species generated in photoexcited neat film of **TPD-C12** suggests that the nature of the species generated in the NP samples is either the TPD radical cation (TPD$^{\bullet+}$) or an intermolecular charge-transfer exciton (see the last paragraph of section 6.2.1.2). This was further investigated by studying the excited state

dynamics of TPD in the mixed-ligand systems – **AuS-Cx-TPD(DDT$_{60}$)** (x = 3, 4, 8, 12) and is described in section 6.2.2.2.

Regardless of the nature of the species generated in **AuS-C3-TPD** and **AuS-C4-TPD**, the efficiency of its formation depends on the length of the alkyl linker between the TPD moiety and the surface-anchoring thiol group. This conclusion is supported by the fact that in the case of **AuS-C8-TPD** and **AuS-C12-TPD** the abovementioned species is not observed at all.

*6.2.2.2. Fs NIR-TA of **AuS-Cx-TPD(DDT$_{60}$)** systems (x = 3, 4, 8, 12)*

Figure 6.17 shows the spectral distributions of preexponential amplitudes and the corresponding lifetimes obtained for the best fits of fs NIR-TA data acquired for toluene solutions of **AuS-Cx-TPD(DDT$_{60}$)** systems (x = 3, 4, 8, 12). It can be seen that in the case of **AuS-C8-TPD(DDT$_{60}$)** and **AuS-C12-TPD(DDT$_{60}$)** fitting of the data resulted in the spectral distributions of preexponential amplitudes closely resembling the shape of the early-time spectrum of photoexcited **TPD-C12** in toluene (black line in Figures 6.17c and d). Additionally, the excited-state lifetimes of these mixed-ligand systems were found to be the same, within experimental uncertainty, as those found for the corresponding high-TPD-coverage systems (see Figure 6.15a and b). This suggests that there is little or no TPD-coverage influence on the dynamics of the deactivation of the TPD excited state in the systems incorporating **TPD-C8-thiol** and **TPD-C12-thiol** ligands.[j]

[j] This is true only within the limits of coverage described here, i.e., down to the coverage of ca. 40% with respect to the high-TPD-thiol-coverage samples. The fs NIR-TA signals in the case of **AuS-Cx-TPD(DDT$_{90}$)** systems (x = 3, 4, 8, 12), i.e., the lowest TPD-thiol-coverage systems that were described in Chapter 5, showed rather small contribution to ΔOD from photoexcited TPD moieties and, conversely,

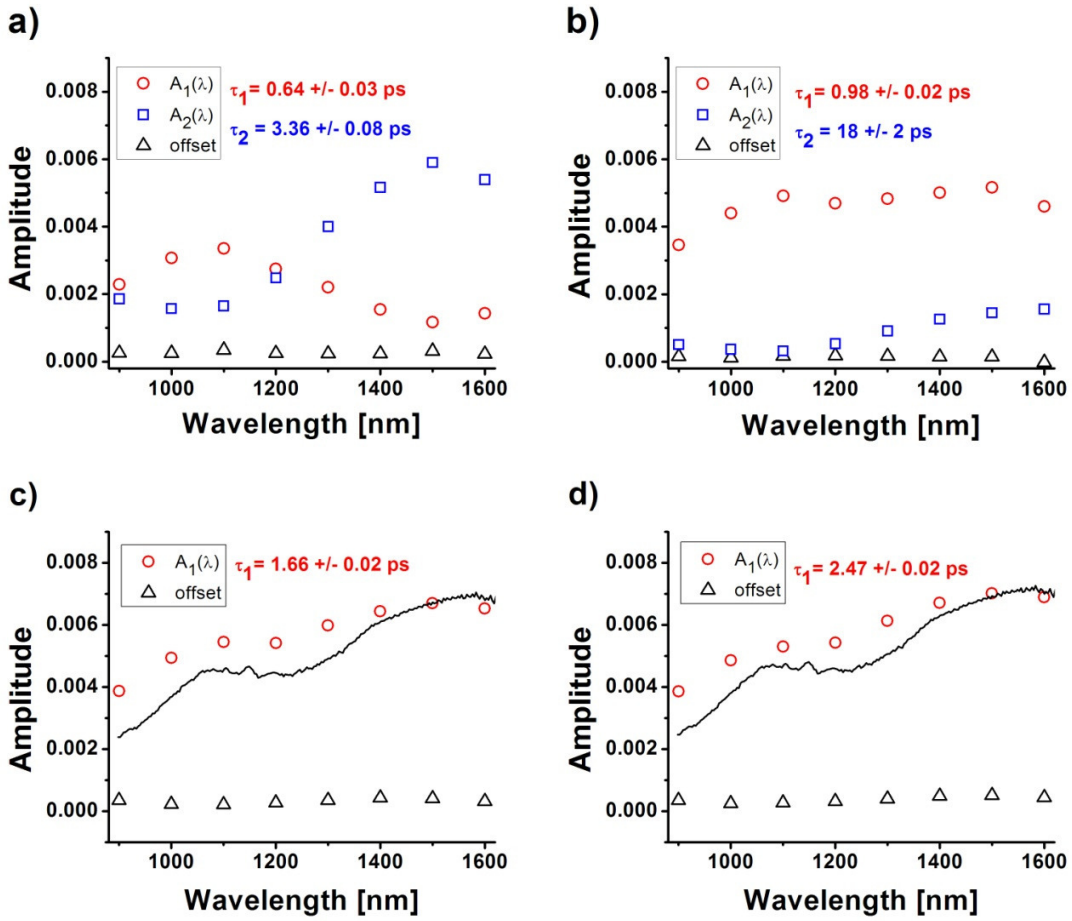

Figure 6.17. Spectral distributions of preexponential amplitudes and the corresponding lifetimes obtained by fitting the fs NIR-TA data for toluene solutions of a) **AuS-C3-TPD(DDT$_{60}$)**, b) **AuS-C4-TPD(DDT$_{60}$)**, c) **AuS-C8-TPD(DDT$_{60}$)**, and d) **AuS-C12-TPD(DDT$_{60}$)**. A sum of two exponential functions was used in the fitting routine in the case of a) and b) and a single exponential function was used for fitting in the case of c) and d).[k] The black solid lines in c) and d) correspond to a transient spectrum of photoexcited **TPD-C12** in 0.1 M toluene solution after pump-probe delay of ca. 1 ps.

large contributions from the metallic cores of Au NPs. Due to these complications the fs NIR-TA data acquired for those systems are not discussed here.

[k] Fitting the data obtained for **AuS-C8-TPD(DDT$_{60}$)** and **AuS-C12-TPD(DDT$_{60}$)** with a sum of two exponential functions in each case resulted in best fit which showed two components of practically the same lifetime. Thus, a single exponential function was used for fitting fs NIR-TA data acquired for these two samples.

As can be seen in Figures 6.17a and b, the fitting of data acquired for toluene solutions of **AuS-C3-TPD(DDT$_{60}$)** and **AuS-C4-TPD(DDT$_{60}$)** resulted, in each case, in two components with significant amplitudes and with lifetimes that are somewhat different from those found for the corresponding high-TPD-thiol-coverage systems (see Figures 6.15a and b for comparison). The spectrally-distinct species which was present in **AuS-Cx-TPD** (x = 3, 4) is also found in the case of **AuS-C3-TPD(DDT$_{60}$)** and **AuS-C4-TPD(DDT$_{60}$)**. However, its abundance seems to be smaller for the low-TPD-thiol-coverage samples. This can be inferred from the fact that the preexponential amplitudes $A_2(\lambda)$ in the spectral region 1300-1600 nm in Figures 6.17a and b show smaller values (relative to the corresponding $A_1(\lambda)$ in the spectral region 900-1200 nm for the same sample) than the amplitudes $A_2(\lambda)$ found for **AuS-Cx-TPD** (x = 3, 4), (see Figures 6.15a and b for comparison). This suggests that the formation of the spectrally-distinct species depends on the TPD-thiol coverage.

Additional evidence for the effect of TPD-thiol coverage on the ultrafast dynamics of the TPD excited-state in the systems incorporating **TPD-C3-thiol** and **TPD-C4-thiol** is presented in Figures 6.18a and b. Normalized kinetic traces recorded at 1600 nm – the wavelength at which the spectrally-distinct species discussed above exhibits most prominent signal – are shown for **Au-Cx-TPD** and **Au-Cx-TPD(DDT$_{60}$)** systems (x = 3, 4). As can be seen from the figure, there are substantial differences in the shapes of the kinetic traces, i.e., in both cases (Figure 6.18a and b) the normalized kinetic traces recorded at 1600 nm for the **Au-Cx-TPD(DDT$_{60}$)** systems show lower signal at longer delay times. This confirms that the formation of the spectrally-distinct species, which shows longer lifetime than the lifetime of the initially-excited state of TPD, in the Au NP

systems incorporating **TPD-C3-thiol** and **TPD-C4-thiol** is less efficient for systems in which the TPD-thiol coverage is lower.

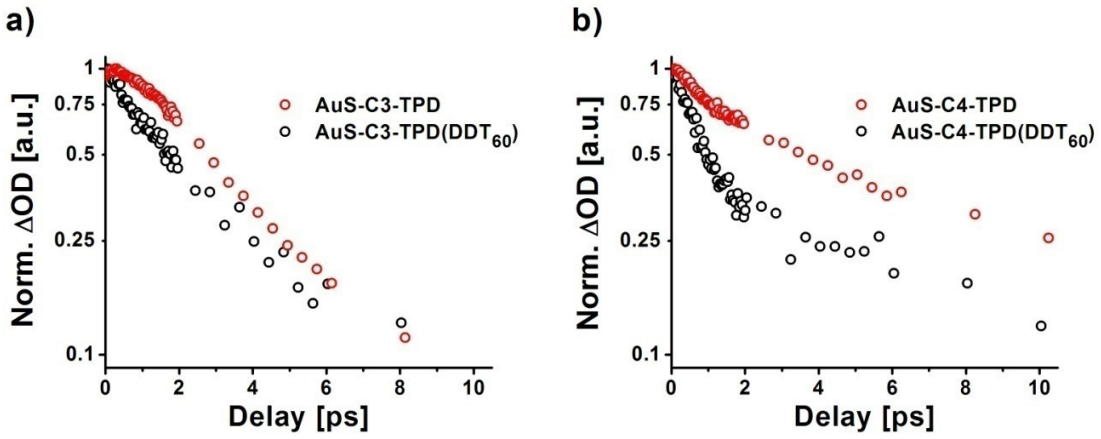

Figure 6.18. Normalized kinetic traces at 1600 nm for a) Au NPs incorporating **TPD-C3-thiol** and b) Au NPs incorporating **TPD-C4-thiol**. The contributions of metallic cores of Au NPs were subtracted as described in section 6.2.2.13 of Chapter 2.

6.2.2.3. Discussion of the fs NIR-TA data

The nature of the species generated in Au NPs incorporating **TPD-C3-thiol** and **TPD-C4-thiol** is not clear. As mentioned before, the spectral signature of the species suggests either TPD radical cation ($TPD^{\bullet+}$) or an intermolecular charge-transfer exciton. The photoinduced formation of $TPD^{\bullet+}$ in the NP systems could, in principle, proceed either via an electron transfer from the photoexcited TPD moiety to the metallic core of the Au NP, or via an electron transfer to a neighboring TPD moiety. While there have been several reports suggesting an electron transfer from photoexcited dyes to gold NPs,[4,21,22] the data described here favor the scenario involving dye-dye interaction. In particular, the observed TPD-thiol-coverage dependence of the spectrally-distinct-species

formation efficiency suggests that an intermolecular process is involved. This is further supported by the similarity of the fs NIR-TA data measured for the NP systems incorporating **TPD-C3-thiol** and **TPD-C4-thiol** with the data obtained for the neat film of **TPD-C12**. As in the case of the **TPD-C12** neat film, it is not clear whether the spectrally-distinct species is in fact $TPD^{\bullet+}$ formed after an electron transfer from the photoexcited TPD moiety to a ground-state TPD (which would result in the formation of $TPD^{\bullet-}$), or an intermolecular complex with a charge-transfer character (intermolecular charge-transfer exciton). However, in the context of this work, the distinction between the two is rather subtle. In the case of the photoinduced electron transfer an ion pair would be formed, which would remain bound by the Coulombic interactions[11] and which would exhibit the NIR spectrum of $TPD^{\bullet+}$. On the other hand, the formation of a charge-transfer exciton would also manifest itself with the NIR spectrum similar to that of $TPD^{\bullet+}$ and, as in the case of the ion pair after the photoinduced electron transfer, it would result in intermolecular binding, only in this case not solely via the Coulombic interactions as electronic coupling between neighboring TPD moieties would be involved.[19]

It is important to reiterate that the systems incorporating **TPD-C3-thiol** and **TPD-C4-thiol** show similar behavior to that observed in the neat film of **TPD-C12**. The fact that this solid-like behavior is seen in the photoexcited NP systems incorporating the two shortest alkyl spacers but not in the systems involving **TPD-C8-thiol** and **TPD-C12-thiol**, can be related to the average dye–dye distance. Due to the curvature of the NP surface and the different lengths of the spacers (from ca. 0.5 nm for C3- and ca. 1.6 nm for fully extended C12-linkers, respectively), the dye–dye distance is expected to be

approximately 1.5 times larger in **AuS-C12-TPD** than in **AuS-C3-TPD**.[23,l] As discussed above, the formation of the spectrally-distinct species most likely involves an intermolecular process involving two, or more TPD moieties. Thus, the distance between the TPD moieties in the NP systems, smaller in the nanostructures incorporating TPD-thiols with shorter alkyl spacers, plays a crucial role in facilitating dye-dye interactions which lead to the formation of the intermolecular species. This behavior is opposite to the report on TC-SPC measurements of Au NP / pyrene-Cx-thiol systems where the excimer formation was proposed to be progressively more efficient in nanostructures incorporating longer alkyl spacers between the pyrene moiety and Au NP surface.[6]

The experiments described in the preceding sections show that there is an influence of the structure of TPD-thiols incorporated in the Au NP systems on the TPD-excited-state lifetime. The total rate of deactivation of the TPD excited state, k_1, is the sum of the radiative, k_r, and nonradiative, k_{nr}, rates:[10,11]

$$k_1 = k_r + k_{nr} \qquad \textbf{Equation 6.15}$$

The radiative rates for the NP systems studied here have not been established due to problems with instability of fluorescence signal during data acquisition. However, the radiative rate of **TPD-C12** in toluene solution can be calculated from:[10,11]

$$k_r = \frac{\eta_{fl}}{\tau_{TPD-C12}} \qquad \textbf{Equation 6.16}$$

[l] Assuming for simplicity the same molecular footprint of the TPD-Cx-thiols and fully extended alkyl spacers in both **AuS-C3-TPD** and **AuS-C12-TPD**, the calculated ratio of average dye-dye distances for the two systems were calculated according to $\frac{D_{AuS-C12-TPD}}{D_{AuS-C3-TPD}} = \frac{r_{Au\,NP}+d_{C12}}{r_{Au\,NP}+d_{C3}}$, where $D_{AuS-Cx-TPD}$ is the average dye-dye distance in AuS-Cx-TPD system, and $r_{Au\,NP} + d_{Cx}$ is the sum of the NP radius ($r_{Au\,NP}$, here 1.7 nm) and the length of the fully extended alkyl spacer (d_{Cx}, 0.5 nm and 1.6 nm for C3 and C12 linkers, respectively).

where η_{fl} is the fluorescence quantum yield of **TPD-C12** in toluene solution (0.80 for deoxygenated toluene solution, see section 6.2.1.1) and $\tau_{TPD\text{-}C12}$ is the lifetime of **TPD-C12** in toluene solution (1.07 ns, as measured by TC-SPC for deoxygenated toluene soltuion, see section 6.2.1.1). The value of k_r, calculated according to Equation 6.16, was found to be 0.75×10^9 s^{-1}. This is ca. three orders of magnitude lower than the total rates of deactivation of TPD excited state, k_1 (shown in Figure 6.19). Additionally, the radiative rate of deactivation of the TPD moiety on the surface of Au NPs studied herein is most likely even lower than the value found for **TPD-C12**. This is based on the observation that the molar extinction coefficient of the **TPD-C12-thiol** attached to the surface of NPs is smaller than that of the free dye in solution, as described in section 5.3.6.3 of Chapter 5 and as shown in Figure 5.23. Since the radiative rate is proportional to the integrated molar extinction coefficient,[10,24] it is expected that the observed reduction of the molar extinction coefficient of **TPD-C12-thiol** upon binding to Au NPs translates into the reduction of k_r. Thus, the value of k_r is most likely ca. two or more orders of magnitude smaller than the total deactivation rates of TPD excited state in the Au NP systems studied here. This implies:

$$k_1 \approx k_{nr} \qquad \textbf{Equation 6.17}$$

Based on the literature reports on the dependence of the nonradiative rate of organic fluorophores attached to Au NPs, thought to be dominated by energy transfer to the gold NP, on the distance between the fluorophore and the NP surface, r, the relation $k_{nr} \propto \frac{1}{r^4}$ was found for a variety of systems (this mechanism of energy transfer was termed nanosurface energy transfer, NSET).[24,25] In the case of the well-known dipole-dipole energy transfer (Förster resonance energy transfer, FRET) the energy-transfer rate

can be described by $k_{FRET} \propto \frac{1}{r^6}$.[10,11] Thus, if energy transfer is the dominating channel of deactivation, it can be written:

$$\log k_{nr} \propto -n \log r \qquad \textbf{Equation 6.18}$$

where n = 4 for NSET and n = 6 for FRET.

Figure 6.19 shows the dependence of the decay rates of the TPD excited state in the NP systems studied herein as a function of the number of methylene groups in the alkyl linker between the TPD moiety and the surface-anchoring thiol group.[m]

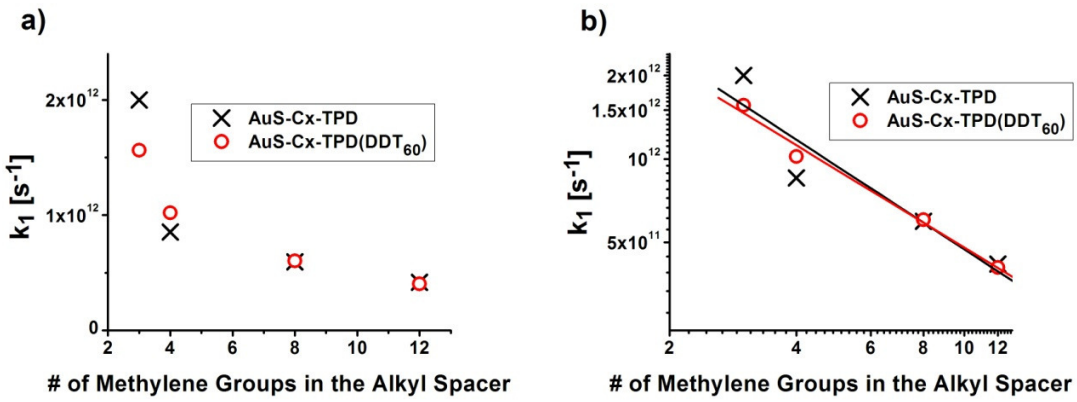

Figure 6.19. Dependence of the rate of deactivation of the excited state of TPD in the NP systems studied herein on the number of methylene units in the alkyl spacer between the TPD moiety and the surface-anchoring thiol group. The data were plotted on a) linear plot, and b) log-log plot. The solid lines show the linear fits of the data for **AuS-Cx-TPD** systems (black line) and for **AuS-Cx-TPD(DDT$_{60}$)** systems (red line).

First, it can be seen that the calculated rates do not depend strongly on the TPD-thiol coverage. Second, the TPD-excited-state deactivation rates plotted against the

[m] These were calculated according to $k_1 = (1/\tau_1)$ where k_1 is the rate of deactivation of the TPD excited state and τ_1 is the lifetime of the TPD excited state (see Figures 6.15 and 6.17) found from fitting data for **AuS-Cx-TPD** and **AuS-Cx-TPD(DDT$_{60}$)** systems.

number of methylene units in the alkyl linker between the dye and the surface-anchoring thiol group, i.e., plotted against the distance of the TPD moiety from the NP surface, show a linear dependence on a log-log plot (Figure 6.19b). Each data set was fitted with a linear function resulting with the best fits described by the slopes of -0.99 and -0.93 for **AuS-Cx-TPD** and **AuS-Cx-TPD(DDT$_{60}$)** sample series, respectively. The values of the slopes suggest that, according to Equation 6.18 with which the observed linear dependence is consistent, and considering experimental errors, the dependence of the nonradiative deactivation rate of the TPD excited state on its distance from the NP surface takes the form:

$$k_{nr} \propto \frac{1}{r} \qquad \textbf{Equation 6.19}$$

If the nonradiative rate is dominated by the energy transfer, as seems to be the case,[n] it can be written:

$$k_{nr} \approx k_{ET} \propto \frac{1}{r} \qquad \textbf{Equation 6.20}$$

where k_{ET} is the rate of energy transfer from the TPD excited state to the metallic core of the Au NP. This is rather surprising considering that NSET rate depends on fourth and FRET rate on sixth power of $\frac{1}{r}$, respectively.

[n] The existence of the additional nonradiative deactivation channel in the case of NPs incorporating **TPD-C3-thiol** and **TPD-C4-thiol**, i.e., the formation of the spectrally-distinct species, complicates things. However, the rates of the formation of the spectrally-distinct species are most likely not dominant as the excited-state lifetime of the TPD excited state does not depend strongly on the TPD-thiol coverage.

6.2.2.4. Ultrafast depolarization of TPD-thiol-coated Au NPs

Figure 6.20 shows anisotropy decays measured for toluene solutions of **AuS-Cx-TPD** systems (x = 3, 4, 8, 12) at 1500 nm.[o] Since at this wavelength TPD excited-state absorption dominates, i.e., the contribution to the measured ΔOD from the metallic cores of Au NPs is small, the calculated anisotropy is related to the orientation of the photoexcited TPD moieties with respect to the direction of the pump-pulse polarization. The changes of anisotropy in time give insights into the dynamics of reorientation of transition dipole moments of electronic transitions probed by fs NIR-TA (see Figure 6.7 for the description of the molecular origin of TA anisotropy).

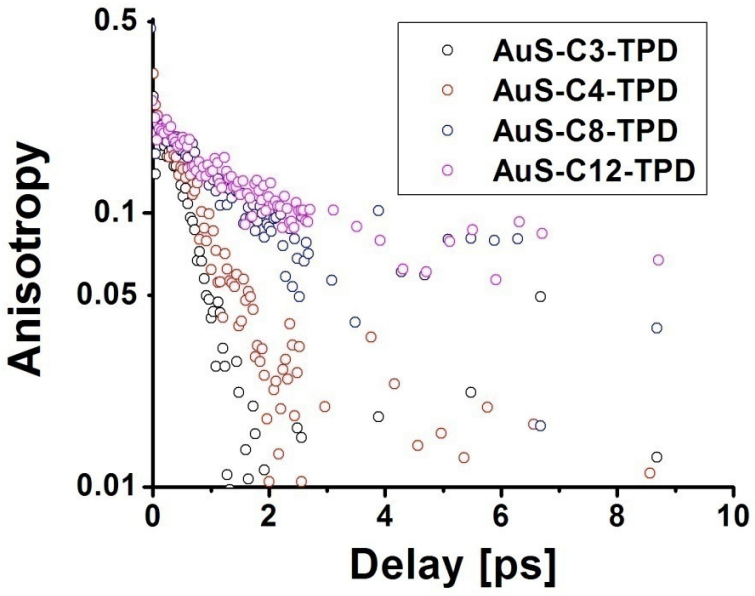

Figure 6.20. Anisotropy decays at 1500 nm measured for toluene solutions of **AuS-Cx-TPD** (x = 3, 4, 8, 12). The time-zero delay is defined as the delay between the pump and the probe pulses at which the rising edge of the signal of transient absorption was recorded.

[o] The anisotropy was calculated according to Equation 6.2.

It can be seen that the depolarization of the photoexcited TPD moieties is ultrafast for all NP systems shown in Figure 6.20. This is rather surprising as the depolarization measured for **TPD-C12** in toluene solution was much slower, on the order of 320 ps, and it was consistent with the mechanism of depolarization via rotational diffusion (see Figure 6.8 and related discussion in section 6.2.1.1). It is unlikely that the large volume **AuS-Cx-TPD** systems (x = 3, 4, 8, 12) exhibit faster rate of rotational diffusion in toluene solution than the much smaller free **TPD-C12** dye.[7] Thus, the mechanism of depolarization is most likely not related to the rotation of the Au NPs.

Another possibility is that the observed depolarization is caused by reorientation of the photoexcited TPD moieties within their free volume on the surface, i.e., reorientation of the TPD moieties which is independent of the movement of the whole NP. As discussed in Chapter 5 section 5.3.4 and in section 6.2.2.3 of this chapter, the NP-surface curvature influences the average dye-dye distance, i.e., as supported by the ^{1}H NMR spin-spin relaxation measurements, systems with longer alkyl linkers between the TPD moiety and the surface-anchoring thiol group exhibit larger average dye-dye distances. Thus, the free volume accessible to each surface-bound TPD moiety depends on the length of the alkyl linker. What follows is that reorientation of TPD moiety after the photoexcitation is expected to proceed at the highest rate for **AuS-C12-TPD** and the lowest rate is expected for **AuS-C3-TPD** due to more steric hindrance in the latter system. However, as seen in Figure 6.20, the opposite trend is observed, i.e., the anisotropy decay is fastest for **AuS-C3-TPD** and it becomes slower as the length of the alkyl linker between the TPD moiety and the surface-anchoring thiol group increases.

This suggests that the mechanism of depolarization is not likely to involve reorientation of the dye itself.

Ultrafast depolarization based on fluorescence measurements has been reported for a system incorporating silver nanoparticles and organic fluorophores, with the rate on the order of 50 fs.[7] This was rationalized in terms of dipole-dipole energy transfer, or FRET, between the densely-packed chromophores which resulted in the energy migration on the Ag NP surface and led to depolarization of the sample.[7] In order to test if a similar mechanism of depolarization takes place in the Au NP systems studied herein, a set of experiments was performed to address the TPD-thiol coverage dependence of the anisotropy decay rate. The dipole-dipole energy transfer rate, k_{FRET}, is characterized by a strong dependence of the distance between the energy donor and the energy acceptor, r, and is described by $k_{FRET} \propto \frac{1}{r^6}$.[10,11] Thus, lowering the TPD-thiol coverage on the surface of Au NPs is expected to cause a large change in the depolarization rate, i.e., a large change in the rate of anisotropy decay. Figures 6.21a-d show comparisons of anisotropy decays measured at 1500 nm for toluene solutions of **AuS-Cx-TPD** systems with those measured for the corresponding low TPD-thiol-coverage systems **AuS-Cx-TPD(DDT$_{60}$)** (x = 3, 4, 8, 12).

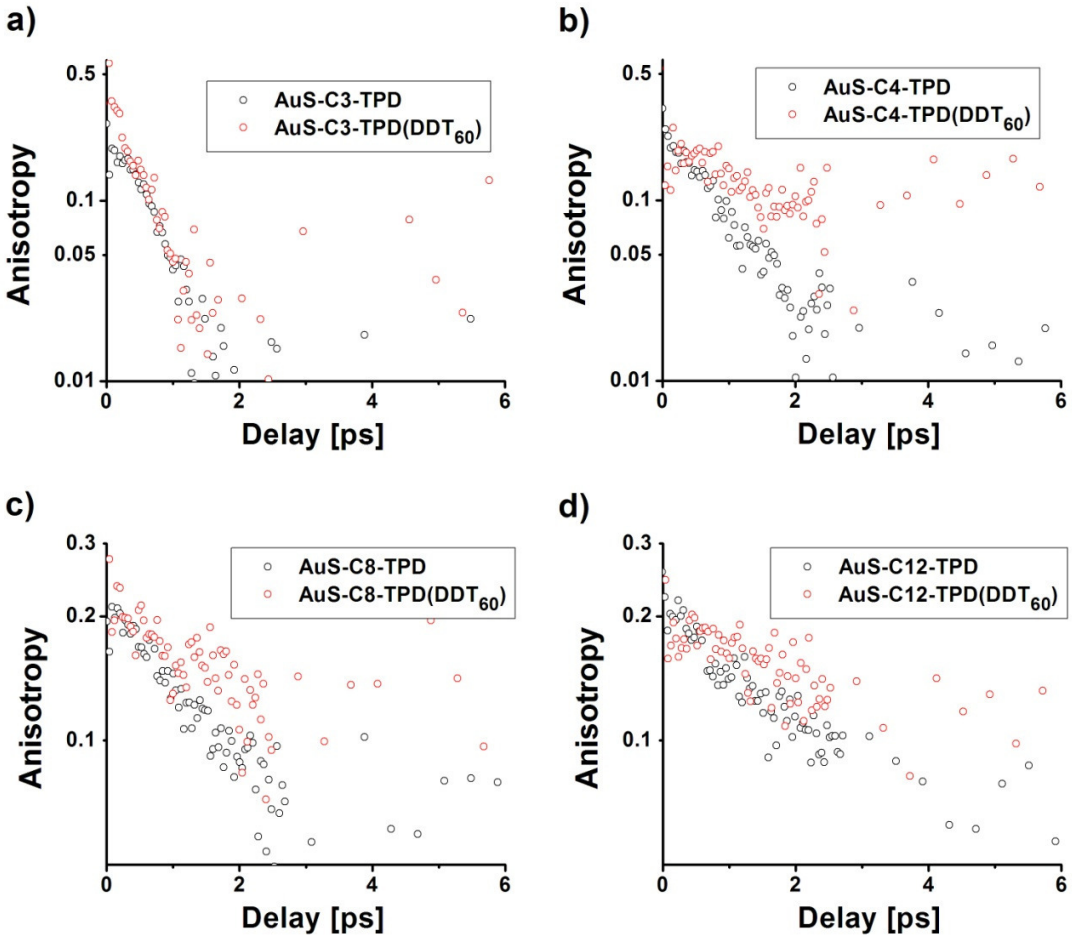

Figure 6.21. Anisotropy decays at 1500 nm measured for toluene solutions of **AuS-Cx-TPD** and **AuS-Cx-TPD(DDT$_{60}$)** systems (x = 3, 4 , 8, 12). The time-zero delay is defined as the delay between the pump and the probe pulses at which the rising edge of the signal of transient absorption was recorded.

The TPD-thiol coverage is reduced by ca. 60% in **AuS-Cx-TPD(DDT$_{60}$)** systems with respect to the corresponding high-TPD-coverage NPs (see Table 5.1). Additionally, ^{1}H NMR experiments suggest that in the mixed-ligand systems the distribution of TPD-thiol ligands on the surface of NPs is statistical, i.e., phase separation of different ligands on the surface is not likely (see Chapter 5, section 5.3.4). The TPD-thiol footprints (i.e., the values of average surface area occupied by one TPD-thiol molecule) in **AuS-Cx-**

TPD(DDT$_{60}$) systems are ca. 2.5 times as large as TPD-thiol footprints in the corresponding **AuS-Cx-TPD** nanostructures (see Table 5.2). This means that the average distance between the dyes on the surface of a gold NP in **AuS-Cx-TPD(DDT$_{60}$)** systems is ca. 1.6 times as large as the average dye-dye distance in **AuS-Cx-TPD** nanostructures.[p] This implies that the rate of FRET in the mixed-ligand systems should decrease by ca. $(1.6)^6 \approx 17$ times relative to the dye-dye energy transfer rate in **AuS-Cx-TPD** systems. However, as can be seen in Figure 6.20, there is very little, if any, influence of the TPD-thiol coverage on the rate of anisotropy decay in all of the investigated samples. This disfavors the dye-dye energy transfer as the mechanism leading to the depolarization of the photoexcited samples.

The nature of the phenomenon leading to the ultrafast TA-anisotropy decay in the studied samples is not clear. The lack of significant TPD-thiol-coverage dependence on the depolarization rate and the observed dependence of the rate on the length of the alkyl linker between the TPD moiety and the surface-anchoring thiol group suggest that the metallic core of the NP may be involved in the depolarization. However, based on the acquired data the role of the metal in the mechanism of the ultrafast depolarization of photoexcited TPD moieties is not clear.

[p] This is based on the dependence $\frac{\pi r_{low\ cov.}^2}{\pi r_{high\ cov.}^2} = \frac{\theta_{TPD}(low\ cov.)}{\theta_{TPD}(high\ cov.)}$ where $r_{low\ cov.}$ is the average TPD-TPD distance in a **AuS-Cx-TPD(DDT$_{60}$)** system, $r_{high\ cov.}$ is the average TPD-TPD distance in the corresponding **AuS-Cx-TPD** system, and θ_{TPD}*(low cov.)* and θ_{TPD}*(high cov.)* are the TPD-thiol footprints found for a **AuS-Cx-TPD(DDT$_{60}$)** and for the corresponding **AuS-Cx-TPD** system, respectively.

6.3. Conclusions

Nanostructures based on bis(diarylamino)biphenyl-based dye molecules attached to the surface of Au NPs via alkylthiol linkers of varying length were studied in the context of their photophysics. The excited-state ultrafast dynamics of the bis(diarylamino)biphenyl moieties in the hybrid Au NP-organic dye systems were monitored in the NIR spectral range with the use of a broadband fs transient absorption technique. The excited-state lifetime of the bis(diarylamino)biphenyl moiety in close proximity to the metallic core of a gold NP was found to be more than two orders of magnitude shorter than the lifetime of the same free chromophore in NP-free toluene solution. This excited-state quenching was attributed mainly to the energy transfer from the photoexcited dye to the metallic core of the Au NP.

It was shown that the alkyl-spacer length between a Au NP and the covalently attached bis(diarylamino)biphenyl moiety has a profound impact on the resulting excited-state dynamics. In particular, the excited-state decay rate of the bis(diarylamino)biphenyl moiety was shown to depend on the length of the alkyl linker and the decay rate was found to be inversely proportional to the distance between the dye and the metal surface. The effect of the alkyl-spacer length between a Au NP and the covalently attached bis(diarylamino)biphenyl moiety was shown to be manifested not only in the dye–NP energy transfer, but also in the presence of a deactivation channel involving the formation of an intermolecular species. It was argued that this deactivation channel is facilitated by the short dye–dye distance in nanostructures incorporating short alkyl spacers between the dye and the metal surface. Additionally, it was discovered that assembling bis(diarylamino)biphenyl moieties on the surface of a Au NP has a large impact on the

depolarization rate of the photoexcited samples. The studied systems exhibited ultrafast transient absorption anisotropy decays with a clear regression of the depolarization rate with the length of the alkyl linker between the bis(diarylamino)biphenyl moiety and the surface-anchoring thiol group. A variety of possible mechanisms of depolarization were discussed and the metallic core of a Au NP was suggested to take part in the process.

6.4. References

(1) Thomas, K. G.; Kamat, P. V. *Acc. Chem. Res.* **2003**, *36*, 888-898.
(2) Dulkeith, E.; Morteani, A. C.; Niedereichholz, T.; Klar, T. A.; Feldmann, J.; Levi, S. A.; van Veggel, F. C. J. M.; Reinhoudt, D. N.; Moller, M.; Gittins, D. I. *Phys. Rev. Lett.* **2002**, *89*, 203002/1-203002/4.
(3) van Herrikhuyzen, J.; Janssen, R. A. J.; Schenning, A. P. H. J.; Meskers, S. C. J. *Chem. Phys. Lett.* **2007**, *433*, 340-344.
(4) Barazzouk, S.; Kamat, P. V.; Hotchandani, S. *J. Phys. Chem. B* **2005**, *109*, 716-723.
(5) Fan, C.; Wang, S.; Hong Janice, W.; Bazan, G. C.; Plaxco, K. W.; Heeger, A. J. *Proc. Natl. Acad. Sci. U. S. A.* **2003**, *100*, 6297-301.
(6) Ipe, B. I.; Thomas, K. G. *J. Phys. Chem. B* **2004**, *108*, 13265-13272.
(7) Varnavski, O. P.; Ranasinghe, M.; Yan, X.; Bauer, C. A.; Chung, S.-J.; Perry, J. W.; Marder, S. R.; Goodson, T. *J. Am. Chem. Soc.* **2006**, *128*, 10988-10989.
(8) Shang, L.; Qin, C.; Wang, T.; Wang, M.; Wang, L.; Dong, S. *J. Phys. Chem. C* **2007**, *111*, 13414-13417.
(9) Griffin, J.; Singh, A. K.; Senapati, D.; Rhodes, P.; Mitchell, K.; Robsinson, B.; Yu, E.; Ray, P. C. *Chem. Eur. J.* **2009**, *15*, 342-351.
(10) Lakowicz, J. R. *Principles of Fluorescence Spectroscopy*; 3rd ed.; Springer: New York, 2006.
(11) Suppan, P. *Chemistry and Light*; The Royal Society of Chemistry: Cambridge, 1994.
(12) Mank, D.; Raytchev, M.; Amthor, S.; Lambert, C.; Fiebig, T. *Chem. Phys. Lett.* **2003**, *376*, 201-206.
(13) Liu, K.-L.; Lee, S.-J.; Chen, I. C.; Hsu, C.-P.; Yeh, M.-Y.; Luh, T.-Y. *J. Phys. Chem. A* **2009**, *113*, 1218-1224.
(14) Fuchs, H.; Zimmermann, J.; Röder, B. *Opt. Commun.* **2003**, *220*, 119-127.
(15) Takaya, T.; Hamaguchi, H.-o.; Iwata, K. *J. Chem. Phys.* **2009**, *130*, 014501.
(16) Vragovic, I.; Calzado, E. M.; Diaz Garcia, M. A. *Chem. Phys.* **2007**, *332*, 48-54.
(17) Verbouwe, W.; Van der Auweraer, M.; De Schryver, F. C.; Piet, J. J.; Warman, J. M. *J. Am. Chem. Soc.* **1998**, *120*, 1319-1324.
(18) Ishii, H.; Sugiyama, K.; Ito, E.; Seki, K. *Adv. Mater.* **1999**, *11*, 605-625.
(19) Tiago, M. L.; Northrup, J. E.; Louie, S. G. *Phys. Rev. B: Condens. Matter* **2003**, *67*, 115212.
(20) Wang, Z.; Mazumdar, S.; Shukla, A. *Phys. Rev. B: Condens. Matter* **2008**, *78*, 235109.
(21) Ipe, B. I.; Thomas, K. G.; Barazzouk, S.; Hotchandani, S.; Kamat, P. V. *J. Phys. Chem. B* **2002**, *106*, 18-21.
(22) Kotiaho, A.; Lahtinen, R.; Lehtivuori, H.; Tkachenko, N. V.; Lemmetyinen, H. *J. Phys. Chem. C* **2008**, *112*, 10316-10322.
(23) Hostetler, M. J.; Wingate, J. E.; Zhong, C. J.; Harris, J. E.; Vachet, R. W.; Clark, M. R.; Londono, J. D.; Green, S. J.; Stokes, J. J.; Wignall, G. D.; Glish, G. L.; Porter, M. D.; Evans, N. D.; Murray, R. W. *Langmuir* **1998**, *14*, 17-30.
(24) Jennings, T. L.; Singh, M. P.; Strouse, G. F. *J. Am. Chem. Soc.* **2006**, *128*, 5462-5467.

(25) Ghosh, S. K.; Pal, T. *Phys. Chem. Chem. Phys.* **2009**, *11*, 3831-3844.

CHAPTER 7

CONCLUSIONS

7.1. Introduction

The studies presented in this thesis were focused on understanding the electronic and spectroscopic aspects of interactions between metallic gold and organic dyes. In particular, the influence of a series of organic π-conjugated thiols, self-assembled on flat gold surfaces, on the electronic properties of the metal was studied with the use of ultraviolet photoelectron spectroscopy (UPS). Also, the effects of the metal on the molecular energy levels in these self-assembled monolayers (SAMs) were investigated. These studies were described in detail in Chapters 3 and 4. Further, the influence of gold nanoparticles on the spectroscopic properties of bis(diarylamino)biphenyl-based organic fluorophores that were covalently attached to the metal surface was investigated with the use of a fs transient absorption technique and was discussed in Chapters 5 and 6. This chapter summarizes the findings in the context of the gained knowledge, potential impact and outlook.

7.2. Influence of π-Conjugated Stilbene Thiols on the Work Function of Gold and the Energy Level Alignment at the Organic / Metal Interface

The UPS studies of 4'-substituted-4-stilbene thiolate SAMs on flat gold revealed that the work function of the metal was significantly affected by the organic adlayers – the reduction of the work function was found to be as large as 1.3 eV. Further, the extent of the work-function change showed a dependence on the substituent present in the

stilbene backbone. It was shown that the observed work-function changes, i.e., changes in the vacuum level close to the surface, induced by the organic adsorbates could be qualitatively rationalized invoking the concept of the electrostatic potential of the dipole moments of the 4'-substituted-4-stilbene thiolates at the metal / organic interface.

The ability to tune the local vacuum level close to the surface with organic materials is of great interest to the organic electronics applications (OEA) community.[1] In particular, the use of monolayers consisting of π-conjugated thiols, which have been shown to exhibit charge-carrier-transport characteristics that can potentially enhance the efficiency of charge injection at the metal / organic interface,[2,3] has been identified as an approach towards building more efficient metal electrodes for OEA.[4] The ability to tune the work function of gold surface with stilbene thiolate-based SAMs, which has been demonstrated in this thesis, is promising in the context of the abovementioned approach.

The position of the molecular energy levels of organic electronic materials (the highest occupied molecular orbital, HOMO, and the lowest occupied molecular orbital, LUMO) with respect to the Fermi level of the metal has been recognized as crucial for efficient charge injection from the metal into the organic layer, i.e., the closer the molecular energy level to the Fermi level, the more efficient the transport.[3,4] Traditionally, materials with low ionization potential (IP) have been used in order to position the HOMO close to Fermi level of metal electrodes.[1] From the experiments described in Chapter 4 it was found that the positions of HOMOs with respect to the Fermi level in the 4'-substituted-4-stilbene thiolates SAMs on gold did not depend significantly on the substituent in the 4' position. It was further shown that even though the IPs of the substituted stilbene thiols were significantly different, that difference did

not manifest itself in different positions of HOMOs with respect to the Fermi level. The rationalization of this behavior was related to the changes in the vacuum level close to the surface that was caused by the dipolar adsorbates. It was argued that for the studied systems the decrease in the IP of the SAM constituent coincided with the increased extent of the drop of the vacuum level close to the surface. The two counteracting effects caused the positions of HOMOs to be nearly the same with respect to the Fermi level of the metal, despite of the significant differences in the IPs of the constituents of the SAMs. This finding is rather significant as it shows that the changes in IP do not necessarily lead to different positions of the molecular energy levels with respect to the Fermi level and that the change in the work function can suppress the effects of IP. It should be noted that to the author's best knowledge this is the first experimental report showing such behavior in SAMs involving π-conjugated thiols and, thus, it would be prudent not to generalize the effects observed here.

One can envision a series of possible experiments that could show rather unequivocally whether the position of the HOMO of an adsorbate with respect to the Fermi level is affected by the adsorbent-induced change in the vacuum level close to the surface. Figure 7.1 shows a schematic of systems that could serve as candidates for such experiments. The π-conjugated backbone of the presented systems is based on the Schiff-base structure which can be prepared in two ways, as shown in the figure. For a given end-substituent R, the molecular IPs of the two different structures would be expected not to differ significantly. However, assuming similar structures of the SAMs, the dipole moment projections on the surface for the two structures would be quite different. This would result in structures showing different work functions for the two systems, i.e.,

different vacuum levels close to the surface, but rather similar molecular IPs. This would in principle allow for testing the effect of the vacuum level close to the surface on the position of HOMO with respect to the Fermi level of the metal.

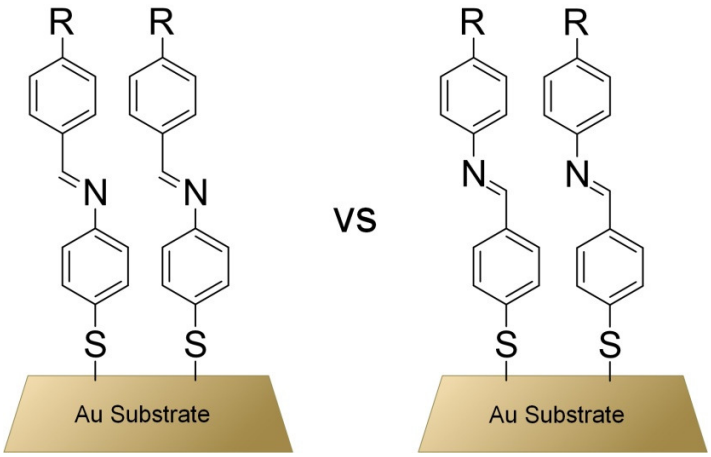

Figure 7.1. SAMs with different Schiff base backbones which could potentially result in opposite dipole moments on the surface. R = π-donating and π-accepting groups.

7.3. Ultrafast Excited-state Deactivation of Bis(diarylamino)biphenyl-based Fluorophores Attached to Gold Nanoparticles

The studies of bis(diarylamino)biphenyl-thiol (TPD-thiol) coated gold nanoparticles (Au NPs) showed that the excited-state deactivation of the organic fluorophore attached to the metal surface is ultrafast – the lifetime of the dye was found to be reduced by more than two orders of magnitude with respect to the lifetime of the same free molecule in the absence of Au NPs. This finding is of significant importance as it implies that in applications taking advantage of the excited states of similar dyes, e.g. in optical pulse suppression applications, preparing systems in which Au NPs are in close

proximity to the dyes will most likely result in quenching of the exciting states, and will likely limit the ability of the dyes to perform their desired function. For example, there are reports proposing the use of Au and Ag NPs in photovoltaic applications to take advantage of the local field enhancements near the particle surface, and to increase the rate of absorption of organic chromophores.[5,6] However, while there is a possibility of taking advantage of the local field enhancements, the chromophores placed in the close proximity of Au NPs may experience quenching due to the energy transfer to the Au NP, similarly to what was described in this thesis.

The existing reports regarding energy transfer from organic fluorophores to Au NPs have shown that the dependence of the distance between the dye and the Au NP surface, *r*, on the nonradiative rate of excited-state deactivation, k_{nr}, can be described by: $k_{nr} \propto \frac{1}{r^4}$.[7,8] However, these reports have focused only on systems in which the distance between the dye and the Au NP was rather large (7 – 17 nm), and the studied organic fluorophores included only green and red-fluorescent dyes.[7,8] The observed dependence of the distance between the dye and the Au NP surface on the nonradiative rate of TPD-excited-state deactivation has been found to follow: $k_{nr} \propto \frac{1}{r}$, and is thought to be dominated by energy transfer from the photoexcited dye to the metallic core of the Au NP. To the best of the author's knowledge this is the first report of the nonradiative deactivation rate of photoexcited blue-fluorescent organic dyes placed in close proximity (ca. 1 nm) of Au NPs. The observed distance dependence is rather surprising and opens questions regarding the exact mechanism of the energy transfer. These can be, in principle, addressed by designing future experiments involving probing ultrafast

dynamics of dyes with different fluorescent properties, in particular the spectral range of emission, from those of TPD.

The excited-state decay of the dyes attached to Au NPs studied herein has been found to proceed via an additional deactivation channel in the systems incorporating short alkyl linkers between the dye and the surface-anchoring thiol group. These systems exhibited solid-like behavior showing a photoinduced formation of a species similar to a species photogenerated in the neat film of TPD. It has been suggested that the formation of the species involved a dye-dye interaction, which was facilitated by the close dye-dye distance in the Au NPs systems incorporating the short alkyl linkers. This shows that the excited-state dynamics in dye-coated Au NPs can be affected not only by interactions of the photoexcited dyes with the metallic core of a Au NP but also by dye-dye interactions.

It is important to note that this work demonstrates it is feasible to selectively probe ultrafast excited-state dynamics of organic dyes attached to Au NPs by employing fs transient absorption technique in the NIR region. This opens the door for future studies of systems in which parameters such as NP size and photophysical properties of the dye can be varied systematically.

7.4. References

(1) Ishii, H.; Sugiyama, K.; Ito, E.; Seki, K. *Adv. Mater.* **1999**, *11*, 605-625.
(2) Bumm, L. A.; Arnold, J. J.; Cygan, M. T.; Dunbar, T. D.; Burgin, T. P.; Jones, L., II; Allara, D. L.; Tour, J. M.; Weiss, P. S. *Science (Washington, D. C.)* **1996**, *271*, 1705-07.
(3) Wold, D. J.; Frisbie, C. D. *J. Am. Chem. Soc.* **2001**, *123*, 5549-5556.
(4) Campbell, I. H.; Kress, J. D.; Martin, R. L.; Smith, D. L.; Barashkov, N. N.; Ferraris, J. P. *Appl. Phys. Lett.* **1997**, *71*, 3528-3530.
(5) Kim, S.-S.; Na, S.-I.; Jo, J.; Kim, D.-Y.; Nah, Y.-C. *Appl. Phys. Lett.* **2008**, *93*, 073307.
(6) Lee, J. H.; Park, J. H.; Kim, J. S.; Lee, D. Y.; Cho, K. *Org. Electron.* **2009**, *10*, 416-420.
(7) Jennings, T. L.; Singh, M. P.; Strouse, G. F. *J. Am. Chem. Soc.* **2006**, *128*, 5462-5467.
(8) Yun, C. S.; Javier, A.; Jennings, T.; Fisher, M.; Hira, S.; Peterson, S.; Hopkins, B.; Reich, N. O.; Strouse, G. F. *J. Am. Chem. Soc.* **2005**, *127*, 3115-3119.